Unlocking oncogene dependent cell death in pancreatic tumours

Anna Elisabeth Richards

Thesis submitted for the award of PhD

March 2023

Summary

Despite advances in our understanding of pancreatic ductal adenocarcinoma (PDAC) over the past few decades, it remains associated with a 5-year survival rate of less than 10% and accounts for over 90% of all pancreatic cancer cases. Non-specific symptoms result in patients presenting with advanced, often unresectable disease at diagnosis. In this setting, current standard-of-care treatment only extends survival by 10-12 months, highlighting an urgent need for the development of more targeted therapeutic approaches.

Present in over 90% of all human PDAC tumours, mutant KRAS (mKRAS) represents a crucial target in the drive to improve therapeutic approaches. Amongst many malignant signalling roles, mKRAS hijacks apoptosis-inducing TRAIL-R signalling to instead drive non-canonical, pro-survival pathways in PDAC. The anti-apoptotic protein, cFLIP, suppresses canonical TRAIL-induced apoptosis. Using a combination of complete genetic deletion and small molecule inhibition, we aimed to determine whether cFLIP inhibition was sufficient to re-activate canonical TRAIL signalling and, therefore, specifically induce apoptosis within mKRAS PDAC cells.

We demonstrated that human PDAC tumours expressing high levels of cFLIP, TRAIL and TRAIL-Rs were associated with significantly reduced survival. Moreover, cFLIP deletion (FLIPi) successfully sensitised a resistant panel of KRAS-mutant PDAC cell lines to TRAIL-induced apoptosis *in vitro*. Similarly, tamoxifen-induced FLIPi within PDAC tumours in a novel, genetically engineered mouse model lead to increased levels of apoptosis *in vivo*. Whilst *ex vivo* FLIPi in tumour-derived organoids established from the same transgenic model resulted in significantly reduced organoid viability, particularly in combination with exogenous TRAIL. Finally, a novel small molecule cFLIP inhibitor, OH14, significantly increased apoptosis in the classical *pdx1-Cre;* LSL-*KRAS*^{G12D}*;* LSL-*Trp53*^{R172H} (KPC) transgenic model of PDAC *in vivo*.

Overall, these results support the further investigation of cFLIP inhibition as a therapeutic intervention specifically targeting KRAS-mutant PDAC tumours in the hope of improving the survival outcomes of this aggressive malignancy.

Acknowledgements

Firstly, I would like to thank my supervisor Prof. Richard Clarkson for the opportunity to undertake my PhD project in his lab and for providing me with support and guidance as I navigated this long journey. I would also like to thank my co-supervisor Dr. Catherine Hogan for introducing me to the world of the pancreas and for her support and mentorship throughout the project. Equally, I would like to thank my co-supervisor Prof. Jen Morton and her team at the Cancer Research UK Beatson Institute who were invaluable in setting up the preclinical models and provided much-appreciated expertise and knowledge. I would also like to acknowledge the support of my funders, the Pancreatic Cancer Research Fund (PCRF), without whom, this project and the related travelling to present my findings would not have been possible

I am hugely grateful to my colleagues and friends at ECSCRI who supported me through the project and made it much more enjoyable. I would particularly like to thank all past and present members of the Clarkson and Hogan labs, including Rhiannon French, Kok Yung Lee, Gillian Seaton, Markella Alatsatianos, Beatriz Salvador Barbero, Liam Hill and Joshua D'Ambrogio for their support in teaching me the necessary laboratory techniques and their contribution of ideas throughout the project. Additionally, I am indebted to Dr. Helen Pearson and her lab for enabling me to work whilst writing up this thesis and for her much-appreciated support and mentorship. I'd like to thank Dr. Stephen Paisey for his enthusiasm and support in training and assisting me with the PET imaging components of this project, as well as for kindly proofreading the relevant sections of my thesis. Equally, I would like to thank Prof. Kevin Bradley for sharing his knowledge and expertise to assist with the PET imaging analysis. I would also like to thank the T2 and HP Facility teams for their invaluable assistance with the transgenic components of this project, including Patrick Mason, Rebecca Underwood, Paul Chapman and Asif Jeelani.

Finally, I would like to extend a massive thank you to my family and friends for their support and for providing a welcome escape when things got tough. Particularly, my parents, Lynda and Paul Richards, my rock, Shweta Rajput, and Peppy for always being there no matter what.

Abbreviations

APAF1 Apoptotic peptidase activating factor 1

CASP3 Caspase 3

CASP7 Caspase 7

CASP8 Caspase 8

CASP9 Caspase 9

CC3 Cleaved Caspase 3

cDNA complementary DNA

cFLIP cellular FLICE-like inhibitory protein

CRISPR Clustered regularly interspaced short palindromic repeats

CTB Cell titer blue

DD Death domain

DED Death effector domain

DISC Death Inducing Signalling Complex

DR Death Receptor

EGFR Epidermal Growth Factor Receptor

EPCCL Established Pancreatic Cancer Cell Line

FADD Fas associated via death domain

FBZ Fenbendazole

FQ Fluoroquinone

GAP GTPase Activating Protein

GDP Guanosine disphosphate

GEF Guanine Nucleotide Exchange Factor

GEMM Genetically Engineered Mouse Model

GEPIA2 Gene Expression Profiling Interactive Analysis 2

GTP Guanosine triphosphate

HDAC Histone deacetylase

KRAS Kirsten Rat Sarcoma

MAPK Mitogen-activated protein kinase

MIP Maximum intensity projection

MMP-9 Matrix Metalloproteinase-9

MOMP Mitochondrial outer membrane permeabilisation

MPD Membrane proximal domain

NF-κB - Nuclear factor kappa-light-chain-enhancer of activated B cells

PCD Programmed cell death

Pdx1 Pancreatic and Duodenal Homeobox 1

PDCL Primary-derived Pancreatic Cancer Cell Line

PI3K Phosphatidylinositol 3-kinase

pro-CASP8 Pro-caspase 8

pro-CASP9 Pro-caspase 9

pro-CASP10 Pro-caspase 10

Rac1 Ras-related C3 botulinum toxin substrate 1

RAF Rapidly accelerated fibrosarcoma

RANKL Receptor activator of nuclear factor kappa-B ligand

RCD Regulated cell death

RNAse Ribonuclease

ROCK Rho-associated Kinase

shRNA Short hairpin RNA

SUV Specific uptake value

TME Tumour microenvironment

TNF-SF Tumour necrosis factor super family

TNF-R SF Tumour necrosis factor receptor super family

TP53 Tumour protein p53

TRAIL TNF-related apoptosis inducing ligand

XIAP X-linked inhibitor of apoptosis protein

Table of Contents

Table of Figures

Table of Tables

1 Introduction

1.1 Pancreatic Ductal Adenocarcinoma (PDAC)

As the fourth leading cause of cancer-related deaths in Europe, pancreatic cancer is an aggressive malignancy that is associated with a 5-year survival rate of only 11% (Ferlay et al. 2018; Siegel et al. 2022).

Pancreatic Ductal Adenocarcinoma (PDAC) accounts for over 90% of all pancreatic cancer cases (Orth et al. 2019). PDAC incidence varies widely between countries, with Europe and North America associated with the highest incidence (roughly 9.5 per 100,000 males and 7 per 100,000 females) and the lowest rates recorded in Africa and Central Asia (roughly 1 per 100,000 males and 0.7 per 100,000 females). However, PDAC incidence rates and associated deaths are predicted to double over the next decade, particularly in Western countries. Many emerging public health challenges, including an ageing society and an ever-increasing rise in obesity, smoking and alcohol consumption are also known risk factors thought to drive PDAC development (Olson et al. 2010). Indeed, the majority of PDAC cases appear to be sporadic and not associated with any known genetic predisposition, with modifiable lifestyle factors thought to accelerate disease progression through exposure to toxic DNA damage-inducing agents (for example tobacco) and inflammation (Orth et al. 2019; Ushio et al. 2021; Partyka et al. 2023). Equally, alternative pathological conditions of the pancreas, including the new onset of diabetes (NOD) and chronic pancreatitis, have also been shown to greatly increase pancreatic cancer risk. Non-modifiable, hereditary factors (for example mutations in the BRCA-2 gene) are associated with roughly 10% of all PDAC cases, with a known family history resulting in a 9- to 32-fold increase in the risk of developing the disease (Grover and Syngal 2010; Partyka et al. 2023).

1.1.1 PDAC Treatment Landscape

Currently, surgical resection combined with systemic chemotherapy and radiation represents the only potentially curative PDAC treatment (Cloyd et al. 2017). However,

due to a lack of specific symptoms, most patients present in the clinic with advanced and unresectable disease (Werner et al. 2013; Orth et al. 2019). Progress in chemotherapeutic regimes over the past 20-30 years has gradually improved disease-free and overall survival in the short term (<12 months), but this has yet to meaningfully impact longer-term (5-10 years) rates (Siegel et al. 2022). Consistently low survival rates indicate a need for improved treatments and earlier diagnosis, developed in accordance with an increasing understanding of disease aetiology and heterogeneity.

1.1.2   PDAC Heterogeneity

PDAC is thought to arise following a stepwise accumulation of mutations in the acinar cell population of the pancreas, leading to progression through a series of pre-invasive pancreatic intraepithelial neoplasia (PanIN) and ultimately resulting in metastatic PDAC ***(Figure 1.1)*** (Gopinathan et al. 2015; Orth et al. 2019). Invasive disease is associated with early dissemination of tumour cells and a notoriously dense desmoplastic stromal microenvironment, potentially underlying the frequent resistance to conventional chemotherapy. Desmoplasia represents a key pathological feature of PDAC, involving the formation of a highly fibrotic tumour microenvironment which mainly consists of cancer-associated fibroblasts (CAFs) and the deposition of a dense extracellular matrix (ECM) to form a supportive and notoriously protective physical barrier around the tumour cells (Erkan et al. 2012).
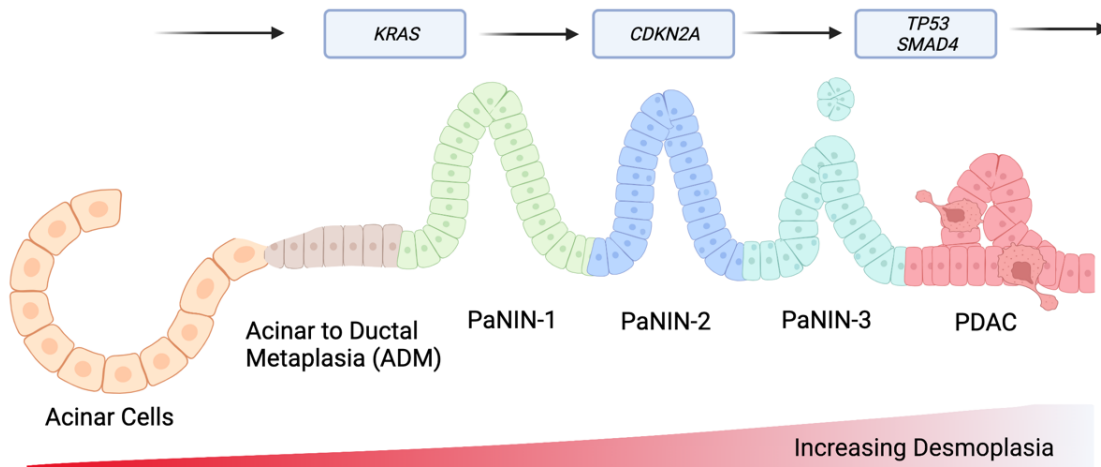
Figure 1-1 Development and progression of pancreatic ductal adenocarcinoma (PDAC).
A step-wise accumulation of several key mutations and increasing desmoplasia is thought to result in the transformation of normal exocrine pancreatic acinar cells into an invasive PDAC tumour. Acinar to Ductal Metaplasia (ADM) begins the process, whereby acinar cells acquire a more ductal cell-like phenotype. Due to further mutations and cellular expansion, these pre-malignant cells begin to transform into various stages of non-invasive pancreatic intra-epithelial neoplasia (PaNIN). Due to further accumulation of mutations, high grade PaNIN-3 ultimately leads to metastatic PDAC which is often highly aggressive and resistant to most therapeutic approaches. Figure adapted from Orth et al (2019) and created with Biorender.com.

Human PDAC can be divided into stages based on disease malignancy and prognostic potential. Stage I includes very small, non-metastatic tumours from <2cm diameter (Stage IA) up to and including those with a diameter of 4cm (Stage IB) (Shin and Kim 2020). Stage II encapsulates larger, non-metastatic tumours with >4cm diameter (Stage IIA) and those which are rendered 'unresectable' due to involvement with key arteries (Stage IIB). Stage III involves any size tumour with no regional lymph node metastasis (Stage IIIA) or those with metastasis in 1-3 regional lymph nodes (Stage IIIB). Whilst Stage IV describes the most advanced, metastatic tumours, with the liver, lung and peritoneum representing the most common known metastatic sites (Peixoto et al. 2015).

Despite an accumulation of various mutations during disease progression and a high level of tumour heterogeneity, certain genes are frequently mutated in the majority of human PDAC tumours (Bailey et al. 2016). Mutations in three common tumour suppressor genes (*CDKN2A, TP53, SMAD4)* often arise during disease progression

(Almoguera et al. 1988; Grimont et al. 2022). As one of the most frequently mutated genes in human cancers, *TP53* encodes the TP53 transcription factor protein and is vital to regulate homeostatic cell growth and limit tumorigenesis when functioning normally (Hu et al. 2021). However, over 50% of all human pancreatic tumours harbour various mutations in the *TP53* gene. Mutations can lead to the loss of tumour suppressive functions (LOFs) or, conversely, the gain of functions (GOFs) that promote tumour growth. Tumour-suppressive functions include driving apoptotic cell death and senescence via cyclin-dependent kinase inhibitor 1 (p21) and Bcl-2-associated X protein (Bax) transcription in response to external and internal stressors, whilst tumour-promoting functions following GOF mutations in the *TP53* gene include driving inflammation and metabolic reprogramming via Nuclear factor kappa B (NF-kB) and BReast CAncer gene 1 (BRCA-1) transcription. TP53-mutant tumours have been shown to progress more rapidly and show an impaired response to anti-tumour therapies, resulting in worsened prognosis (Mccubrey et al. 2022). Indeed, in the later stages of PDAC, over 75% of tumours bear some form of functional loss of the TP53 protein.

However, of even greater importance in the context of PDAC, are activating mutations in the *KRAS* gene, as mutant KRAS is associated with over 90% of all PDAC cases.

1.2   KRAS: The master oncogenic regulator

Oncogenic KRAS is known to exert a variety of pro-tumourigenic effects within cells, enhancing disease malignancy and driving metastasis in a variety of human cancers, particularly PDAC (Kamisawa et al. 2016; Bannoura et al. 2021).

Belonging to the Rat Sarcoma (RAS) family of genes, Kirsten RAS (*KRAS*) encodes a small GTPase protein responsible for regulating vital intracellular signalling pathways (Bannoura et al. 2021). When functioning normally, KRAS alternates between active, Guanosine triphosphate (GTP)-bound states and inactive, Guanosine diphosphate (GDP)-bound states to operate as a molecular switch within cells. An inactive, GDP-bound state is common within quiescent cells.

1.2.1 KRAS Signalling

Activation of KRAS occurs following stimulation of transmembrane receptors, including Epidermal Growth Factor Receptor (EGFR), by extracellular signalling molecules *(Figure 1.2)* (Prior et al. 2012). Upon stimulation, KRAS exchanges GDP for GTP, thereby initiating a cascade of downstream signalling pathways. These pathways include crucial cell survival and proliferation pathways such as Rapidly accelerated fibrosarcoma (RAF)/ Mitogen-activated protein kinase (MAPK) and protein kinase B (Akt)/ Phosphatidylinositol 3-kinase (PI3K).

Guanine-nucleotide Exchange Factors (GEFs) facilitate the exchange of GDP to GTP, whilst GTPase Activating Proteins (GAPs) catalyse intrinsic KRAS GTP hydrolysis. Both GEFs and GAPs are responsible for tightly regulating the cycling of KRAS in normal cell settings. GEFs prevent GTP exchange in the absence of extracellular stimuli and GAPs accelerate GTP hydrolysis to rapidly return KRAS back to the inactive state.
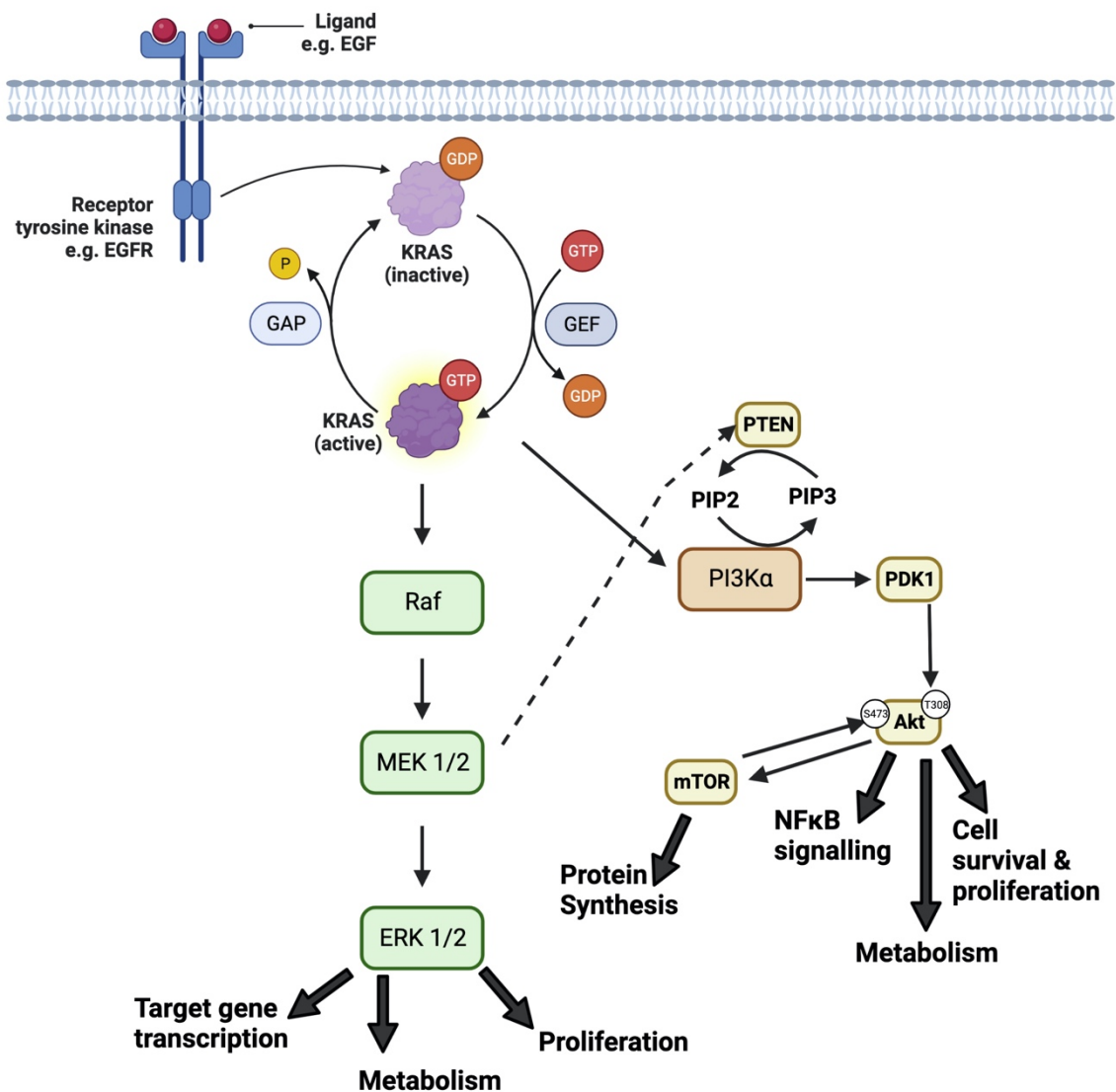
Figure 1-2 KRAS Signalling Pathways.
KRAS is typically sequestered at the cell membrane in an inactive, GDP-bound state. The activation of receptor tyrosine kinases by their respective ligands leads to intracellular receptor conformation changes and kinase activation, ultimately resulting in the recruitment of Guanine-nucleotide Exchange Factors (GEFs) to the cell membrane. GEFs can then interact with the inactive KRAS protein to promote a conformational change and the subsequent exchange of GDP for GTP. Activated KRAS then results in the recruitment and activation of a variety of downstream effector pathways, including Raf/Mek/Erk and PI3K/Pdk1/Akt. Raf is able to bind to an effector region of KRAS-GTP, leading to the translocation and activation of Raf at the cell membrane. Raf in turn, initiates the subsequent downstream activation and phosphorylation of the mitogen-activated protein kinase pathway (RAF-MEK1/2-ERK 1/2), thereby driving pro-survival cell signalling. Activated MEK 1/2 can also activate anti-tumourigenic signalling by facilitating the membrane recruitment of known tumour-suppressor, PTEN. KRAS drives increased proliferation and survival via the activation of the PI3K-PDK1-AKT pathway. Activated, GTP-bound KRAS directly activates the p110 subunit of PI3K, stimulating the conversion of PIP2 to PIP3 and thereby offering docking sites for downstream proteins, including PDK1 and Akt. PDK1 then phosphorylates and activates Akt at the T308 site. Among many crucial roles, Akt is responsible for removing mTOR suppression (via TSC2 phosphorylation), thereby resulting in elevated mTOR activity. Furthermore, Akt is able to directly activate the mTOR complex 2 (mTORC2), ultimately catalysing the full activation of Akt following its phosphorylation at the S473 site by mTORC2. The conversion of PIP2 to PIP3 is antagonised at the membrane in the presence of PTEN. Figure adapted from Eser et al. (2014) and "KRAS Signaling; The O'Bryan Laboratory", by BioRender.com (2023). Retrieved from https://app.biorender.com/biorender-templates.

1.2.2   RAS mutations

Mutant forms of the RAS proteins are prevalent in a wide variety of tumour cells (Prior et al. 2012). *RAS* mutations impair the protein's ability to hydrolyse GTP, thus resulting in a permanently active, GTP-bound state. Aberrant RAS hyperactivity within cells facilitates several key hallmarks of cancer including increased cellular proliferation and survival (Eser et al. 2014; Hanahan 2022).

1.2.3   KRAS mutations in PDAC

As mentioned previously, KRAS is the most prevalent RAS family member within PDAC, with over 90% of all human PDAC tumours possessing some form of *KRAS* mutation (Grimont et al. 2022). Various *KRAS* mutations have been documented, with an activating point mutation in codon 12 occurring most frequently in PDAC tumours (Bannoura et al. 2021). This mutation results in a single amino acid substitution from glycine to either aspartic acid, valine, arginine, alanine or cysteine *(Table 1.1)*. KRAS G12D (Glycine -> Aspartic Acid) represents the dominant isoform found in PDAC.

The G12 site is found at the active site of the KRAS protein, consisting of two switch regions (Switch-I, residues 25-40; Switch II, residues 60-74) and a phosphate-binding loop (P-loop, residues 10-17) (Vatansever et al. 2019). Residues in the active site regulate the GTPase function of KRAS by binding to the phosphate groups of GTP, with the Switch regions also being responsible for influencing the binding of effector and regulatory proteins. Therefore, mutations in codon 12 result in direct conformational changes with the KRAS protein active site. For example, a G12D mutation in the P-loop results in a bulkier and negatively charged side group being projected into the active site, causing a steric hindrance to GTP hydrolysis. This impairs the GTPase function of KRAS, thereby 'locking' the protein in its active (GTP-bound) state. Mutant KRAS signalling has been shown to be crucial in both the initiation and maintenance of invasive PDAC (Collins et al. 2012). Further research has also elucidated its vital role in cell death signalling and anti-tumour immunity (Von Karstedt and Walczak 2020).

Table 1-1 Frequency of point mutations at Codon 12 of the KRAS gene in human PDAC tumours.
Adapted from Prior et al. (2012) who used the COSMIC v52 database to obtain data representing the total numbers of tumours with each point mutation. The most frequent mutations found in PDAC tumours are highlighted in bold. The single-base mutations which generate each amino acid substitution are also indicated.

KRAS	Codon 12: GGT	
Substitution	Name of Mutation	% of tumours
-C-	G12A	2
T--	G12C	3
-A-	**G12D**	**49**
C--	G12R	12
A--	G12S	3
-T-	**G12V**	**31**

Despite only differing at the level of a single amino acid substitution, studies have shown that each missense mutation at the G12 site of KRAS leads to vastly different structural and biochemical consequences (Hobbs et al. 2016). Indeed, PDAC tumours possessing only KRAS G12R mutations have been associated with increased overall survival, whilst KRAS G12D mutant tumours were associated with the worst overall survival. At the signalling pathway level, the KRAS-G12D isoform has been associated with decreased affinity for its downstream Raf effector, in comparison to G12A, G12V and G12R isoforms (Huang et al. 2021b). Furthermore, a study investigating non-small cell lung carcinoma (NSCLC) demonstrated that KRAS G12D but not KRAS G12C-expressing cell lines showed increased levels of AKT phosphorylation (Ihle et al. 2012). Thereby suggesting that the G12D mutation may induce a conformational or biochemical change resulting in the favouring of the PI3K-Akt pathway by activated KRAS, as opposed to the Raf-Mek-Erk pathway (Figure 1.2).

1.2.4 Targeting mutant KRAS in Pancreatic Cancer

Despite ongoing research and increasingly promising pre-clinical results, direct targeting of mutant KRAS in pancreatic cancer has yet to translate into beneficial clinical outcomes (Parkin et al. 2018; Choi et al. 2019).

However, recent progress in this area has proved successful within the non-small-cell lung carcinoma (NSCLC) field. Like PDAC, NSCLC is frequently associated with mutant KRAS, which is found in roughly 30% of all NSCLC cases (Biernacka et al. 2016). Following promising results, an inhibitor specific to the KRAS G12C mutation, AMG-510, was developed and has recently been granted FDA approval for treatment of KRAS G12C mutant NSCLC (Skoulidis et al. 2021). Previously considered "un-druggable" due to its high affinity for GTP and lack of alternative binding pockets, this recent development raises hope that successful, direct targeting of other mutant KRAS isoforms is achievable (Bannoura et al. 2021). However, the clinical validation of inhibitors specific to the far more prevalent G12D isoform will be necessary to increase the potential impact of this therapy in treating PDAC tumours. Whilst research to this end is ongoing, and preclinical data is highly encouraging, it is also pertinent to explore other means of exploiting the oncogene's prevalence in this inherently therapy-resistant disease (Bannoura et al. 2022; Hallin et al. 2022; Wang et al. 2022).

Due to its role as a 'master regulator' within tumour cells, mutant KRAS is involved in many important downstream signalling pathways, including the pro-survival PI3K-PDK1-Akt pathway *(Figure 1.2)*. Inhibitors targeting some of these downstream effector pathways are currently in development for PDAC, however, these have also been associated with limited clinical efficacy (von Karstedt et al. 2015; Bannoura et al. 2021). Therefore, the drive to find a clinically feasible method of targeting the prevalence of oncogenic KRAS in PDAC continues.

1.3 TRAIL and its receptors

The TNF-related apoptosis inducing ligand (TRAIL) signalling pathway has been shown to function downstream to mutant KRAS in pancreatic tumour cells (von Karstedt et al. 2015).

1.3.1 TRAIL

As a member of the TNF super family (TNF-SF), TRAIL is synthesised as a Type II transmembrane protein (Locksley et al. 2001). TNF-SF members are mainly expressed as

transmembrane or cleaved, soluble proteins by activated immune cells. Therefore, tumours are constitutively exposed to a variety of TNF-SF ligands, including TRAIL, due to the abundance of immune cells recruited to the tumour microenvironment (TME) (Aggarwal 2003; Von Karstedt and Walczak 2020).

1.3.2 Human TRAIL Receptors

TNF-SF ligands bind to members of the corresponding TNF Receptor super family (TNF-R SF) (Locksley et al. 2001; Von Karstedt and Walczak 2020). Six members of the receptor super family are known as Death Receptors (DR) as they also contain a cytoplasmic 'death domain' (DD) adaptor, which is required for activating cell death pathways. Two of the most extensively researched DRs are the two TRAIL receptors, TRAIL-R1 and TRAIL-R2 (also known as DR4 and DR5 respectively).

TRAIL is able to bind to 5 different receptors in humans, comprising two which contain a DD (DR4 and DR5), two which do not contain a DD (TRAIL-R3 and TRAIL-R4) and Osteoprotegerin (OPG), a soluble RANKL receptor, which has been shown to also bind TRAIL *(Figure 1.3)* (Von Karstedt and Walczak 2020). Non-DD-containing TRAIL receptors are commonly referred to as 'decoy receptors', which are thought to sequester TRAIL and prevent its interaction with the DD-containing receptors, thereby inhibiting the initiation of apoptosis as their lack of a functional DD prevents them from activating cell death pathways. However, little evidence currently exists to support this theory in the absence of over-expression conditions. Indeed, previous studies in a variety of cancer types found a generally low endogenous expression level of decoy receptors, thereby requiring the stable overexpression of either isoform to reliably inhibit TRAIL-induced apoptosis (Degli-Esposti et al. 1997; Bouralexis et al. 2003; Mérino et al. 2006).
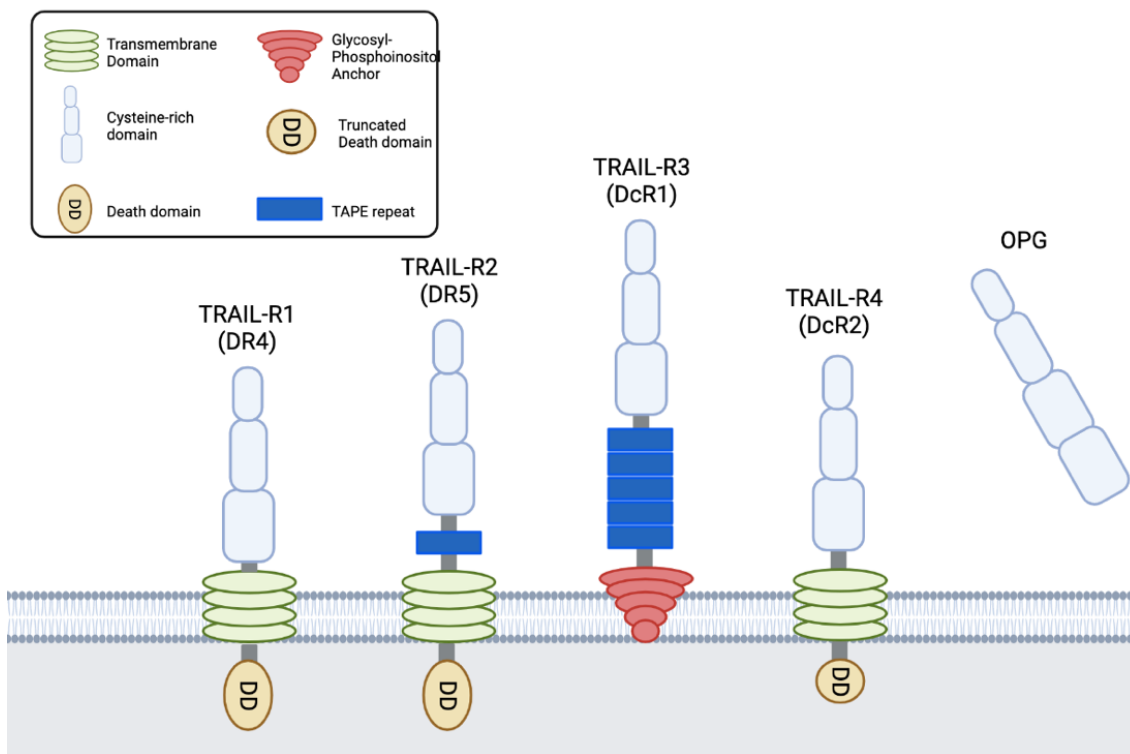
Figure 1-3 Structure of human TRAIL receptors.
The TRAIL cytokine can bind to four membrane-bound and one soluble receptor. Due to the presence of a functional death domain (DD), TRAIL binding to DR4 or DR5 can induce apoptosis. DcR1 and DcR2 and the soluble receptor osteoprotegerin (OPG) do not possess functional DDs and therefore cannot instigate apoptosis upon TRAIL binding. Figure adapted from Lemke et al. (2014) and created using Biorender.com.

1.3.3 Murine TRAIL Receptors

In mice, TRAIL is only able to bind to one receptor containing a DD (mTRAIL-R) which shows sequence homology to both human TRAIL DRs (DR4 and DR5) (Wu et al. 1999; Von Karstedt et al. 2017). Two additional murine TRAIL receptors which do not contain a DD have also been identified (mDcTRAIL-R1 and mDCTRAIL-R2).

1.3.4 TRAIL Signalling and tumour cells

TRAIL and its receptors have been extensively studied following the ground-breaking discovery that treatment with recombinant TRAIL selectively induced apoptosis within tumour cells *in vivo*, leaving normal cells unharmed (Ashkenazi et al. 1999; Lynch et al. 1999). This selectivity is key, as many other TNF-SF members, including TNF and CD95L, are able to induce apoptotic pathways in cells by binding to their respective cognate receptors, however, stimulating their activation induces systemic toxicity due to non-

specific targeting of normal, non-tumour cells (Ogasawara et al. 1993; Roberts et al. 2011; Modiano and Bellgrau 2016). The tumour selectivity of TRAIL may occur due to the frequent upregulation of DRs by certain tumour cells, including PDAC (Daniels et al. 2005). It should be noted that this upregulation does not occur in all tumours. However, tumours with elevated DR expression appear to exhibit innate resistance to TRAIL-induced apoptosis (Keane et al. 1999; Lemke et al. 2014).

1.4   Apoptosis and TRAIL Signalling

1.4.1   Apoptosis

Apoptosis is a conserved form of regulated cell death (RCD) that often underlies the cytotoxic effect of conventional chemotherapies, including those used to treat pancreatic cancer (Haag et al. 2011). RCD is a key feature of tissue turnover and developmental processes, involving the targeted elimination of damaged or potentially harmful cells to maintain physiological homeostasis (Jacobson et al. 1997; Galluzzi et al. 2018).

Cells undergoing apoptosis *in vivo* generally retain low levels of metabolic activity and plasma membrane integrity to facilitate their rapid phagocytosis (Green et al. 2016). This process, termed "efferocytosis", maintains tissue health through the recruitment of phagocytes to dying cells. Phagocytes can recognise, engulf and clear the apoptotic cells due to a carefully balanced feedback mechanism, which involves the ability of macrophages to reduce the secretion of pro-inflammatory cytokines upon the engulfment of apoptotic cells, and, instead, stimulate an anti-inflammatory environment to mediate resolution and repair conditions *in vivo* (Doran et al. 2020). Due to the absence of phagocytes, end-stage apoptosis *in vitro* is often associated with a complete breakdown of the plasma membrane, a response likely to induce significant pro-inflammatory signalling and a potentially harmful immune response if it occurred *in vivo* (Galluzzi et al. 2018).

Apoptosis can be triggered due to extracellular microenvironment disruption (extrinsic apoptosis) or intracellular stress (intrinsic apoptosis) *(Figure 1.4)* (Fuchs and Steller

12

2015). Both pathways differ in terms of signal transduction, however, both share a requirement for key regulatory cysteine-dependent proteases, known as caspases, in order to execute apoptosis (Mcilwain et al. 2013). Executioner caspases rapidly cause apoptotic cell death through the cleavage of proteins involved in key cellular functions (Kale et al. 2018). The proteolytic activity of executioner caspases drives cellular destruction and is responsible for many morphological and biochemical characteristics of apoptosis, including DNA fragmentation and the exposure of phosphatidylserine (PS) on the extracellular surface (Galluzzi et al. 2018).
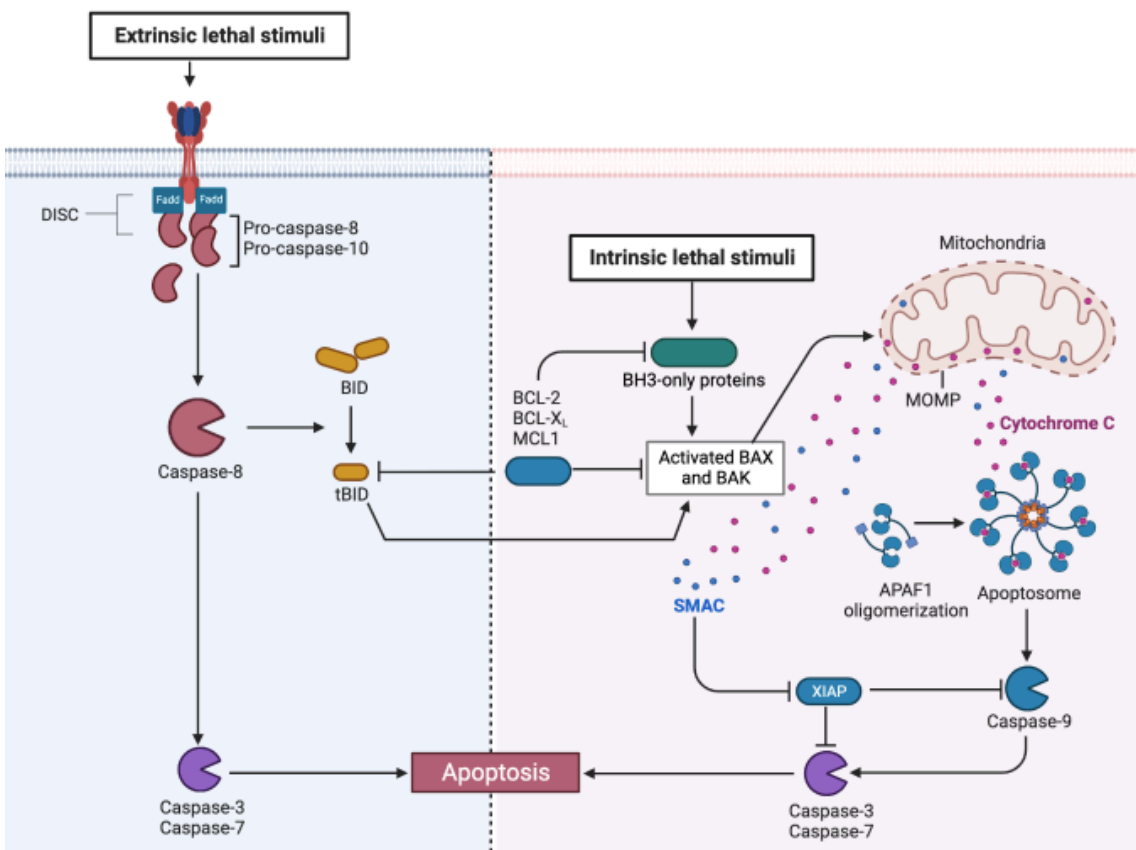
Figure 1-4 Intrinsic and extrinsic apoptotic cascades.
Intrinsic Apoptosis occurs following intracellular lethal stimuli, including growth factor starvation, and requires irreversible mitochondrial outer membrane permeabilisation (MOMP) which is mediated by activated BCL2 family proteins (BAX and/or BAK). MOMP involves the formation of pores within the mitochondrial outer membrane, enabling the release of pro-apoptotic factors, including cytochrome c and SMAC. Cytochrome c binds to APAF1 and pro-caspase 9 in a deoxyATP-dependent manner to form the Apoptosome, which leads to caspase 9 activation. Whilst SMAC facilitates apoptosis by associating with inhibitor of apoptosis (IAP) family members including XIAP. Activated caspase 9 then goes on to proteolytically activate the other executioner capsases (caspase-3 and caspase-7) which are responsible for apoptotic cellular destruction. **Extrinsic Apoptosis** is activated by extracellular stimuli, including the activation of death receptors. Primarily initiated by proximity-induced caspase-8 activation, extrinsic apoptosis can activate the intrinsic apoptotic pathway via cleavage of BID to form truncated BID (tBID) which activates BAX and/or BAK. However, extrinsic apoptosis can also occur through direct caspase-8 mediated activation of caspases-3 and -7 in certain cell types. *Adapted from Galluzzi et al. (2018) and "Apoptosis Extrinsic and Intrinsic Pathways", by Biorender.com (2022). Retrieved from https://app.biorender.com/biorender-templates. APAF1 = apoptotic peptidase activating factor 1; BAX = BCL2 associated X, apoptosis regulator; BAK = BCL2 antagonist/killer 1; BID = BH3 interacting domain death agonist; SMAC = second mitochondrial activator of caspases; XIAP = X-linked inhibitor of apoptosis (XIAP).*

1.4.1.1 Intrinsic Apoptosis

A variety of intracellular stresses are known to activate the intrinsic apoptotic pathway, including irreversible DNA damage, growth factor starvation and accumulation of reactive oxygen species (ROS) (Brumatti et al. 2010; Roos et al. 2016; Galluzzi et al. 2018).

Unlike the extrinsic pathway, intrinsic apoptosis requires the irreversible process of mitochondrial outer membrane permeabilisation (MOMP). MOMP is tightly regulated by pro- and anti-apoptotic members of the BCL-2 protein family (Kale et al. 2018). Interactions between BCL-2 family members directly determine cell fate, with the relative abundance and affinity of each member, in addition to relevant upstream apoptotic stimuli, proving crucial in enabling the execution of the intrinsic apoptotic pathway.

Should the balance tip towards pro-apoptotic members of the BCL-2 family, intrinsic apoptosis is triggered by the formation of pores within the mitochondrial outer membrane. This leads to the release of pro-apoptotic factors, including cytochrome c, from the mitochondrial intermembrane space into the cytosol (Galluzzi et al. 2018). Cytosolic cytochrome c is then able to bind apoptotic peptidase activating factor 1 (APAF1) and pro-caspase 9 (pro-CASP9) to form an apoptosome. The apoptosome

activates pro-CASP9, thereby releasing activated caspase 9 (CASP9) enzymes which catalyse the activation of the other executioner caspases (CASP3 and CASP7).

As discussed in section 1.1.2, the TP53 transcription factor can influence the intricate balance between BCL-2 family members, as non-mutant forms of TP53 drive the expression of pro-apoptotic BCL-2 family member, Bax, to promote apoptosis in response to external or internal stressors, such as exposure to DNA-damaging agents and hypoxia (Lavin and Gueven 2006; Hu et al. 2021). LOF mutations in the TP53 gene, a common feature in advanced PDAC tumours, may therefore negatively tip the balance between BCL-2 family members and, thereby, impair the apoptotic capacity of the tumour cell.

1.4.1.2 Extrinsic Apoptosis

Extrinsic apoptosis occurs in response to extracellular stimulation which is detected by specialised plasma membrane receptors (Galluzzi et al. 2018). The apoptotic signal is driven primarily by activated caspase-8 (CASP8) and expedited by the executioner caspases, particularly caspase-3 (CASP3).

Extrinsic apoptosis can be initiated by two classes of plasma membrane receptor: death receptors (DRs) or dependence receptors. Dependence receptors activate apoptosis should levels of their cognate ligands drop below a particular threshold. Whereas death receptors, including the TRAIL DRs, require the binding of their cognate ligand in order to induce extrinsic apoptosis.

Two major mechanisms of apoptosis in response to DR activation are thought to exist, effectively dividing cells into "Type I" or "Type II" categories (Barnhart et al. 2003; Jost et al. 2009; Galluzzi et al. 2018). "Type I" cells include thymocytes and mature lymphocytes and solely require CASP8-dependent activation of CASP3 and CASP7 to drive apoptosis. "Type II" cells include the majority of cancer cells and require the downstream activation of the intrinsic apoptotic pathway in order to execute apoptosis in response to DR stimulation.

1.4.2   TRAIL-induced Apoptosis

TRAIL binding to its death receptors (DR4 & DR5) initiates the extrinsic apoptotic cascade by stabilising pre-existing receptor homotrimers (Lemke et al. 2014; Galluzzi et al. 2018). Stabilisation of the TRAIL DRs results in an intracellular receptor conformation change and enables the death domain-dependent recruitment of adaptor molecule Fas associated via death domain (FADD). The binding of FADD leads to the formation of a death inducing signalling complex (DISC) and promotes the recruitment, maturation, and activation of the initiator pro-caspase 8 (pro-CASP8). The binding of initiator pro-caspases to FADD at the DISC results in the formation of a linear chain of pro-CASP8 molecules due to death effector domain (DED)-dependent interactions. Proximity-induced homo-dimerisation within the chain leads to caspase 8 (CASP8) activation following auto-proteolytic cleavage.

Within "Type I" cells, CASP8 activation is sufficient to activate downstream CASP3 and induce apoptosis. However, "Type II" cells require the CASP8-mediated cleavage of pro-apoptotic BCL-2 family member, Bid, to release activated truncated Bid (tBid) (Wei et al. 2000; de Miguel et al. 2016). tBid facilitates the insertion of other pro-apoptotic BCL-2 family members into the mitochondrial outer membrane, resulting in the activation of MOMP and execution of the downstream intrinsic apoptotic pathway. In the absence of negative, anti-apoptotic regulation, the TRAIL-induced apoptotic pathway rapidly induces apoptosis, with cell death observed *in vitro* within 2-4 hours of induction (Cheng and Ferrell 2018).

1.4.3   Anti-Apoptotic Proteins

Tight regulation of TRAIL-mediated apoptosis occurs at all levels of the cascade in order to prevent excessive cell death in healthy tissues (de Miguel et al. 2016). These regulatory mechanisms are often hijacked by tumour cells in their mission to evade apoptosis. Regulation begins at the expression level of TRAIL receptors, with the balance between levels of DD-containing and non-DD-containing receptors potentially dictating the intracellular response to TRAIL binding.

From the formation of the DISC to eventual executioner caspase activation, various anti-apoptotic proteins function to regulate progression of the canonical apoptotic pathway. These range from cellular FLICE-like inhibitory protein (cFLIP) which functions at the beginning of the cascade to prevent CASP8 maturation all the way to X-linked inhibitor of apoptosis protein (XIAP) which binds the downstream executioner caspases and prevents their proteolytic activity (Irmler et al. 1997; Bratton et al. 2002).

1.4.4 Non-Canonical TRAIL Signalling Pathways

In addition to the ability of anti-apoptotic proteins to inhibit TRAIL-induced apoptosis, several studies have also highlighted alternative, non-apoptotic functions of TRAIL signalling (Aggarwal 2003; Ishimura et al. 2006; Trauzold et al. 2006; Azijli et al. 2013). Importantly, these non-canonical responses appear to drive aggressive, metastatic phenotypes in tumour cells. It is proposed that, in cells resistant to TRAIL-induced apoptosis, TRAIL binding is not sufficient to activate the canonical pathway. This tips the balance towards non-canonical activity, including the activation of NF-κB. NF-κB signalling has a variety of both pro-apoptotic and anti-apoptotic regulatory roles within cells. However, it is thought that in the context of non-canonical TRAIL stimulation, NFκB contributes to the promotion of a migratory, invasive response.

1.4.5 Oncogenic KRAS and Non-Canonical TRAIL Signalling in PDAC

Interestingly, KRAS mutations appear to drive constitutive TRAIL signalling in pancreatic tumour cells *in vivo*, but this does not lead to a corresponding increase in apoptosis (von Karstedt et al. 2015). It was found that KRAS-mediated suppression of Rho-associated Kinase (ROCK) lead to increased Rac1 expression. Increased levels of Rac1 were then able to associate with the membrane-proximal domain (MPD) of TRAIL receptor, DR5, in humans or mTRAIL-R in mice, thereby leading to Rac1 activation and the promotion of malignant signalling via the PI3K pathway in pancreatic tumour cells *(Figure 1.5).*
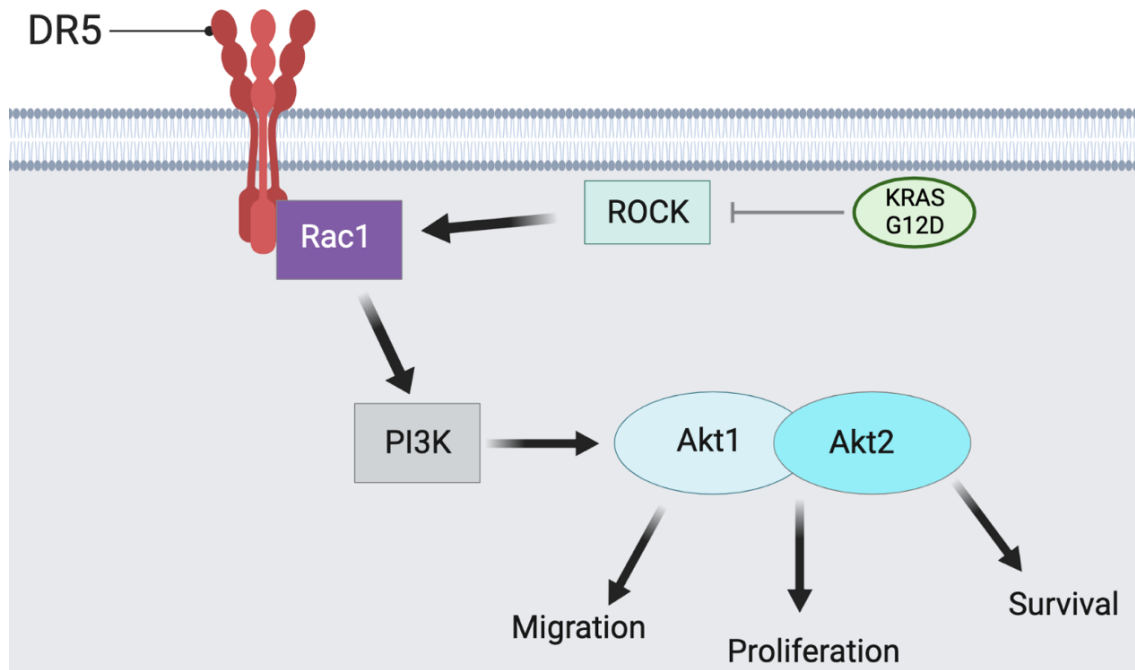
Figure 1-5 Non-canonical TRAIL signalling in KRAS mutant PDAC cells.
The inhibition of Rho associated kinase (ROCK) by the G12D mutant isoform of Kirsten Rat Sarcoma (KRAS) results in increased expression of Rac1 in PDAC tumour cells. Rac1 associates with the membrane proximal domain of the DR5 TRAIL receptor in order to drive downstream, PI3K-mediated increases in migration, proliferation and survival pathways. Figure created using Biorender.com. *Rac1 = Ras-related C3 botulinum toxin substrate 1; PI3K = Phosphatidylinositol 3-kinase; DR5 = Death receptor 5; TRAIL = TNF-related apoptosis inducing ligand; PDAC = Pancreatic ductal adenocarcinoma.*

1.5   cFLIP as a putative therapeutic target in PDAC

1.5.1   cFLIP

As previously mentioned, cFLIP is a potent anti-apoptotic protein functioning at the beginning of the TRAIL-mediated apoptotic cascade to regulate activity of the DISC and the progression of the canonical apoptosis pathway (Irmler et al. 1997; de Miguel et al. 2016).

cFLIP is recruited to the DISC following the initial binding of FADD to pro-CASP8 and serves as a crucial regulator of CASP8 activity (Hughes et al. 2016). Although commonly referred to as an 'anti-apoptotic protein', different mRNA splice variants of cFLIP hugely influence its regulation of the apoptotic cascade (Irmler et al. 1997; Krueger et al. 2001).

1.5.2 Role of cFLIP splice variants in apoptosis regulation

Human cells express three protein isoforms of cFLIP, the 26kDa cFLIP short (cFLIP-S), the 24kDa cFLIP-R and the 55kDa cFLIP long (cFLIP-L) isoforms (Safa 2012; Hughes et al. 2016; Humphreys et al. 2018). Mice have been found to only possess cFLIP-R and cFLIP-L isoforms (Ueffing et al. 2008). As truncated versions of pro-CASP8, both cFLIP-S and cFLIP-R only contain tandem DED repeats and exclusively function in an anti-apoptotic manner by blocking catalytically active interactions of pro-CASP8 molecules at the DISC (Hughes et al. 2016).

cFLIP-L isoforms almost completely mimic the structure of pro-CASP8, however, they lack its proteolytic capacity due to the absence of a catalytic cysteine residue. cFLIP-L isoforms have been associated with both pro- and anti-apoptotic roles, due to their context-dependent ability to activate or inhibit CASP8 (Chang 2002; Yu et al. 2009; Kavuri et al. 2011).

Through a co-operative and hierarchical process, cFLIP isoform recruitment to the DISC via heterodimerisation with pro-CASP8 is promoted following the binding of FADD to pro-CASP8 *(Figure 1.6)* (Hughes et al. 2016). The composition of these heterodimers is often vital in determining the fate of DR activation within cells. Interestingly, pro-CASP8/cFLIP-L heterodimers appear to stimulate DED-mediated recruitment of additional pro-CASP8 molecules to the DISC, thereby driving apoptosis. It has also been shown that pro-CASP8/cFLIP-L heterodimers function to inhibit RIPK3-dependent programmed necrosis (Oberst et al. 2011). Conversely, pro-CASP8/cFLIP-S heterodimers lack enzymatic activity and represent powerful pro-CASP8 activation inhibitors (Hughes et al. 2016). However, high levels of either cFLIP-S or cFLIP-L have been shown to inhibit formation of pro-CASP8 oligomers and potently prevent DISC activation.
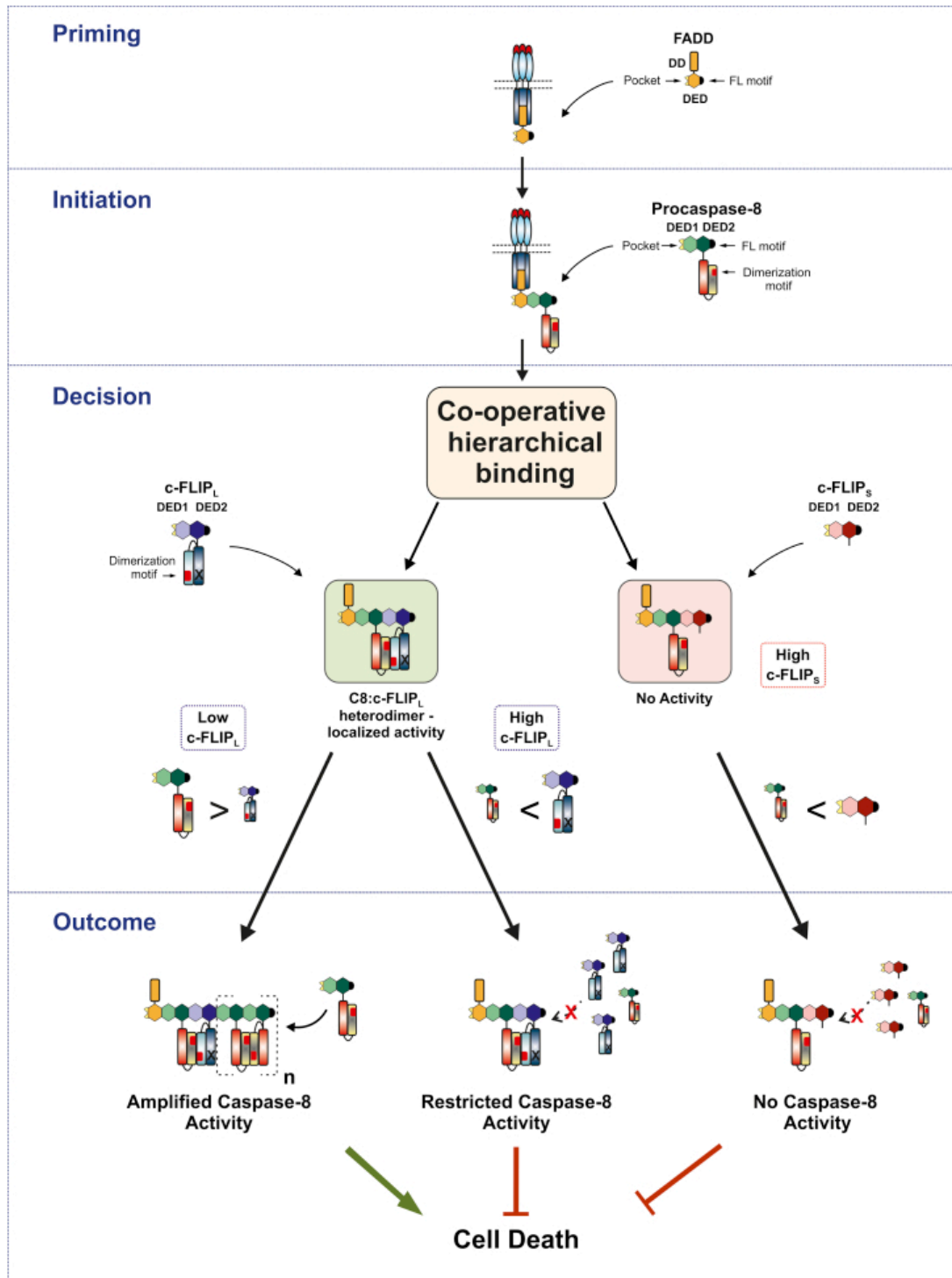
Figure 1-6 Hierarchical model depicting cFLIP isoform-dependent apoptotic regulation.
The DD-dependent binding of FADD to activated death receptors represents the 'priming' event which leads to 'initiation' via DED-dependent recruitment of pro-caspase 8 to FADD. Proximity-induced homodimerisation of pro-caspase 8 results in the activation of caspase 8. During the 'decision' process, expression levels of the different cFLIP isoforms directly influence the downstream outcome of pro-caspase 8 recruitment. Heterodimers formed of cFLIP-L and procaspase-8 can promote increased procaspase-8 recruitment and, ultimately, drive cell death, providing cellular levels of cFLIP-L are low. High expression levels of cFLIP-L results in the restriction of procaspase-8 oligomer assembly and heterodimer activity, thereby inhibiting cell death. cFLIP-S cannot easily form DED oligomers; therefore cFLIP-S exclusively inhibits cell death. Figure taken from Hughes et al. (2016). *cFLIP = cellular FLICE inhibitory protein; DD = Death domain; DED = Death effector domain; FADD = Fas associated via death domain.*

1.5.3 cFLIP in PDAC

Recent findings suggest that cFLIP is only expressed by malignant pancreatic cells, with the anti-apoptotic protein being detected in PanIN and PDAC primary histological samples but not in normal pancreatic ducts (Haag et al. 2011). A range of KRAS mutant PDAC cell lines have also been shown to express varying levels of cFLIP-L and cFLIP-S, which, importantly contrasts with low to non-existent expression in KRAS wild type (WT) and normal pancreatic duct epithelial cells (Haag et al. 2011; Johnston et al. 2020). Collectively, these findings suggest that healthy, normal cells and tissues have little requirement for cFLIP expression, whilst the protein becomes far more important during tumorigenesis and tumour growth.

Patient stratification according to the expression level of *CFLAR* (the gene encoding cFLIP) and *TNFRSF10B* (the gene encoding DR5) also results in different disease-free survival outcomes within PDAC patient cohorts (Johnston et al. 2020). ***Figure 1.7*** shows that tumours with high expression of either gene are associated with worsened prognosis, with high *CFLAR* expression significantly decreasing disease-free survival. A positive correlation between *CFLAR* and *TNFRSF10B* expression levels also indicates that patients with high levels of cFLIP also possess high levels of DR5. This suggests that the worsened prognosis associated with high expression of cFLIP and/or DR5 may be due to PDAC tumours upregulating cFLIP to prevent a canonical apoptotic response to the increased levels of DR5 which may be required to drive non-canonical, malignant TRIAL signalling, as described in Section 1.4.5.
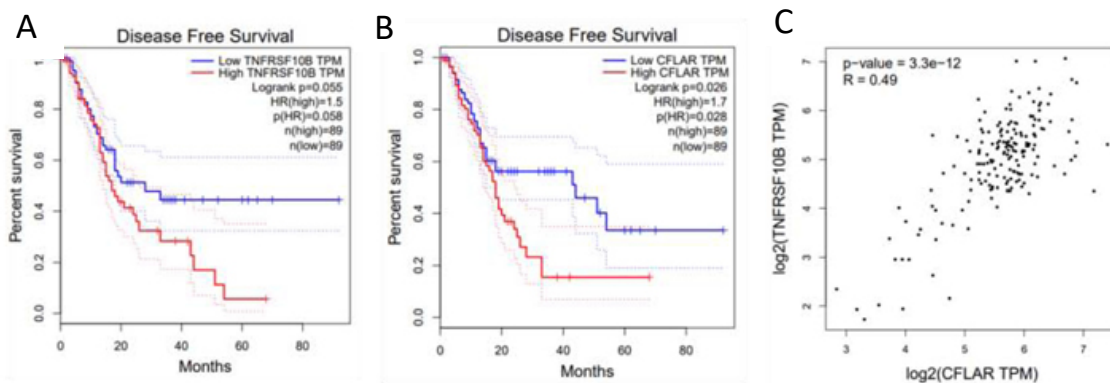
Figure 1-7 Impact of CFLAR and TNFRSF10B expression on PDAC clinical prognosis.
A, B Disease free survival plots comparing patients with high and low expression of genes encoding TRAIL DR5 (TNFRSF10B) and cFLIP (CFLAR) respectively. **C** Correlation plot showing a positive correlation between expression of both genes within the patient tumour cohort. Figure adapted from Johnston et al. (2020) and derived from their findings using GEPIA.com RNASeq data.

1.5.4   cFLIP and resistance to TRAIL-induced apoptosis in cancer

Likely due to its anti-apoptotic function, cFLIP is frequently overexpressed in a wide range of cancers, including, but not limited to, NSCLC, PDAC, colorectal cancer and prostate cancer (Ryu et al. 2001; Korkolopoulou et al. 2007; Haag et al. 2011; Mccourt et al. 2012; Riley et al. 2013). It should also be noted that cFLIP is able to promote a variety of pro-survival and pro-invasion signalling pathways in addition to its anti-apoptotic role, although the exact mechanisms underlying the role of cFLIP in pro-survival signalling remains poorly understood. *(Figure 1.8)* (Safa et al. 2019).
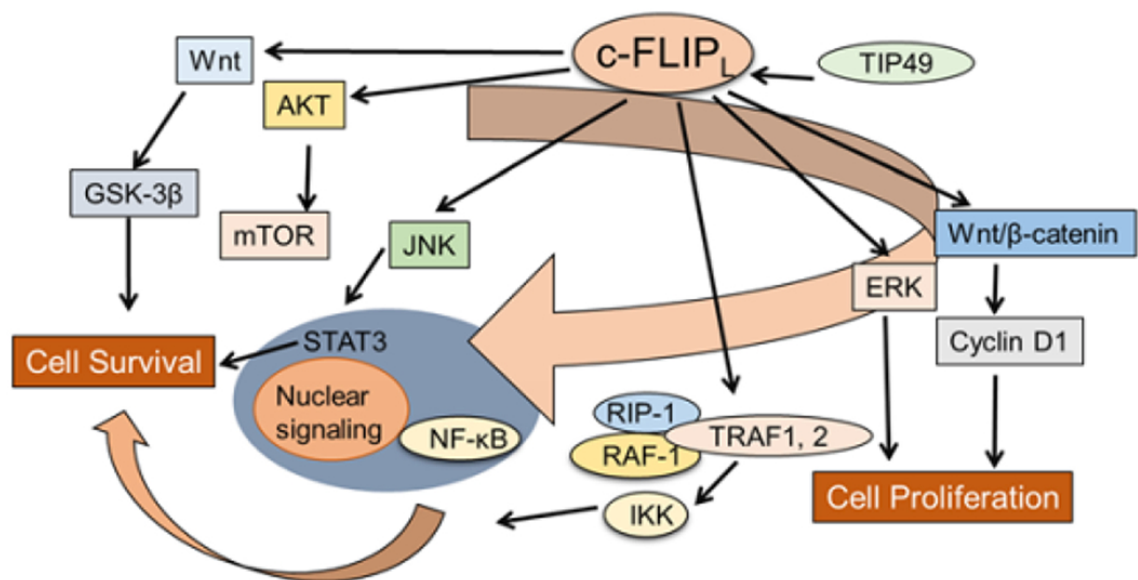
Figure 1-8 Involvement of cFLIP-L isoform with pro-survival and pro-proliferation signalling pathways.
In addition to its role as an anti-apoptotic protein, cFLIP activates and/or upregulates a variety of cytoprotective, pro-survival signalling proteins, including Akt, Raf-1 and Wnt. For example, elevated expression levels of cFLIP-L have been shown to activate NF-kB and ERK signalling by binding to relevant adaptor proteins in each pathway, including Raf-1. Furthermore, cFLIP enhances the canonical, pro-survival Wnt signalling pathway by inhibiting the proteasomal degradation of β-catenin. Many of these interactions remain poorly understood but appear to contribute to the role of cFLIP in promoting therapeutic resistance and malignancy in tumours. Figure adapted from Safa et al. (2019). *cFLIP = cellular FLICE-inhibitory protein; Akt = Protein Kinase B; Raf-1 = Raf-1 Proto-Oncogene, Serine/Threonine Kinase; NF-kB = Nuclear factor kappa B. ERK = extracellular-signal-regulated kinase.*

Interestingly, cFLIP has been shown to interact with and promote several signalling pathways known to function downstream to activated KRAS in tumours, including Raf-Mek-Erk and Akt-mTOR (Kataoka et al. 2000; Kataoka and Tschopp 2004; Safa et al.

2019). As discussed in section 1.2.2, different KRAS mutations at the G12 codon can impact the protein's affinity with specific downstream pathways (Huang et al. 2021b). For example, a KRAS G12D mutant appears to preferentially drive the Akt-mTOR pathway in comparison to the Raf-Mek-Erk pathway. This suggests that the ability of cFLIP to directly bind to and activate Raf-1 to drive the pro-survival ERK pathway, may function as a compensatory mechanism in the presence of KRAS G12D, thereby enhancing malignant signalling. Indeed, in addition to the role of cFLIP in inhibiting apoptosis, a synergy between mutant KRAS and cFLIP to drive simultaneous activation of both downstream KRAS target pathways, may underlie the poor prognosis associated with PDAC tumours that express high levels of cFLIP protein (Johnston et al. 2020).

Therapeutic resistance and immune evasion have consistently been associated with the upregulation of cFLIP within tumour cells (Medema et al. 1999; Safa et al. 2019). Indeed, the over-expression of cFLIP found in so many varieties of human cancers, including PDAC, has been shown to drastically worsen their prognosis (Riley et al. 2013; Schmid et al. 2013; Yao et al. 2016; Humphreys et al. 2018; Johnston et al. 2020). Recently, it has transpired that subcellular localisation of cFLIP may represent an equally important prognostic biomarker, with high levels of cytoplasmic cFLIP associated with decreased overall survival in NSCLC patients compared to high levels of nuclear cFLIP (Humphreys et al. 2018). cFLIP appears to exert such a prominent prognostic effect due to its role in conferring resistance to a broad range of anti-cancer agents (Safa et al. 2019).

1.5.5 cFLIP inhibition

The silencing or inhibition of cFLIP has successfully restored apoptotic signalling and enhanced chemosensitivity in a variety of cancers (Piggott et al. 2011; Safa and Pollok 2011; Huang et al. 2016; Safa et al. 2019). cFLIP inhibition also represents an effective method of sensitising the notoriously chemo-resistant cancer stem cell (CSC) compartment of certain tumours to chemotherapeutic or TRAIL-mediated targeting (Piggott et al. 2011; Zhitao et al. 2015; Safa 2016). Effective elimination of CSCs is vital in removing the key pool of stem-like tumour cells with the capacity to drive metastasis and re-initiate tumour growth following treatment (Safa et al. 2019).

1.5.5.1 Indirect cFLIP targeting

Various standard-of-care chemotherapies, including 5-fluorouracil (5-FU), gemcitabine and paclitaxel, have been shown to indirectly induce a decrease in cFLIP mRNA expression across many tumour cell line models (Humphreys et al. 2018). However, the mechanism of action underlying this response remains poorly understood and cell-type specific.

Histone deacetylase (HDAC) inhibitors are frequently reported to decrease cFLIP mRNA expression and induce chemosensitivity within a range of tumour cells (Rao-Bindal et al. 2013; Venza et al. 2014; Humphreys et al. 2018). HDAC inhibitors, such as vorinostat and romidepsin, are approved by the US Food and Drug Administration (FDA) to alter gene expression patterns and induce apoptosis in neoplastic cells by targeting epigenetic regulator enzymes, HDACs (Parveen et al. 2023). Inappropriate HDAC expression is frequently responsible for pro-tumour gene repression in a variety of cancer types. HDAC inhibitors are known to increase the cytotoxic response to conventional chemotherapy (Shabason et al. 2010). However, their off-target impact on the expression of a wide range of alternative genes impairs their clinical feasibility as a viable method of cFLIP inhibition (Humphreys et al. 2018). Additionally, due to the role of cFLIP in maintaining tissue homeostasis in healthy, non-diseased skin and intestinal cells, systemic cFLIP gene repression may directly underlie some of the off-target side-effects observed (Weinlich et al. 2013).

1.5.5.2 Direct cFLIP targeting

Selective targeting of cFLIP presents a promising avenue which avoids the potential off-target effects of indirect cFLIP inhibitors. Although challenging, directly targeting the role of cFLIP in inhibiting apoptosis, as opposed to complete cFLIP repression at the gene level, increases the likelihood of a tolerable therapeutic approach by reducing the risk of systemic, off-target cytotoxicity. Due to its high levels of structural homology to pro-CASP8, direct targeting of cFLIP poses an intricate problem.

1.5.6 Development of a novel small molecule cFLIP inhibitor

Our laboratory is currently in the process of developing a novel small molecule cFLIP inhibitor, which was discovered by *in silico* protein modelling, and has been shown to target the DED1 binding pocket of cFLIP (Hayward, unpublished). Crucially, this small molecule inhibitor, OH14, does not interrupt the function of pro-CASP8 or pro-CASP10, thereby enabling the progression of TRAIL-induced apoptosis. However, it does prevent the interaction of cFLIP with FADD and pro-CASP8. It has been shown to successfully sensitise cancer cell lines to TRAIL-mediated apoptosis and selectively target cancer stem cells (CSCs), enabling extended tumour-free survival *(Appendix A1 & A2)* (Hayward, French and Lee, unpublished).

1.5.7 Targeting cFLIP to re-activate TRAIL-induced Apoptosis in PDAC

Recent work suggests that cFLIP inhibition may represent a viable therapeutic approach in the race to discover more targeted and tolerable treatment methods for PDAC.

Short hairpin RNA (shRNA) inhibition of either cFLIP-S or cFLIP-L was sufficient to sensitise resistant PDAC cell lines to TRAIL-induced apoptosis *in vitro* (Haag et al. 2011)*.* Indirect cFLIP suppression using 5-FU or cisplatin also sensitised primary-derived human PDAC cell lines to TRAIL-induced apoptosis, underlining the potential clinical relevance of the approach.

1.6 The "cFLIP switch" hypothesis

The discovery that non-canonical TRAIL/DR5 signalling appears to promote malignancy in KRAS-mutant PDAC tumour cells (von Karstedt et al. 2015) suggests that these cells may be utilising an internal 'brake' to evade the canonical apoptotic response. This work proposes that cFLIP functions as this 'brake', maintaining tumour cell viability whilst malignant signalling pathways facilitate disease progression and drive the tumour-promoting properties of TRAIL signalling in PDAC. We, therefore, hypothesise that direct inhibition of cFLIP should be sufficient to "flip the switch" and re-activate apoptosis, thereby selectively eliminating KRAS-mutant PDAC cells *(Figure 1.9).*
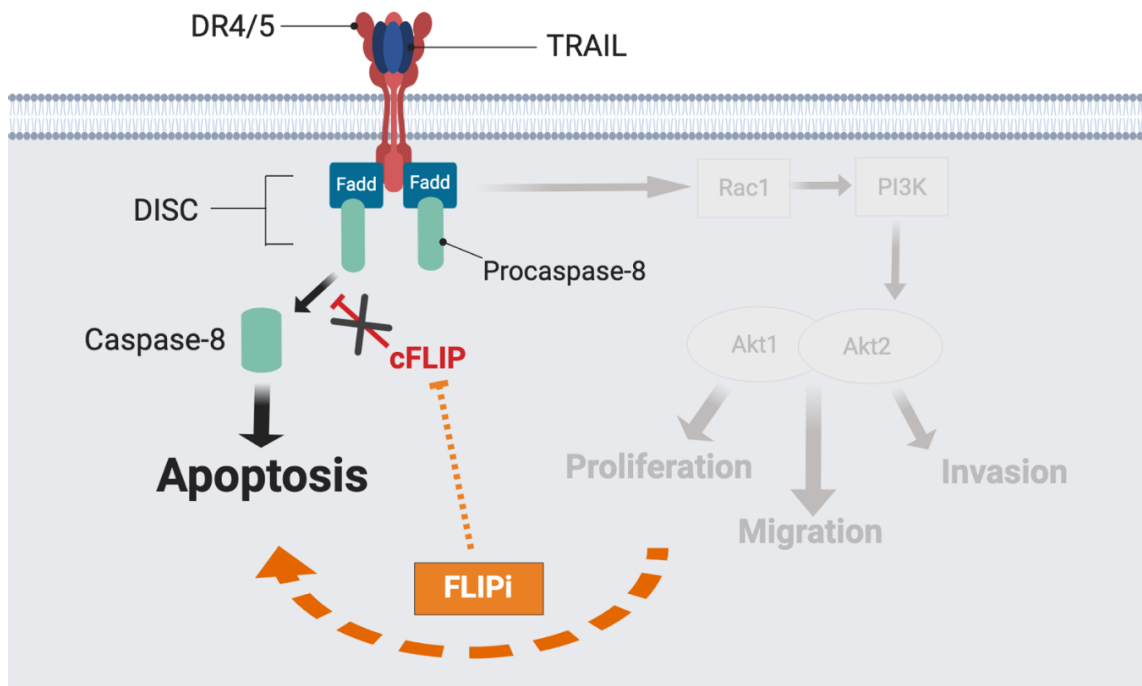
Figure 1-9 Hypothetical model depicting potential response to cFLIP inhibition (FLIPi) in KRAS-mutant PDAC cells.
Mutant KRAS drives non-canonical, Rac1-mediated malignant signalling in PDAC cells. It is hypothesised that removal of potent anti-apoptotic protein cFLIP will be sufficient to re-activate apoptosis specifically within these tumour cells by removing the 'brakes' from the canonical TRAIL-induced apoptotic pathway. Figure created with Biorender.com.

This hypothesis is supported by recent data demonstrating that high expression levels of cFLIP and TRAIL receptor, DR5, result in significantly reduced disease-free survival of PDAC patients (Johnston et al. 2020). Furthermore, previous attempts to inhibit cFLIP expression in select PDAC cell lines have successfully sensitised resistant cells to TRAIL-mediated apoptosis (Haag et al. 2011). Along with many others, our laboratory has also proven the potential of cFLIP inhibition in re-activating apoptosis within a variety of different cancer types, ultimately resulting in the development of a novel small molecule inhibitor of cFLIP, OH14 (Hayward, unpublished).

1.7   Project Aims & Objectives

Therefore, this work aims to determine whether inhibition of cFLIP (FLIPi) is sufficient to re-activate canonical apoptotic signalling in pancreatic tumour cells *in vitro*, *in vivo* and *ex vivo*. This approach may result in increased levels of apoptosis specifically within KRAS-mutant PDAC cells, potentially leading to an observable reduction in tumour volume and increased overall survival *in vivo*.

Ultimately, the potential of inhibiting cFLIP as a novel therapeutic approach will be evaluated to specifically re-activate apoptosis within the 90% of human PDAC tumours which harbour a mutation in KRAS.

Briefly, the aims of this project are to:

- Utilise *in vitro* models to determine and potentially stratify the response of human PDAC cell lines to cFLIP inhibition.
- Determine the clinical feasibility and potential of cFLIP inhibition in PDAC using immune-competent *in vivo* models.
- Establish PDAC tumour organoids to better interrogate the response of murine tumour cells to cFLIP inhibition *ex vivo*.

2 Materials & Methods

2.1 *In vitro* Techniques

2.1.1 Established Cell Lines

A panel of seven established human pancreatic cancer cell lines (Panc10.05, ASPC-1, HPAF-II, CFPAC-1, Capan-2, SW1990 and BxPC-3) were kindly provided by Dr C. Hogan and Prof R. Clarkson (European Cancer Stem Cell Research Institute, Cardiff University). These cell lines were selected as they possess a wide range of well-characterised mutations which are frequently associated with PDAC. ***Table 2.1*** summarises the findings of the Catalogue of Somatic Mutations in Cancer (COSMIC) database. Five out of the six selected cell lines possess KRAS mutations, which are known to be key drivers of PDAC and are found in over 90% of all human PDAC tumours (Grimont et al. 2022). The BxPC3 cell line was included to represent tumours with wild-type KRAS functional activity. All 7 EPCCLs belong to a collection of 11 well-characterised, two-dimensional (2D) human PDAC cell lines which are routinely used for preclinical investigations (Deer et al. 2010; Low et al. 2021).

Table 2-1 Mutational Status of selected EPCCLs.

Data taken from ATCC and COSMIC Cell lines project database. Hom = Homozygous; Het = Heterozygous

Name	Histology	Tumour Source	Mutant Gene & Zygosity	Gene Sequence	Protein Sequence	References/ ATCC No
Panc 10.05	Adenocarcinoma	Primary	KRAS Het TP53 Het	c.35G>A c.764T>A	p.G12D p.I255N	CRL-2547™
ASPC-1	Adenocarcinoma	Metastasis (Ascites)	CDKN2A Hom FBXW7 Het KRAS Hom MAP2K4 Hom TP53 Hom	c.233_234delTC c.1393C>T c.35G>A c.1?_393+?del c.403delT	p.L78fs*41 p.R465C p.G12D p.? p.C135fs*35	(Chen et al. 1982)
HPAF-II	Adenocarcinoma	Metastasis (Ascites)	CDKN2A Hom KRAS Het TP53 Hom	c.85_101del17 c.35G>A c.451C>T	p.R29fs*9 p.G12D p.P151S	(Metzgar et al. 1982)
CFPAC-1	Ductal Adenocarcinoma	Metastasis (Liver)	KRAS Het SMAD4 Hom TP53 Hom	c.35G>T c.1_1659del1659 c.724T>C	p.G12V p.0? p.C242R	(Schoumacher et al. 1990)
SW1990	Adenocarcinoma	Metastasis (Spleen)	CDKN2A Hom KRAS Hom	c.1_471del471 c.35G>A	p.0? p.G12D	CRL-2172™
BxPC3	Adenocarcinoma	Primary	CDKN2A Hom MAP2K4 Hom SMAD4 Hom TP53 Hom	c.1_471del471 c.1041_1200del160 c.1_1659del1659 c.659A>G	p.0? p.? p.0? p.Y220C	(Tan et al. 1986)
Capan-2	Adenocarcinoma	Primary	KRAS HET	c.35G>T	p.G12V	HTB-80™

2.1.2 Patient-Derived Primary Cell Lines (PDCLs)

The Kinghorn Cancer Centre (TKCC) cell lines were established from primary patient-derived PDAC xenografts and have since undergone extensive sequencing and profiling to determine their respective underlying mutational burden (Waddell et al. 2015; Bailey et al. 2016; Humphrey et al. 2016). The Clarkson lab interrogated the RNASeq data for 50 cell lines included in the study and selected TKCC-05 and TKCC-07 for further analysis. These lines were kindly donated by the Bailey lab (Glasgow University, UK) and chosen due to the differential expression of cFLIP, the two functional TRAIL receptors (-R1 and -R2) and TRAIL ligand (Figure 2.1). Both lines were found to possess significantly mutated forms of key PDAC oncogenic drivers including KRAS (p.G12V) and TP53 (p. G245S and p. Q165* respectively) following mutational landscape analysis conducted by Humphrey and Dryer and colleagues (Humphrey et al. 2016; Dreyer et al. 2021).
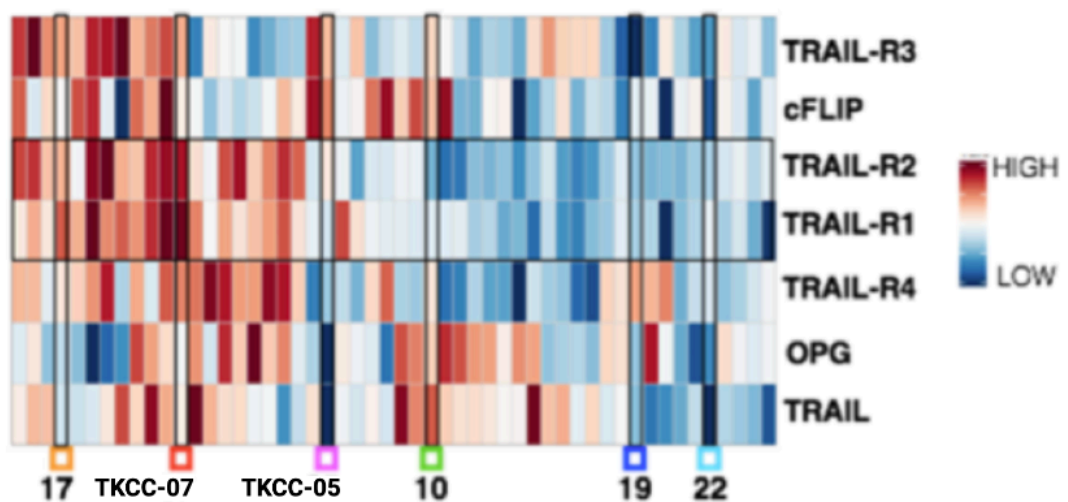
Figure 2-1 cFLIP and TRAIL pathway expression profile of selected TKCC PDCLs.
Heatmap showing comparative RNA expression level of genes encoding various components of the TRAIL pathway in primary-derived PDAC cell lines (PDCLs). Data kindly provided by the Bailey lab (Glasgow University) and analysed by the Clarkson lab (Cardiff University). TKCC = The Kinghorn Cancer Centre.

2.1.3 Cell Line Maintenance

Unless otherwise specified, cell lines were maintained in the appropriate media, as recommended by the American Type Culture Collection (Manassas, VA, USA) or the appropriate modified medium for the primary-derived lines (***Table 2.2, 2.3 & 2.4)***. Each media was also supplemented with 10% foetal bovine serum (ThermoFisher Scientific, MA, USA) and 1% penicillin/streptomycin (ThermoFisher Scientific, MA, USA). All cells were grown in a 37°C incubator containing 5% CO_2 and passaged every four to five days, at recommended ratios for each cell line. Media was changed every two to three days.

Table 2-2 Media requirements of select EPCCLs

Cell Line	Media recommended by the ATCC
Panc 10.05	RPMI-1640
ASPC-1	
BxPC3	
SW1990	Leibovitz's L-15
Capan-2	McCoy's 5A (Modified) Medium
CFPAC-1	Iscove's Modified Dulbecco's Medium (IMDM)

Table 2-3 Modified media requirements of the TKCC-05 PDCL

Component	Add	Final concentration	UK Catalogue number
DMEM/F12	500ml (remove 56ml media first)		11320-074 (Life Technologies)
HEPES (1M)	7.5ml	15mm	15630106 (Life Technologies)
FBS (filtered)	37.5ml	8%	SH30084.03 (Hyclone)
EGF (1mg/L)	5ul	10ng/ml	PHG0311L (Life Technologies)
Hydrocortisone (1 mg/mL in EtOH)	20ul	40ng/ml	H0888-1G (Sigma)
Insulin ActRApid (100 IU/mL)	0.5ml	0.1IU/ml	12585014 (Life Technologies)
Glucose Solution 10%	6ml	0.12%	G8644 (Sigma)
Test media overnight at 37oC and the following day add antibiotics to the bottle.			
Penicillin/streptomycin (100x stock)	5ml		15070063 (Life Technologies)
Gentamicin (2000x stock)	0.25ml		15750037 (Life Technologies)

Table 2-4 Modified media requirements of the TKCC-07 PDCL

Component	Add	Final concentration	UK Catalogue Number
M199/F12 (HAM) Mix at 1:1 ratio	500ml (remove 69ml first)		M199: 31150-022 (Life Technologies) F12 HAM: 21765 (Life Technologies)
HEPES	7.5ml	15mM	15630106 (Life Technologies)
2mM Glutamine (100x stock)	5ml		25030024 (Life Technologies)
EGF (1mg/ml)	10ul	20ng/ml	PHG0311L (Life Technologies)
Hydrocortisone (1mg/ml)	20ul	40ng/ml	H0888-1G (Sigma)
apo-Transferrin (2.5 mg/mL stock)	5ml	5ug/ml	T1147-500mg (Sigma)
Insulin ActRApid (100 IU/mL)	1ml	0.2 IU/ml	12585014 (Life Technologies)
Glucose Solution 10%	3ml	0.06%	G8644 (Sigma)
FBS (filtered)	37.5ml	7.5%	SH30084.03 (Hyclone)
Tri-iodotyronine (0.1 ug/mL)	2.5ul	0.5pg/ml	T6397-100mg (Sigma)
MEM vitamins (100x)	5ml		11120037 (Life Technologies)
O-phosphoryl ethanolamine (20 mg/mL)	50ul	2ug/ml	P0503-1g (Sigma)
Test media overnight at 37oC and the following day add antibiotics to the bottle.			
Penicillin/streptomycin (100x stock)	5ml		15070063 (Life Technologies)
Gentamicin (2000x stock)	0.25ml		15750037 (Life Technologies)

When 80 to 100% confluency was achieved, cells were passaged at appropriate ratios, as recommended by the ATCC (VA, USA). Media was removed from the flask and replaced with 0.25% Trypsin-EDTA (Invitrogen, CA, USA) to cause cell detachment from the flask surface. Cells were permeabilised following seven to nine minutes of incubation in Trypsin, at 37°C with 5% CO_2. Once all cells became round and detached from the bottom of the flask, 7ml of the appropriate culture medium was added. The media, trypsin and cells were then extracted and centrifuged at 1000rpm for 5 minutes. Following centrifugation, the supernatant was aspirated, and the pellet was resuspended in 1ml culture medium. Cells were then seeded at the recommended ratios into new flasks and returned to the incubator.

2.1.4   Freezing Cells

Cells that had undergone a relatively low number of passages were selected for freezing, to avoid genetic drift which may occur with increasing passage numbers. $1x10^6$ cells were resuspended in 1ml freezing media (Dulbecco's Modified Eagle's Medium (DMEM) (Gibco, Germany) supplemented with 10% Dimethyl Sulfoxide (DMSO; Sigma, Missouri, USA) in cryo tubes (ThermoFisher Scientific, MA, USA). Tubes were wrapped in tissue and stored in sealed polystyrene boxes at -80°C for at least two days, before being transferred on dry ice to liquid nitrogen storage.

2.1.5   Establishing Cells from Storage

Cells taken from -80°C or liquid nitrogen storage were transferred to dry ice before being rapidly defrosted and added to 5ml of the appropriate culture medium. Cells were then centrifuged at 1000rpm for 5 minutes. Supernatant was removed and the pellet resuspended in 1ml of appropriate medium. All resuspended cells were then transferred to 7ml fresh culture medium and maintained as previously described.

2.1.6   Seeding cells for functional assays

To seed specific quantities of cells for functional assays, cells were detached from the flask surface and resuspended in 1ml media as described in section 2.1.3. Cells were then counted manually using a haemocytometer or automatically using Fast Read Slides

(Immune Systems, UK). Appropriate dilutions were performed to account for different types of plates. 100ul of cells at the appropriate dilution in media were added to each well of a 96-well plate, whilst 2ml of cells at the appropriate dilution was added to each well of a 6-well plate.

2.1.7 *In vitro* cFLIP Inhibition

2.1.7.1 *small interfering RNA (siRNA) Constructs & Rationale*

Small interfering RNA (siRNA) was used to inhibit expression of cFLIP in PDAC cell lines. siRNAs were selected as the preferred method of targeting cFLIP in this context, as they are able to transiently silence genes of interest whilst avoiding the significant cost and time commitments required for alternative RNA interference methods including CRISPR/Cas9. siRNA inhibits functional protein expression by mediating targeted RNA degradation (Hu et al. 2020).

A commercially available pool of siRNA sequences targeting human cFLIP mRNA (SMARTPool: ON-TARGETplus, Dharmacon, CO, USA) was used to inhibit cFLIP expression. Whilst a pool of commercially available, non-targeting siRNA sequences were used as control (SMARTPool: ON-TARGETplus, Dharmacon, CO, USA). siRNA sequences are shown in **Table 2.5**. The SMARTpool reagents (a mixture of three different siRNAs targeting a single gene) enable the guaranteed targeting of all transcript/splice variants associated with a single gene, as recorded in the RefSeq database (Parsons et al. 2009; Discovery 2023). Therefore, all isoforms arising from the splice variants of the gene encoding cFLIP (cFLIP-L, cFLIP-S and cFLIP-R) would be targeted by the SMARTpool reagents to ensure complete genetic knockdown, however, data regarding sequence alignment is not readily available,

Table 2-5 siRNA sequences

siRNA	Target Sequence (5'-3')	Catalogue Number
Human control ON-TARGETplus SMART Pool	UGGUUUACAUGUCGACUAA UGGUUUACAUGUUGUGUGA UGGUUUACAUGUUUUCUGA UGGUUUACAUGUUUUCCUA	Dharmacon D-001810-10
Human cFLAR ON-TARGETplus SMART Pool	GUGCCGGGAUGUUGCUAUA CAAGCAGUCUGUUCAAGGA CAUGGUAUAUCCCAGAUUC CCUAGGAAUCUGCCUGAUA	Dharmacon L-003772-00-0005

2.1.7.2 siRNA transfection

Approximately 100,000 cells/ml were prepared as described in section 2.1.6. A master mix of siRNA reagents was also prepared according to quantities listed in **Table 2.6** for a 96-well plate.

Table 2-6 siRNA Transfection Reagents

	96-well Plate	6-well Plate	
Reagent	Vol per well (ul)	Vol per well (ul)	Company
OptiMEM	20	3000	ThermoFisher Scientific (MA,USA)
Lipofectamine RNAi MAX	0.3	9	
siRNA (20nM)	0.066	42	Dharmacon (CO, USA)

The master mix was added to each well of a 96-well plate and incubated for 20 minutes at room temperature, before 100ul of cells at the appropriate dilution in media were seeded on top of the mix and incubated at 37°C for 48 hours.

2.1.7.3 Treatment of cell lines with small molecule cFLIP inhibitor (OH14)

Several cell lines were also selected to determine the effect of a novel small molecule cFLIP inhibitor, OH14. The specificity of OH14 in directly inhibiting the ability of cFLIP to prevent the formation of the DISC has previously been demonstrated by members of the Clarkson lab. Cell lines used were Panc10.05, ASPC-1, SW1990 and HPAF-II. Approximately 100,000 cells/ml were seeded in triplicate in a 96-well plate. After twenty-four hours, cells received either 100µM OH14 in 0.1% DMSO (kindly provided by members of the Clarkson lab) or DMSO (Sigma, Missouri, USA) alone.

2.1.7.4 Controlling for non-caspase-mediated apoptotic death & monitoring apoptosis

Twenty-four hours following siRNA transfection or at the same time as OH14 treatment, cells were treated with 50 µM Pan Caspase Inhibitor Z Vad-FMK (R&D Systems, MN, USA) or Dimethyl Sulfoxide (DMSO; Sigma, Missouri, USA). For siRNA assays, another dose of caspase inhibitor or DMSO was provided in addition to IncuCyte® Annexin V Green Reagent (Essen Bioscience, MI, USA), at a dilution of 1:1,000, following an additional 24 hours. For OH14 assays, the Annexin V Green reagent was added at the same time as the OH14 and caspase inhibitors. The pan-

caspase inhibitor, Z Vad-FMK, is known to efficiently prevent the *in vitro* activity of all apoptosis-related caspase activities at micromolar concentrations (Chauvier et al. 2007).

2.1.7.5 Treatment with exogenous TRAIL

Following an hour of incubation with the Annexin V reagent, certain cells were treated with 20ng/ml recombinant human TNF-Related Apoptosis Inducing Ligand (TRAIL) (super-killer TRAIL, ENZO Life Sciences), whilst others remained untreated.

2.1.7.6 IncuCyte apoptosis assay

Cells undergoing apoptosis are known to express Phosphatidylserine (PS) on the outer cell surface. The Annexin V reagent conjugated to a fluorescent dye binds to PS and emits fluorescence which can be detected and quantified in real-time using the Incucyte S3 Live Cell Analysis platform (Essen Bioscience, MI, USA).

Following cFLIP inhibition, Annexin V reagent was added to each well, as described in Section 2.1.7.4. Cells were then maintained in the Incucyte S3 Live Cell Analysis platform (Essen Bioscience, MI, USA), with response recorded every one to two hours for a total of at least 18 hours. Four fields of view were taken per well. IncuCyte® S3 software (Essen Bioscience, MI, USA) was used to generate optimised masks to detect fluorescent and non-fluorescent (phase) cells. This enabled the area of fluorescent cells per image to be normalised to area of non-fluorescent cells. Three technical repeats were performed per cell line and each experiment was repeated independently at least three times.

2.1.7.7 Statistical Analysis

GraphPad Prism 9 software (GraphPad, CA, USA) was used to analyse the data. Results are expressed as mean ± SEM. For Incucyte data with multiple timepoints and treatment groups, a repeated measures one-way analysis of variance (ANOVA) was performed with Tukey correction. For each statistical analysis presented as part of this thesis, data was first tested for normality using GraphPad Prism 9 software to run a Shapiro-Wilk standard deviation normality test and a quantile-quantile (QQ) plot graphical test for

normality. Subsequent statistical tests were then selected according to whether the data was normally distributed.

2.2 Quantification of cFLIP protein content in cell lines: Western Blotting

Differences in cFLIP expression across each cell line was evaluated, to determine whether absolute level of cFLIP expression may influence response to cFLIP inhibition. Western blot enables the identification of proteins through molecular weight-based separation (Mahmood and Yang 2012). Separation is achieved using gel electrophoresis, producing a band for each protein. The gel is then transferred to a membrane which can be incubated with antibodies specific to the protein of interest and detected by developing the membrane. The thickness of the antibody-bound band directly corresponds to the absolute amount of protein present. ***Figure 2.2*** summarises the process.
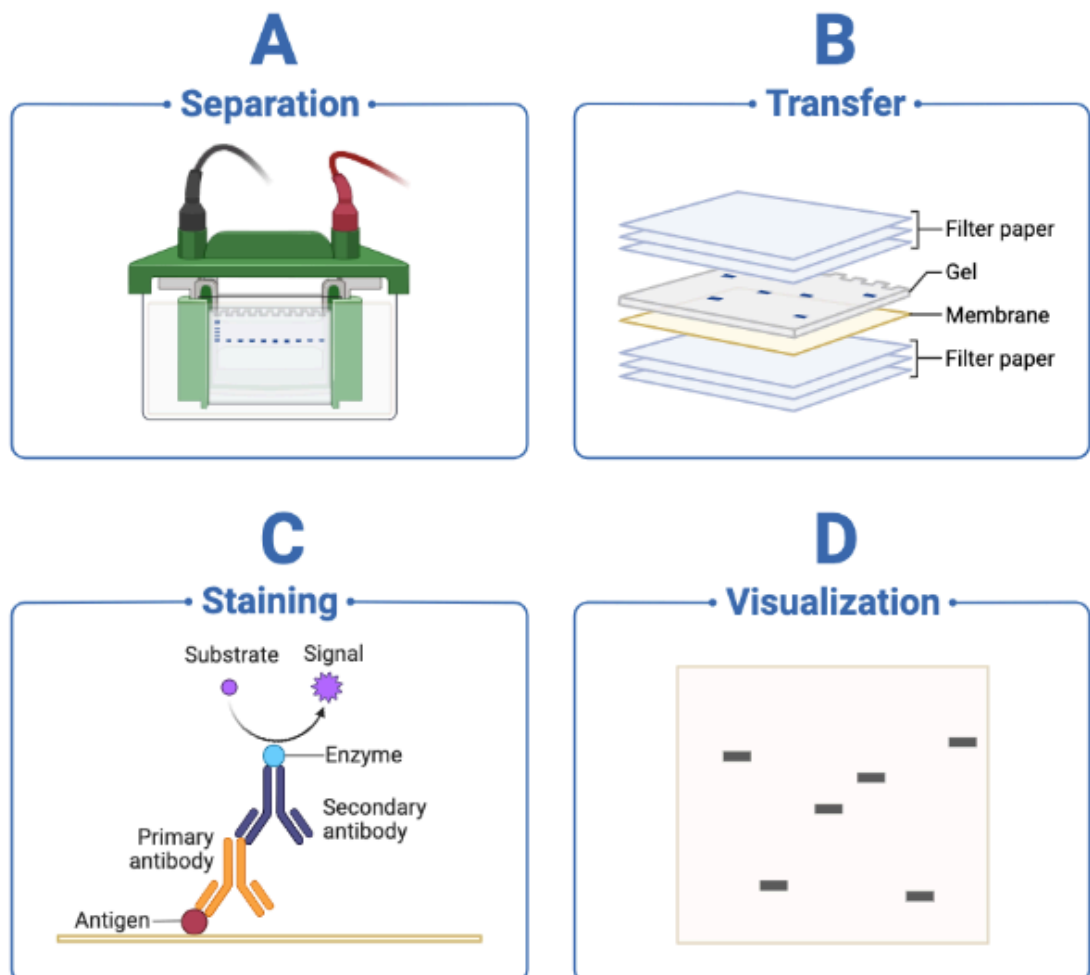
Figure 2-2 General Western Blot workflow.
Reprinted from "Western Blotting Workflow" by Biorender.com (2022). Retrieved from https://app.biorender.com/biorender-templates.

2.2.1   Whole cell lysate harvesting and protein extraction

Once 80-90% confluency was achieved, cells were detached from the flask surface as described in section 2.1.3. The cell, media and trypsin mixture were then centrifuged for 5 minutes at 1250rpm. After centrifugation, the supernatant was removed, and cells were resuspended in 500ul Phosphate Buffered Saline (PBS – ThermoFisher) before being centrifuged for another 5 minutes at 1250rpm. Resuspension with PBS followed by centrifugation was repeated one further time before the supernatant was discarded and the dry cell pellets were stored at -80°C if not being used immediately.

Cell pellets were resuspended in ice-cold RIPA buffer *(Table 2.7)* containing 1x Protease/Phosphatase Inhibitor cocktail (Cell Signalling Technologies). Cells were homogenised by passing through a 23-gauge needle eight times before being incubated on ice for 30-45 minutes. Cells were then centrifuged at 4°C and 13,000rpm for 15 mins. Following centrifugation, 85ul of supernatant was collected and added to 20ul of 2x Laemmli Buffer (Bio-rad). This protein solution was boiled at 95°C for 2 minutes before being stored at -20°C if not being used immediately.

Table 2-7 RIPA buffer components

Component	Quantity	Catalogue Number
1M Tris Base (pH 7.4)	5ml	Sigma (#77-86-1)
10% Nonidet-P40	10ml	Roche (#17545999)
Sodium Deoxycholate	0.25g	ThermoScientific (#89904)
5M Sodium Chloride (NaCl)	3ml	Sigma (#59222C)
0.25M Egtazic Acid (EGTA)	0.4ml	Sigma (#03777)
H20	*Add up to 100ml total*	

Lysate protein concentration was determined using a Pierce™ BCA Protein Assay Kit (ThermoFisher, MA, USA). The BCA assay was performed according to manufacturer instructions. Protein concentration of lysates was determined following comparison with standard samples containing known concentrations of Bovine Serum Albumin (BSA) dissolved in RIPA buffer. Protein concentration was measured using a CLARIOstar (BMGLabTech) plate reader.

2.2.1 Gel production and Protein Separation

Proteins within each lysate were separated according to size by gel electrophoresis using a mini 12% acrylamide gel. Gel components are listed in **Table 2.8**. The resolving gel (pH 8.8) was first loaded between two glass plates separated by a 1mm spacer. A small layer of methanol was then added on top of the liquid resolving gel to ensure gel integrity and then the gel was incubated at room temperature for roughly 40 minutes. Once the resolving gel had set, a stacking gel (pH 6.8) was then loaded between the plates, on top of the solid resolving gel. A 1mm comb was inserted into the stacking gel, which was then left to set at room temperature for approximately 30-40 minutes.

Table 2-8 Western Blot gel composition.

Resolving Gel			Stacking Gel		
Component	Quantity	Catalogue Number	Component	Quantity	Catalogue Number
H_2O	2.5ml		H_2O	3.2ml	
Tris Base in H_2O (1.5mM; pH 8.8)	2.5ml	Sigma (77-86-1)	Tris Base in H_2O (0.5mM; pH 6.8)	1.25ml	Sigma (77-86-1)
50% Glycerol	2ml	Sigma (56-81-5)	30% Acrylamide/Bis-acrylamide	500µl	Sigma (A3699)
30% Acrylamide/Bis-acrylamide	3ml	Sigma (A3699)	10% Sodium Dodecyl Sulfate (SDS)	50µl	Sigma (151-21-3)
10% Sodium Dodecyl Sulfate (SDS)	100µl	Sigma (151-21-3)	Tetramethylethylenediamine (TEMED)	5µl	Sigma (T9281)
Tetramethylethylenediamine (TEMED)	15µl	Sigma (T9281)	10% Ammonium Persulfate (APS)	50µl	Sigma (A3678)
10% Ammonium Persulfate (APS)	30µl	Sigma (A3678)			

Once the stacking gel had set, 20ug of protein from each lysate was loaded into wells using a glass needle for enhanced accuracy. A 10kDa protein ladder (ThermoFisher, MA, USA) was used to ensure detected bands were of the expected size for the protein of interest. The space between gels was flooded with 1x Running Buffer (**Table 2.10)** and a 300V power pack (Bio-rad) was set to 180V and used to run the gel at room temperature for 1 hour.

Table 2-9 Composition of stock buffer used to make western blot running and transfer buffers

10x Tris/Glycine Buffer		
Component	Quantity	Catalogue Number
Tris Base	30.3g	Sigma (77-86-1)
Glycine	144g	VWR (56-40-6)
	Dissolve in 1L H_2O & set pH to 8.3	

Table 2-10 Composition of western blot running and transfer buffers

1x Running Buffer		1x Transfer Buffer	
Component	Quantity	Component	Quantity
H_2O	890ml	H_2O	700ml
10x Running Buffer	100ml	10x Running Buffer	100ml
10% SDS	10ml	Methanol	200ml

2.2.2   Wet Transfer

To transfer the separated proteins from the gel to a Poly(vinylidene fluoride) (PVDF) membrane for future antibody staining, a wet transfer was performed once the gel had run for 1 hour and the protein ladder had visibly separated enough so that different bands were easily distinguishable.

Gels were incubated at room temperature in 1x Transfer Buffer *(Table 2.10)* for 10 minutes. All transfer equipment was also initially soaked in 1x Transfer Buffer to ensure membrane and gel remained wet throughout the procedure. The PVDF membrane was briefly soaked in 100% methanol prior to being added to 1x Transfer Buffer separate from the incubating gel. Care was taken throughout to avoid contact of membrane with potential sources of protein contamination including gloves, with tweezers being used to handle the membrane.

Transfer equipment was assembled as detailed in **Figure 2.1-B**, with the membrane being placed carefully over the gel and then sandwiched between two sponges and several layers of filter paper. Assembled transfer equipment was then added to a transfer tank (Bio-rad) which was filled with 1x Transfer Buffer. The transfer tank also contained an ice pack to ensure the reaction did not overheat. A 300V power pack (Biorad) was used to run the transfer at 80V for 45 minutes.

2.2.3   Membrane Blocking & Primary Antibody Staining

Once proteins had transferred from the gel to the membrane, the membrane was blocked to prevent the non-specific binding of the primary antibodies. Blocking was achieved by incubating the membrane in 5% milk (Marvel, UK) dissolved in 0.1% PBS-Tween (PBS-T) for 1 hour at room temperature on a shaker set to 20-25rpm.

Once membranes were blocked, the visible protein ladder was then used as a guide to cut the membrane with a scalpel to enable the simultaneous staining of multiple proteins, providing enough of a size difference existed between them.

Primary antibodies were dissolved in 0.5% BSA PBS-T at concentrations detailed in **Table 2.11.** Cut sections of membrane were then added carefully to tubes containing the relevant primary antibody and incubated overnight at 4°C on a RollerMixer.

2.2.4   Secondary Antibody Staining

Following primary antibody incubation, membranes were washed for 5 minutes in PBS-T on a shaker set to 20-25rpm. Washing was repeated three times before membranes were placed in tubes containing goat anti-mouse secondary antibody in 0.5% BSA/PBS-T **(Table 2.11)**. Membranes were incubated in secondary antibody for three hours at 4°C on the RollerMixer. Washing, as described above, was then repeated and membranes were stored in PBS-T at 4°C if not being used immediately.

Table 2-11 Antibodies used for western blot

Target	Host Species	Species Reactivity	Classification	Dilution	Catalogue Number
cFLIP	Mouse	Human	Primary Antibody	1:200	Enzo 7F10 (ALX-804-961-0100)
GAPDH	Mouse	Mouse, rat, human, rabbit	Primary Antibody	1:10,000	Santa Cruz 6C5 (sc-32233)
Immunoglobulins (HRP)	Goat	Mouse	Secondary Antibody	1:2000	Agilent (P0447)

2.2.5   Detection

To visualise protein bands, membrane sections were placed face-up inside a clear plastic sleeve. Immobilon Forte Western HRP substrate (Merck Millipore) was added to cover the surface of the membrane. Membranes were incubated in Western HRP substrate for 1 minute. A Chemi Blot instrument (Bio-rad) was used to detect the signal produced, with images being taken at specific timepoints across an exposure time range of 1 second to 10 minutes.

2.2.5.1   Protein Quantification

Density of target bands normalised to density of internal control protein (GAPDH) was used to indicate expression level of the target protein. ImageLab software (Biorad) was used to prepare images ready for analysis using ImageJ (Schneider et al. 2012). Data was then presented using GraphPad Prism 9 software (GraphPad, CA, USA).

2.3   RNA Expression: RNA sequencing Data (RNASeq)

2.3.1   GEPIA2 Pipeline to analyse patient pancreatic tumour and normal pancreas datasets

The Gene Expression Profiling Interactive Analysis 2 (GEPIA2) web server and processing pipeline was used to interrogate PDAC and normal pancreas RNA sequencing (RNASeq) expression data (Tang et al. 2019). This tool was selected for investigating the overall impact of cFLIP expression in pancreatic tumours due to its functionality, ease of use and access to large sample sizes for tumour and normal tissues. Each GEPIA2 analysis was performed using RNASeq data obtained from The Cancer Genome Atlas Program

(TCGA) (Pancreatic Adenocarcinoma n=179; Normal Pancreas n=4) and the Genotype Tissue Expression (GTEx) project (Normal Pancreas n=167) (Weinstein et al. 2013).

2.3.1.1 GEPIA2 Stage Plot

The GEPIA2 stage plot tool was used to create an expression violin plot showing cFLIP gene expression across each pathological stage of pancreatic cancer. Differential gene expression was assessed using one-way ANOVA with the pathological stage included as a variable. Expression data in transcripts per million (TPM) were first log_2 transformed for differential analysis and results are presented as $log_2(TPM +1)$.

2.3.1.2 GEPIA2 Box Plot

The GEPIA2 box plot tool was used to generate box plots presenting differences in gene expression of cFLIP and TRAIL receptors in PDAC compared to normal pancreas samples. Expression data were first $log_2(TPM +1)$ transformed for differential analysis and the log_2 fold change (log_2FC) defined as *median(Tumour) - median(Normal pancreas)*. Differential gene analysis was calculated using a one-way ANOVA. Genes with a fold-change threshold ($|log2FC|$) greater than 1 and a p-value lower than the cutoff (p=0.01), were considered to be differentially expressed genes. Data was presented using a jitter size of 0.4, which ensured dots weren't plotted directly on top of each other and avoided the effect of overplotting.

2.3.1.3 GEPIA2 Pearson's Correlation Analysis

Pairwise Pearson gene expression correlation analysis was performed using the GEPIA2 platform. Data was presented as correlation scatter plots demonstrating the correlation between expression of different pairs of key genes. Expression data in transcripts per million (TPM) were log_2 transformed for data visualisation after analysis.

2.3.1.4 GEPIA2 Survival Analysis

To determine the impact of key genes on pancreatic cancer patient overall and disease-free survival, the GEPIA2 survival analysis tool was used to generate Kaplan-Meier Survival plots. A customised "TRAIL-related" gene signature panel was utilised to assess

the collective impact of high vs low expression of cFLIP, TRAIL and both TRAIL death receptors on survival. The Cox proportional hazards model was applied to generate a hazard ratio (HR) and corresponding p-values, comparing the rate of deaths in patients with high vs low expression of genes of interest.

2.3.2 ENSEMBL-EBI Expression Atlas to analyse RNA expression in PDAC cell lines

The ENSEMBL-EBI Expression Atlas platform (release 38) was used to analyse RNAseq data collected by the 'Cancer Cell Line Encyclopedia' project (Barretina et al. 2012) and determine the expression levels of cFLIP, TRAIL and both TRAIL death receptor genes in the panel of established human PDAC cell lines which were used to investigate the *in vitro* response to cFLIP inhibition. GraphPad Prism 9 software (GraphPad, CA, USA) was used to produce a heatmap to visualise the expression levels derived from the ENSEMBL-EBI platform.

2.4 *In vivo* Experiments

2.4.1 Animal Husbandry

All animal experiments were conducted with Cardiff University Animal Welfare and Ethical Review Board (AWERB) approval, in accordance with UK Home Office regulations and under valid Personal and Project licences. Mice received free access to standard animal diet and water, with a maximum of four mice of the same sex housed per cage. Appropriate environmental enrichment was provided for both breeding stock and experimental animals, with regular health and well-being inspections occurring in accordance with regulatory requirements. Tick@Lab software (A-Tune Software Inc, USA) was used for colony management.

2.4.2 Genetically Engineered Mouse Model (GEMM) Technology

2.4.2.1 Cre/loxP Recombination technology

Due to a range of useful biological characteristics, the laboratory mouse *(Mus musculus)* is frequently used as the animal model of choice for studying human disease *in vivo* (Rosenthal and Brown 2007; Gurumurthy and Lloyd 2019). Mice and humans share highly conserved genetic homology, underpinning the use of mouse models in the development of genetic engineering technologies for the study of human disease.

The Cre/*loxP*-mediated recombination system is frequently used for mammalian gene editing and is found in a wide variety of PDAC GEMMs. Encoded by the bacteriophage P1, the 38kDa recombinase enzyme (Cre) belongs to the integrase family of site-specific recombinases (Tronche et al. 2002). Members of the integrase protein family are involved in the regulation of gene expression in many micro-organisms, including Archaea and yeast. Cre recognises a 34bp *loxP* DNA target on the P1 genome and catalyses reciprocal DNA recombination between two *loxP* sites *(Figure 2.3)*. The sequence of DNA found between two *loxP* sites is referred to as being 'flanked by *loxP*' or '*floxed*'. A *LoxP* site consists of an 8bp spacer which separates two 13bp inverted Cre monomer recognition sites. The asymmetric core spacer sequence orientates each *loxP* site (Nagy 2000).

Cre-mediated DNA recombination occurs through the cooperative binding of two Cre monomers to one *loxP* site, forming a dimer (Tronche et al. 2002). Two *loxP* sites are then bridged together following the formation of Cre tetramers, whereby two dimers come together. If both *loxP* recombination sites are in the same orientation, then the Cre-mediated bridging of these sites leads to either the excision or integration of the *floxed* DNA sequence. However, if the two sites are in opposing orientations, then DNA inversion is induced.
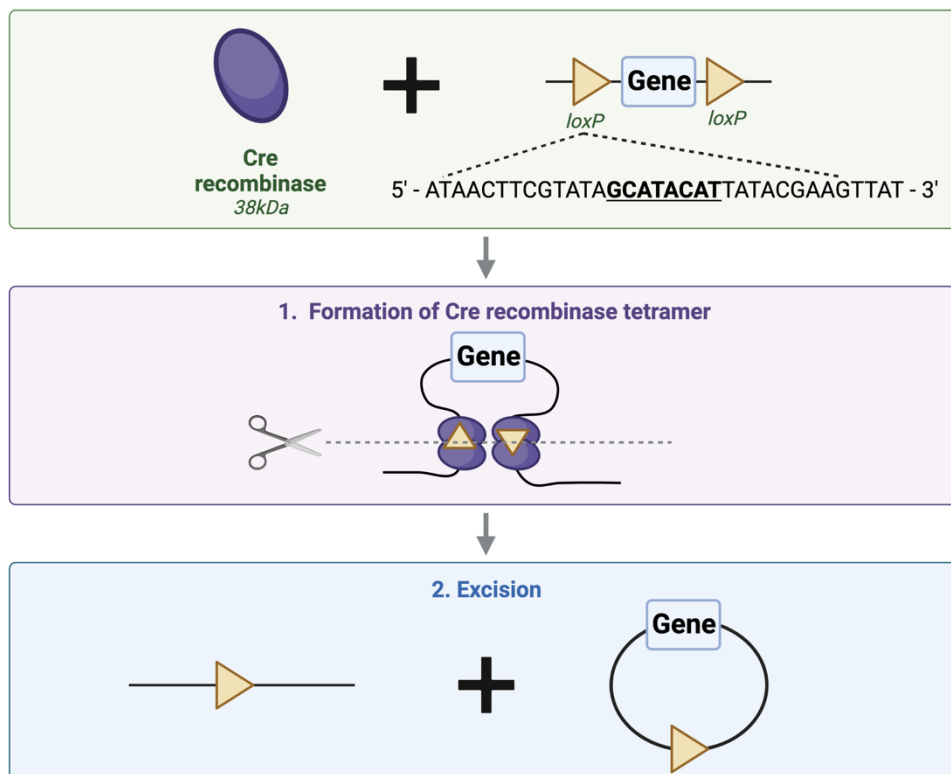
Figure 2-3 Schematic overview of Cre recombinase mechanism of action.
The binding of Cre monomers to a pair of Cre recognition sites within the loxP sequence leads to the formation of Cre dimers. Two Cre dimers on separate loxP sites come together to form a Cre tetramer. The asymmetric core 'spacer' sequence (bold & underlined) within the loxP sequence dictates the orientation of the each loxP site. Cre-mediated bridging of two loxP sites in the same orientation leads to excision of the loxP-flanked gene, whilst bridging of loxP sites in opposing orientations leads to DNA inversion. Figure created with Biorender.com.

Despite originating in micro-organisms, the Cre/*loxP* system also works efficiently in organisms with far larger genomes and has been used extensively to induce DNA recombination events in mammals, plants, and insects (Sauer and Henderson 1988; Tronche et al. 2002). GEMMs often involve spatiotemporally regulated DNA recombination events, whereby the Cre/*loxP* system is modified to target specific cell types at specific timings (Kim et al. 2018). Cell type-specific promoters or enhancers are used to drive the expression of Cre in the cell or tissue type of interest. For example, the *pdx1* promoter is used to drive the expression of transgenes exclusively within the pancreatic epithelium. However, despite providing spatial regulation, the use of the *pdx1*-promoter results in Cre-mediated recombination from embryonic day 8.5 (E8.5), due to its expression by the very first pancreatic progenitor cells in the foetal mouse which give rise to all mature cells of the adult pancreas (Hingorani et al. 2003; DeCant et al. 2014). Given that many human diseases, including PDAC, often arise later in life, GEMMs involving the constitutive activation of Cre at such an early developmental time point, may not fully recapitulate human disease complexities and may interfere with pancreatic development.

Therefore, combining the spatial regulation of Cre expression with a modified, tamoxifen-inducible Cre protein (CreER^{T2}), facilitates spatiotemporal control of Cre-mediated recombination events and better reflects the human setting (Feil et al. 1997; Kim et al. 2018). Formed by the fusion of a Cre protein to an oestrogen receptor containing a mutated ligand binding domain (ER-LBD), CreER^{T2} temporally regulates the activation of Cre by sequestering the protein in the cytoplasm, bound to heat shock protein 90 (HSP90). The binding of synthetic steroids (including tamoxifen) disrupts the interaction between CreER^{T2} and HSP90, leading to the translocation of CreER^{T2} into the nucleus and facilitating the binding of Cre to its target *loxP* sites. Tamoxifen is generally delivered systemically via intraperitoneal (IP) injection to induce recombination in GEMMs, relying on the spatial regulation provided by tissue-specific promoters to ensure recombination only occurs within target cell types.

2.4.2.2 Flp/FRT Recombination technology

Despite its frequent use in a range of GEMMs, the Cre/*loxP* system is not the only means of inducing DNA recombination. Indeed, the Flp/*FRT* system functions in a similar manner to Cre/*loxP* technology, whereby the flippase recombinase enzyme (Flp) targets Flp recombinase target (*FRT*) sequences engineered to flank an endogenous DNA sequence of interest (Dymecki 1996). Unlike Cre, FLP is encoded by *Saccharomyces cerevisiae* instead of the P1 bacteriophage, however, DNA recombination is induced in a similar manner (Sadowski 1995; DeCant et al. 2014; Schönhuber et al. 2014). A mammalian-optimised version of Flp (known as Flp-o) was developed for use in GEMMs due to its improved recombination efficiency (Farley et al. 2000). The combination of Flp/*FRT* and Cre/*loxP* in the same GEMM facilitates the conditional and inducible sequential targeting of genes at different time points or in different cell types (DeCant et al. 2014). This may better recapitulate the stepwise acquisition of mutations that occurs during tumour development or facilitate targeting a gene of interest within intact, fully formed tumours.

2.4.3 The KPC GEMM of PDAC

The transgenic model of PDAC used in Chapter 5 of this thesis was a variation of the classical, widely used *pdx1-Cre;* LSL-*KRAS^{G12D};* LSL-*Trp53^{R172H}* (KPC) GEMM (Hingorani et al. 2005; Gopinathan et al. 2015). Kindly provided by the Hogan lab (Cardiff University, UK), the tamoxifen-inducible *pdx1-CreER^{T2};* LSL-*KRAS^{G12D/+};* LSL-*Trp53^{R172H/+};* *Rosa26^{LSL-tdRFP}* (KPC) model (Jackson et al. 2001; Gu et al. 2002; Luche et al. 2007) provided temporospatial control over Cre activation in a GEMM known to drive PDAC with 100% penetrance, leading to clinically relevant tumour-related characteristics, including metastases and clinical symptoms, such as cachexia (a muscle-wasting condition) *(Figure 2.4 A)*.

The KPC model incorporates the insertion of a *loxP*-flanked stop codon (*LSL*) before an activating point mutation (G12D) in the *KRAS* gene and a dominant negative mutation (R172H) in *Trp53.* Additionally, this modified KPC model involves the insertion of inverted pairs of *LSL* sites surrounding a tandem-dimer red fluorescent protein (td-RFP) sequence which was inserted into intron 1 of the Rosa26 locus (Luche et al. 2007). Under

the control of the *pdx1* promoter, CreER^T2 is exclusively expressed in pancreatic epithelial cells and, following tamoxifen induction, functions to excise the aforementioned floxed sequences, thereby driving the expression of mutant *KRAS* and *Trp53* within the adult mouse pancreas. Additionally, Cre-mediated inversion of the *td-RFP* sequence results in the expression of endogenous red fluorescent protein (RFP) by all successfully recombined cells, with Cre-mediated inversion of the td-RFP sequence previously shown to occur in 100% of successfully recombined cells (Luche et al. 2007).

For each relevant experiment detailed in this thesis, CreER^T2 activity in the KPC model was induced following a single systemic IP injection of 1μg tamoxifen (#T5648; Merck, USA) dissolved in Corn Oil (Merck, USA; 100μl per mouse of 10μg/ml solution). Both male and female mice were injected between 6-8 weeks of age and developed sporadic PDAC tumour growth over the following 6-45 weeks.

2.4.3.1 Inhibition of cFLIP in the KPC GEMM of PDAC

The experiments detailed in Chapter 5 of this thesis involved the use of the KPC mouse to investigate the efficacy of our lab's novel small molecule cFLIP inhibitor, OH14, as discussed in Section 2.1.7.3.

Mice received a previously determined high dose (data not shown) of 80mg/kg OH14 once PDAC tumour burden was confirmed. To prepare the OH14, a 160mg/ml stock solution was prepared under aseptic conditions, consisting of 160mg OH14 powder dissolved in 1ml DMSO. The stock was then separated into 50μl aliquots and stored at -20°C until required. Immediately prior to dosing, a 50μl stock aliquot of OH14 was added to 950μl warm sterile water for injection (B. Braun, Germany) to give a working concentration of 8mg/ml. 10μl per gram of mouse body weight of working 8mg/ml OH14 stock was then administered via a single IP injection using a 26-gauge needle. This dose was provided daily until the mouse reached their ethically determined endpoint. The DMSO control was prepared and administered in the same manner, following the addition of a 50μl pure DMSO aliquot to warm sterile water.

2.4.4 Novel KPF-FLIP GEMM of PDAC

Whilst the modified KPC GEMM of PDAC provides temporospatial regulation over the activation of Cre and, therefore, results in the expression of mutant KRas and p53 within the adult pancreatic epithelium, it is not possible to further manipulate genes of interest within this model. Therefore, to investigate the effect of FLIPi in PDAC *in vivo*, a primary aim of the experiments detailed in Chapter 4 of this thesis was to establish a novel transgenic model to facilitate cFLIP deletion within intact, immune-competent PDAC tumours. The combination of Cre/*loxP* technology with the Flp/*FRT* system provides an ideal method of modelling such conditions, by utilising different enzymes for the regulation of different genes.

Thanks to assistance kindly provided by our collaborators in the Morton lab (CRUK Beatson Institute, Glasgow, UK), a novel transgenic combination was established consisting of the dual recombinase *Pdx1-Flp; FSF-Kras$^{G12D/+}$; Trp53$^{frt/+}$; Rosa26$^{CAG-FSF-CreERT2}$* (KPF) GEMM of PDAC developed by Schönhuber et al. and the conditional, *LSL-cFLAR* (cFLIP$^{fl/fl}$) GEMM developed by Zhang and He (JAX stock #022009; The Jackson Laboratory, USA) (Zhang and He 2005; Schönhuber et al. 2014). Following an elaborate breeding strategy, this resulted in the establishment of the novel *Pdx1-Flp; FSF-Kras$^{G12D/+}$; Trp53$^{frt/+}$; Rosa26$^{CAG-FSF-CreERT2}$; LSL-cFLAR* (KPF-FLIP) GEMM of PDAC **(Figure 2.4 B)**.

Pdx1-Flp functions in a similar manner to the frequently used *pdx1-Cre* and induces recombination in each cellular compartment of the pancreas (islets, ducts, and acini), as well as low levels of extra-pancreatic recombination in the duodenum, stomach and bile duct (Schönhuber et al. 2014).

Driven by *pdx1*, Flp is expressed at E8.5 and functions to excise an *FRT-stop-FRT (FSF)* codon before an activating point mutation (G12D) in the *KRAS* gene. Flp also excises one FSF-flanked *Trp53* allele and removes an *FSF* codon which precedes a gene encoding CreER^{T2} under the control of the CAG promoter on the *Rosa26* locus. These initial KPF mutations result in the constitutive expression of mutant KRas and tamoxifen inducible Cre, along with hemizygous deletion of p53, specifically within pancreatic epithelial cells.

Schönhuber et al. found that the KPF GEMM (in the absence of $Rosa26^{CAG-FSF-CreERT2}$) was associated with a median survival of 150 days (roughly 40 weeks of age; n=12), reflecting the sporadic development of PDAC tumour burden induced by this transgenic background. Our novel KPF-FLIP background also involved the ubiquitous expression of floxed *cFLAR* alleles. Due to the expression of Cre[ERT2] specifically within the KRas/p53 mutant pancreatic epithelial cells, systemic IP delivery of tamoxifen should therefore be sufficient to excise exon 2 of *cFLAR,* and induce cFLIP deletion, only within successfully recombined pancreatic cells. However, it should be noted that recent, unpublished limitations involving seemingly worse penetrance of the Flp-FRT system when compared to Cre-LoxP to drive PDAC in GEMMs have been observed by our lab and others in the field. These will be detailed further in Chapter 4 of this thesis. Furthermore, the KPF-FLIP model relies upon the constitutive activation of Flippase to induce KRAS and p53 mutations during embryogenesis. Therefore, the model cannot fully recapitulate the step-wise accumulation of mutations most often observed in adult, mature cells of the pancreas.
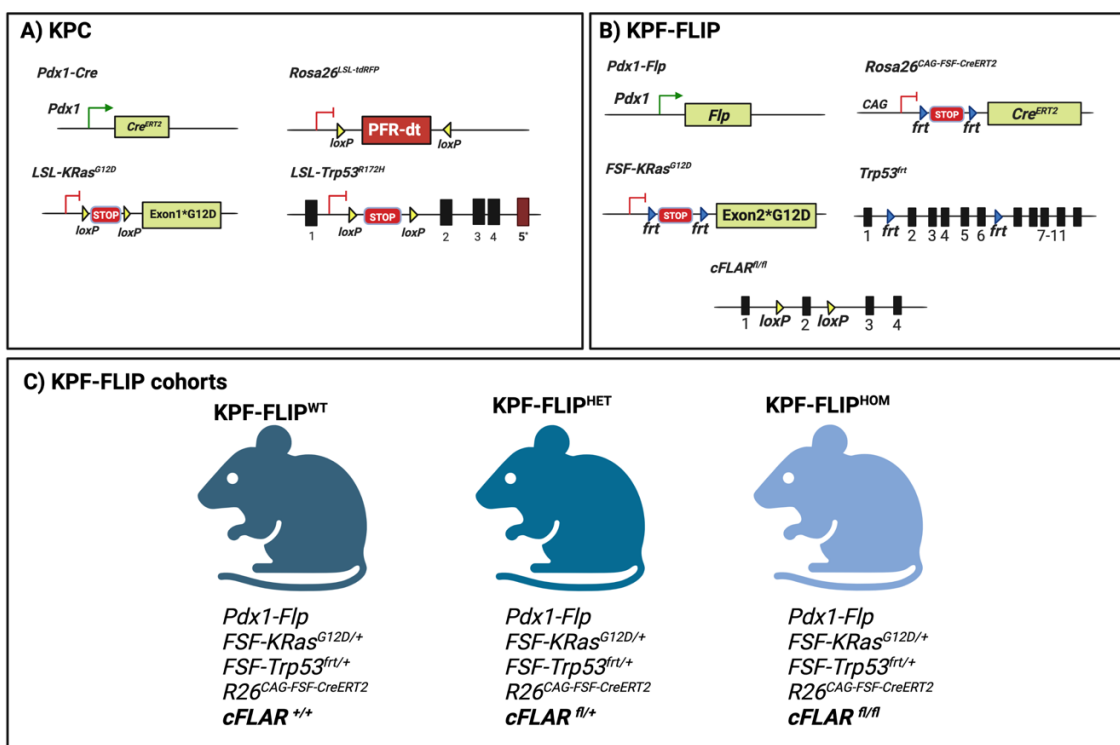
Figure 2-4 Overview of the GEMMs of PDAC used for Chapters 4 and 5 of this thesis.
A Genetic background of the tamoxifen-inducible pdx1-CreER[T2]; LSL-KRAS[G12D/+]; LSL-Trp53[R172H/+]; Rosa26[LSL-tdRFP] (KPC) mouse model. **B** Genetic background of the dual recombinase Pdx1-Flp; FSF-Kras[G12D/+]; Trp53[frt/+]; Rosa26[CAG-FSF-CreERT2]; LSL-cFLAR (KPF-FLIP) mouse model. **C** Overview of the experimental KPF-FLIP cohorts used in Chapter 4 of this thesis. GEMM = Genetically engineered mouse model; PDAC = Pancreatic ductal adenocarcinoma. Figure created with Biorender.com.

As previously mentioned, our collaborators in the Morton lab (CRUK Beatson, Glasgow, UK) kindly performed initial F1 and F2 breeding crosses under Specified and Opportunistic Pathogen Free (SOPF) conditions. Initially, cFLIP^fl/fl animals purchased from the Jackson Laboratory (JAX stock #022009) were crossed into the Morton lab's in-house KPF-*FSF-Rosa26^CAG-CreERT2* breeding stock to generate appropriate breeding pairs for shipment to Cardiff University. Unless otherwise stated, all subsequent experiments using the transgenic mouse models in this project were conducted in Cardiff University by the author of this thesis.

Given that homozygous expression of floxed *KRAS^G12D* transgenes is embryonic lethal (JAX stock #008179, The Jackson Laboratory, USA), the *FRT-KRAS^G12D* allele was maintained with heterozygous expression within the breeding colony. Additionally, homozygous expression of *FRT*-flanked *Trp53* (*Trp53^frt/frt*) results in rapidly accelerated tumour development and minimal survival time when compared with its heterozygous expression on the KPF background (median survival of 85 days compared to the median of 150 days respectively) (Schönhuber et al. 2014). Therefore, the *FRT*-flanked *Trp53* allele was also maintained with heterozygous expression within the colony, to better reflect the slow, stepwise development of PDAC observed in the clinic. Maintaining heterozygosity in each allele involved crossing *pdx1-Flp; KRAS^+/+; Trp53^frt/+* or *pdx1-Flp; KRAS^+/+; Trp53^frt/frt* mice with *pdx1-Flp; KRAS^G12D/+; Trp53^+/+* mice to generate the required experimental cohorts, as outlined by **Figure 2.4-C**. Due to the complex combination of alleles required, only around 20% of all pups born possessed the desired experimental genotype.

Once mice reached sexual maturity and genotypes had been determined, adult mice were placed in breeding cages consisting of either one male and one female (breeding pair) or one male and two females (breeding trio). All pups were weaned at around 21 days and ear biopsies were taken to be sent to Transnetyx for genotyping using real-time PCR (Transnetyx, USA). Mice were then promptly allocated to experimental or breeding cohorts as soon as genotypes were confirmed.

Unfortunately, due to University-level regulations, breeding pairs were unable to immediately enter SOPF conditions after being transferred from Glasgow to Cardiff. Therefore, the initial Cardiff breeding colony was established and maintained in conventional housing in a comparatively 'dirtier' (not SOPF barrier-maintained) unit, whilst sufficient genotypes were acquired to perform embryonic re-derivation of the colony into SOPF conditions. Due to the nature of the breeding crosses, relevant experimental KPF-FLIP animals were generated alongside the required breeding animals in the 'dirtier' unit. However, these experimental animals had to remain in the dirtier conditions until their respective endpoints. During this time, routine pathogen screens at the 'dirtier' unit reported the presence of pinworm and repeated *Pasteurella pneumotropica Heyl* infections. Therefore, all mice were also treated with the appropriate treatments to eradicate each infection from the unit, under the guidance of the Named Veterinary Surgeon (NVS). Once the breeding colony was successfully re-derived into conventional housing under SOPF conditions at Cardiff, this newly established colony was not exposed to any form of pathogen.

2.4.4.3   cFLIP inhibition in the KPF-FLIP GEMM of PDAC

Given the sporadic nature of KPF-FLIP tumour development, experimental animals received regular monitoring for tumours, consisting of bi-weekly weight checks and abdominal palpation for abnormal, rough-edged masses. Any mouse with a mass that was flagged following palpation and present during at least the next two routine checks was designated as a tumour-bearing animal. Once tumour burden was detected, floxed cFLIP was deleted specifically within the successfully recombined PDAC cells through the administration of tamoxifen to induce the Flp-driven Cre^{ERT2}.

Tamoxifen administration involved the preparation of a 20mg/ml stock solution, by dissolving 20mg tamoxifen powder (#T5648; Merck, USA) in 2µl of 100% ethanol and 998µl corn oil (Merck, USA). The stock solution was then protected from light and incubated with agitation for at least 4 hours at 50°C until the powder had completely dissolved. The stock solution could be stored for up to 7 days at 4°C but was generally used immediately. Mice received 4µl of the tamoxifen stock solution per gram of body

weight (80mg/kg), delivered via IP injection using a 26-gauge needle at roughly the same time each day for three consecutive days.

2.4.5 Diagnosis and longitudinal monitoring of PDAC tumours

As detailed in Section 2.5.4.3, manual abdominal palpation was used to routinely screen experimental animals for PDAC tumour burden. Whilst this method of tumour screening is recommended for preclinical trials involving GEMMs of PDAC, it is generally combined with high-resolution ultrasound imaging to confirm tumour presence and non-invasively monitor changes in tumour volume (Sastra and Olive 2013; Gopinathan et al. 2015). Unfortunately, this technology was not available at Cardiff University and could not be used to assist with the diagnosis or monitoring of tumour burden in our two GEMMs. Therefore, an additional aim of the experiments detailed in Chapter 5 of this thesis was to determine the ability of the clinical positron emission tomography (PET) imaging agent 18F-fluorodeoxyglucose (^{18}F-FDG) to detect PDAC tumours when combined with computerised tomography (CT). Whilst high-resolution ^{18}F-FDG PET/CT is routinely used for the diagnosis and staging of human PDAC tumours in the clinic, its use as an imaging tool for the monitoring of PDAC GEMMs receives very limited reference in the literature (Fendrich et al. 2011; Knight et al. 2017; (NICE) 2018).

As a radioactive glucose analogue, ^{18}F-FDG exploits the increased glucose uptake rate associated with rapidly dividing cancer cells, even in the presence of an adequate supply of oxygen (known as the Warburg effect) (Warburg 1931; Laking and Price 2001; Hanahan and Weinberg 2011; Knight et al. 2017). Following rapid accumulation within cancer cells, ^{18}F-FDG is phosphorylated in a similar manner to glucose. However, unlike glucose-6-phosphate, ^{18}F-FDG-6-phosphate is resistant to all subsequent downstream glucose processing, resulting in its retention within the cell. The PET imaging modality then reports the 3-dimensional distribution of retained ^{18}F-FDG as a function of time (Ribeiro et al. 2022).

2.4.5.1 *[18]F-FDG PET/CT imaging of the KPC GEMM of PDAC*

Following collaboration and assistance kindly provided by colleagues at the Wales Research & Diagnostic PET Imaging Centre (PETIC, Cardiff University), a high-resolution

¹⁸F-FDG PET/CT imaging and analysis methodology was optimised for the detection of PDAC within the KPC GEMM. An overview of the imaging process is provided in **_Figure 2.5_**.
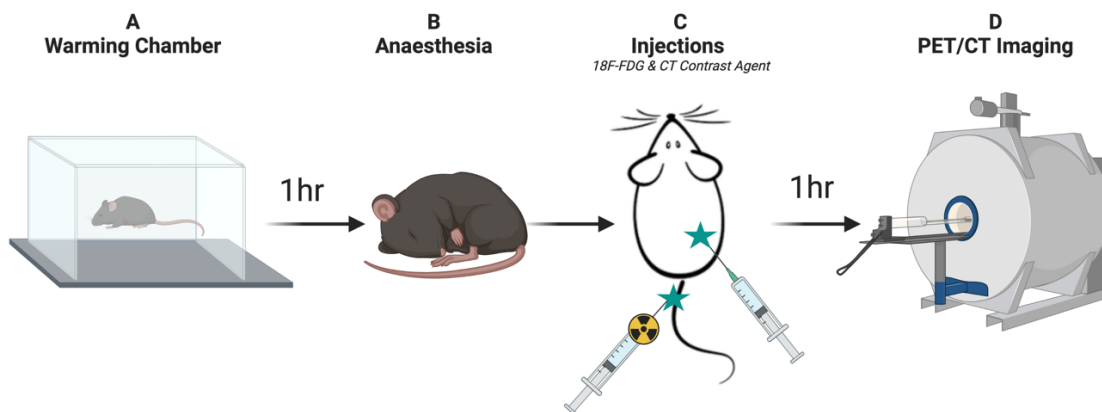
Figure 2-5 Schematic overview of ¹⁸F-FDG PET/CT imaging procedure.
¹⁸F-FDG was administered via tail vein injection, whilst an IP injection was used to administer iohexol CT contrast agent (GE Healthcare). A small animal PET/CT camera (Mediso nanoscan 122S) was used to obtain images of ¹⁸F-FDG distribution after a 1-hour uptake time. Figure created using Biorender.com. ¹⁸F-FDG PET/CT = ¹⁸F-fluorodeoxyglucose Positron emission tomography/Computerised tomography; IP = intra-peritoneal.

2.4.5.2   Measures to reduce background ¹⁸F-FDG uptake by non-tumour cell types

As ¹⁸F-FDG accumulates within any cell requiring glucose for metabolic activity, several environmental factors were controlled prior to the PET/CT scan to reduce the basal metabolic rate of the mouse. To minimise handling-induced anxiety, mice were acclimatised by regular handling which occurred during routine manual screening for tumours, as detailed in Section 2.5.4.3.

Two hours prior to commencing the scan, mice were isolated in a clean warming box without access to food but containing some form of environmental enrichment to provide shelter and reduce anxiety levels, often a handling tube from the home cage. Mice were initially placed in a warming box set to 36°C for 45 minutes, according to industry guidelines (Ribeiro et al. 2022) **_(Figure 2.5 A)_**. When housed between 26-34°C (the so-called thermoneutral zone), mouse body temperature is largely controlled by conduction and heat convection, with minimal metabolic activity roughly equal to the basal metabolism rate. Due to the high basal metabolic rate of the mouse, it is advised to maintain body temperature between 36.5-38°C to ensure the majority of ¹⁸F-FDG is

sequestered by tumour cells and to remove as much background uptake as possible. After 45 minutes, mice were transferred to another warming box, set to 38°C, and housed there for 15 minutes. This further reduced the basal metabolic rate and ensured maximum dilation of the tail vein to assist with the subsequent administration of ^{18}F-FDG. Finally, following the 1-hour period of warming and fasting, mice were anaesthetised using a pre-warmed inhalation anaesthetic chamber filled with a vaporiser set to emit 5% isoflurane (Vet Tech Solutions Ltd) carried by 100% oxygen, to minimise ^{18}F-FDG uptake by muscle and brain cells. Once mice became immobile, anaesthesia was then maintained via inhalation of 1.5-2.5% isoflurane for the rest of the imaging procedure *(Figure 2.5 B)*. Sterile, unmedicated Lacri-lube eye ointment (Allergan Ltd) was applied to prevent corneal damage during prolonged anaesthesia.

2.4.5.3   Administration of ^{18}F-FDG

As soon as possible after mice were stably anaesthetised, roughly 10-15 MBq of radioactive ^{18}F-FDG suspension was administered via tail vein injection using a Micro-Fine+ 29G 1ml insulin syringe (BD, USA) protected by a lead syringe guard *(Figure 2.5 C)*. The ^{18}F-FDG was clinical-grade and was either prepared internally by PETIC (Cardiff University) or purchased from an external supplier (Alliance Medical Ltd). Immediately following tail vein injection, the residual radioactivity in the syringe was quantified and the timings of injection and syringe measurements were noted. 100μl of CT contrast agent, Omnipaque[TM] (iohexol; GE Healthcare, USA), was also administered via IP injection. Mice were then maintained under anaesthesia at roughly 37°C for a further 1 hour.

2.4.5.4   PET/CT imaging

Following the hour of incubation with ^{18}F-FDG, mice were placed on the scanner bed containing temperature control and a breathing cone to supply a constant flow of 1.5-2.5% isoflurane. Mouse breathing rate was monitored using a small pneumatic pillow throughout the PET/CT imaging procedure, to ensure the maintenance of appropriate levels of anaesthesia. The mouse bed was then inserted into a small animal PET/CT camera (nanoscan 122S, Mediso, Hungary). Once the bed was positioned within the field-of-view using the CT imager, a 10-minute PET imaging protocol was initiated

(Figure 2.5 D). Immediately following PET imaging, a 5-minute CT scan was performed to facilitate spatial reconstruction of PET data.

Once imaging was complete, anaesthesia was removed, and mice were carefully placed on VetBed in a warming box set to 36°C to recover. Once mice were moving freely around the box and appeared sufficiently alert, they were returned to their home cage with free access to food, water, and environmental enrichment.

2.4.5.5   Regulatory Requirements

All users involved in the PET/CT imaging process were registered radiation workers, having completed the mandatory health and safety training courses. Any exposure to radiation was carefully monitored and workers attended annual health check-ups to ensure safe levels of exposure were maintained. Radioactive mice were housed within designated radiation rooms, associated with appropriate access restrictions, until the radiation had decayed to safe levels. Mice were still monitored according to Home Office welfare requirements during this time before being returned to standard holding conditions, as detailed in Section 2.5.1.

Due to Home Office project licensing requirements, each individual mouse only received a maximum of 9 PET/CT scans within its lifetime. Mice were regularly monitored for any adverse side effects to the semi-routine PET/CT scans.

2.4.5.6   PET/CT Data Analysis

Nucline^{TM} NanoScan all-modality imaging acquisition software (version 3.04.01; Mediso, Hungary) was used to acquire and reconstruct data generated by the PET/CT camera to create DICOM 3D image files. PET scans were reconstructed using the default settings of Mediso's proprietary Teratomo 3D reconstruction algorithm with a matrix size of 0.4x0.4x0.4mm. The reconstructed PET file was overlaid onto the reconstructed CT file for analysis using the VivoQuant post-processing software (version 4.0patch3; Invicro, USA). Using these PET/CT 3D images, the VivoQuant software facilitated the selection of relevant regions of interest (ROIs) around organs or PDAC tumours, using a combination of manual selection and connected threshold region-filling tools. Radioactive uptake

within ROIs was measured in a variety of different ways and used to select the most appropriate method for the non-invasive monitoring of tumour growth.

2.4.5.7 Sequential scan alignment

Given the importance of monitoring tumour growth in the same mouse over a longitudinal sequence of PET/CT scans, it was vital that this was not impacted by the altered positioning of the mouse and the movement of mobile abdominal contents, including PDAC tumours, between scans. Therefore, collaboration with colleagues at PETIC (Cardiff University) resulted in the development of a novel method to align sequential scans to ensure similar abdominal positioning.

Due to their retroperitoneal localisation, the kidneys are far less mobile than intraperitoneal organs and do not drastically change their anatomical positioning over time (Kalra et al. 2022). Therefore, it was decided to align each consecutive 3D scan from an individual mouse to the same initial, baseline scan (ideally one taken before the detection of a tumour) according to the positioning of the kidneys.

The positioning of the kidneys in a scan from a later time point was aligned to that of a baseline scan with the VivoQuant Reorientation registration tool (Invicro, USA) *(Figure 2.6)*. This enabled the 3D PET/CT image of the later scan to be re-orientated until the kidneys were positioned in roughly the same location as those of the baseline scan. This scan alignment method was repeated for all subsequent scans of the same mouse, with the protocol being applied to each mouse analysed to ensure consistent monitoring of tumour development.
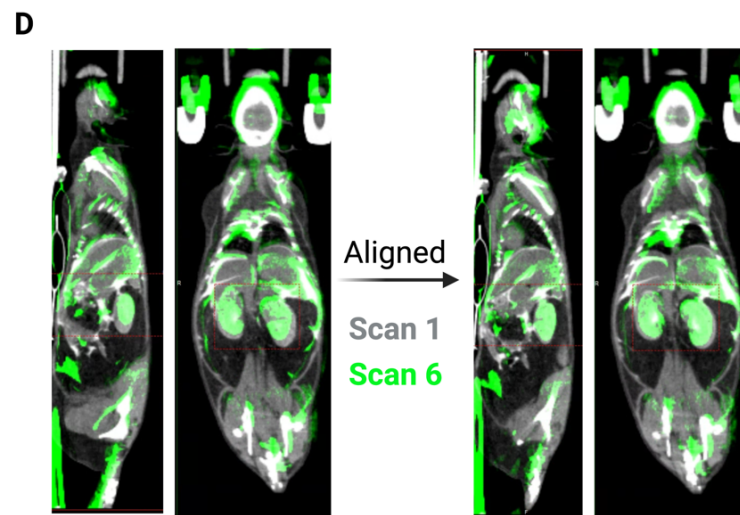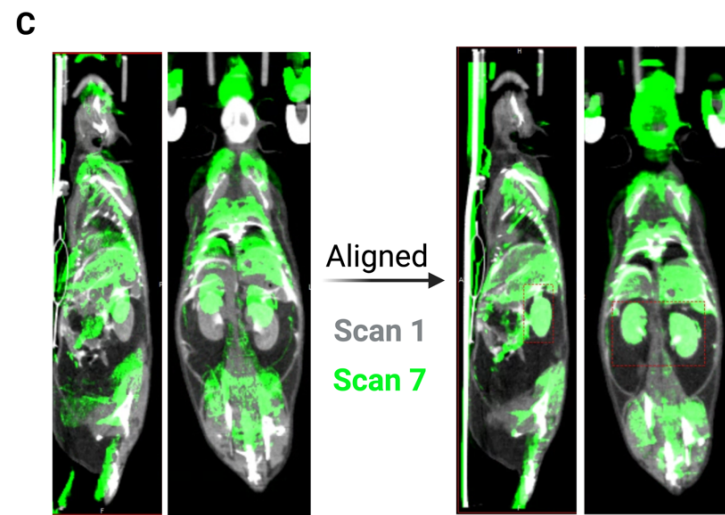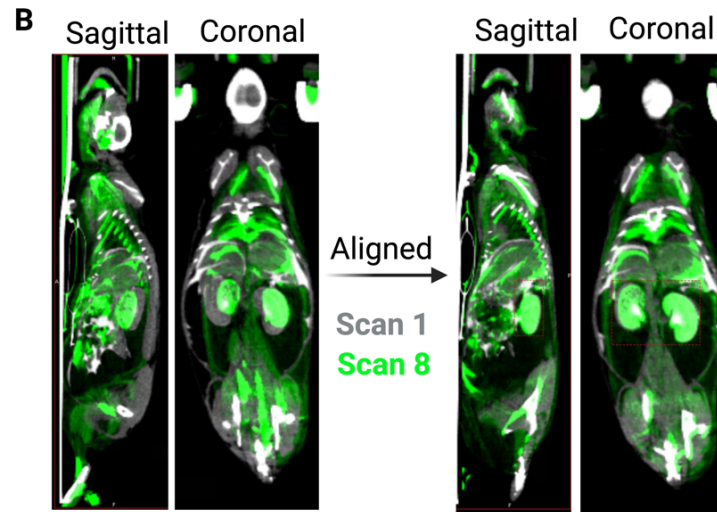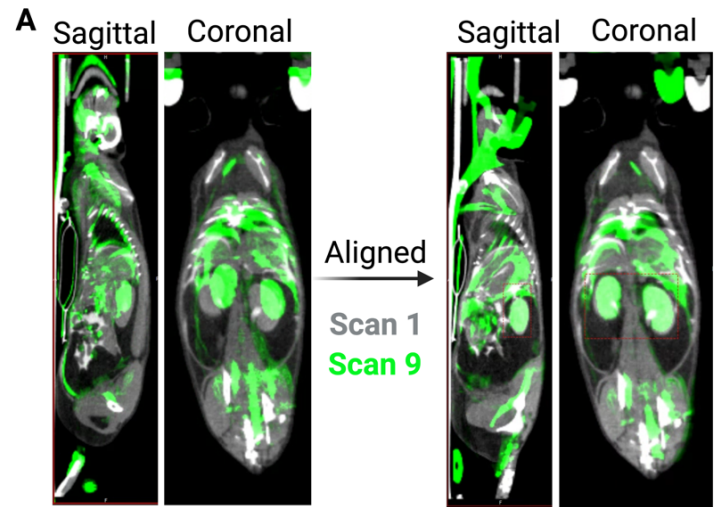
Figure 2-6 Schematic overview of novel scan alignment method.
A-D Coronal cross sections of CT images intersecting at the positioning of the kidneys, all taken from the same mouse at different time points. Each consecutive scan (#6-9; green CT image) was aligned according to the positioning of the kidneys in the baseline Scan 1 (grey CT image). The 3D scan requiring alignment was aligned to the 3D baseline scan using VivoQuant software (Invicro). Figure created with Biorender.com.

2.4.6 Tissue harvest and processing

Once mice reached either a short-term treatment time point or an ethical welfare-related humane endpoint *(Figure 2.7)*, mice were culled using a Schedule 1 approved method and tumours were dissected immediately. Relevant organs known to be sites for PDAC metastases were also harvested, comprising the lungs, liver, and diaphragm. Each tumour and organ were placed in 10% neutral buffered formalin (Merck) and fixed overnight at 4°C. Following overnight incubation, formalin-fixed tissues were then transferred to sterile PBS and stored at 4°C prior to embedding in paraffin. Formalin-fixed, paraffin-embedded (FFPE) samples were stored in appropriately sized histocasettes and cut into sections (approx. 4µm thick) mounted on microscopy slides. Sections were either stained with a standard procedure for haematoxylin and eosin (H&E) or stored for immunohistochemical (IHC) use. Paraffin embedding, sectioning and H&E staining were performed by Cardiff University School of Biosciences Bioimaging Research Hub.

Parameter	Animal ID	Score
Appearance	Normal	0
	General Lack of grooming	1
	Staring coat, ocular and nasal discharges	2
	Piloerection, reduction in pallor	3
	Hunched, cold to touch	5
Food and water intake	Normal	0
	5% weight loss	1
	Up to 20% weight loss	4
	Over 20% weight loss	12
Natural Behaviour	Normal	0
	Minor changes e.g. Lack of nest	1
	Less mobile and alert, isolated or restless	2
	Vocalisation, reduction in grip reflex	4
	Laboured breathing, self mutilation	12
Provoked Behaviour	Normal	0
	Minor depression or exaggerated response	1
	Moderate change in expected behaviour	2
	Reacts violently (eg. Evasion or biting on handling) or very weak and precomatose	6
Palpable tumour size	0-5mm longest dimension	0
	5-10mm longest dimension	3
	>17mm longest dimension / ulceration	12
		Total:

Figure 2-7 Clinical scoring morbidity chart to prevent the suffering of pre-clinical models.
The chart was used to monitor all animal models included in this thesis, according to guidelines stipulated in the AWERB- and Home Office-approved project licence. Experimental animals were regularly monitored and scored against the morbidity chart. Scores of 4-11 required regular monitoring and pain relief, if necessary. An animal with a score of >12 was considered to have reached the ethical endpoint and was terminated using a Schedule 1 approved method. AWERB = Cardiff University animal welfare and ethical review board.

2.4.7 Immunohistochemistry

Following the mounting of FFPE tissue sections onto microscopy slides, as described in Section 2.5.6, sections were used for immunohistochemistry (IHC) investigations. Enabling the quantification and visualisation of proteins within sectioned tissue, IHC was used to measure the impact of cFLIP inhibition or deletion at the cellular level within the KPF-FLIP and KPC GEMMs of PDAC. Whilst reagents and conditions are often specific to the antigen of interest, the IHC protocol used to detect cleaved-caspase 3 (CC-3), a known marker of apoptotic cells, is detailed below. Unless otherwise stated, all washes consisted of 3x five-minute submersion of slides in PBS supplemented with 0.1% Tween-20 (PBS-T) with gentle agitation.

2.4.7.1 De-wax, Rehydration of Tissue Sections and Antigen Retrieval

FFPE tissue sections were deparaffinated with two five-minute washes in xylene. Sections were then re-hydrated by submersion for 3 minutes each time in decreasing concentrations of ethanol (2x 100%, 1x 95% and 1x 70%). Slides were then transferred to distilled water.

Slides were added to pre-heated 1x Citrate Buffer (pH 6.0) in a pressure cooker. To prepare 1x Citrate Buffer, a 10x stock solution *(Table 2.12)* was diluted 1:10 in dH_2O. Slides were heated at 100% for 5 minutes in a microwave (or until the pressure gauge popped up). Power was then decreased to 40% and slides were incubated for a further five minutes. Once the pressure was safely released, the pressure cooker lid was removed, and the slides remained in the buffer for a further 30-45 minutes to cool to room temperature.

Table 2-12 Composition of 10x Citrate Buffer stock solution

Component	Quantity	UK Catalogue Number
Sodium Citrate	23.52g	Sigma (W302600)
Citric Acid	3.84g	Sigma (251275)
H_2O	500ml	
Set pH to 6.0 and store at 4°C		

2.4.7.2 Blocking

Following antigen retrieval, slides were washed, and a PAP pen (Abcam, UK) was used to draw a hydrophobic barrier around the tissue section on the microscopy slide. Peroxidase Blocking Solution (Agilent, USA) was then added to each slide and held inside the hydrophobic barrier for twenty minutes at room temperature. Following further washes, slides were incubated in 5% Normal Goat Serum (NGS) in PBS-T for one hour at room temperature.

2.4.7.3 Primary Antibody

A primary antibody targeting murine CC-3 (CST #9661) was diluted 1:300 in 5% NGS and added to the appropriate sections prior to overnight incubation at 4°C. One slide received 5% NGS alone to control for non-specific secondary antibody binding.

2.4.7.4 Secondary Antibody

Following overnight incubation, the slides were washed once again. Sections were then incubated for thirty minutes at room temperature with a biotinylated goat anti-rabbit secondary antibody (Vector Labs, CA, USA), diluted 1:200 in 5% NGS. Following further washes, slides were incubated with Vectastain Elite ABC kit reagents (Vector Labs, CA, USA) for 30 minutes, prepared according to manufacturer instructions.

2.4.7.5 Secondary Antibody Detection (DAB)

Final washes were followed by the addition of Dako DAB+ Chromogen liquid (Agilent, CA,
USA) to sections, according to the manufacturer's instructions. To determine the optimum time of DAB exposure, slides were constantly monitored for any colour change under an upright brightfield microscope (Leica, Germany). Once positive staining became visible, the DAB chromogen liquid was removed and replaced with PBS-T. Slides were then washed with distilled H20.

2.4.7.6 Counterstain and Mounting

Slides were counterstained with haematoxylin (Atom Scientific, Vienna, Austria) for thirty seconds, followed by a two-minute rinse in running tap water. Sections were then dehydrated in increasing concentrations of ethanol (from 70% to 100%) before being cleared by 2x 5-minute washes in xylene. Finally, Di-N-Butyle Phthalate in Xylene (DPX) was used to mount sections with glass coverslips.

2.4.7.7 Imaging and Quantification

Mounted IHC and H&E-stained tissues were scanned and digitised using an Olympus Slide Scanner (Olympus Corp, Japan). QuPath open-source software (Bankhead et al. 2017) was used to quantify the total number of CC-3 positive cells compared to the total number of negative cells in each tumour or tissue. The QuPath cell classification automated training method was adapted to classify cells within a tissue section according to morphological differences at the cell-type level *(Figure 2.8)*. For example, following extensive annotating and training using data from at least five different tissue sections, QuPath was able to distinguish tumour cells from stromal infiltrate and necrotic cells or separate the different cellular components of the pancreas (i.e. acinar, islet and ductal cell types). Hence, it was possible to quantify CC-3 positivity in each separate cellular compartment. Equally, the same CC-3-stained sections were used to measure the percentage of morphologically distinct necrotic cells compared to total number of tumour cells. Although not a completely accurate method for quantifying necrosis, optimisation attempts involving IHC-based detection of a known necrotic marker, phosphorylated Mixed lineage kinase domain-like pseudokinase (pMLKL), were unsuccessful (Li et al. 2021).
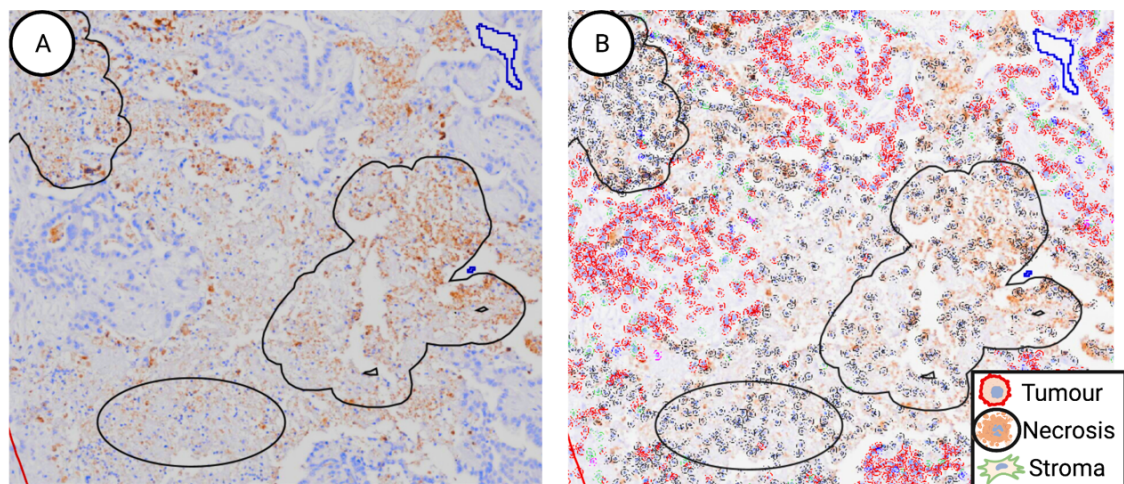
Figure 2-8 Representative images demonstrating the ability of QuPath software to distinguish different cell types within an IHC-stained tumour tissue section.
A Representative tumour section stained for CC-3. B The same tumour section with a QuPath-generated cell mask applied. Cell annotations with a red border represent tumour cells, those with a black border represent morphologically distinct necrotic cells and those with a green border represent the stroma. Regions highlighted by free-drawn annotations in A and B demonstrate the process of training QuPath to distinguish between different cell types, with those shown highlighting necrotic cells. This information was then used to train QuPath to distinguish cell types in each tumour section, without needing to manually annotate the entire tumour. Data processed and analysed using QuPath open-source software (Bankhead et al. 2017). Figure created with Biorender.com.

2.4.8 Quantification of recombination efficacy in KPF-FLIP GEMM of PDAC

Unfortunately, despite extensive optimisation attempts, it was not possible to quantify the level of cFLIP protein deletion achieved within the induced KPF-FLIP mice. The IHC method described in Section 2.5.7 and the Western Blot method described in Section 2.2 were modified to optimise a wide range of antibodies which apparently provided specific detection of the murine version of cFLIP protein, however, none of the methods attempted resulted in specific staining *(Table 2.13; Figure 2.9)*. Similarly, a small section of each tumour was snap-frozen on dry ice during dissection and stored at -80°C before being processed for DNA extraction. Extracted tumour DNA was used to optimise a genomic PCR to detect Cre-mediated excision of exon 2 of the *CFLAR* gene and compare the expression level of the excised sequence to levels of the floxed sequence. However, despite the design of four novel primer sequences and the use of Jax-recommended primers, it was not possible to specifically detect the excision within the scope of this project (data not shown). Work to confirm cFLIP protein deletion within the KPF-FLIP GEMM is therefore ongoing beyond the scope of the experiments detailed in this thesis.
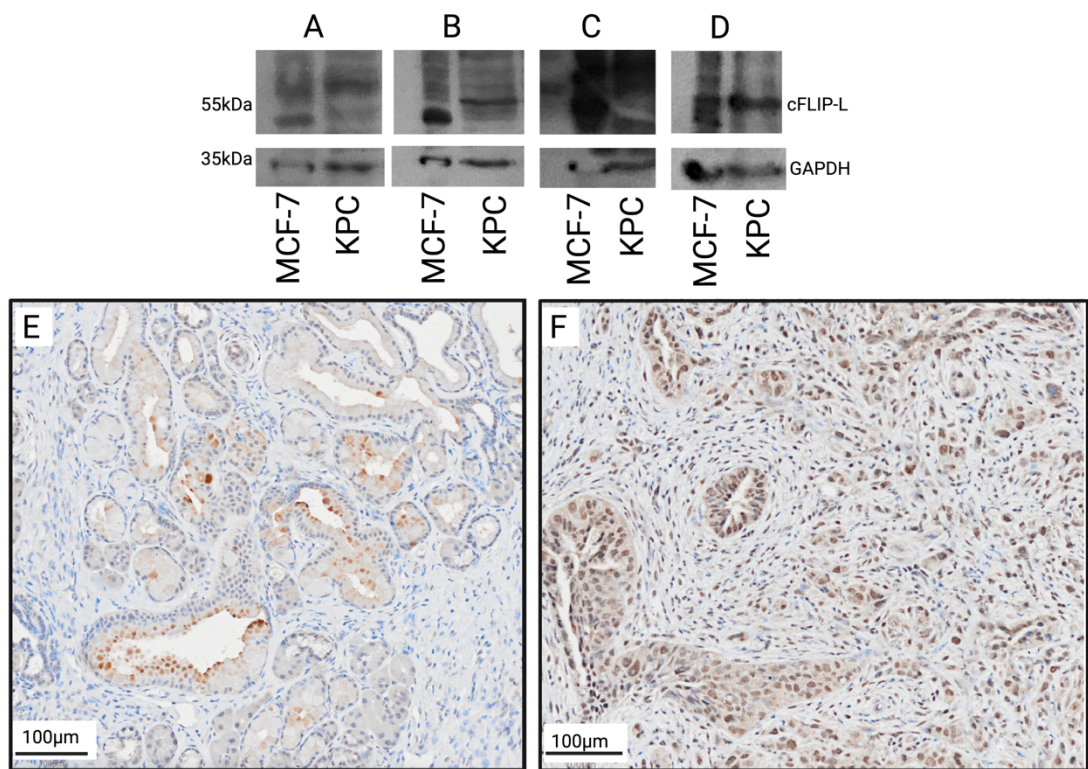
Figure 2-9 Representative images of optimisation attempts to detect the murine form of cFLIP protein.
A-D Western blot using four different primary antibodies that are advertised as targeting murine cFLIP protein. Antibodies investigated consisted of **A** D16A8 (CST #8510), **B** AF821 (Biotechne), **C** 5D8 (Abcam), and **D** H-150 (Santa-Cruz #sc-8346). Antibody specificity tested using cell lysate taken from a human breast cancer cell line known to express cFLIP protein (MCF-7) and a primary tumour-derived mouse PDAC cell line (KPC). **E-F** Representative images of PDAC tissue sections following immunohistochemistry using antibodies that are advertised as targeting murine cFLIP protein. Antibody used in images was H-150 (Santa-Cruz #sc-8346) following citrate (pH 6) antigen retrieval. **E** KPF-FLIP cFLIP$^{+/+}$ wild-type control. **F** KPF-FLIP cFLIP$^{-/-}$ knock-down control, harvested 72 hours following full tamoxifen dosing regimen (3x daily intraperitoneal tamoxifen injections (80mg/kg)). Figure created using Biorender.com.

Table 2-13 Summary of attempts to optimise immunohistochemistry staining for murine cFLIP in KPF-FLIP-derived PDAC tumour sections.
KPF-FLIP = Pdx1-Flp; FSF-KrasG12D/+; Trp53frt/+; Rosa26CAG-FSF-CreERT2; LSL-cFLAR. KD cntrl = KPF-FLIP$^{fl/fl}$ tumours following full tamoxifen-mediated induction of Cre recombinase; *Ab = Antibody; Nuc = nuclear staining.*

Antibody	Brand	Species	Antigen Retrieval Attempted	1º Ab Conc	2º Ab Conc	DAB Timings (minutes)	Outcome	Non-specific staining in KD cntrl?
G-11	Santa Cruz	Mouse	Citrate (pH 6) Prot K (enzyme)	1:200	1:200	8 5	Cytoplasm & Stroma	Y Y
H-150	Santa Cruz	Rabbit	TE (pH 9) Citrate (pH 6) Prot K (enzyme)	1:200	1:200	1.75 3 10	Some - Islets Cyto & Nuc None	- Y (nuclear) -
AF821	R&D Systems	Rabbit	TE (pH 9) Citrate (pH 6) Prot K (enzyme)	1:200	1:200	1.5 2 1	None Acinar Acinar	?
D16A8	Abcam	Rabbit	TE (pH 9) Citrate (pH 6) Prot K (enzyme)	1:200	1:200	10 10 10	None None None	NA
NF6	Enzo	Mouse	TE (pH 9) Citrate (pH 6) Prot K (enzyme)	1:200	1:200	0.5 2 0.5	Stroma Stroma Stroma	NA

However, members of the Clarkson lab were ultimately able to optimise an RNAScope[(R)] assay to detect cFLIP mRNA transcripts within FFPE-sections (Figure 2.10 A&B) (Wang et al. 2012). As an in-situ hybridisation (ISH) method, the RNAScope[(R)] assay enables amplification and visualisation of single RNA molecules within cells. Using a probe specially customised to target the transcript encoding cFLIP, each single transcript can be visualised as a distinct chromogenic dot following the use of the RNAScope[(R)] 2.5 HD Reagent Kit - RED (ACD, Biotechne, USA) according to manufacturer instructions. Tissues were taken from either KPF-FLIP$^{fl/fl}$ or KPF-FLIP$^{+/+}$ mice that had received full tamoxifen-mediated Cre induction, as described in Section 2.4.4.3. Demonstrating the efficiency of tamoxifen induction, roughly 50% less cFLIP transcripts were detected per cell in the KPF-FLIP$^{-/-}$ (0.32 +/- 0.05SEM) setting when compared to KPF-FLIP$^{+/+}$ (0.59 +/- 0.06SEM) (Figure 2.10 C). However, work to translate these results into the impact of FLIPi on actual cFLIP protein expression and activity remains ongoing.
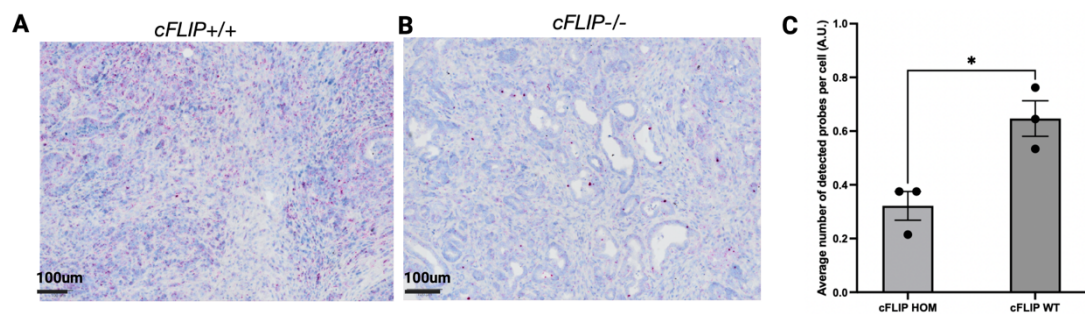
Figure 2-10 cFLIP mRNA transcript detection in cFLIP$^{+/+}$ and cFLIP$^{-/-}$ PDAC tumours taken from the KPF-FLIP GEMM.
Representative images following RNAScope[(R)] in-situ hybridisation detection of cFLIP mRNA transcripts in **A** PDAC tumours with wild-type cFLIP expression (cFLIP$^{+/+}$) that had received a full tamoxifen induction and **B** cFLIP$^{fl/fl}$ PDAC tumours that had received a full tamoxifen induction to induce cFLIP deletion (cFLIP$^{-/-}$). Each chromogenic dot represents a single mRNA transcript. **C** Representative cFLIP expression was quantified according to the average number of detected probes in each cell. Data analysed using QuPath software which facilitated the use of a subcellular detection module to quantify the number of chromogenic dots per cell. Data represents mean ± SEM (n=3). Statistical significance calculated using Welch's t-test and presented using GraphPad Prism 10 software (Graphpad, USA). Full tamoxifen induction consisted of 1x daily intraperitoneal injection of 80mg/kg Tamoxifen given daily for 3 days, animals were then harvested 3 days following the final dose. KPF-FLIP = *Pdx1-Flp; FSF-Kras$^{G12D/+}$; Trp53$^{frt/+}$; Rosa26$^{CAG-FSF-CreERT2}$; LSL-cFLAR*.

2.5 *Ex vivo* Tumour-Derived Organoid experiments

To investigate the potential of FLIPi for targeting PDAC cells *ex vivo*, tumour-derived organoids were established from the novel KPF-FLIP GEMM of PDAC described in section 2.4. Whilst a range of established pancreatic cancer cell lines have provided vital insight into the genetic landscape of PDAC and the response of tumour cells to treatment, their two-dimensional (2D) nature does not recapitulate many complex *in vivo* traits, including tumour heterogeneity and interactions with the microenvironment (Low et al. 2021). Equally, although *in vivo* GEMMs of PDAC better reflect these characteristics, they are also associated with significant time and monetary constraints (Pérez–Mancera et al. 2012; Boj et al. 2015; Tuveson and Clevers 2019). Therefore, taking these considerations into account, model systems have since been developed to facilitate high throughput preclinical investigations that are associated with reduced time and monetary costs. Model systems include three-dimensional (3D), tumour-derived organoids (hereafter referred to as organoids for ease). Organoids can be established from both primary patient or GEMM tumours and are known to retain primary tumour epigenetic, genetic and morphological characteristics in a comparatively simpler setting (Debruyne et al. 2022). As self-organising structures, organoids effectively meet the 3Rs principle (namely Replacement, Reduction and Refinement) by minimising the requirement for animal experimentation and maximising the data generated by a single GEMM (Russell and Burch 1959). Demonstrating higher complexity than classical cell-line-derived spheroids, organoids recapitulate primary tumour heterogeneity and have been shown to mimic patient-specific drug responses (Debruyne et al. 2022). Therefore, this model was included to better evaluate the response of KRAS-mutant PDAC cells to FLIPi.

2.5.1 Establishment of tumour-derived organoids
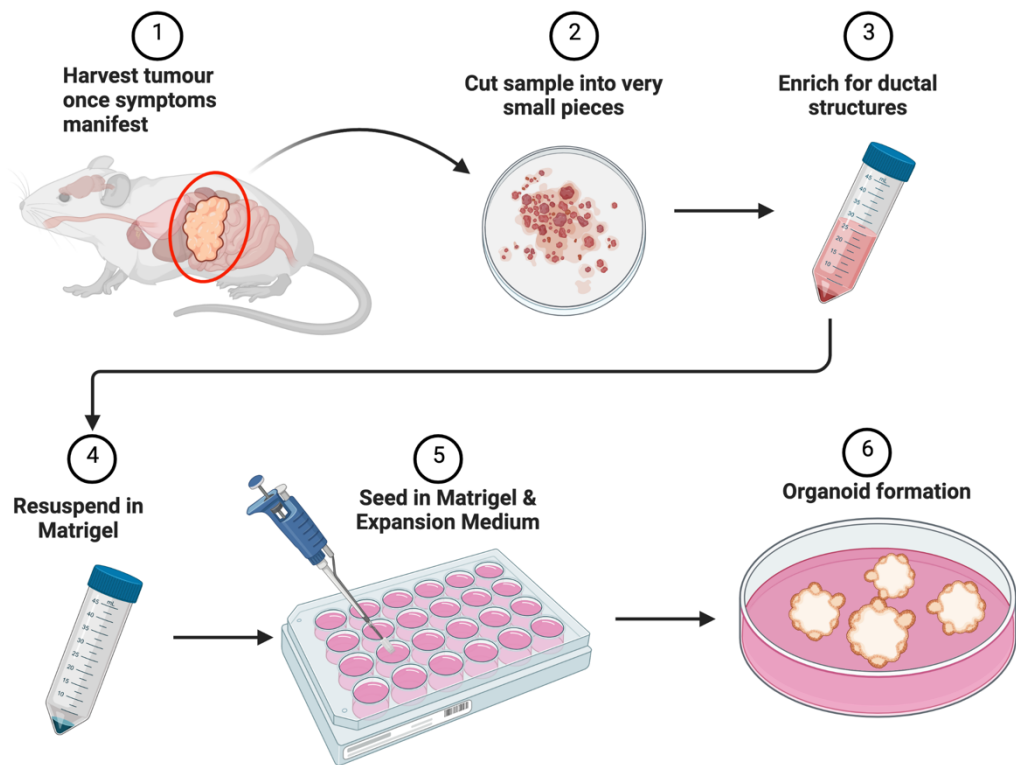
Figure 2-10 Schematic overview of process to establish PDAC-derived tumour organoids from the KPF-FLIP GEMM.
Figure created with Biorender.com. *PDAC = pancreatic ductal adenocarcinoma; KPF-FLIP = Pdx1-Flp; FSF-KrasG12D/+; Trp53frt/+; Rosa26CAG-FSF-CreERT2; LSL-cFLAR; GEMM = Genetically engineered mouse model.*

2.5.1.1 Ductal Isolation

As summarised by ***Figure 2.10***, a small section of tissue was taken from an uninduced, KPF-FLIP$^{fl/fl}$ tumour and immediately stored in cold PBS before being transferred to a sterile tissue culture hood. Care was taken to avoid isolating the intestine during the harvesting procedure, preventing a key source of future contamination. Once in the tissue culture hood, the tumour section was washed briefly in 100% Ethanol, followed by an additional brief wash in PBS. The section was then placed in a 100mm petri dish and minced using fine scissors until resembling a pulp-like consistency. The minced tissue was then transferred to a 50ml centrifuge tube, with 35ml of ice-cold Wash medium ***(Table 2.14)*** added on top. The solution was then mixed to dislodge any adipose tissue, which floated to the top of the solution once tissue pieces had settled at the bottom of the tube. Roughly 30ml of the supernatant was discarded to remove any

floating adipose tissue. This wash process was repeated a further time before the supernatant was removed and 35ml of Digestion Solution *(Table 2.15)*, which had been pre-warmed to 37°C, was added to the minced tumour tissue. The digestion mixture was then incubated on a shaker at 37°C for 45 minutes. After the initial incubation, the solution was mixed using a 10ml stripette and inspected under a microscope for the presence of clean ductal structures. If none were present, the solution was returned to the shaker for another 30 minutes. This check for ductal structures was repeated every 30 minutes for a period of up to 2 hours.

Once ductal structures appeared in the solution, the supernatant was transferred to a new 50ml centrifuge tube. Ice-cold wash medium was added to the supernatant to increase the volume to a total of 50ml. The solution was then centrifuged at 300g and 8°C for 5 minutes to pellet the material. The supernatant was then discarded and replaced with a further 50ml ice-cold wash medium, with the pelleting procedure repeated to remove any remaining digestion solution.

Table 2-14 Composition of organoid wash medium

Component	Add	Final concentration	UK Catalogue Number
StableCell™ DMEM - high glucose	500ml		D0819-500ML (Merck)
GlutaMAX	5ml	1%	Gibco (#35050061)
FBS	5ml	1%	Gibco (#11573397)
Penicillin/Streptomycin	5ml	1%	Life Technologies (#15070063)

Table 2-15 Composition of organoid digestion solution

Component	Add	Final concentration	UK Catalogue Number
Wash Medium	35ml		*Table 2.13*
Collagenase Type I	4.375mg	0.125mg/ml	Sigma (#C9407)
Dispase II	4.375mg	0.125mg/ml	Life Technologies (#17105-041)

Table 2-17 Composition of organoid basal medium

Component	Add	Final concentration	UK Catalogue Number
Advanced DMEM/ F12	500ml		12634010 (ThermoFisher)
GlutaMAX	5ml	1%	Gibco (#35050061)
Penicillin/Streptomycin	5ml	1%	Life Technologies (#15070063)
HEPES	5ml	10mM	Sigma (#83264)

Table 2-16 Composition of organoid expansion medium

Component	Add	Final concentration	UK Catalogue Number
Basal Medium (store @ 4°C for 2wks)	15ml		
B27 Supplement (without Vitamin A)	300ul	1:50	17504044 (ThermoFisher)
N2 Supplement	150ul	1:100	17502048 (ThermoFisher)
n-Acetyl-L-cysteine	150ul	1.25mM	A9165-5G (Merck)
To add fresh with each use:			
Recombinant Human R-spondin-1	1:1000	5% (vol/vol)	120-38 (PeproTech)
Nicotinamide	1:100	10mM	N0636
Recombinant human [Leu^{15}]-Gastrin I	1:1000	10nM	G9145 (PeproTech)
Recombinant mouse FGF-10	1:1000	100ng/ml	450-61 (PeproTech)
Recombinant murine Noggin	1:1000	25ng/ml	250-38 (PeproTech)

2.5.1.2 Seeding of ductal tumour cells

Following the removal of digestion solution, the supernatant was discarded, and the pellet was resuspended gently in 50μl of ice-cold Matrigel Growth Factor Reduced (GFR) Basement Membrane Matrix (Corning, USA). The Matrigel suspension was added to the centre of a well in a 24-well cell culture plate (Corning, USA) that had been pre-warmed to 37°C. The plate was then incubated at 37°C for 5-10 minutes or until the Matrigel dome had solidified. 500μl of pre-warmed expansion medium *(Table 2.17)* was then added to the well and the plate was placed in a tissue culture incubator at 37°C

containing 5% CO_2. Expansion medium was changed every 3-4 days. Three-dimensional (3D) organoids generally became visible within 7 days and were ready for passaging within 14 days post-isolation.

2.5.1.3   Organoid Maintenance & Passaging

Once organoids were established, the expansion media continued to be changed every 3-4 days. Organoids were routinely passaged at a ratio of 1:4 – 1:6 every 5-7 days, depending on when they reached roughly 80% confluency within the Matrigel dome. To passage, media was removed from the well and replaced by 1ml of ice-cold Wash medium *(Table 2.14)*. A pipette was used to manually dissociate the Matrigel dome through pipetting up and down and scraping before the organoid suspension was transferred to a 15ml centrifuge tube containing 9ml Basal Medium *(Table 2.16)*. To ensure all basement matrix could be properly washed from the organoids, no more than 3 wells of a 24-well culture plate were pooled into one centrifuge tube. The suspension was then centrifuged at 250-300g and 8°C for 5 minutes. Depending upon the size of organoids in the wells that were being passaged, the speed of this centrifugation step could range from 250-300g. Smaller organoids were centrifuged at speeds closer to 300g whilst larger organoids were centrifuged at speeds closer to 250g. The supernatant was then discarded, leaving roughly 2ml of supernatant above the pellet. Organoids were resuspended in the remaining medium, before Basal medium was added to a total volume of 10ml. The suspension was then centrifuged again at 250g and 8°C for 5 minutes. All supernatant was aspirated and the pelleted cell aggregates were resuspended in the appropriate volume of ice-cold Matrigel (50μl per well of a 24-well plate). The matrix suspension was then immediately seeded into the centre of each well in a pre-warmed 24-well plate and incubated at 37°C for 5-10 minutes, or until the Matrigel polymerised. Pre-warmed expansion media was then overlaid on top of the Matrigel domes and the plate was returned to the incubator for routine growth.

2.5.1.4   The freezing of Organoids

As with the 2D cell lines, organoids that had undergone a relatively low number of passages were selected for freezing to avoid transcriptional drift associated with increasing passages. To prepare the organoids for freezing, Matrigel domes were

manually dissociated in 1ml of ice-cold wash medium with a pipette, as described in Section 2.5.1.3. Organoid suspension was then transferred to a 15ml centrifuge tube containing 9ml basal medium before being centrifuged at 150g and 8°C for 5 minutes. The supernatant was removed, leaving roughly 2ml of supernatant above the pelleted cell aggregates. Organoids were resuspended in the remaining supernatant and the tube was centrifuged again at 200g and 8°C for 5 minutes. Following this final centrifugation, the supernatant was fully discarded, and the pelleted cell aggregates were resuspended in 500μl of ice-cold Recovery™ Cell Culture Freezing Medium (ThermoFisher, USA) per well. The suspension was immediately added to a cryo tube (ThermoFisher, USA), with one well allocated to each tube, and transferred to a Mr. Frosty™ Freezing Container (ThermoFisher, USA). Mr Frosty™ containers facilitate the optimal rate of cooling (approximately -1°C / minute) for cell preservation. Following at least 24 hours at -80°C, tubes were then transferred on dry ice to long-term liquid nitrogen storage.

2.5.1.5   Establishing organoids from storage

Organoids taken from -80°C or liquid nitrogen storage were transferred on dry ice for rapid defrosting by thawing at 37°C for 2-3 minutes. Once thawed, the suspension was transferred to a 15ml falcon containing 10ml of pre-warmed basal medium and centrifuged at 300g for 5 minutes. The supernatant was then discarded, and the pellet was resuspended in 50µl Matrigel to be seeded as a dome into the centre of a well in a pre-warmed 24-well culture plate. The plate was then incubated at 37oC and 5% CO2 for 10 minutes to allow the Matrigel to polymerise before 500µl of expansion medium was added over the dome. Organoids were then maintained as described in Section 2.5.1.3.

2.5.2   *Ex vivo* model optimisation

A variety of methods exist for the monitoring of organoid viability *ex vivo* (Debruyne et al. 2022). However, the model's 3D nature poses unique limitations which interfere with the ability to measure response to therapy whilst simultaneously recapitulating crucial *in vivo* characteristics. Indeed, many *ex vivo* viability detection methods, including flow cytometry and immunohistochemistry, involve destructive sample processing and, therefore, the loss of 3D context. Live-cell imaging using fluorescent dyes can be

employed to maintain 3D context and monitor longitudinal therapeutic response. However, these approaches are also affected by various limitations including limited probe and dye diffusion or probe ability to penetrate across the multiple cellular layers found in larger organoids (Reiche et al. 2022).

2.5.2.1   Live cell imaging optimisation

Given that this model system was new to our group, initial optimisation experiments were conducted to determine the most time- and cost-efficient method of monitoring the impact of FLIPi within the scope of this project. As such, organoids were split as described in Section 2.5.1.3 and seeded into either pre-warmed 96-well tissue culture plates (Corning, USA) or an 8-well, glass bottom μ-Slide plate (ibidi, Germany) as small clusters of cells embedded in either 10μl or 30μl of Matrigel (Corning, USA) respectively. Organoids were left to self-organise and establish for 24 hours before being monitored according to various viability parameters. Conducting the assay in a 24-well plate format was also considered, however, the cost of required reagents was beyond the scope of this project.

Initially, to preserve 3D integrity and monitor apoptosis in the organoids, live cell imaging methods were explored. A known apoptosis-inducer, Ionomycin (Santa Cruz Biotechnology, USA), was used to confirm the sensitivity of assays for detecting apoptotic cell death *ex vivo*. Produced by the *Streptomyces conglobactus* bacterium, membrane-permeable Ionomycin functions as a calcium ionophore which facilitates the transfer of calcium ions (Ca^{2+}) in and out of cells. Ionomycin-induced increases in cellular calcium levels have been shown to trigger cell death through apoptosis and autophagy (Takei and Endo 1994; Park et al. 1996; Gil-Parrado et al. 2002; Pinton et al. 2008). Glass bottom imaging plates (ibidi, Germany) were used for live TimeLapse imaging of organoids following ionomycin (10μM in DMSO) or DMSO control treatment and, subsequently, for whole-well fixation and immunofluorescence imaging at predetermined time points.

Briefly, apoptosis was monitored in real-time using a non-toxic NucView 405 CASP-3 fluorogenic substrate (Biotium, USA). Without interfering with apoptosis, the NucView

dye enters cells as a high-affinity DNA-binding fluorogenic dye linked to the CASP- 3/7 recognition sequence (DEVD) *(Figure 2.11)*. This engineered caspase substrate is initially non-fluorescent and remains within the cytoplasm. However, during apoptosis, activated CASP- 3/7 can cleave its substrate and release the high-affinity DNA-binding dye which then translocates to the nucleus. The cleaved dye expresses blue fluorescence following its binding to DNA and therefore functions as a nucleic marker of cells undergoing apoptosis.

A high-affinity DNA-Binding dye is linked to the Caspase-3 peptide substrate DEVD

Non-toxic, non-fluorescent substrate enters cells

Nucleus

Cytoplasm

After caspase cleavage in apoptopic cells, the high-affinity DNA dye is released and will fluoresce upon binding to DNA
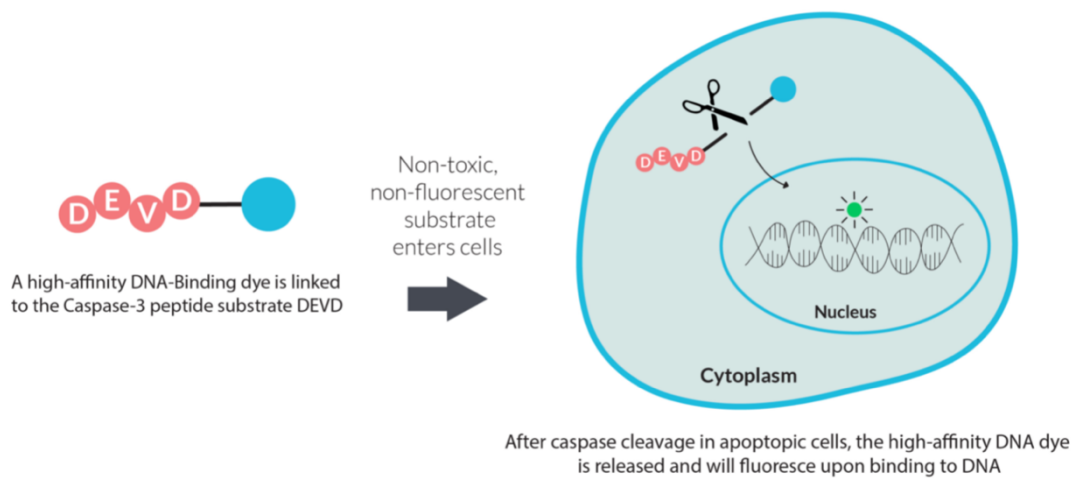
Figure 2-11 Schematic overview of the NucView-405 reagent mechanism of action.
Figure taken from Biotium.co.uk.

In certain instances, it was possible to monitor NucView-405 accumulation, and therefore, apoptosis using real-time TimeLapse microscopy following ionomycin treatment *(Figure 2.11)*. However, the dye did not appear to penetrate most organoids, rendering this method too costly and time-consuming for the scope of this project.
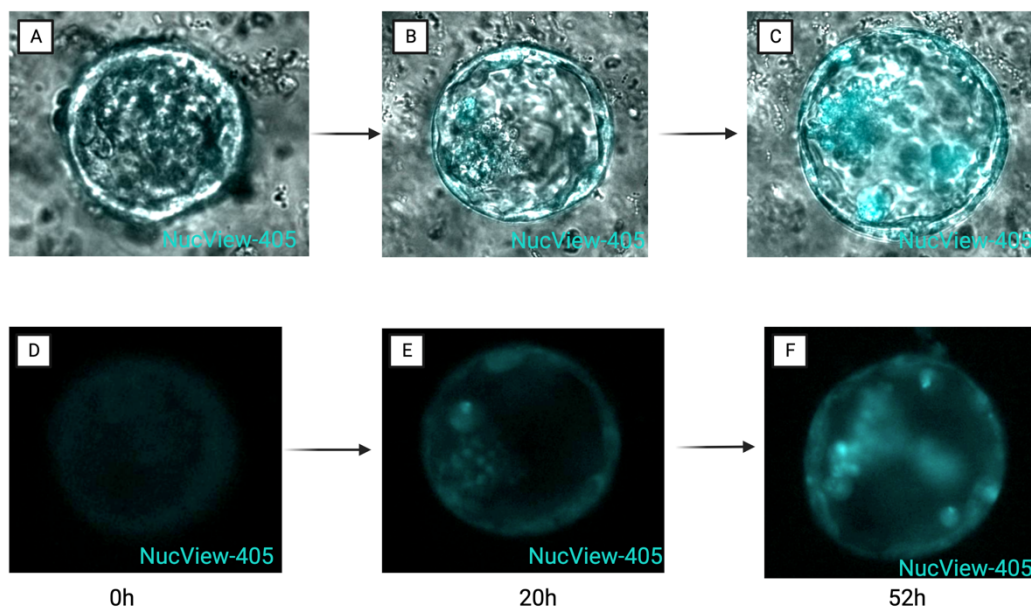
Figure 2-12 Representative images of the same murine PDAC-derived organoid at set timepoints following ionomycin treatment to induce apoptosis.
Cells undergoing apoptosis shown in cyan due to fluorescence activity of NucView-405 reagent (Biotium, USA) **A-C** Blue (405nm) channel overlaid above phase (brightfield) channel. **D-F** Blue channel only of the same organoid. Images taken from a Time-lapse movie captured using a Leica fluorescence microscope and the LasX software (Leica, Germany). Images processed using Fiji software (Schindelin et al. 2012).

As the NucView 405 probe withstands formalin-fixation and cell permeabilisation, organoids underwent whole-well fixation and immunofluorescent staining immediately following Time-lapse imaging, with minimal damage to 3D integrity.

Organoids were fixed in their wells with 10% formalin for 30 minutes at room temperature (RT) before formalin was replaced with PBS and wells were incubated for 10 minutes on a rocker at RT. PBS was carefully removed, and wells were then washed with a solution containing PBS and 0.03% Triton X-100 (Merck) (PBS-Tx) for a further 10 minutes on a rocker at RT. PBS-T was then removed and cells were permeabilised by a 15-minute incubation in PBS containing 0.052% Triton X-100 and 0.05% Sodium dodecyl sulphate (SDS) at RT. After 15 minutes, the permeabilisation solution was replaced with PBS-Tx and wells were washed for 15 minutes on a rocker at RT. Two further PBS-Tx washes were performed before wells were incubated in blocking solution (PBS-T + 10% FBS) for 2 hours at RT, to block any non-specific primary antibody binding. After the 2-

hour incubation, the blocking solution was replaced by a primary antibody targeting CC-3 diluted in the blocking solution, at dilutions detailed in **Table 2.18**, and wells were incubated overnight at 4°C. Following the overnight incubation, wells underwent 3 sequential 15-minute washes with PBS-Tx before wells were incubated with an AlexaFluor 488 secondary antibody (ThermoFisher) and Phalloidin-Atto647N (Merck), at dilutions detailed in **Table 2.18,** for 2 hours at RT. Wells were then washed a further 3 times with PBS-Tx before being imaged in PBS by a Confocal microscope (Zeiss, Germany).

Table 2-18 Summary of antibodies used for immunofluorescent staining of organoids

	Type of Antibody	Species	Dilution	Fluorescent?	UK Catalogue Number
Cleaved Caspase-3 (ASP175)	Primary	Rabbit	1:300	NA	9661 (Cell Signalling Technologies)
Phalloidin	Atto conjugated probe	NA	1:1000	Atto 647N	65906 (Merck)
NucView 405	DNA Dye (Live imaging)	NA	2µM	405nm	10407 (Biotium)
IgG (H+L) Highly Cross-Adsorbed Secondary Antibody	Secondary conjugated antibody	Goat anti-rabbit	1:1000	AlexaFluor 488	A-11034 (ThermoFisher)

Although this method retained organoid 3D structure and NucView 405 fluorescence, the penetration efficiency of fluorescent antibodies proved problematic. Phalloidin-Atto647N (Merck, Germany) was used to label F-actin filaments for the distinction of individual cells within each organoid. However, z-stack imaging using a Confocal microscope (Zeiss, Germany) revealed limited depth-penetration, whereby Phalloidin fluorescence intensity decreased depending on the positioning of the cells within the organoid **(Figure 2.13 A, C & D)**. Cells at the base of the organoid (closest to the bottom of the plate) expressed very low levels of fluorescence, compared to cells at the top of the organoid (furthest from the bottom of the plate). This effect was particularly prominent in larger organoids (>200µm diameter), suggesting that either dense cellular layers or residual Matrigel were impairing the penetrance of antibodies and preventing the labelling of the lower half of each organoid. Similarly, the co-stain of NucView 405 and CC-3 primary antibody was detected successfully following ionomycin treatment

but only towards the upper region of the organoid (furthest from the bottom of the plate). The antibodies appeared to co-localise and suggest that dead or dying cells undergoing apoptosis were being removed from the outer cellular layer into the organoid lumen *(Figure 2.12 B)*. However, limited fluorescence penetration in each organoid complicated quantification efforts as it was not possible to determine whether apoptotic cells exclusively localised within the upper region of each organoid or whether the detection method was simply unable to penetrate the entire 3D structure.
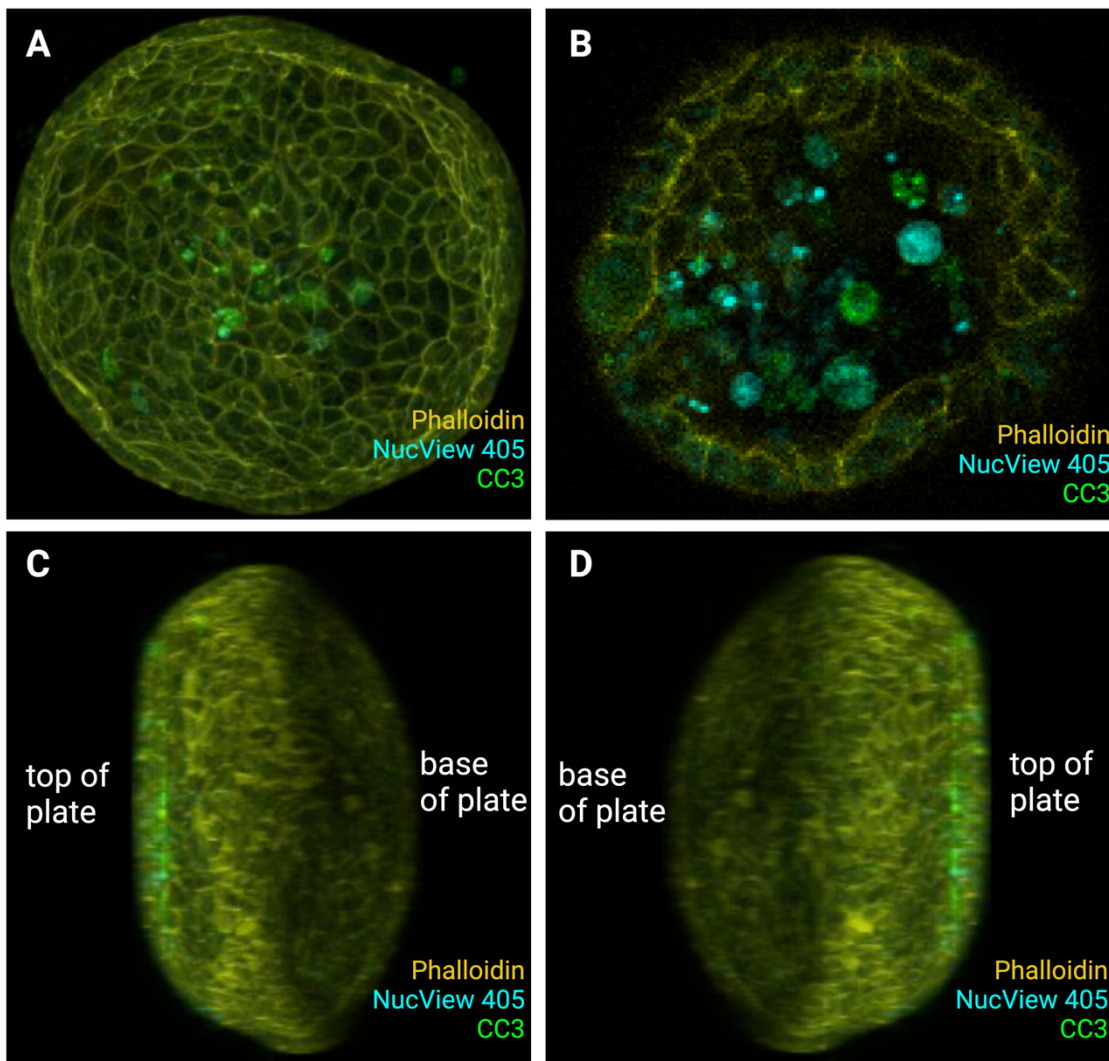
Figure 2-13 Representative immunofluorescent staining of murine PDAC-derived organoids depicting the limited depth penetration of dyes.
A Maximum intensity 3D projection (MIP) of an imaging z-stack encompassing the entire organoid. **B** Representative section taken from the z-stack showing NucView-405 and CC-3 localisation within the organoid lumen. **C-D** View of the same organoid when the z-stack MIP is viewed at 90º (**C**) and 270º (**D**) angles. Images taken using a confocal microscope (Zeiss, Germany) and processed using Fiji software (Schindelin et al. 2012). Figure created using Biorender.com.

2.5.2.2 Organoid viability assay optimisation

Following the limitations affecting the quantification of apoptosis *ex vivo*, it was decided that quantification of relative organoid viability would be a more efficient method to investigate the response to FLIPi within KPF-FLIP$^{fl/fl}$ tumour-derived organoids within the time constraints of this project. The cell titer blue (CTB) viability assay (Promega, USA) was therefore used to estimate the number of viable cells within each well over time. CTB measures the metabolic capacity of cells using the indicator dye, resazurin. Only viable cells can reduce resazurin to the highly fluorescent resorufin. Therefore, cell viability is measured according to fluorescence intensity following incubation with the CTB resazurin reagent, thereby providing a relative quantification of the amount of metabolically active (viable) cells in each well.

Initially, organoids were split as described in Section 2.5.1.3 and seeded into pre-warmed 96-well culture plates in 10µl Matrigel domes. 100µl Expansion Media was overlaid on top of the Matrigel and organoids were allowed to establish over 24 hours at 37°C and 5% CO_2. Following the 24-hour incubation, optimal CTB incubation time for organoid culture was assessed at a range of time points following the addition of 20µl CTB to the media in each well *(Figure 2.14 A)*. Relative cell viability was quantified in terms of overall fluorescence intensity measured by a CLARIOstar (BMGLabTech) plate reader set to $530nm_{Ex}/590nm_{Em}$. No significant difference was recorded in fluorescence between each time point, suggesting that 30 minutes of incubation with CTB reagent is sufficient to detect the reduction of resazurin to the fluorescent resorufin by organoids. Therefore, 30 minutes was selected as the optimal CTB incubation time and used for all subsequent assays. As CTB measurements and timings are known to be cell- and/or model-type specific, it is not possible to include a positive control cell/organoid line to aid in determining optimal incubation time. However, results were compared to a 'blank' control well which contains only cell culture media without cells, to ensure that the fluorescence recorded was not due to background artefact. The specificity of CTB was then determined following the incubation of organoids with Ionomycin for 48 hours to induce cell death, dosed as described in Section 2.5.2.1 *(Figure 2.14 B)*.

The viability of organoids was determined following 24 to 96 hours of culture using the CTB assay and compared to the manual quantification of the total number of organoids and their average diameter per well *(Figure 2.14 C-F).* Although CTB is non-toxic and can efficiently monitor longitudinal cell viability in 2D, institute colleagues had previously noted a propensity for CTB to become trapped in the Matrigel and impact sequential measurements in 3D cultures (Data not shown; Velasco Martinez, unpublished). Therefore, it was necessary to set up separate technical repeats for each time point to monitor CTB over time in the organoids. Given the additional costs associated with this approach and the inability to monitor the same well over time, it was decided to use the manual quantification of the total number of organoids as an estimate of cell viability in response to FLIPi *ex vivo*. Although it is not possible to identify organoids containing dead or dying cells with this approach, the trend in total number of organoids measured over time did roughly correlate with the trend seen following the CTB assessment of cell viability. Regardless of changes in viability or total number, organoid diameter continually increased over time.
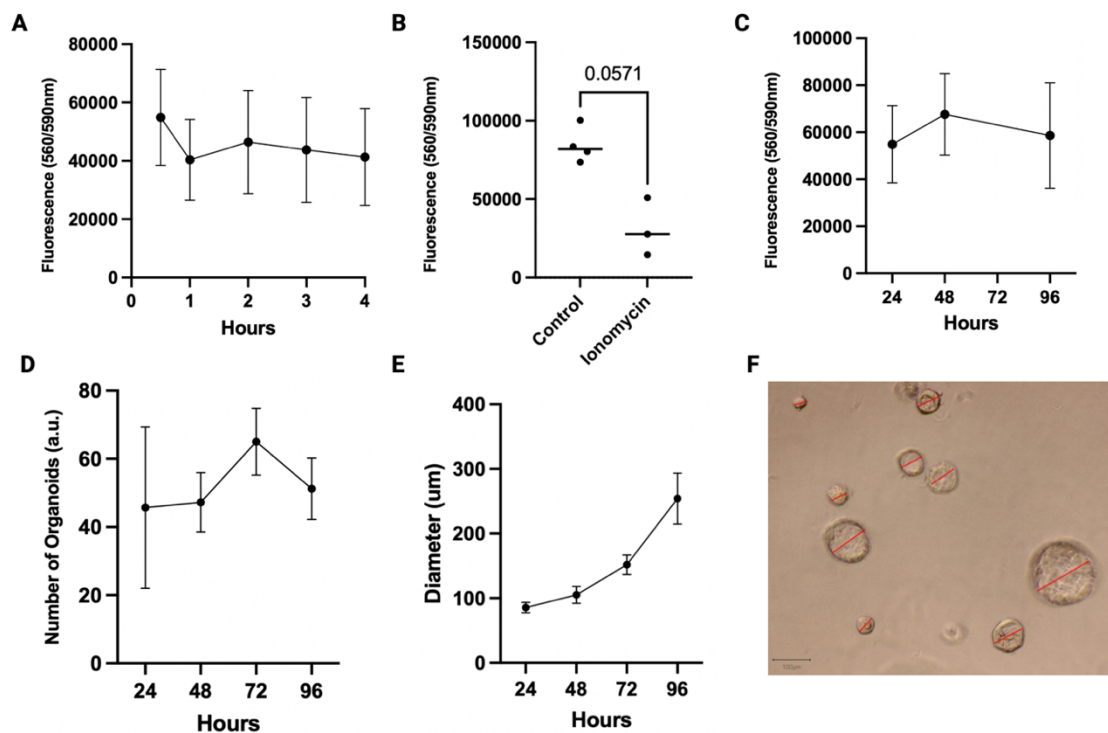
Figure 2-14 Assessing the viability of murine PDAC-derived organoids *ex vivo*.
A-C Fluorescence emitted by organoid cultures following the addition of cell titre blue reagent (Promega, USA). **A** Fluorescence emitted at set timepoints to determine optimal incubation timing for the reagent. **B** Fluorescence emitted 48 hours after ionomycin (10μM) or DMSO control treatment. **C** Fluorescence emitted by organoids under standard culture conditions to assess viability over time. **D** Absolute number of organoids per well of a 96-well plate when counted manually using a brightfield microscope (Zeiss, Germany). **E** Average diameter of organoids per well in a 96-well plate. **F** Representative image showing standard method of quantifying organoid diameter through the use of QuPath software (Bankhead et al. 2017).

2.5.3 Inhibition of cFLIP *ex vivo*

Given the capacity of organoids to retain genetic and epigenetic characteristics of the primary tumour, cells within KPF-FLIP^fl/fl organoids express a tamoxifen-inducible Cre recombinase and *loxP*-flanked copies of the gene encoding cFLIP (*CFLAR*). However, institute colleagues had previously found that the tamoxifen dose required for *ex vivo* recombination was toxic to PDAC-derived organoids (Data not shown; Salvador Barbero & Hill, unpublished). Therefore, a commercially available Cre Recombinase Adenovirus (AdCre; Vector BioLabs, USA) was purchased to be taken up by cells within the organoids and express a codon optimised Cre Recombinase (iCre) which could then bind at the *loxP* sites flanking exon 2 of the gene encoding cFLIP (*CFLAR*) and, ultimately, result in cFLIP deletion within the organoids. The recombination efficiency of AdCre was determined using a fluorescent mCherry Adenovirus (Ad-mCherry; Vector BioLabs, USA), which expressed the improved red fluorescent protein, mCherry, under the control of the same promoter and incorporated on the same viral backbone as the AdCre *(Table 2.19).*

Table 2-19 Composition of adenoviral vectors.
Viruses purchased from Vector BioLabs, USA. iCre = codon optimised Cre recombinase

	Ad-mCherry	Ad-CMV-iCre
Viral Backbone	Human Adenovirus Type5 (dE1/E3)	Human Adenovirus Type5 (dE1/E3)
Promoter	CMV (ubiquitous)	CMV (ubiquitous)
Reporter	mCherry	-

2.5.3.1 Adenoviral Transfection

Adenoviruses are relatively large, non-enveloped viruses consisting of three key structural components for gene delivery, namely a hexon, a knobbed fiber and a penton base (Lee et al. 2017). The hexon protein forms the icosahedral structure of the viral capsid, whilst the knobbed fibers protrude from the penton bases and are crucial in facilitating receptor binding and internalisation. Following the binding of the fibers to host cell glycoprotein receptors, the virus is endocytosed into the host cell, facilitating the release of the internal nucleocapsid containing the viral double-stranded DNA. The viral nucleocapsid then translocates to the host cell's nucleus to initiate linear, extra-chromosomal replication of the viral DNA. In the case of the commercially available Ad-CMV-iCre and Ad-mCherry, this results in the expression of a codon-optimised Cre recombinase or the mCherry fluorescent protein respectively within the host cell.

2.5.3.2 Determining the optimal viral titer for organoid recombination

To ensure efficient recombination within the majority of organoids in each well, organoids were infected with Ad-mCherry as a control to ensure the virus could penetrate the Matrigel dome and to determine the optimal viral titer required. Organoids were split as described in Section 2.5.1.3 and seeded as small clusters of cells in 10µl Matrigel in a 96-well tissue culture plate. Domes were incubated at 37°C for 10 minutes to enable Matrigel polymerisation, before being overlaid with 100µl Expansion Media and incubated at 37°C and 5% CO2 for 24 hours. After incubation, media was replaced with fresh media containing Ad-mCherry at various titers *(Table 2.20)* and placed in the Incucyte S3 Live Cell Analysis platform (Essen Bioscience, MI, USA) for imaging and incubation at 37°C and 5% CO_2. It was not possible to use the Incucyte analysis software to accurately quantify the percentage of mCherry-positive organoids. However, the images obtained by the Incucyte were used to manually quantify the total number of organoids expressing red fluorescence per field of view. mCherry-positive organoids were classified as any organoid that expressed red fluorescence in over 50% of its surface area. The number of mCherry-positive organoids was then normalised to the total number of organoids (>50µm diameter) per field of view and expressed as a percentage. This optimisation assay resulted in the selection of $1x10^7$ PFU/ml (1µl/ml) as the optimal titer for inducing successful recombination in the majority of organoids

per well and was then used in subsequent experiments to explore the response to AdCre-mediated FLIPi *ex vivo*.

Table 2-20 Summary of Ad-mCherry viral titer optimisation assay.
Ad-mCherry adenovirus purchased from Vector BioLabs (USA). FOV = field of view

Concentration (µl/ml)	Viral Titer (PFU/ml)	% mCherry positive organoids (per FOV) 96-hours post infection	+/- SEM (%)
0	0	0	0
0.2	$1x10^6$	53.7	1.2
1	$1x10^7$	73.0	2.3
1.5	$1.5x10^7$	71.0	4.0

2.5.3.3 Adenoviral infection of organoids and assessment of viability

To induce AdCre-mediated deletion of cFLIP *ex vivo*, organoids were seeded and incubated for 24 hours, as described in Section 2.5.3.1. After 24 hours, media was replaced with fresh expansion media containing either 1µl/ml AdCre or 1µl/ml Ad-mCherry control *(Figure 2.15)*, and cells were placed in the Incucyte S3 Live Cell Analysis platform (Essen Bioscience) to monitor recombination efficiency, as detailed in Section 2.5.3.1. The total number of organoids per well was also manually quantified each day and a representative image was taken to quantify the average organoid diameter per well. These values were normalised to the total number of organoids and average diameter per well that was observed immediately prior to adenoviral infection (0-hour time point).

Twenty-four hours following adenoviral infection, certain wells were treated with 20ng/ml recombinant human TNF-Related Apoptosis Inducing Ligand (TRAIL) (super-killer TRAIL, ENZO Life Sciences), whilst others remained untreated. The plate was then returned to the Incucyte and incubated for a further 48 hours, with the number of organoids and their average diameter quantified every 24 hours. The assay was repeated independently at least three times, with a minimum of four technical repeats included per experiment.
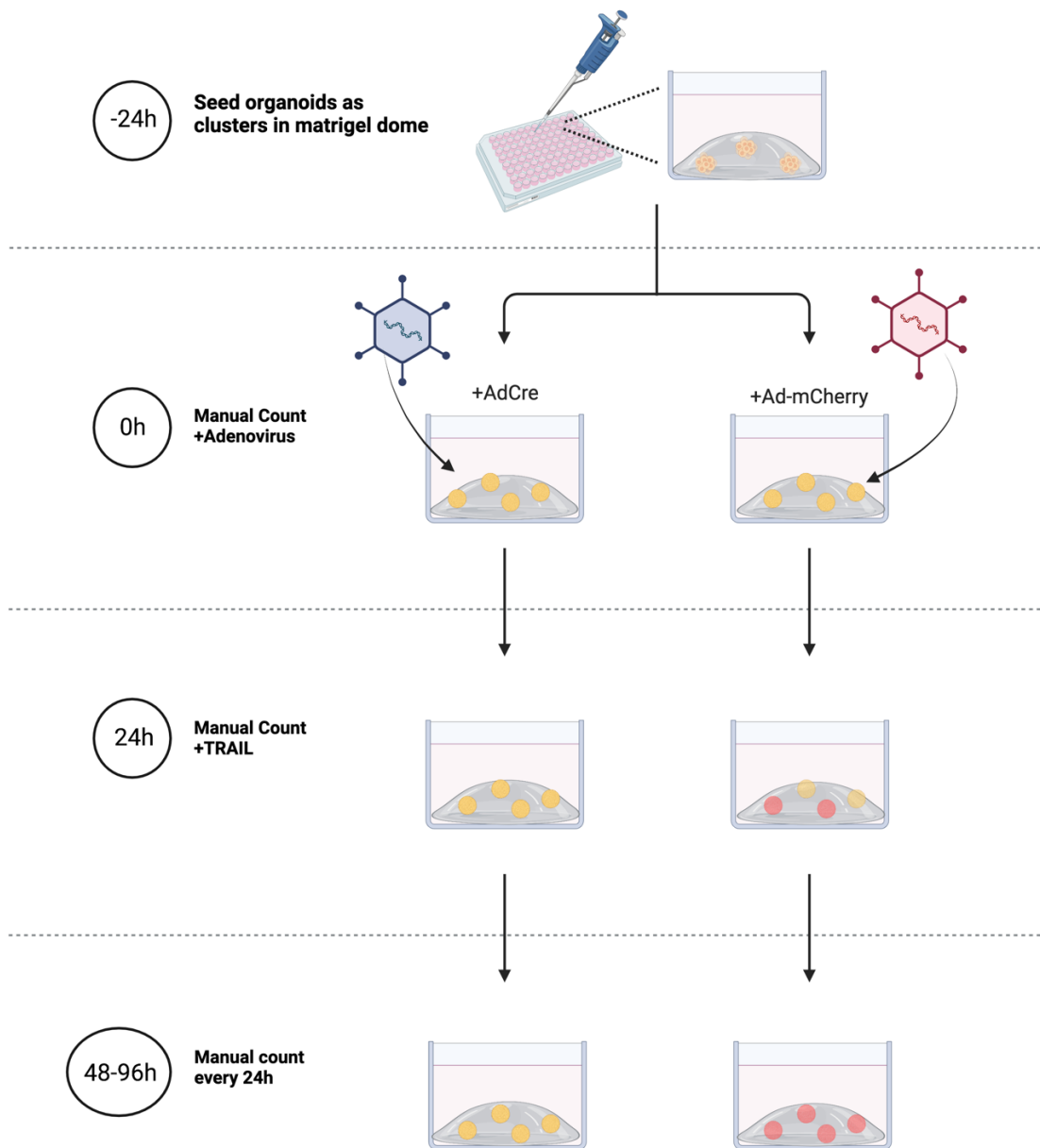
Figure 2-15 Schematic overview of adenoviral infection protocol to induce cFLIP deletion in PDAC-derived tumour organoids from the KPF-FLIP GEMM.

Organoids were seeded as clusters of cells in a 10μl Matrigel dome and incubated at 37°C and 5% CO_2 for 24 hours. The number of organoids per well was then manually quantified, prior to the addition of 1μl/ml adenovirus. 24 hours after adenoviral infection, exogenous TRAIL was added to certain AdCre- and Ad-mCherry-treated wells, with others left as untreated controls. The number of organoids was counted every 24 hours until endpoint (96-hour timepoint). Figure created with Biorender.com. *PDAC = pancreatic ductal adenocarcinoma; KPF-FLIP = Pdx1-Flp; FSF-KrasG12D/+; Trp53frt/+; Rosa26CAG-FSF-CreERT2; LSL-cFLAR; GEMM = Genetically engineered mouse model; AdCre = Cre recombinase adenovirus (Ad-CMV-iCre adenovirus - Vector Biolabs, USA); Ad-mCherry = fluorescent mCherry adenovirus (Vector Biolabs, USA); TRAIL = Super-killer TRAIL (ENZO Life Sciences).*

2.5.3.4   Statistical Analysis

GraphPad Prism 9 software (GraphPad, USA) was used to analyse the data. Results are expressed as mean ± SEM. For data with multiple time points and treatment groups, a repeated measures two-way analysis of variance (ANOVA) was performed with Tukey correction. For comparisons between two unpaired datasets, a Mann-Whitney U t-test was performed.

3 Investigating the response of Pancreatic Ductal Adenocarcinoma cells to cFLIP inhibition *in vitro*

3.1 Introduction

Despite major advances in our understanding of PDAC development and heterogeneity, patient prognosis and treatment options have unfortunately not seen a corresponding improvement over the past few decades (Ferlay et al. 2018; Siegel et al. 2020). Developing a targeting strategy which takes advantage of the prevalence of oncogenic KRAS remains a fundamental aim, due to its expression in over 90% of all human PDAC tumours (Grimont et al. 2022).

As discussed in section 1.4.5, mutant KRAS has been shown to drive malignant, non-canonical TRAIL signalling in PDAC tumour cells (von Karstedt et al. 2015). Despite a wide range of cancers upregulating TRAIL receptor expression, the resistance of tumour cells to canonical TRAIL-induced apoptosis has been well studied (Lemke et al. 2014). Tumour-driven expression of key anti-apoptotic proteins enables apoptosis evasion and facilitates malignant, non-canonical pathways.

cFLIP was identified as a crucial inhibitor of TRAIL-induced apoptosis as part of the drive to sensitise tumour cells to TRAIL (Safa 2012). As detailed in section 1.5, cFLIP inhibits the initial stages of TRAIL-induced apoptosis, preventing downstream caspase activation. Previous work in our laboratory has demonstrated that suppression of cFLIP can successfully sensitise the notoriously difficult-to-target breast cancer stem cell population to TRAIL-mediated killing (Piggott et al. 2011). Similar sensitisation effects have been observed in other cancer types, including PDAC, whereby cFLIP inhibition sensitised two established and one primary-derived PDAC cell line to TRAIL-induced apoptosis (Haag et al. 2011).

Indirect cFLIP inhibition has been associated with the anti-tumour cytotoxic effect of various standard-of-care chemotherapeutics, including those used to treat PDAC (Haag et al. 2011; Humphreys et al. 2018). However, chemotherapy can also lead to systemic,

off-target toxicity which can make treatment regimens difficult to tolerate. Given a recent immunohistology study by Haag et al. which found elevated cFLIP expression in human pre-malignant (PanIN) and PDAC cells, direct cFLIP inhibition may provide a more targeted approach to induce cytotoxic responses exclusively within these tumour cells (Haag et al. 2011).

Our laboratory has demonstrated the efficacy of complete siRNA-induced cFLIP knockdown in a variety of cancer cell lines (Piggott et al. 2011). Complete knockdown studies can be useful *in vitro* to determine response to precise protein targeting in the absence of confounding variables, such as drug metabolism. However, despite exciting progress involving the *in vivo* delivery of genetic targeting approaches, an effective vector or delivery system with minimal limitations has yet to be developed (Dastjerd et al. 2022). Therefore, our laboratory is currently developing a novel small molecule inhibitor (OH14 – Olivia Hayward, unpublished) which specifically targets the role of cFLIP in its inhibition of TRAIL-induced apoptosis by preventing its recruitment to the DISC and, therefore, OH14 enables the progression of the apoptotic cascade.

Given the combined upregulation of cFLIP and KRAS-driven, TRAIL receptor-mediated malignant signalling in PDAC, these cells may be responsive to cFLIP inhibition to re-activate canonical, TRAIL-induced apoptosis (Haag et al. 2011; von Karstedt et al. 2015). To determine the prognostic relevance of this hypothesis, the experiments in this chapter first built upon findings by Johnston et al. which showed that PDAC tumours expressing high levels of cFLIP are associated with significantly reduced Disease-Free Survival (Johnston et al. 2020). We sought to determine the expression levels and any associated survival impact of cFLIP and relevant TRAIL pathway components in a large cohort of patient PDAC tumour samples.

Here we also expand upon the promising *in vitro* work published by Haag et al., which used two established PDAC cell lines (ASPC-1 and PancTu1) and one primary PDAC line (ULA-PaCa) (Haag et al. 2011). To better reflect patient heterogeneity, we investigated whether cFLIP inhibition is sufficient to re-activate TRAIL-induced apoptosis *in vitro* in a wider panel of established and patient-derived primary cell lines (EPCCLs and PDCLs

respectively). We then utilised this panel to determine whether cell lines could aid in stratifying the response of PDAC tumours to cFLIP inhibition and to establish an *in vitro* model to investigate the potential of this approach in more detail at the molecular level.

3.2 Chapter Aims

1.   To establish the prognostic relevance of targeting cFLIP in pancreatic cancer.

2.   To characterise the response of EPCCLs and PDCLs to cFLIP siRNA inhibition

3.   To determine the response of EPCCLs to our lab's novel small molecule cFLIP inhibitor (OH14)

4.   To determine whether the response to cFLIP inhibition can be stratified according to expression levels of cFLIP, TRAIL DRs and/or TRAIL

3.3   Results

3.3.1   cFLIP and TRAIL pathway expression is elevated in human Pancreatic Cancer

The binding of TRAIL to its constitutive death receptors (DR4 and DR5) activates canonical, caspase-mediated apoptosis. However, the expression of anti-apoptotic proteins, such as cFLIP, inhibits the canonical pathway, thereby facilitating pancreatic tumour growth and metastasis in a DR5-dependent manner in KRAS-mutant PDAC cells (von Karstedt et al. 2015). We, therefore, hypothesised that cFLIP inhibition should be sufficient to specifically re-activate canonical apoptosis within KRAS mutant PDAC cells. To investigate the prognostic relevance of cFLIP and TRAIL-R expression in PDAC, we interrogated the GEPIA2 RNASeq analysis platform, as discussed in section 2.3.1.

Firstly, significantly elevated TRAIL ligand expression was detected in PDAC tumour samples when compared with normal pancreatic samples, indicating upregulation of the pathway within PDAC *(Figure 1A)*. The expression of DR4 and DR5 was also increased in the PDAC setting, with DR4 expression significantly increased but DR5 not quite reaching significance. Of note, levels of DR5 in the normal pancreas were around four-fold greater than pancreatic levels of DR4 and remained comparatively higher than DR4 in the tumour setting. This suggests that significant upregulation of DR5 may not be required by tumour cells, as the baseline expression level is already comparatively high in the normal pancreas. Importantly, cFLIP expression was also significantly greater in the tumour vs normal setting, thereby confirming the immunohistology findings of Haag et al. (2011).

As described in section 1.1.2, PDAC severity can be subclassified into stages based on tumour size and metastatic spread. The least severe and most treatable form of the disease falls into Stage I, with the most advanced, metastatic tumours categorised as Stage IV. To determine whether cFLIP upregulation is associated with specific stages of PDAC progression, a GEPIA2 stage plot was produced *(Figure 1B)*. We discovered that certain key differences in cFLIP expression levels can be observed across different stages of PDAC. Although these different expression levels did not quite reach significance (F value = 1.95; p = 0.0881), inter-tumour variation in cFLIP expression appears to be associated with the disease stage. Indeed, stage IA showed the most consistent level of

cFLIP expression, as most cases clustered around the median expression value, indicating cFLIP is upregulated in the majority of small, non-metastatic PDAC tumours. Whereas intermediatory stages IB – IIB possessed the greatest variation in expression levels, with some tumours expressing comparatively lower or higher levels of cFLIP than their group's respective median level. Finally, most of the advanced, Stage III-IV tumours appear to show greater consistency in cFLIP expression than their more intermediate counterparts. Importantly, median cFLIP expression at each pathological stage of PDAC remained greater than that seen in baseline, normal pancreatic samples. Most intermediate cases showed upregulation of cFLIP expression compared to baseline; however, it should be noted that some cases did not. Taken together, this data indicates a role for cFLIP across all stages of PDAC, including the most advanced, least treatable stages and suggests it may represent an important target for treatment due to its ubiquitous tumour-associated upregulation.

It has previously been shown that PDAC patients expressing 'high' levels of cFLIP have significantly reduced disease-free survival compared to 'low' cFLIP tumours (Johnston et al. 2020). We were able to replicate this data using the GEPIA2 platform (Logrank p=0.026; HR(high) = 1.7; p(HR)=0.028) *(Figure 3.1C)*. However, a similar impact of 'high' cFLIP expression on overall survival was not discovered, with no significant difference existing between 'high' and 'low' expression (Logrank p=0.34) *(Figure 3.1D)*. This suggests that cFLIP may be more involved in facilitating tumour relapse following treatment than in overall tumour malignancy.

To determine the prognostic role of the upregulation of TRAIL and its receptors, the GEPIA2 platform was then used to separate PDAC patient prognosis according to tumour expression of a custom TRAIL death receptor (DR) gene signature. The gene signature was designed to include the genes encoding TRAIL, DR4 and DR5. Patient tumours that expressed high levels of this TRAIL DR gene signature were also associated with significantly reduced disease-free survival compared to tumours with low expression levels (Logrank p=0.0056; HR(high)=1.9; p(HR)=0.0064) *(Figure 3.1E)*. However, in contrast to cFLIP expression, tumours expressing high levels of TRAIL and its death

receptors were also associated with significantly reduced overall survival (Logrank p=0.0047; HR(high)=1.8; p(HR)=0.0053).

Collectively, this data suggests that the upregulation of TRAIL, DR4 and DR5 in PDAC tumours *(Figure 3.1A)* worsens patient survival *(Figure 3.1E-F)*. When coupled with the upregulation and associated negative prognostic role of cFLIP *(Figure 3.1 A-C)*, this supports the hypothesis that certain PDAC cells are upregulating cFLIP expression to evade canonical TRAIL-induced apoptosis and, instead, drive malignant non-canonical signalling.
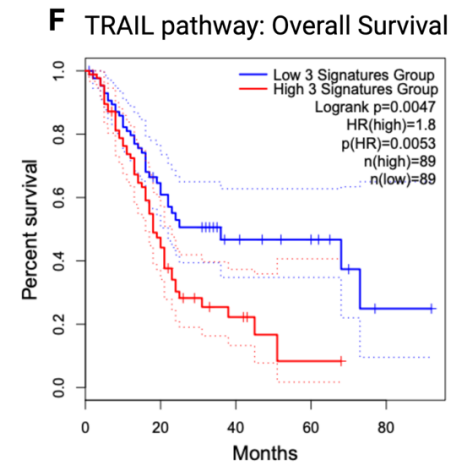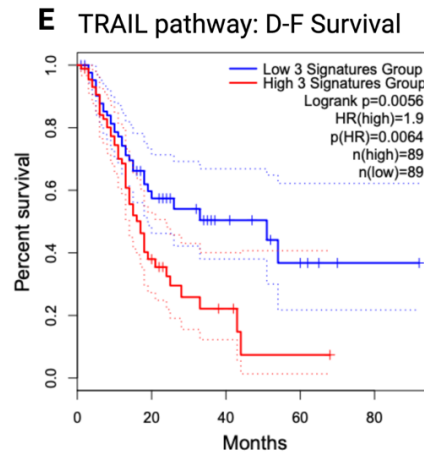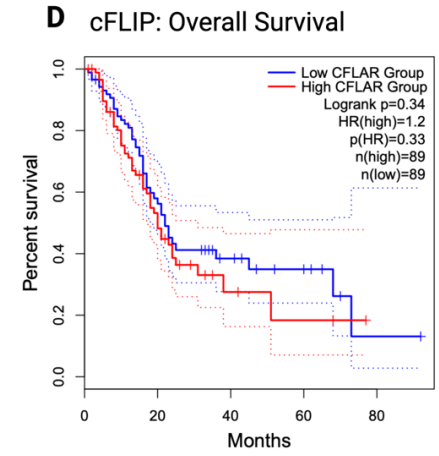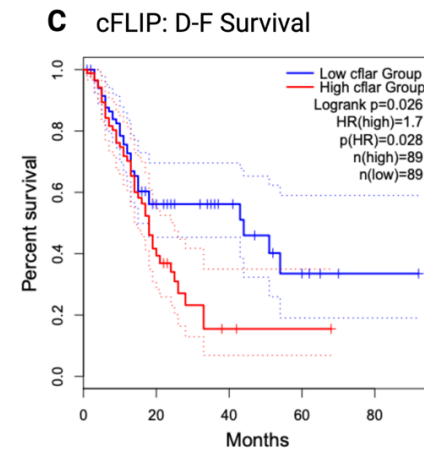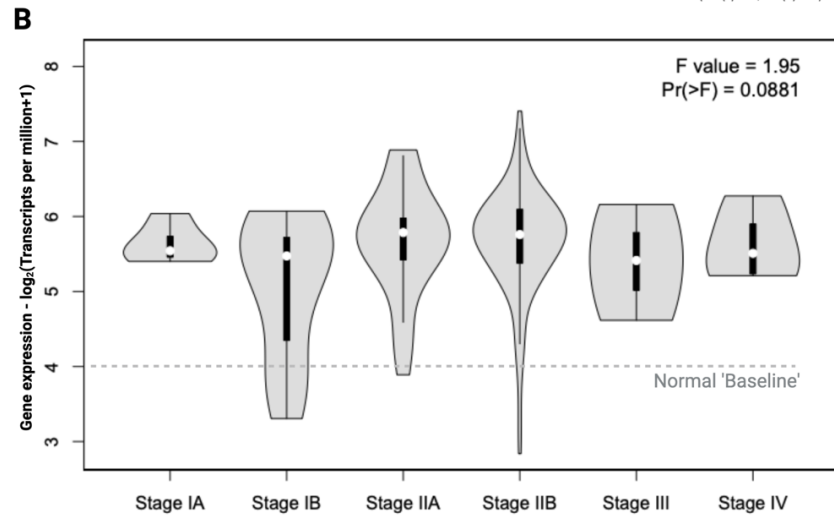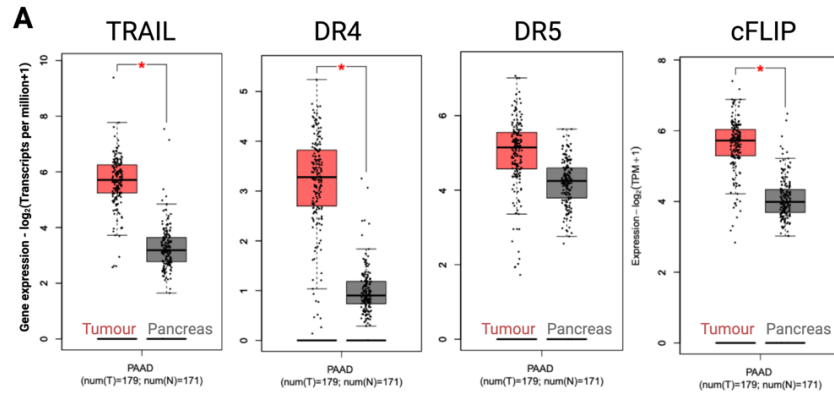
Figure 3-1 Expression of cFLIP, TRAIL and its death receptors in human PDAC and their prognostic relevance.
A Boxplot showing the expression level of genes encoding TRAIL, its two constitutive death receptors (DR4 & DR5) and cFLIP in human PDAC compared to normal pancreas (|Log2FC| Cutoff = 1; p-value cutoff = 0.01; Jitter size = 0.4; Tumour (T) n=179; Normal pancreas (N) n=171). **B** Stage plot comparing variation in expression of the gene encoding cFLIP (CFLAR) across each pathological stage of pancreatic cancer. Stage IA represents the lowest level of PDAC malignancy, namely small, non-metastatic tumours (<2cm diameter), whilst Stage IV includes the most advanced, metastatic tumours. Differential expression assessed using one-way ANOVA on log2(TPM+1) data. Dotted line represents median CFLAR expression taken from pancreas dataset shown in **A**. **C-D** Survival curves investigating the prognostic impact of CFLAR expression levels in terms of disease-free and overall survival. **C** replicates the findings of Johnston et al. (2020) **E-F** Survival curves investigating the prognostic impact of a customised TRAIL death receptor gene signature in terms of disease-free and overall survival. 'TRAIL pathway' signature includes the genes encoding TRAIL, DR4 and DR5 (TNFSF10, TNFRSF10A and TNFRSF10B respectively). For all survival curves, a median group cutoff was used, with dotted lines representing 95% confidence intervals. Data for each plot was analysed using the GEPIA2 web server and processing pipeline, using PDAC and normal pancreas RNA Sequencing data from the TGCA and GTEx project databases (Tang et al. 2019). *HR = Cox proportional Hazard Ratio; PAAD = PDAC; * = p<0.05.*

3.3.2 EPCCL panel demonstrates differential susceptibility to siRNA cFLIP inhibition (FLIPi)

Given that human PDAC tumours exhibit upregulated cFLIP expression and potentiated TRAIL pathway expression, we wished to determine whether direct cFLIP inhibition would be sufficient to reactivate the canonical TRAIL apoptotic pathway in PDAC cells.

A panel of seven EPCCLs, Panc10.05, ASPC-1, HPAF-II, CFPAC-1, Capan-2, SW1990 and BxPC3, were selected as they represent a well-established, cost-effective, and easily manipulatable platform for preclinical investigations, as detailed in Section 2.1.1. To determine whether cFLIP siRNA inhibition (FLIPi) was sufficient to de-repress the TRAIL-mediated apoptotic pathway, an Annexin V assay was performed to identify cells undergoing apoptosis. Cells were treated with either FLIPi or the non-targeting scrambled RNA (scRNA) control in the presence or absence of exogenous TRAIL ligand. Caspase inhibitors were also used in certain cell lines to ensure that any observed changes in cell death were due to caspase-dependent apoptosis and not an alternative function of cFLIP. A varying response in the amount of annexin-V stained cells was observed across all cell lines and in response to the different treatment combinations *(Figure 3.2)*.

FLIPi lead to significant sensitisation of most cell lines to TRAIL-mediated apoptosis, particularly Panc10.05 and ASPC-1 *(Figure 3.2 A-B)*. However, supplemental TRAIL was necessary in most cases to induce such a response. Interestingly, FLIPi appeared to sensitise HPAF-II and CFPAC-1 cells to TRAIL-induced apoptosis *(Figure 3.2 E-F*), but this effect was not rescued by the addition of caspase inhibitors *(Appendix A-3)*, suggesting the activation of an alternative, non-caspase dependent apoptotic pathway. Capan-2 and SW1990 also both appeared to be sensitised by FLIPi *(Figure 3.2 C-D)*, however, it is not yet known if this response was caspase-dependent.

Finally, the only KRAS wild-type cell line in the panel, BxPC-3, appeared to be intrinsically sensitive to supplementation with TRAIL *(Figure 3.2 G)*. FLIPi was not required to increase levels of apoptosis, however, it did seem to potentiate the effect.

Collectively, these data support the findings of Haag et al., in that cFLIP inhibition can sensitise PDAC cells to TRAIL-induced apoptosis *in vitro* (Haag et al. 2011). The range in susceptibility of the EPCCL panel to FLIPi suggests that patient stratification according to predicted response may be possible, however, no common underlying mutations could be linked to specific responses.

Interestingly, whilst KRAS mutant cell lines were primed to drive TRAIL signalling, the exogenous delivery of TRAIL ligand was required in most cases to observe a significant sensitisation effect of FLIPi. FLIPi alone was sufficient to induce a small, non-significant increase in apoptosis in certain cell lines and, whilst this response was greater than the response to TRAIL alone, the combination of FLIPi and TRAIL resulted in significantly increased levels of apoptosis in most cell lines *(Figure 3.3)*. This suggests that the constitutive activation of DR5-mediated, malignant signalling observed by von Karstedt et al., may not be replicated in our panel of EPCCLs, possibly due to the absence of TRAIL-supplying immune cells or the lack of cell-autonomous TRAIL signalling (von Karstedt et al. 2015).
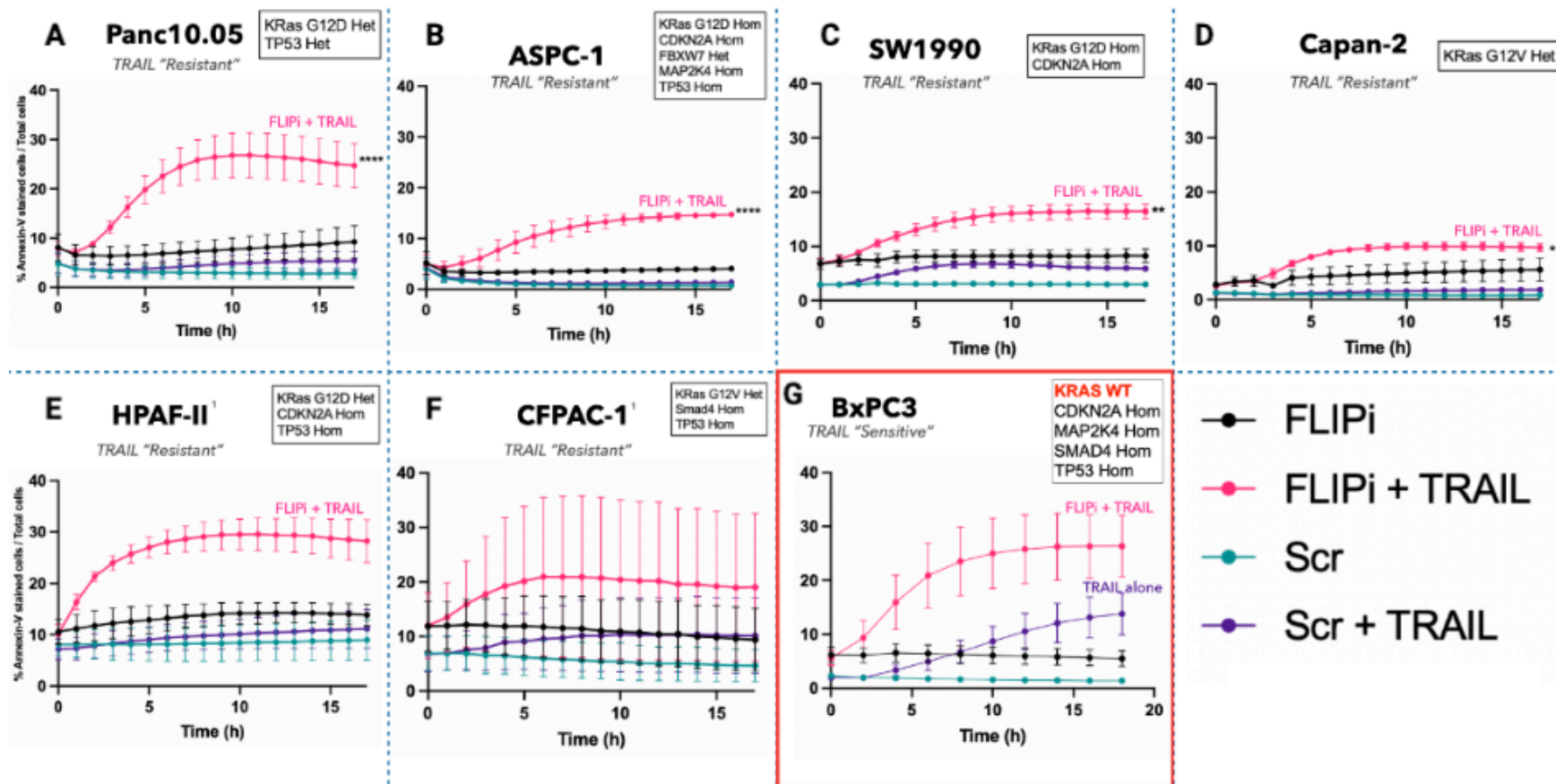
Figure 3-2 Longitudinal apoptotic response of Established Pancreatic Cancer Cell Line (EPCCL) panel to siRNA cFLIP inhibition (FLIPi) with and without exogenous TRAIL.
Annexin-V-stained cells represent those undergoing apoptosis, which was normalised to total number of cells in each well. Cells were pre-incubated with siRNA for 48 hours prior to the addition of Annexin V (and TRAIL where relevant). Timepoint 0h on each graph indicates the point at which Annexin V and TRAIL was added. Data represents mean ± SEM for a total of at least 3 independent repeats per cell line. **A-F** Apoptotic response of KRAS-mutant cell lines. **G** Apoptotic response of a KRAS wild-type (WT) cell line. Data was collected using the Incucyte S3 Live Cell Analysis platform (Essen Bioscience). Statistical significance calculated using two-way ANOVA with Tukey correction for multiple comparisons. $p<0.05$ (*), $p<0.01$ (**), $p<0.001$ (***), $p<0.0001$ (****). FLIPi = siRNA targeting cFLIP. Scr = scrambled RNA; TRAIL = recombinant human TRAIL.
[1]Cell lines whose apoptotic response was not rescued by the addition of pan-caspase inhibitor (Z-vad-FMK).
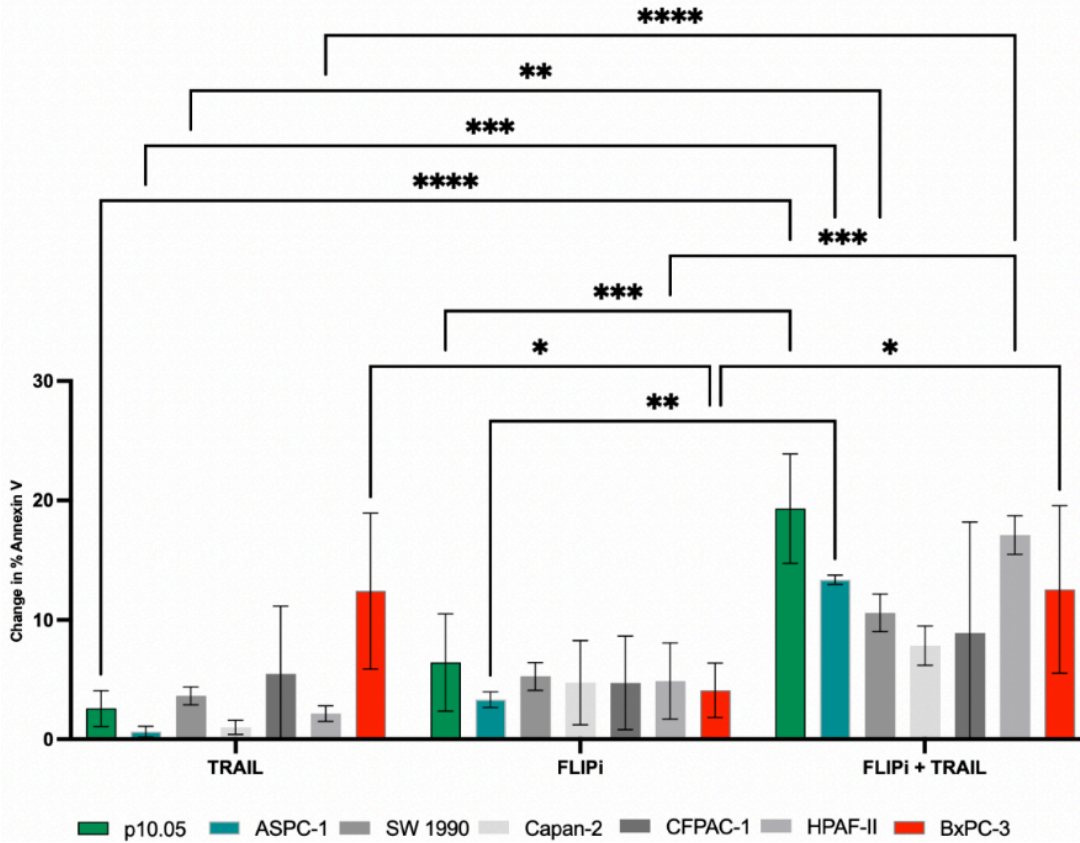
Figure 3-3 Change in apoptosis in EPPCL panel 17 hours post addition of exogenous TRAIL.
Annexin-V stained cells represent those undergoing apoptosis, which was normalised to total number of cells in each well to produce a percentage of cells undergoing apoptosis. The percentage of cells undergoing apoptosis at the end of the assay in **Figure 3.2** (17h timepoint) was normalised to percentage of apoptotic cells in the relevant controls (TRAIL alone and FLIPi alone were normalised to Scr alone; FLIPi + TRAIL was normalised to Scr + TRAIL). KRAS-mutant cell lines with the most significant difference in levels of caspase-dependent apoptosis are highlighted in green. Response of the KRAS WT cell line (BxPC3) highlighted in red. Data represents mean ± SEM for a total of at least 3 independent repeats per cell line, with 3 technical replicates included in each independent experiment. Statistical significance calculated using two-way ANOVA with Tukey correction for multiple comparisons. *p<0.05 (*), p<0.01 (**), p<0.001 (***), p<0.0001 (****). 17h post addition of TRAIL = 65h post addition of siRNA; FLIPi = siRNA targeting cFLIP. Scr = scrambled RNA; TRAIL = recombinant human TRAIL.*

3.3.3 cFLIP and DR5 expression is not significantly associated with EPCCL response to FLIPi

Given that underlying mutation status did not appear to provide a consistent biomarker of response to FLIPi in the EPCCLs, we interrogated cell line expression levels of cFLIP, TRAIL and its death receptors (DR4 and DR5) to determine whether these may provide an alternative biomarker of response.

As detailed in Section 2.3.2, RNASeq data collected by 'The Cancer Cell Line Encyclopedia' (TCCLE) (Barretina et al. 2012) was investigated using the ENSEMBL-EBI expression atlas *(Figure 3.4 A)*. We discovered that expression levels of cFLIP, DR4 and TRAIL were reasonably consistent across each cell line, with BxPC-3 and SW1990 expressing the lowest level of cFLIP mRNA and some of the highest levels of DR5. DR5 expression was relatively high in all cell lines, with ASPC-1 possessing the greatest expression level at 298 TPM compared with the lowest-expressing cell line, Capan-2, at 61 TPM. Levels of DR4 and TRAIL were comparatively lower than DR5 for each cell line. This supports the notion that these cells were primed to drive the non-canonical, DR5-dependent signalling observed *in vivo* by von Karstedt et al. but, due to a lack of TRAIL *in vitro*, were unable to activate the pathway in the absence of the ligand (von Karstedt et al. 2015). Equally, it was anticipated that the KRAS WT cell line, BxPC3, would express low levels of cFLIP but relatively high levels of DR4 and DR5 due to its inherent sensitivity to exogenous TRAIL.

Whilst relative expression of the cFLIP-L isoform at the protein level *(Figure 3.4 B-C)* corresponded to the cFLIP RNA expression level for most cell lines, SW1990 in our lab showed comparatively high levels of cFLIP-L protein, thereby contrasting with the low RNA expression recorded in the TCCLE database.

As more cell lines and genes were included in the TCCLE database and RNA expression roughly correlated with relative cFLIP protein content in our EPPCL panel, we utilised RNA expression levels to identify potential biomarkers of response to FLIPi. A linear regression was conducted to test the association between gene expression and fold change in apoptosis following FLIPi supplemented with exogenous TRAIL. There was no

significant relationship between apoptotic response and the expression level of any of the genes (cFLIP, DR4, DR5 and TRAIL) *(Figure 3.4 D)*. However, the regression plots demonstrated a non-significant, positive association between cFLIP or DR5 expression level and apoptotic response and a slightly negative association between TRAIL expression level and apoptotic response. Levels of DR4 expression do not appear to be associated with apoptotic response.

A Pearson Correlation test was then conducted to test the degree to which the two variables are related. This confirmed that a positive, non-significant correlation exists between cFLIP or DR5 expression and fold change in apoptosis following FLIPi + TRAIL (r = 0.6534 and 0.4052 respectively; p = 0.1115 and 0.3672). Virtually no correlation was found between levels of DR4 and response to FLIPi (r=0.03516; p=0.9403). The correlation test also confirmed the slightly negative, non-significant correlation between the expression of TRAIL and response to FLIPi (r = -0.2778; p = 0.5464).

Collectively, these data demonstrate that each cell line expressed different levels of cFLIP, TRAIL and both TRAIL DRs. FLIPi may be more effective at sensitising cells with high expression levels of cFLIP and/or DR5 RNA to TRAIL-induced apoptosis, however, this was not significant. Conversely, tumour cells with comparatively high levels of TRAIL expression were associated with a weaker apoptotic response to FLIPi + TRAIL than those with low TRAIL expression levels.
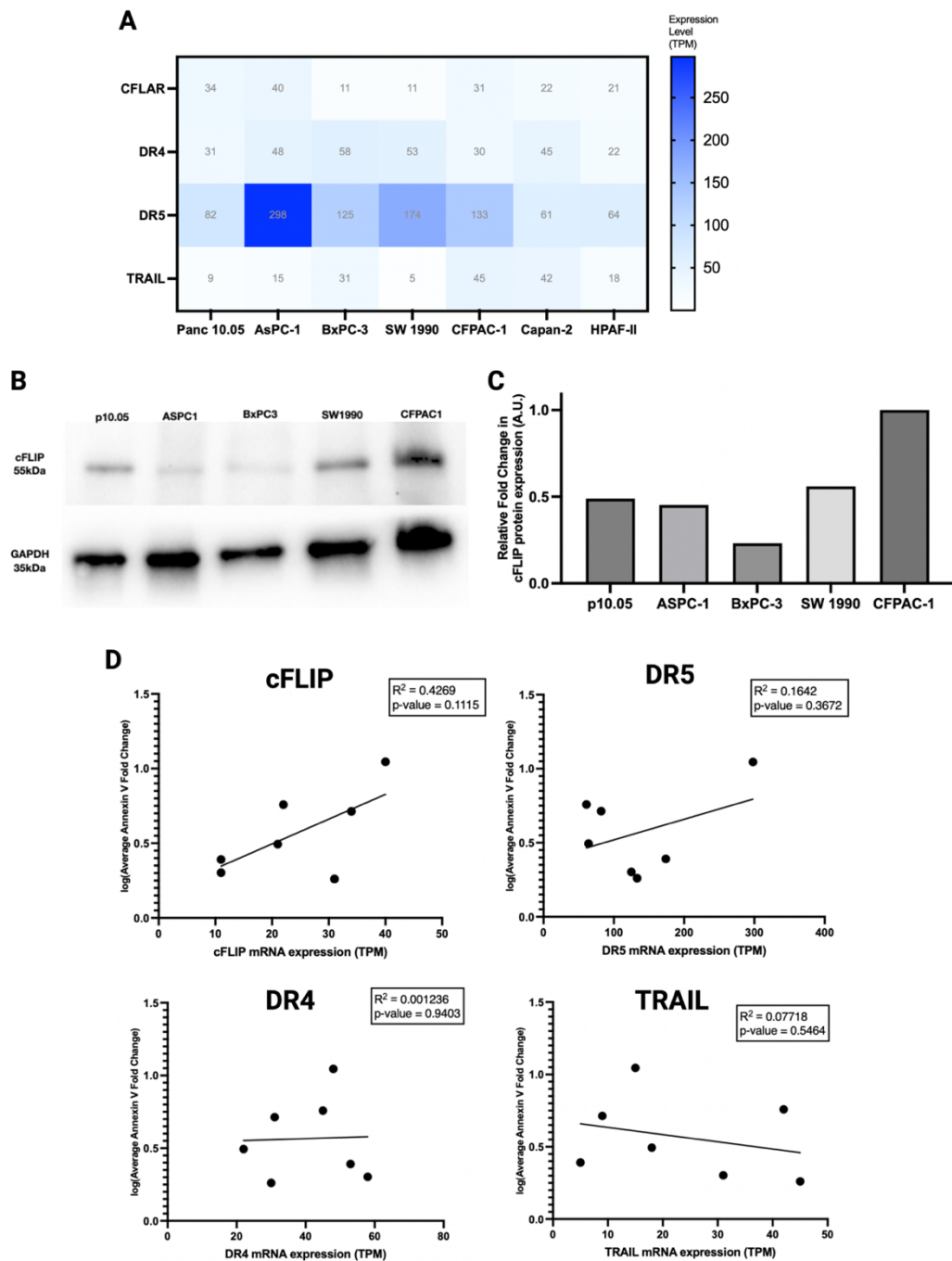
Figure 3-4 Relative expression levels of cFLIP, TRAIL and TRAIL receptor RNA and protein in panel of EPCCLs.
A Heatmap showing RNA expression level of genes encoding cFLIP (CFLAR), DR4 (TNFRSF10A), DR5 (TNFRSF10B) and TRAIL (TNFSF10) in PDAC cell lines. Data taken from 'The Cancer Cell Line Encyclopedia' RNA-Seq project (Barretina et al. 2012). Data was processed using ENSEMBL-EBI Expression Atlas Release 38 – (Papatheodorou et al. 2020).**B** Western Blot demonstrating cFLIP-long (cFLIP-L) protein expression in select EPCCLs. **C** Western Blot Densitometry bar chart comparing relative cFLIP-L expression in the EPCCL panel. Densitometry data normalised to GAPDH loading controls. **D** Scatterplots with simple linear regression lines showing log-transformed average fold change in percentage annexin-V-stained cells following FLIPi + TRAIL in **Figure 3.2** (17h timepoint) plotted against each cell line's respective RNA expression level of cFLIP, DR4, DR5 and TRAIL RNA. *17h timepoint = 65h post addition of siRNA, 17h post addition of TRAIL + Annexin V; TPM = transcripts per million.*

3.3.4   FLIPi sensitises primary-derived PDAC cell lines to TRAIL

As detailed in section 2.1.2, two KRAS^{G12V}-mutant, patient-derived PDAC cell lines, TKCC-05 and TKCC-07, were also included in the study due to their differential expression of cFLIP and TRAIL receptors. Although established cell lines are generally more robust and easier to work with, their ability to proliferate indefinitely increases the risk of genetic drift from the originating tumour with increasing passages (Kaur and Dufour 2012). Primary-derived cell lines have a more finite lifespan but are known to better reflect underlying patient tumour characteristics than established cell lines. Therefore, it was important to also include these in an investigation of the clinical relevance of FLIPi in KRAS-mutant PDAC.

Interestingly, the TKCC-05 cell line, taken from a tumour with high cFLIP expression, but low TRAIL expression, showed high levels of an inherent sensitivity to exogenous TRAIL alone *(Figure 3.5 A)*. FLIPi in combination with TRAIL in this line did increase the overall level of caspase-dependent apoptosis when compared to TRAIL alone, however, TRAIL alone was sufficient to activate caspase-dependent apoptosis. An effect that was not observed in EPCCLs with high cFLIP expression.

Conversely, the TKCC-07 cell line expressed high levels of TRAIL death receptors, DR4 and DR5, with baseline expression of cFLIP, and required FLIPi to activate apoptosis in response to exogenous TRAIL supplementation *(Figure 3.5B)*. Whilst FLIPi alone in this line induced a significant increase in apoptosis, the combination of FLIPi with TRAIL enhanced this response. Notably, the apoptotic responses in the TKCC-07 line were only partially rescued by caspase inhibitors *(Appendix A-4)*, suggesting a non-caspase-dependent apoptotic pathway may contribute to the overall increase in apoptosis.
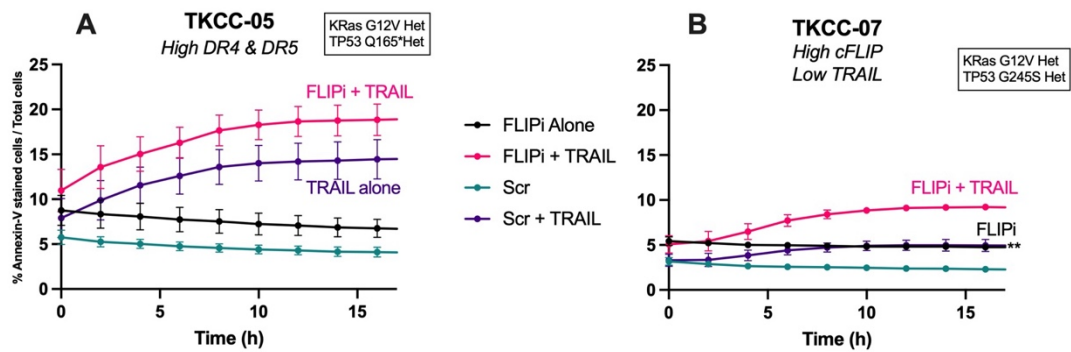
Figure 3-5 Longitudinal apoptotic response of KRAS-mutant primary patient-derived pancreatic cancer cell lines (PDCLs) to FLIPi with and without exogenous TRAIL.
Annexin-V-stained cells represent those undergoing apoptosis, which was normalised to total number of cells in each well. Cells were pre-incubated with siRNA for 48 hours prior to the addition of Annexin V (and TRAIL where relevant). Timepoint 0h on each graph indicates the point at which Annexin V and TRAIL was added. Data represents mean ± SEM for a total of at least 3 independent repeats per cell line. Data was collected using the Incucyte S3 Live Cell Analysis platform (Essen Bioscience). Statistical significance calculated using two-way ANOVA with Tukey correction for multiple comparisons. *p>0.05 (ns), p<0.01 (**). FLIPi = siRNA targeting cFLIP. Scr = scrambled RNA; TRAIL = recombinant human TRAIL.*

3.3.5   Small molecule cFLIP inhibition shows limited efficacy in EPCCLs

As siRNA-mediated genetic knockdown results in almost complete repression of gene expression, it is possible that observed responses may not be due to specifically targeting the pathway of interest. Therefore, we interrogated the response of certain EPCCLs to our lab's targeted small molecule cFLIP inhibitor, OH14, which is currently in development (Hayward, unpublished). OH14 has been proven to specifically interfere with the inhibitory role of cFLIP in the TRAIL-mediated apoptotic pathway without interfering with overall cFLIP expression (Hayward, French & Lee, unpublished). It has also been shown to sensitise various cancer types to TRAIL. OH14 was added at a previously established high dose (100μM) with or without TRAIL to assess EPCCL sensitivity.

Two EPCCLs in which FLIPi exerted the greatest sensitisation effect, Panc 10.05 and ASPC-1 (as detailed in Section 3.3.2), were selected to assess the preclinical potential of OH14 *in vitro*. As with FLIPi, OH14 sensitised the Panc10.05 cell line to caspase-dependent, TRAIL-induced apoptosis *(Figure 3.5 A)*. A very small sensitisation also occurred in the ASPC-1 line, however, this was not on the same scale as the response to FLIPi, was almost identical to the level of apoptosis induced by TRAIL alone and wasn't

fully rescued by caspase inhibitors *(Figure 3.5 B)*. Unlike FLIPi, OH14 alone in both lines exerted a negligible effect on apoptosis and exogenous TRAIL was required to induce any increase in apoptosis.

Taken together, these data suggest that OH14 may effectively sensitise certain EPCCLs to TRAIL-mediated apoptosis, however, further optimisation of dosing conditions may be required to replicate the effect observed in the Panc10.05 line.
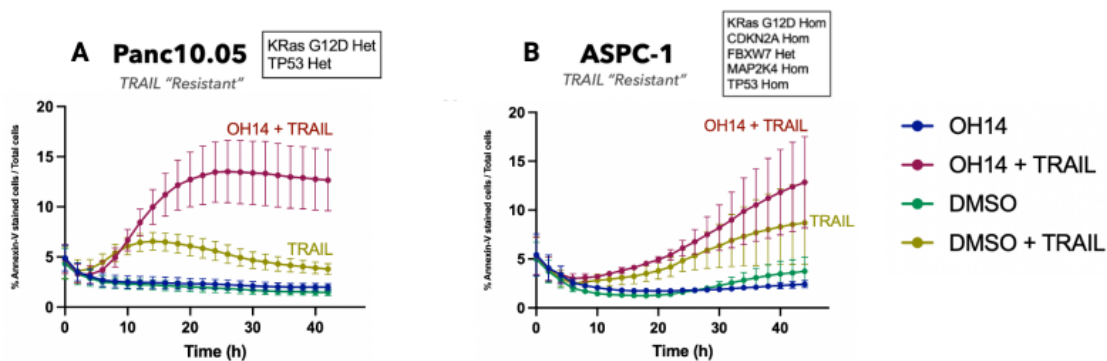
Figure 3-6 Longitudinal apoptotic response of EPCCL panel to small molecule cFLIP inhibitor with and without exogenous TRAIL.

Annexin-V-stained cells represent those undergoing apoptosis, which was normalised to total number of cells in each well. 100uM OH14 and Annexin-V green reagent was added to cells 24 hours after they were seeded. TRAIL was then added 1 hour post OH14 treatment and cells were transferred to the Incucyte S3 Live Cell Analysis platform (Essen Bioscience) for real-time monitoring. Timepoint 0h on each graph indicates the point at which TRAIL was added. Data represents mean ± SEM for a total of at least 3 repeats. *OH14 = Small Molecule cFLIP inhibitor; DMSO = Dimethyl sulfoxide; TRAIL = recombinant human TRAIL.*

3.4   Discussion

In this chapter, the potential of cFLIP inhibition (FLIPi) to target KRAS-mutant PDAC cell lines was investigated. Analysis of human RNASeq databases demonstrated that cFLIP expression was significantly higher in pancreatic tumour vs normal samples and, in most cases, this increased expression was detected at each pathological stage of the disease *(Figure 3.1 A-B)*. It should be noted that 'normal' samples used for this analysis were derived from the Genotype tissue expression project (GTEx) and, although the population is as 'normal' as possible relative to the age of the individual, all individuals were deceased organ donors (Carithers et al. 2015). Thus, although each donor had a histologically 'normal' pancreas, and did not have PDAC or pre-malignant pancreatic

lesions, they would have died from some alternative cause; with most older donors having underlying diseases at the time of death. It is not known how these underlying conditions may affect the pancreas or the baseline 'normal' expression level of our genes of interest. For example, conditions such as Type 2 diabetes mellitus can lead to decreased levels of cFLIP in the pancreatic islet compartment (Maedler et al. 2002). Therefore, this caveat regarding the 'normal' population should be taken into consideration whilst interpreting the results.

Interestingly, whilst high cFLIP expression had previously been associated with significantly reduced disease-free survival (Johnston et al. 2020) *(Figure 3.1C)*, we discovered no significant effect of cFLIP expression on overall survival in pancreatic cancer *(Figure 3.1 D)*. Collectively, these findings suggest an important, tumour-specific role for cFLIP. The poor prognostic impact of cFLIP only becomes clear when considering disease-free survival following initial treatment, thereby suggesting that cFLIP may play a key role in therapeutic resistance and disease relapse.

Several key TRAIL pathway components were also upregulated within pancreatic tumours, including significantly increased levels of TRAIL and its DR4 receptor *(Figure 3.1 A)*. Levels of TRAIL death receptor, DR5, were found to be comparatively high in both tumour and normal samples. When grouped as a collective TRAIL death receptor gene signature, high expression of TRAIL, DR4 and DR5 was associated with a significant reduction in disease-free and overall survival *(Figure 3.1 E-F)*. The collating of all three genes into one customised 'signature' was performed as each protein likely works closely together to activate a downstream response to TRAIL signalling. Indeed, when considered as single components, the expression level of each gene, bar DR5, exerts a significant impact on survival. Potentially reflecting its general elevation in both tumour and normal settings *(Figure 3.1A)*, the impact of expression levels of DR5 alone on survival does not quite reach significance. However, combining all 3 death receptor components leads to a greater difference in survival than any component in isolation, suggesting each component may cooperate to facilitate non-canonical, malignant TRAIL-induced signalling. This suggests that the observed upregulation of these genes facilitates both increased tumour malignancy and therapeutic resistance. This supports

the findings of von Karstedt et al., whereby KRAS-mutant PDAC drives malignant signalling via a DR5-mediated pathway (von Karstedt et al. 2015). These findings also support our original hypothesis, that cFLIP expression may be responsible for preventing canonical, TRAIL-mediated apoptosis and thereby facilitating the progression of malignant, DR5-mediated signalling in PDAC.

Having demonstrated the prognostic importance of cFLIP and the TRAIL pathway in PDAC, this chapter then sought to characterise the apoptotic response of a broad panel of seven established pancreatic cancer cell lines (EPCCLs) to siRNA cFLIP inhibition (FLIPi) *(Figure 3.2 & 3.3)*. Each KRAS-mutant cell line demonstrated limited sensitivity to supplementation with exogenous TRAIL alone. FLIPi alone lead to a consistent, >80% reduction in cFLIP mRNA expression in each cell line and induced a greater apoptotic response than TRAIL alone, but this increase in apoptosis was non-significant *(Figure 3.3)*. However, the combination of exogenous TRAIL with FLIPi resulted in a significant increase in apoptosis in all bar one of the KRAS-mutant cell lines. This was an unexpected result as previous findings by von Karstedt et al. suggested that KRAS-mutant PDAC cells were driving cell-autonomous TRAIL signalling (von Karstedt et al. 2015). We had, therefore, hypothesised that FLIPi alone should be sufficient to re-activate apoptosis in this setting. Crucially, however, all published work investigating non-canonical, DR5-mediated malignancy in PDAC was either conducted in a single EPCCL of PDAC (Panc Tu I, not included in our panel) or in genetically engineered mouse models (GEMMs) *in vivo.* Our *in vitro* findings in this chapter support the findings of Haag et al. and suggest that TRAIL-R signalling may not be constitutively driven in many PDAC cell lines *in vitro*, with the *in vivo* setting potentially facilitating a greater level of pathway activation, possibly due to microenvironmental supplementation of TRAIL (Haag et al. 2011). Conversely, constitutive, cell-autonomous TRAIL-R signalling may be active at a low level *in vitro*, likely due to ligand-independent, receptor-receptor interactions, however, this may only be sufficient to drive the non-canonical, malignant pathway, whilst the apoptotic pathway requires enhanced TRAIL-R stimulation. Indeed, cells remain primed to resist canonical TRAIL-induced apoptosis *in vitro*, due to the expression of cFLIP, with FLIPi clearly sensitising KRAS-mutant EPCCLs to exogenous TRAIL-induced apoptosis. However, further investigation into the requirement for exogenous TRAIL and the

activity of the non-canonical TRAIL-R pathway in our EPCCL panel is needed to fully delineate the potential deviation from the findings of von Karstedt et al. (von Karstedt et al. 2015).

Furthermore, the only KRAS-WT cell line included in the study, BxPC-3, was intrinsically sensitive to exogenous TRAIL and, unlike the KRAS-mutant lines, did not require FLIPi sensitisation to induce significant levels of apoptosis in response to TRAIL *(Figure 3.2)*. In line with these findings, it was determined that the TRAIL-sensitive BxPC3 cell line also possessed the lowest expression level of cFLIP protein, with almost half the amount of cFLIP protein detected when compared to the most TRAIL-resistant lines, Panc10.05 and ASPC-1 *(Figure 3.4).* However, a low level of cFLIP was present in the BxPC3 line, likely underlying the potentiated apoptotic effect observed following the combination of FLIPi and exogenous TRAIL. This supports the findings of von Karstedt et al., whereby mutant KRAS is ultimately required to drive malignant DR5-mediated signalling (von Karstedt et al. 2015). The findings of this chapter suggest that KRAS-WT PDAC cells do not need to upregulate cFLIP expression to repress canonical TRAIL signalling as they are not constitutively driving the non-canonical pathway.

The response of primary-derived PDAC cell lines (PDCLs) demonstrated that the difference between KRAS-mutant and KRAS-WT PDAC cells may be more complicated than initially hypothesised. Although both lines (TKCC-05 & -07) possessed non-silent mutations in KRAS; the response of TKCC-05 was very similar to the KRAS-WT BxPC3 established cell line, in that it appeared intrinsically sensitive to TRAIL-mediated apoptosis. Although unexpected, this may reflect the underlying role of additional mutations upon tumour cell signalling, with the TKCC-05 line possessing a far greater number of non-silent mutations than its TKCC-07 counterpart and most established cell lines included in this chapter. There is also the potential that either the BxPC3 or TKCC-05 cell line was approaching its passaging limit and had begun to genetically drift from its tumour of origin.

Given the difference in FLIPi sensitisation across the EPCCL panel and the lack of a common underlying mutation, we explored whether the expression level of key TRAIL

pathway components may represent suitable biomarkers of response to FLIPi as a therapeutic approach in PDAC. A positive, yet non-significant, correlation was observed between the expression level of cFLIP or DR5 and apoptotic response to FLIPi + TRAIL *(Figure 3.4)*. Indeed, the cell line with the lowest cFLIP RNA and protein expression (BxPC3) was also the most sensitive to TRAIL alone. Whilst the line with the highest cFLIP RNA expression (ASPC-1) also showed the greatest fold change in apoptosis following FLIPi + TRAIL. Conversely, a negative but non-significant trend was observed between TRAIL expression and response to FLIPi + TRAIL. The lack of significance between all biomarkers suggests that the absolute RNA expression level of these proteins may not be a crucial factor in determining response to cFLIP inhibition. This is supported by previous findings from our lab and others, which highlight the importance of sub-cellular localisation of cFLIP protein in determining the response of breast cancer cells to FLIPi and in determining the prognosis of NSCLC patients (French et al. 2015; Humphreys et al. 2018). Furthermore, the relative protein expression level of the two death receptors (DR4 & DR5) could not be assessed in this study following a series of unsuccessful antibody optimisation attempts (data not shown). However, the absolute expression of TRAIL and/or DR at the protein level may exert a greater influence over response to FLIPi than the RNA levels. Additionally, it is not yet known whether cFLIP inhibition impacts KRAS activity, with the opportunity for direct or indirect feedback mechanisms to be activated following FLIPi due to the various, non-apoptotic roles of cFLIP, as discussed in Section 1.5.4. Therefore, this may also underlie the heterogeneous responses observed across each cell line. Finally, in addition to KRAS status, a potential biomarker for PDAC cells likely to respond to FLIPi which was not explored in this chapter, may be the activity of non-canonical TRAIL-R pathway components, for example the level of phosphorylated Akt or ERK. Tumour cells with greater non-canonical activity are likely to be more reliant upon the constitutive activation of TRAIL-R signalling, thereby, potentially increasing their susceptibility to FLIPi.

Finally, the efficacy of a novel small molecule cFLIP inhibitor, OH14 (Hayward, unpublished), was assessed in certain EPCCLs. Despite most cell lines appearing to increase apoptosis in response to FLIPi, OH14 only appeared to sensitise the Panc10.05 cell line to TRAIL-mediated, caspase-dependent apoptosis *(Figure 3.6)*. OH14 alone had

virtually no effect on the viability of either the Panc10.05 or the ASPC-1 cell lines. In addition to heterogeneous responses to cFLIP inhibition, it is also possible that the concentration of inhibitor supplied (100µM) may not have been sufficient to disrupt all interactions of cFLIP with the DISC in the ASPC-1 line. Additionally, only one dose of OH14 was supplied to cells prior to the annexin V assay. It is possible that 'unresponsive' cell lines may require repeated exposure to the therapeutic for an effect to be observed. This could be due to many reasons, including the possibility that the inhibitor is metabolised too rapidly or is unable to induce similar levels of inhibition as achieved by complete deletion of protein expression. The specificity of OH14 in only targeting the anti-apoptotic role of cFLIP and not impacting the expression levels of the protein has previously been demonstrated by other members of the Clarkson lab *(Appendix A-1)*, however, it would also be pertinent for future work to involve an assessment of the impact that 100µm OH14 may have upon the non-canonical, Rac1-mediated TRAIL-R pathway.

3.5 Conclusions and Future Work

To summarise, this chapter was crucial in screening a wide variety of cell lines to determine response to FLIPi as a therapeutic approach in PDAC. Whilst it quickly became apparent that constitutive TRAIL signalling mainly observed by von Karstedt et al. *in vivo* was not replicated in our EPCCL panel *in vitro,* this chapter demonstrates the potential of cFLIP inhibition in re-activating apoptosis in KRAS mutant PDAC cells, providing sufficient TRAIL is available (von Karstedt et al. 2015). Although FLIPi sensitised the majority of cell lines to TRAIL-induced, caspase-mediated apoptosis, certain lines (particularly CFPAC-1 and HPAF-II) did not respond. Response heterogeneity may reflect TRAIL-R pathway redundancy, whereby tumours may use alternative anti-apoptotic proteins, such as certain BCL-2 family members and X-linked inhibitor of apoptosis (XIAP) instead of cFLIP to suppress the canonical pathway, as discussed in Section 1.4.3 (Van Dijk et al. 2013). Therefore, future work to investigate the expression level of these alternative proteins and response to their inhibition in PDAC may assist in delineating the underlying mechanisms of resistance to FLIPi in certain cell lines.

Whilst several possible biomarkers of response to FLIPi in the EPCCLs were considered, no significant correlation was discovered in this study. However, it would be pertinent to explore alternatives to absolute RNA expression levels, including sub-cellular localisation of each protein and protein expression of TRAIL and its receptors.

Taken together, these data provide sufficient evidence to support the further investigation of cFLIP inhibition in more complex *in vivo* and *ex vivo* settings, as considered by Chapters 4 and 5 of this thesis.

4 Investigating the response to cFLIP inhibition using novel *in vivo* and *ex vivo* models of Pancreatic Ductal Adenocarcinoma

4.1 Introduction

Experiments detailed in the previous chapter demonstrate that cFLIP inhibition successfully sensitises resistant KRAS mutant PDAC cells to TRAIL-induced apoptosis *in vitro*. However, the requirement for exogenous TRAIL supplementation in this setting was inconsistent with the findings of von Karstedt et al., in which non-canonical TRAIL-receptor (TRAIL-R) signalling was constitutively driven by KRAS-mutant PDAC cells both *in vivo* and in one cell line *in vitro* (von Karstedt et al. 2015). This suggests that the requirement for exogenous TRAIL *in vitro* may be specific to the activation of the cell death pathway, while constitutive, cell-autonomous TRAIL-R signalling is sufficient to activate the alternate, non-canonical pathway *in vitro*.

The EPCCLs used in Chapter 3 of this thesis were part of a collection of 11 well-established, two-dimensional (2D) human PDAC cell lines which have been used to delineate the genetic landscape and develop therapeutic approaches to target PDAC (Deer et al. 2010; Low et al. 2021). They represent a low-cost and easily manipulatable platform which has been extensively characterised. However, a key limitation posed by all established 2D cell lines is a gradual transcriptomic drift away from the genetic profile of the original tumour, potentially reflecting selection events for clonal expansion of populations most suited to monolayer culture conditions (Yu et al. 2019; Low et al. 2021). This drift likely occurs due to increasing passage events which actively select populations best suited to *in vitro* conditions. Whilst we controlled for this by using cell lines at low passage numbers (<20) and including primary-derived cell lines, the lack of key clinical features, including intra-tumour heterogeneity and interactions with the microenvironment, suggests that these results should not be used in isolation when determining the therapeutic potential of cFLIP inhibition in PDAC.

In vivo, preclinical models have been shown to better replicate the complex progression and microenvironment of human PDAC and accurately reflect these features of human disease (Gopinathan et al. 2015). This is particularly pertinent when considering the

contribution of exogenous TRAIL in the susceptibility of PDAC cells to cFLIP inhibition. Endogenous TRAIL is primarily delivered to target cells *in vivo* via cytotoxic immune cells recruited to the tissue microenvironment. Thus *in vivo*, the tumour microenvironment may be more akin to the *in vitro* scenario which includes exogenous TRAIL supplementation. Notwithstanding additional parameters contributed by a 3D *in vivo* tumour microenvironment, it was therefore proposed that PDAC responses to cFLIP inhibition should be examined *in vivo* to ascertain the requirement for exogenous TRAIL in targeting tumour cell viability.

Analysis of tumour responses to cFLIP inhibition *in vivo* is therefore the focus of the next two chapters.

Xenograft models, involving the implantation of established or patient-derived tumour cells or tissues to establish tumours in immunocompromised mice, have been historically crucial for *in vivo* anti-cancer drug evaluation (Rubio-Viqueira et al. 2006; Gopinathan et al. 2015; Xu et al. 2018). As xenograft models can be derived from virtually any established PDAC cell line or primary tumour sample, a vast variety of models exist and are often included in studies to better reflect inter-tumour heterogeneity. Tumours can be implanted subcutaneously to facilitate easy monitoring of tumour growth or tumours can be implanted orthotopically within the murine pancreas, providing a more accurate reflection of human disease and metastasis but necessitating more complex monitoring. However, due to the immunocompromised nature of the model, important interactions between tumours and the immune system can be missed. This can impact performance when therapeutics ultimately progress to efficacy testing in human clinical trials.

Genetically Engineered Mouse Models (GEMMs), with their ability to accurately recapitulate the genotype and phenotype of human PDAC in the presence of an intact immune and stromal microenvironment, offer a more relevant alternative to these xenograft and cell line limitations (Hruban et al. 2006; Gopinathan et al. 2015). Many PDAC GEMMs have been developed, often featuring an activating *KRAS* mutation along with the targeted mutation or deletion of a relevant tumour suppressor gene. These

models were vital in establishing the role of *KRAS* in the initiation of pancreatic disease and the necessity of additional genetic events to drive pancreatic tumour development. Using Cre-Lox and other recombinase enzyme technology, specific genetic manipulation can be spatially and temporally targeted to the pancreas, as discussed in Section 2.4.2 (Feil et al. 1997).

The KPC (*Pdx-1-Cre; LSL-Kras$^{G12D/+}$; LSL-Trp53$^{R172H/+}$*) model represents arguably the most commonly used and well characterised GEMM of PDAC (Hingorani et al. 2005; Low et al. 2021). Facilitating the progression from PanIN to PDAC, KPC mice develop constitutively driven, sporadic tumours in as little as four months from birth, as discussed in Section 2.4.3. This model is also associated with clinically relevant metastatic progression to the liver, lungs, and peritoneum.

However, most genetic studies carried out previously with PDAC GEMMs have involved either germline knockouts or Cre-controlled alleles which are all activated/deleted simultaneously along with initiating oncogenic manipulations, as is the case of the KPC model (Gopinathan et al. 2015). Therefore, investigating the effect of changes to a gene of interest in this system may inadvertently impact tumour initiation and progression. As discussed in Section 2.4.2.2, the advent of flippase-*FRT* (Flp-*FRT*) technology in combination with Cre-Lox has enabled the development of a PDAC GEMM which can model two temporally separate, spatially targeted genetic manipulation events (DeCant et al. 2014; Schönhuber et al. 2014). This chapter involves the establishment of a novel PDAC GEMM (KPF-FLIP), which incorporates the KPF (*Pdx1-Flp; FSF-Kras$^{G12D/+}$; Trp53$^{frt/+}$*) model developed by Schönhuber et al. and uses both methods of recombination technology to enable the deletion of cFLIP specifically within *KRAS-* and *TP53*-mutant PDAC tumour cells *(Figure 4.1 A)*.

The KPF model has previously been shown to reflect similar tumour latency, morphology, survival time and metastatic rate as the commonly used KPC (*Pdx1-Cre; LSL-Kras$^{G12D/+}$; LSL-Trp53$^{R172H/+}$*) model of PDAC *(Figure 4.1 B)* (Hingorani et al. 2005; Schönhuber et al. 2014). However, crucially, the KPF model does not require Cre-Lox technology to initiate PDAC tumour development, as constitutive *KRAS* mutation and

TP53 deletion are under the control of the Flp-*FRT* system. Ultimately, this mutational background, driven by the pancreatic epithelium-specific *pdx1* promoter, results in the sporadic development of immune-competent PDAC tumours. Our collaborators in the Morton lab (CRUK Beatson Institute, Glasgow, UK) introduced a Flp-*FRT* controlled, tamoxifen-inducible Cre (*R26$^{CAG-FSF-CreERT2}$*) and a loxP-flanked copy of the gene encoding cFLIP (*CFLAR$^{fl/fl}$)* to the KPF genetic background to establish the novel KPF-FLIP model. Following confirmation of tumour burden in this model, intraperitoneal injection of tamoxifen enables the Cre recombinase to bind to loxP sites and excise exon 2 of the gene encoding cFLIP, resulting in complete cFLIP protein deletion specifically within the *Pdx1-Flp* driven PDAC tumour cells (Zhang and He 2005).
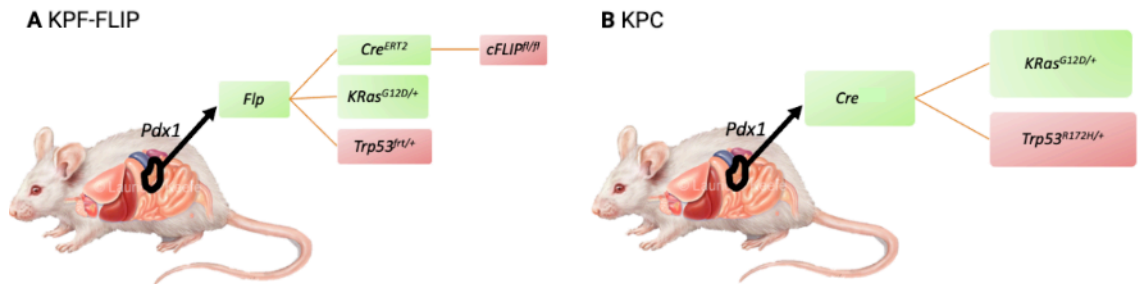
Figure 4-1 Genetic background of two GEMMs of PDAC.
A The KPF-FLIP GEMM, whereby the pdx1 promoter drives the expression of recombinant flippase (Flp) specifically within the pancreatic epithelium. Flp binds at target frt sites to drive constitutive overexpression of the KRAS^{G12D} mutation, hemizygous p53 deletion and expression of tamoxifen-inducible cre recombinase within the pancreas, ultimately leading to sporadic PDAC tumour development. System tamoxifen injection can then be used to activate Cre within established tumour cells. Cre can delete both cFLIP alleles within the tumour cells as they are flanked by genetically engineered loxP sites. **B** The classical KPC GEMM, whereby the pdx1 promoter drives the expression of Cre recombinase specifically within the pancreatic epithelium. Cre binds at target loxP sites to drive constitutive overexpression of the KRAS^{G12D} mutation and a loss-of-function Trp53 mutation within the pancreas, ultimately leading to sporadic PDAC tumour development. *Green boxes = gain of function mutation or expression of indicated gene. Red boxes = loss of function mutation or deletion of indicated gene. Pdx1 = Pancreatic and duodenal homeobox 1; Flp = flippase; Cre = cre recombinase; Cre^{ERT2} = tamoxifen inducible Cre recombinase; GEMM = Genetically engineered mouse model.*
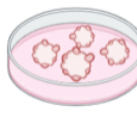
Whilst vital for interrogating tumour response to cFLIP deletion in the context of an intact microenvironment, the sporadic nature of tumour development within PDAC GEMMs is associated with considerable costs, particularly in terms of time and money *(Table 4.1)* (Pérez–Mancera et al. 2012; Boj et al. 2015; Tuveson and Clevers 2019).

Due to the novelty of the KPF-FLIP model, this chapter first focused on establishing its key characteristics, including tumour latency and incidence. Mice were routinely monitored using abdominal palpation to detect PDAC tumours. However, due to the development of *in situ* PDAC tumours amongst surrounding abdominal organs, certain tumours may evade diagnosis until symptoms become apparent. At this point, termination of the mouse would likely be required before even short-term tamoxifen-induced deletion of cFLIP could be completed. To avoid wasting such tumours and to explore the requirement for exogenous TRAIL in an *ex vivo*, three-dimensional (3D) setting, uninduced KPF-FLIP$^{fl/fl}$ tumours were harvested to establish tumour-derived PDAC organoids.

As a 3D model system, organoids recapitulate tissue-specific function and architecture and can be derived from both normal or tumour murine and human tissues (Tuveson and Clevers 2019; Lin et al. 2020). Tumour-derived organoids of PDAC (hereafter referred to as 'organoids' for ease) retain the morphological, genetic, and epigenetic characteristics of the primary tumour but lose the influence of the heterogeneous tumour microenvironment. Combined with their versatility, rapid growth and lower associated cost, they represent a viable alternative to mouse models of PDAC when investigating the potential of therapeutic approaches *(Table 4.1)*. Indeed, patient-derived PDAC organoids (PDOs) are already incorporated in several ongoing clinical trials (NCT03500068; NCT03544255; NCT04469556) to establish their relevance in predicting the drug sensitivity of primary PDAC tumours to improve patient stratification. However, while organoids represent an attractive intermediate model of 3D tissue architecture, limitations remain regarding the influence of adjacent tissue interactions.

Table 4-1 Characteristics of PDAC model systems.
Adapted from Tuveson & Clevers (2019). Created with Biorender.com.

	GEMM	MDO	CL	PDX	PDO
Wild-type cell culture	✓	✓	-	-	✓
Pre-invasive cancer models	✓	✓	-	-	✓
Invasive cancer models	✓	✓	✓	✓	✓
Metastatic cancer models	✓	✓	✓	✓	✓
Cost	££££	££	£	££	££
Time	++++	+	+	++++	++
Success rate	high	med	med	med	med
Throughput therapies	low	med	high	low	med

GEMM = Genetically engineered mouse model; MDO = Murine derived organoid; CLs = Cell lines; PDX = Patient derived xenograft; PDO = Patient derived organoid

Murine KPF-FLIP$^{fl/fl}$ organoids were selected as a more appropriate alternative to primary human organoids for the subsequent experiments detailed in this chapter. Despite the reduced clinical relevance of murine-derived tissues, KPF-FLIP$^{fl/fl}$ organoids retain the genetic background of the primary KPF-FLIP tumour (*Pdx1-Flp; FSF-Kras$^{G12D/+}$; Trp53$^{frt/+}$; R26$^{CAG-FSF-CreERT2}$; cFLIP$^{fl/fl}$*), thereby facilitating *ex vivo*, Cre-mediated deletion of cFLIP within KRAS- and p53-mutant tumour cells in a 3D environment and thus enabling specific targeting of cFLIP *ex vivo*. Moreover, ready access to these murine tissues circumvents the regulatory and financial costs and time associated with the acquisition, establishment, and optimisation of treatment methods for human organoids.

4.2 Chapter Aims

1. Establish a novel, dual recombinase GEMM of PDAC (KPF-FLIP)
2. Investigate the impact of cFLIP deletion within intact pancreatic tumours *in vivo*, using the novel KPF-FLIP GEMM.
3. Determine response to cFLIP deletion *ex vivo* using tumour-derived organoids from the KPF-FLIP GEMM of PDAC

4.3 Results

4.3.1 The establishment of a novel, dual-recombinase GEMM of PDAC to investigate cFLIP deletion within intact tumours

4.3.1.1 KPF-FLIP Histological Characteristics

Prior to commencing *in vivo* preclinical trials, it was necessary to establish our novel KPF-FLIP (*Pdx1-Flp; FSF-Kras$^{G12D/+}$; Trp53$^{frt/+}$; R26$^{CAG-FSF-CreERT2}$; CFLAR$^{fl/fl}$*) GEMM to enable cFLIP deletion within intact, immune-proficient KRAS- and p53-mutant PDAC tumours.

Whilst the KPF (*Pdx1-Flp; FSF-Kras$^{G12D/+}$; Trp53$^{frt/+}$*) model and the combination of *Flp*-FRT and Cre^{ERT2} has been extensively described by Schönhuber et al. and others, our novel allelic signature has yet to be reported (DeCant et al. 2014; Schönhuber et al. 2014). Therefore, it was important to determine the histological characteristics of KPF-FLIP tumours and compare these with the established KPF and KPC (*Pdx1-Cre; LSL-Kras$^{G12D/+}$; LSL-Trp53$^{R172H/+}$*) GEMMs of PDAC.

Despite inter- and intra-tumour heterogeneity, uninduced KPF-FLIP PDAC tumours generally exhibited a well-differentiated, glandular structure, heavily infiltrated by a desmoplastic stroma and necrotic regions *(Figure 4.2 A-C)*. Such structure is highly similar to well-differentiated solid tumours, including those from the classical KPF and KPC GEMMs, as reported in the literature *(Figure 4.2 D & E)* (Schönhuber et al. 2014; Gopinathan et al. 2015). These classical features of murine PDAC contrast dramatically with the highly organised, epithelial characteristics associated with a normal, healthy murine pancreas *(Figure 4.2 F).*
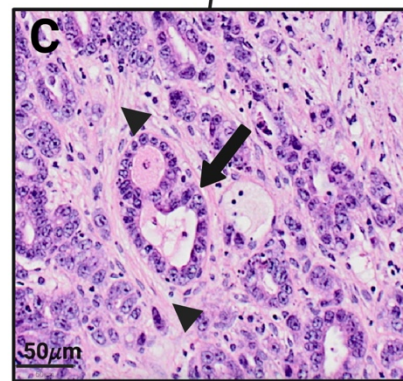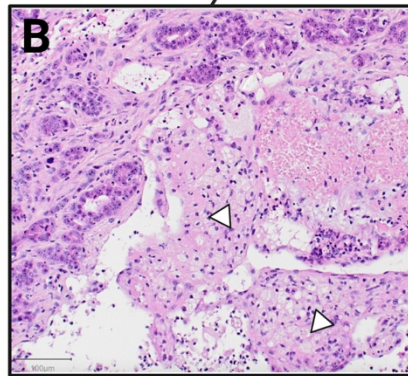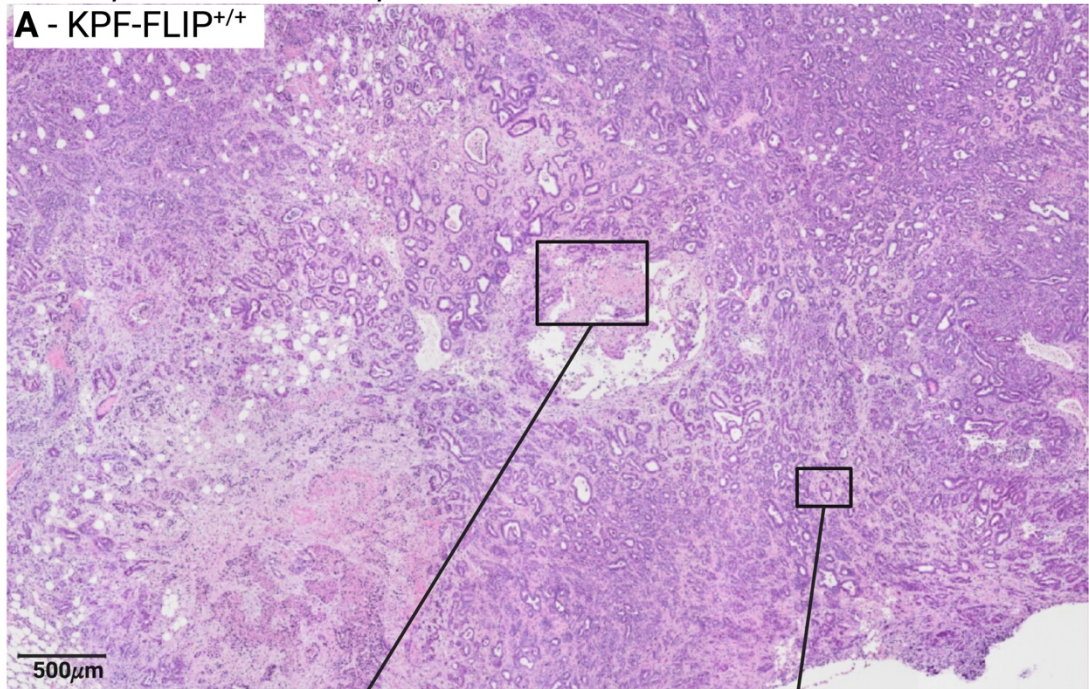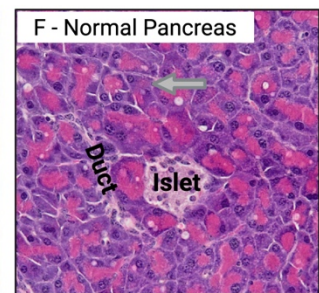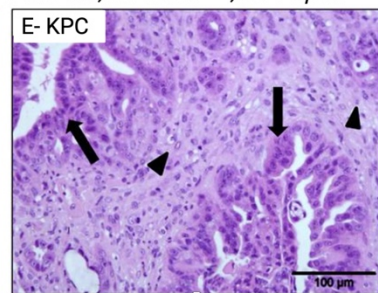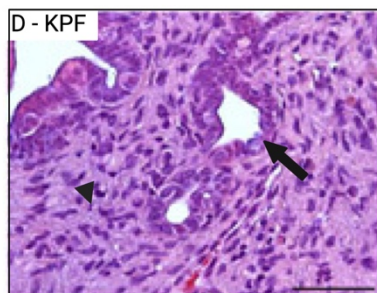
Figure 4-2 **Histological morphology of novel KPF-FLIP GEMM of PDAC compared to established PDAC GEMMs and the normal murine pancreas.**

A-C Representative H&E images demonstrating characteristic morphology of PDAC tumours taken from the KPF-FLIP GEMM. High power magnification demonstrates regions of **B** necrosis (white arrowheads) with immune cell infiltrate and **C** glandular structures (arrows) surrounded by dense stromal infiltrate (black arrowheads). **D** Representative image of classical KPF PDAC tumour morphology, taken from Schönhuber et al (2014). **E** Representative image of classical KPC PDAC tumour morphology, taken from Gopinathan et al. (2015). **F** Representative image of a healthy, normal murine pancreas showing highly organized ductal and pancreatic islet structures surrounded by tightly-packed exocrine acinar cells (grey arrow). Figure created with Biorender.com. *GEMM = Genetically engineered mouse model.*

As discussed in Section 2.4.4, to establish the KPF-FLIP model, our collaborators in the Morton lab (CRUK Beatson Institute, Glasgow, UK) kindly conducted initial breeding to generate a cohort expressing mutant and wild-type (WT) versions of all five desired alleles. A small breeding cohort was then transferred from the CRUK Beatson Institute's Specific and Opportunistic Pathogen Free (SOPF) unit to Cardiff University, to be expanded and produce the required experimental animals for the project.

However, initial breeding and experimental animals could not be directly transferred to SOPF conditions at Cardiff, for reasons outlined in Section 2.4.4.2, and were therefore maintained in conventional housing in an adjacent unit with lower SOPF barrier thresholds (hereafter referred to as the "dirty" unit, as detailed in Section 2.4.4.2). Once sufficient breeding animals were generated, the KPF-FLIP colony was then re-derived into a SOPF unit (hereafter referred to as the "clean" unit) via embryo re-derivation which did not involve any additional backcrosses. Therefore, experimental KPF-FLIP cohorts were either housed in "clean" or "dirty" conditions until their respective endpoints, depending upon the location of their birth.

Throughout the study, it became apparent that the external housing environment was impacting the tumour latency of this novel GEMM. This was confirmed at the end of the study by Kaplan-Meier survival curves *(Figure 4.3 and Figure 4.4 D & E)* and a Log-rank (Mantel-Cox) test which showed significantly shorter tumour latency when KPF-FLIP mice were housed in SOPF conditions compared with those that were not (Chi-square = 8.680; df = 1; p-value = 0.0032). Regardless of housing conditions, it was also clear that tumour incidence was far lower in the KPF-FLIP model in both dirty and clean units (11% and 20% respectively) than in the classical KPC model (81%), which was used for the experiments detailed in Chapter 5 of this thesis *(Figure 4.4 D-F)*. However, despite a clear difference in tumour latency and incidence, neither housing conditions nor genetic background appeared to impact tumour histological morphology, as determined by observational analysis of three H&E sections (cut 100μm apart) taken from each tumour *(Figure 4.4 A-C)*. Due to the lack of morphological differences and the small supply of

tumours, we decided to pool KPF-FLIP tumours from both housing conditions to analyse the response to cFLIP deletion in this GEMM.
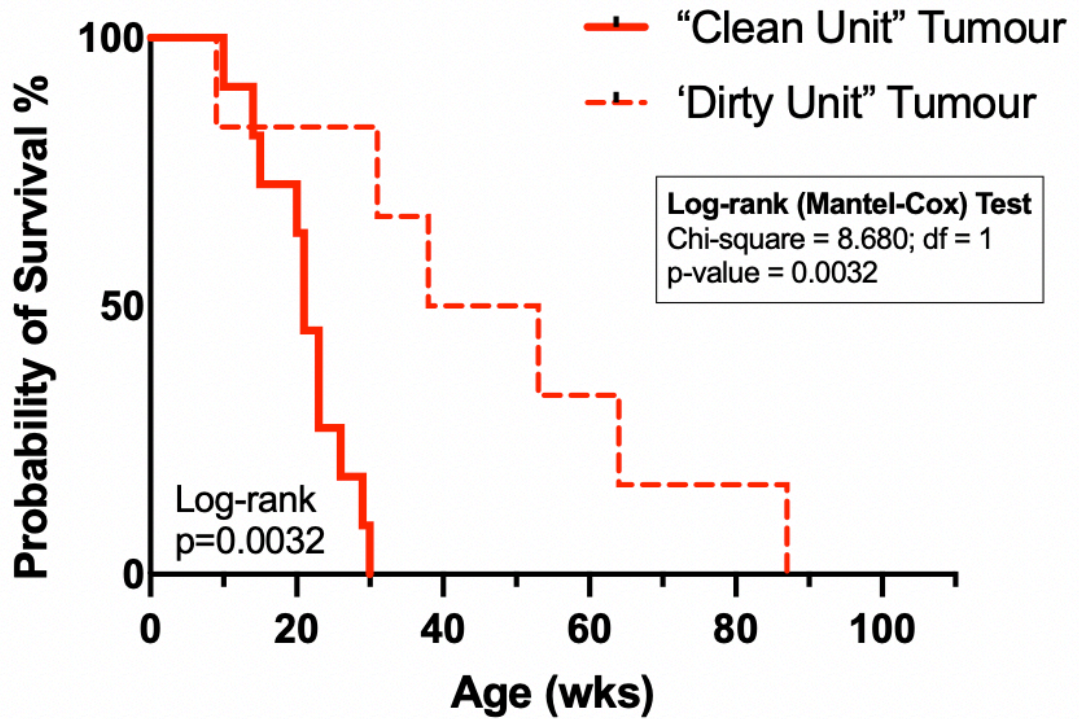
Figure 4-3 Probability of survival of KPF-FLIP mice when housed in 'Clean' or 'Dirty' animal units.
Kaplan-Meier survival curve showing the age of mice at endpoint when harvested with confirmed tumour burden. *'Clean Unit' = Specified and Opportunistic Pathogen Free (SOPF) conditions; 'Dirty' = not SOPF conditions.*

A KPF-FLIP$^{fl/fl}$ PDAC 'Clean Unit'
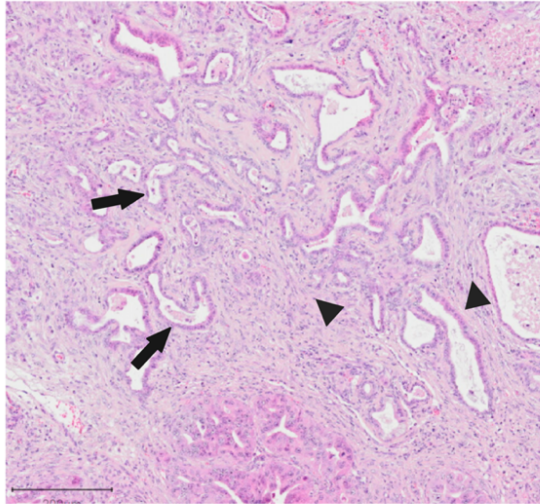
B KPF-FLIP$^{+/+}$ PDAC 'Dirty Unit'
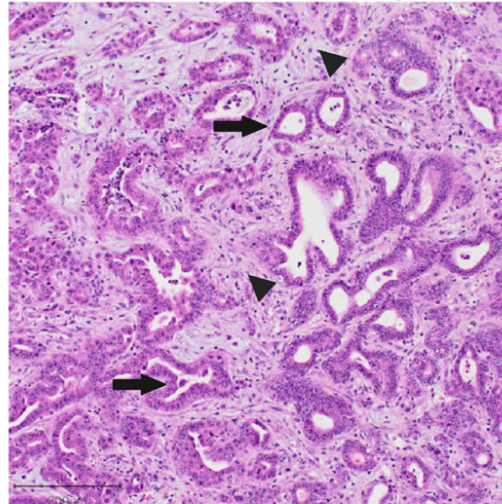
C KPC PDAC

D KPF-FLIP 'Clean' Unit

T2 (n=55)
Tumour n=11 (20%)

n=11
20%

n=44

E KPF-FLIP 'Dirty' Unit

HP (n=53)
Tumour n=6 (11.3%)

n=6
11%

n=47

F KPC (IVCs in Dirty Unit)

PETIC (n=21)
Tumour n=17 (81%)

n=4

n=17
81%
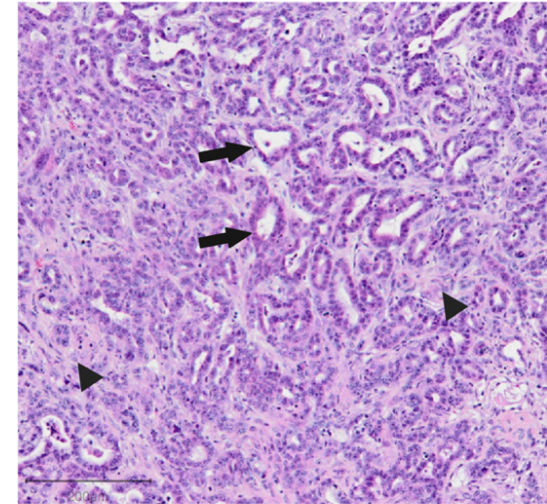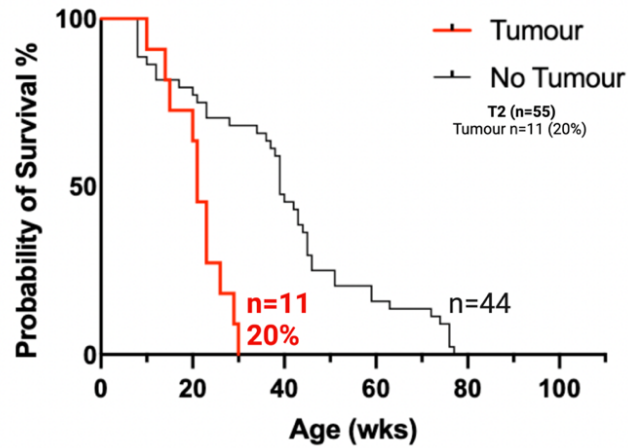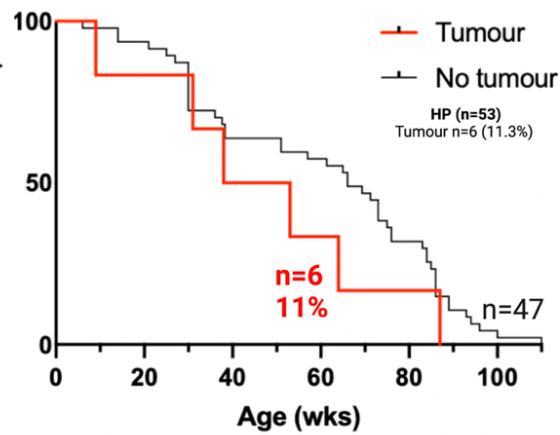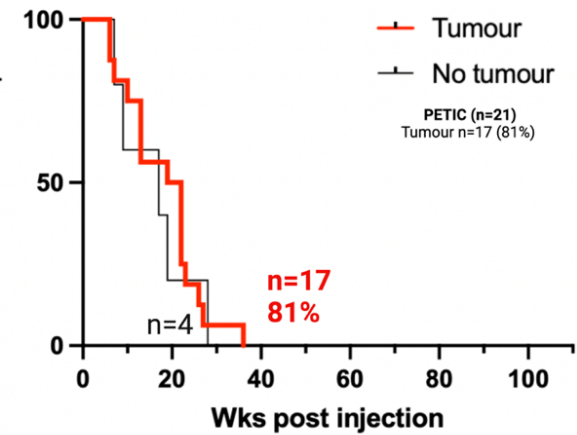
Figure 4-4 Characteristics of the KPF-FLIP GEMM of PDAC when housed in 'Clean' or 'Dirty' environments compared to the classical KPC GEMM of PDAC housed in clean conditions within a 'Dirty' environment.
A-C Representative high-power images taken from 3x H&Es (cut 100um apart) to provide an overview of PDAC tumour architecture in all 3 models. Glandular structures (arrows) surrounded by dense stromal infiltrate (arrowheads) are highlighted **D-F** Kaplan-Meier survival curves demonstrating the proportion of mice culled with confirmed tumour at endpoint compared to mice with no tumour found at endpoint in each unit. Created using Biorender.com. *'Clean Unit' = Specified and Opportunistic Pathogen Free (SOPF) conditions; IVC =Individually ventilated cages.*

4.3.2 Short-term cFLIP deletion does not increase levels of apoptosis in the normal pancreas in novel dual recombinase GEMM of PDAC

To investigate the tumour specificity of cFLIP deletion in the KPF-FLIP GEMM, initially the immediate response to cFLIP deletion was determined in normal pancreatic cells.

The adult pancreas consists of both exocrine and endocrine compartments (Zhou and Melton 2018). Containing morphologically and functionally distinct cell types, these compartments are vital in facilitating the crucial metabolic and hormonal roles of the pancreas. Exocrine cell types include acinar cells which produce a range of digestive enzymes that are secreted into pancreatic ducts for transport to the small intestine. Whilst the endocrine islets contain different cell types which are responsible for the synthesis and secretion of particular hormones, for example, β-cells that produce and secrete insulin.

KPF-FLIP mice without tumours received a daily dose of tamoxifen for three days to silence cFLIP gene expression. Cre recombinase expression was under the control of the Pdx promoter in this model, thereby restricting Cre expression to all mature cell types of the normal, adult pancreas, as detailed in Section 2.4.2.1 (Hingorani et al. 2003; DeCant et al. 2014; Spaeth et al. 2017). Pancreata were then harvested 72 hours following the final dose and the absence of a tumour was confirmed by manual palpation and histology. The level of apoptosis was quantified histologically, according to the proportion of cleaved caspase-3 (CC3) positive cells, as described in Section 2.5.7.

Due to the functional distinction between each cellular compartment, the impact of cFLIP deletion in the normal pancreas was assessed in each individual pancreatic compartment. No increase in CC3 incidence was observed in any functional

compartment of the normal pancreas following short-term cFLIP deletion *(Figure 4.5)*. In the absence of a positive control, staining specificity was validated through manual assessment of positively-stained cell morphology, with CC3 staining observed only within cells exhibiting characteristic apoptotic features, including blebbing, cell shrinkage and apoptotic body formation (Brown et al. 2014).
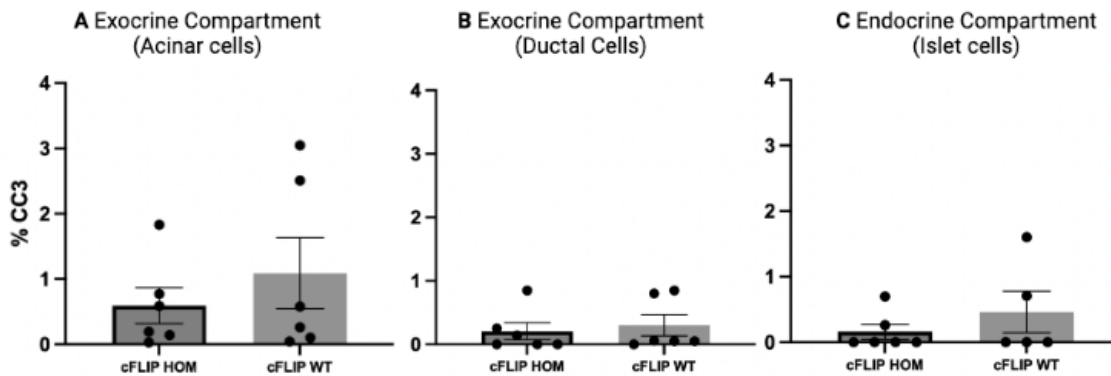
Figure 4-5 Levels of apoptosis in each cellular compartment of the normal murine pancreas following tamoxifen-induced cFLIP deletion.
Apoptosis quantified according to the proportion of CC3 positive cells normalised to the total number of cells per compartment. Data analysed using QuPath software which facilitated the training of an object classifier to distinguish between each pancreatic cell type. Data represents mean ± SEM (minimum n=5). Statistical significance calculated using two-way Mann-Whitney U test following a QQ-plot and Shapiro Wilk normality test.

4.3.3 Short-term cFLIP deletion increases levels of apoptosis and necrosis in PDAC tumours in novel dual recombinase GEM

Given the small cohort of tumours, it was decided to only use the KPF-FLIP model housed at Cardiff University to interrogate the initial, short-term response to cFLIP deletion *in vivo*. In the absence of regulatory anti-apoptotic proteins such as cFLIP, the TRAIL-induced apoptotic pathway leads to rapid cleavage of downstream executioner caspases and, therefore, the initiation of cell death, as detailed in Section 1.4.

To investigate the immediate apoptotic response to cFLIP inhibition, cFLIP gene expression was silenced following the detection of a tumour by manual abdominal palpation, as detailed in Section 2.4.4.3. Briefly, Cre[ERT2] -driven recombination was induced specifically within PDAC cells following a daily intraperitoneal (IP) injection of 80mg/kg Tamoxifen for a total of three days. It is difficult to determine the optimal Tamoxifen dosage and anticipated recombination efficiency due to the wide variation in

administration routes and dosage reported in the literature (Donocoff et al. 2020). However, unpublished data from the Morton lab (CRUK Beatson Institute, Glasgow University, UK) and a study by Andersson et al. in GEMMs of cardiac disease would suggest that the aforementioned dosing regimen should result in rapid and near-complete deletion of the target gene within 6 days of the initial dose (Andersson et al. 2010). Due to the anticipated rapid response of recombination events following tamoxifen induction, combined with the expected rapid induction and execution of apoptosis upon cFLIP withdrawal in cells 'primed' to undergo apoptosis, tumours were harvested three days following the final tamoxifen dose (6 days post the initial dose). Indeed, as discussed in Section 2.4.8, cFLIP silencing at the mRNA level was confirmed via RNAScope$^{(R)}$ assay. The apoptotic response was then quantified histologically, according to the proportion of cleaved caspase-3 (CC3) positive tumour cells relative to the total number of tumour cells. Necrotic cell death was also determined, by morphological assessment, as this is a potential downstream consequence of excessive and uncontrolled cell death and is also a common feature of rapidly growing solid tumours, such as PDAC, whose swift expansion leads to loss of sufficient blood supply to certain regions of the tumour (Ling et al. 2020). Any potential impact of short-term cFLIP inhibition on tumour necrosis was quantified according to the proportion of morphologically distinct necrotic cells compared to the total number of tumour cells, as discussed in Section 2.4.7.8.

Despite relatively small cohorts, cFLIP deletion caused a small, albeit non-significant, incremental increase in apoptosis and necrosis with each additional cFLIP allele excision *(Figure 4.6 A-B)*. Interestingly, cFLIP wild-type (cFLIP$^{+/+}$) controls and cFLIP$^{fl/fl}$ mice which did not receive the full course of tamoxifen treatment (hereafter referred to as 'low dose (LD)') were associated with the lowest CC3 incidence (6.9% +/- 3.2% SEM and 3.0% +/- 1.0% SEM respectively). Mice with only one functional cFLIP copy (heterozygous cFLIP$^{+/-}$ expression) had slightly higher CC3 incidence than both cFLIP$^{+/+}$ and cFLIP^{LD} tumours (8.5% +/- 3.5% SEM). However, tumours in mice lacking both copies of cFLIP (cFLIP$^{-/-}$) were associated with the highest CC3 incidence (14.77% +/- 4.9% SEM) and the highest percentage of morphologically distinct necrotic cells. Indeed, 22.7% +/- 7.2% SEM of cFLIP$^{-/-}$ tumour cells were necrotic, compared to 15.5% +/- 7.1% SEM of the cFLIP$^{+/-}$

tumour cells and 7.2% +/- 4.5% SEM or 13.8% +/- 8.4% SEM of the cFLIP$^{+/+}$ and cFLIP^{LD} tumour cells respectively. Overlapping error bars (p > 0.1 for all comparisons) indicates a variable necrotic background in tumours immediately following FLIPi, potentially reflecting differences in tumour size as opposed to treatment response. For example, necrosis is known to occur when rapid tumour growth exceeds the angiogenic capacity of blood vessels, resulting in regions of particularly large tumours receiving an inadequate blood, and therefore, oxygen supply (Emami Nejad et al. 2021). Hypoxic conditions that are known to occur roughly 180μm or further from tumour blood supply can lead to necrosis. Therefore, a larger tumour would likely possess a greater baseline level of necrosis due to impaired blood supply, resulting in more hypoxia-related necrosis than that observed in a smaller, more perfused tumour.

Comparatively lower levels of apoptosis were detected in the desmoplastic tumour stroma; however, a similar stepwise trend in levels of apoptosis was observed *(Figure 4.6 C-D)*. Although this trend was also non-significant, cFLIP$^{-/-}$ tumours were associated with the highest incidence of CC3-positive stromal cells compared to cFLIP$^{+/-}$, cFLIP$^{+/+}$ and cFLIP-LD tumours.
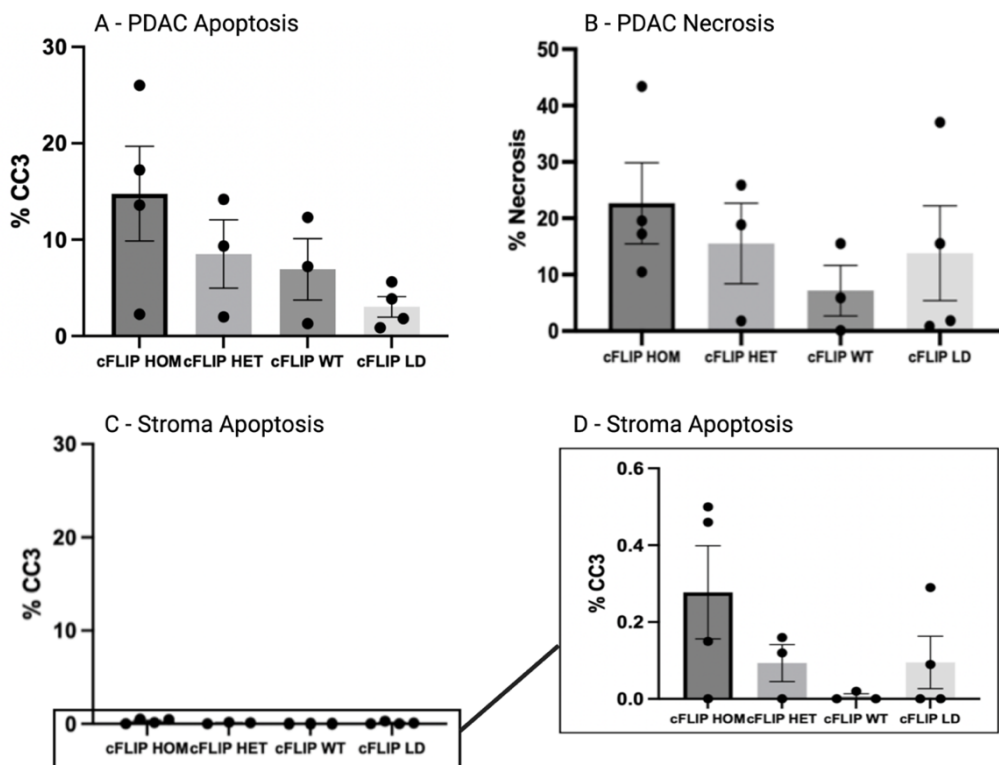
Figure 4-6 Levels of apoptosis and necrosis in PDAC tumours and the surrounding stroma immediately following tamoxifen-induced cFLIP deletion.
A, C & D Apoptosis was quantified according to the proportion of CC3 positive cells normalised to the total number of **A** tumour or **C-D** stromal cells. **B** Necrosis quantified according to the percentage of morphologically distinct necrotic cells normalised to the total number of tumour cells. Data analysed using QuPath software which facilitated the training of an object classifier to distinguish between necrotic and tumour cell types. Data represents mean ± SEM (minimum n=3). Statistical significance calculated using two-way ANOVA with Tukey correction for multiple comparisons. CC3 = Cleaved Caspase 3; cFLIP HOM = cFLIP$^{-/-}$; cFLIP HET = cFLIP$^{-/+}$; cFLIP WT = cFLIP$^{+/+}$; cFLIP LD = cFLIP Low Dose (tumours that did not receive a full tamoxifen induction).

4.3.4 Long-term cFLIP deletion does not significantly affect survival or tumour volume in novel dual recombinase GEMM of PDAC

Given the unpredictability of the KPF-FLIP model when housed at Cardiff, the Morton lab (CRUK Beatson, Glasgow, UK) kindly investigated the long-term impact of cFLIP deletion in PDAC tumours on our behalf. For clarity, all data presented in Section 4.3.4 was obtained and analysed by members of the Morton lab.

As in Section 4.3.3, tamoxifen-induced deletion of cFLIP expression was instigated following confirmation of tumour burden. However, tumours were then allowed to progress until the ethically determined endpoint was reached. Likely due to a limited cohort of KPF-FLIP$^{-/-}$ mice (n=2), long-term cFLIP deletion did not significantly impact overall survival potential when compared to the survival of KPF-FLIP$^{+/+}$ controls (log-rank Mantel-Cox: Chi Square = 0.7897; df = 1; p-value = 0.3742) *(Figure 4.7 A).* Tumour volume was also monitored longitudinally using high-resolution ultrasound technology. However, long-term cFLIP deletion (KPF-FLIP$^{-/-}$) did not cause a significant change in tumour growth when compared to cFLIP-WT (KPF-FLIP$^{+/+}$) tumours *(Figure 4.7 B)*.
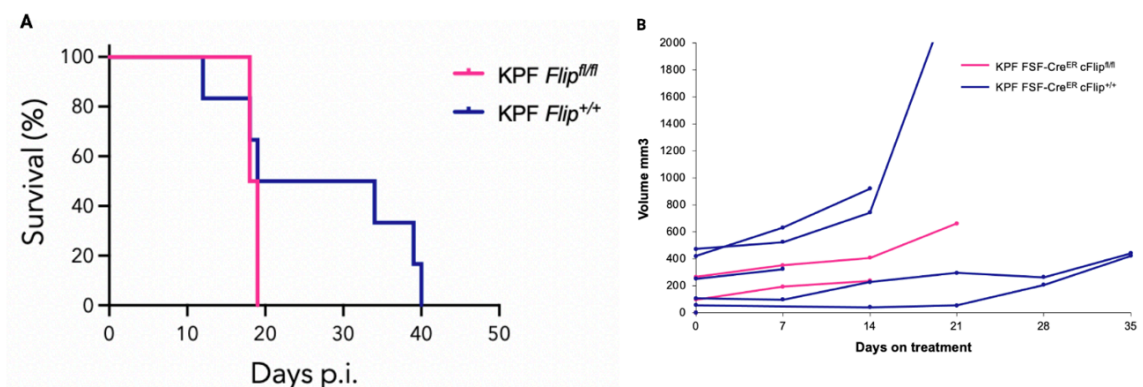
Figure 4-7 Longitudinal response of KPF-FLIP PDAC tumours to tamoxifen-induced cFLIP deletion.
A Kaplan-Meier survival curve following systemic tamoxifen injection to induce Cre-mediated cFLIP deletion. Treatment commenced once tumour burden was confirmed, and mice were aged until reaching the ethically determined endpoint. **B** Non-invasive monitoring of tumour volume following systemic tamoxifen injection. Volume measured using high resolution ultrasound technology. Data obtained and analysed by colleagues in the Morton lab (CRUK Beatson Institute, Glasgow, UK). Days p.i. = Days post induction. Cohorts comprised of n=2 (KPF-FLIP$^{fl/fl}$) and n=5 (KPF-FLIP$^{+/+}$).

4.3.5   KPF-FLIP$^{fl/fl}$ tumour-derived organoids to investigate cFLIP deletion *ex vivo*

To determine the response to cFLIP inhibition in PDAC *ex vivo*, certain uninduced KPF-FLIP$^{fl/fl}$ tumours from the Cardiff-based cohort were used to generate organoids. A full description of organoid culture methods and model characteristics can be found in Section 2.5. Briefly, a small section of PDAC tumour was harvested from an uninduced, KPF-FLIP$^{fl/fl}$ mouse and subsequently minced, washed, and digested using a mixture of Collagenase and Dispase. Ductal structures were then isolated and seeded directly in Matrigel on pre-warmed culture plates. Matrigel domes were overlaid with organoid expansion media, containing the required growth factors. Media was changed regularly, and organoids were passaged and/or frozen when domes became roughly 80% confluent.

Organoids were seeded into 96-well plates as small clusters of cells in a 10ul Matrigel dome for functional assays. Due to previous observations from colleagues in adjacent labs within the host institute, who were performing similar studies on the effects of exogenous tamoxifen in *ex vivo* culture (unpublished, Salvador Barbero & Hill, Cardiff University European Cancer Stem Cell Research Institute), media was supplemented with a Cre Recombinase Adenovirus (AdCre) to excise the loxP-flanked exon 2 of *CFLAR* and delete cFLIP in the organoids. A fluorescent mCherry Adenovirus (Ad-mCherry), containing the same viral backbone and promoter as the AdCre virus, as summarised in Section 2.5.3, was used as a surrogate marker of AdCre recombination efficiency. Following an initial 24-hour incubation, media supplemented with either AdCre or Ad-mCherry was added to organoids. Exogenous TRAIL or DMSO control was then added to the media 24 hours after the viral infection. Organoids were cultured for a total of 96 hours following viral infection (min. n=4, min. 3 independent repeats per timepoint). A

schematic overview summarising the experimental design can be found in Section 2.5.3.2.

4.3.5.1 Determining optimal viral titer for infection of organoids

As detailed in Section 2.5.3.1, Ad-mCherry was purchased to determine the optimal viral titer of AdCre, thereby ensuring efficient recombination within the KPF-FLIP$^{fl/fl}$ organoids. Ad-mCherry expresses the improved red fluorescent protein, mCherry, under the control of the CMV promoter. Transduction efficiency was monitored according to the proportion of organoids with over 50% of their surface area expressing red fluorescence normalised to the total number of organoids in the field of view (FOV).

As shown in *Figure 4.8*, Ad-mCherry was able to successfully penetrate the small volume of Matrigel to efficiently infect KPF-FLIP$^{fl/fl}$ organoids at a variety of viral titers. Even at the lowest titer (0.2ul/ml or 1 x 10^6 PFU/ml), red fluorescence was detected in 53.67% (+/- 1.2% SEM) of all organoids in the field of view 96 hours post-infection *(Figure 4.8 B & E)*. Whilst both the mid-range and highest titer conditions (1ul/ml or 1x10^7 PFU/ml and 1.5ul/ml 1.5x10^7 PFU/ml respectively) led to the infection of most organoids within each field of view by 96 hours post-infection. Control organoids which received no adenovirus demonstrated no expression of red fluorescence *(Figure 4.8 A & E).*

The mid-range Ad-mCherry titer resulted in the expression of red fluorescence by 60% (+/- 8.7% SEM) of all organoids in the field of view 48 hours post-infection *(Figure 4.8 E)*. This rose to 73% (+/- 2.3% SEM) of all organoids by 96 hours *(Figure 4.8 C & E)*. Interestingly, red fluorescence was only detected in 45% (+/-5% SEM) of organoids that received the highest viral titer 48 hours post-infection *(Figure 4.8 E).* Despite an initial difference in infection efficiency, 71% (+/- 4% SEM) of organoids that received the highest viral titer expressed red fluorescence by 96 hours post-infection *(Figure 4.8 D-E)*. Given the similarity between the infection efficiency of the mid-range and the highest viral titer, it was decided to utilise the mid-range titer for all subsequent *ex vivo* experiments.

To determine the impact of the addition of exogenous TRAIL to the media 24 hours post-infection, the proportion of organoids expressing red fluorescence following each different treatment arm was quantified *(Figure 4.8 F)*. The mid-range viral titer of Ad-mCherry in this set of experiments successfully infected 81% (+/- 2% SEM) of all organoids in each well 96 hours post-infection. Similarly, the addition of TRAIL to the Ad-mCherry infected organoids resulted in 79% (+/- 5% SEM) of all organoids in each well expressing red fluorescence 96 hours post-infection. This demonstrated that TRAIL supplementation did not appear to significantly impair the transduction efficiency of the viral vectors. As expected, both AdCre and AdCre + TRAIL resulted in virtually no organoids expressing red fluorescence at each timepoint (0% and 3% +/- 3% SEM respectively at 96 hours post-infection).
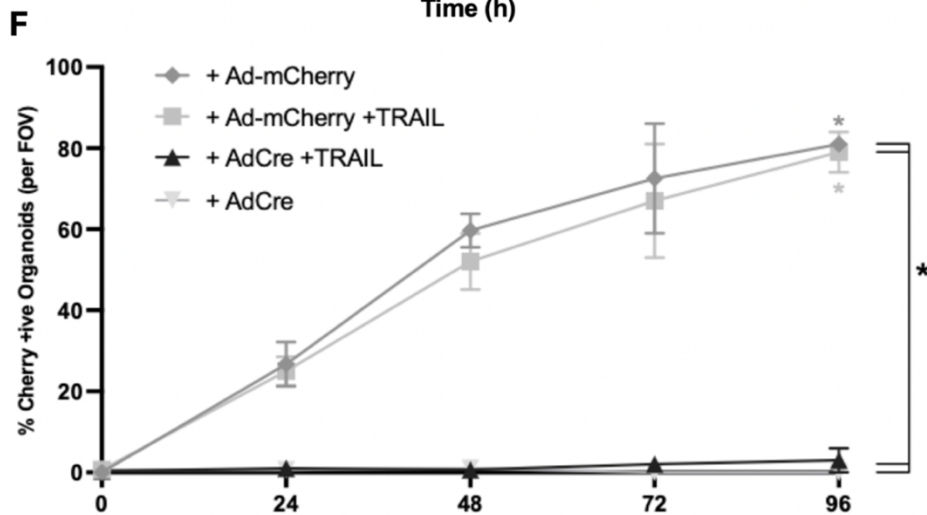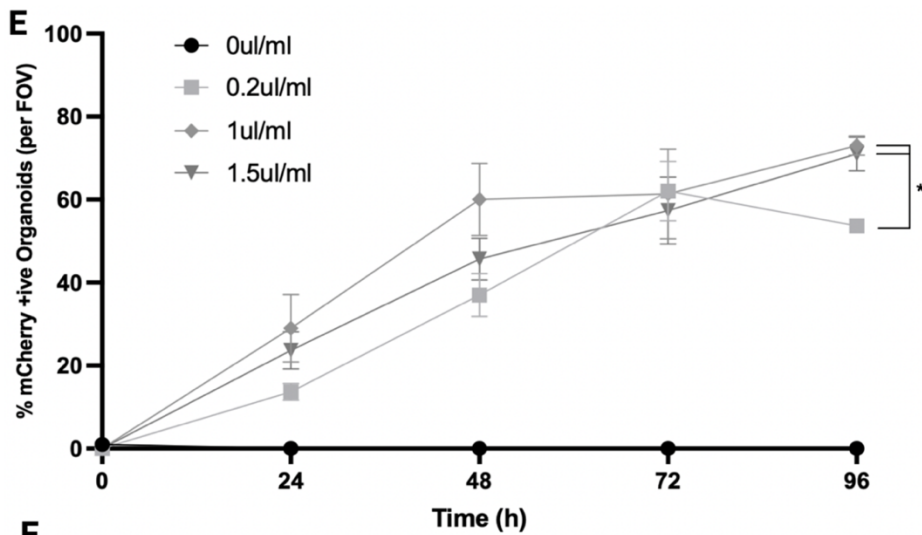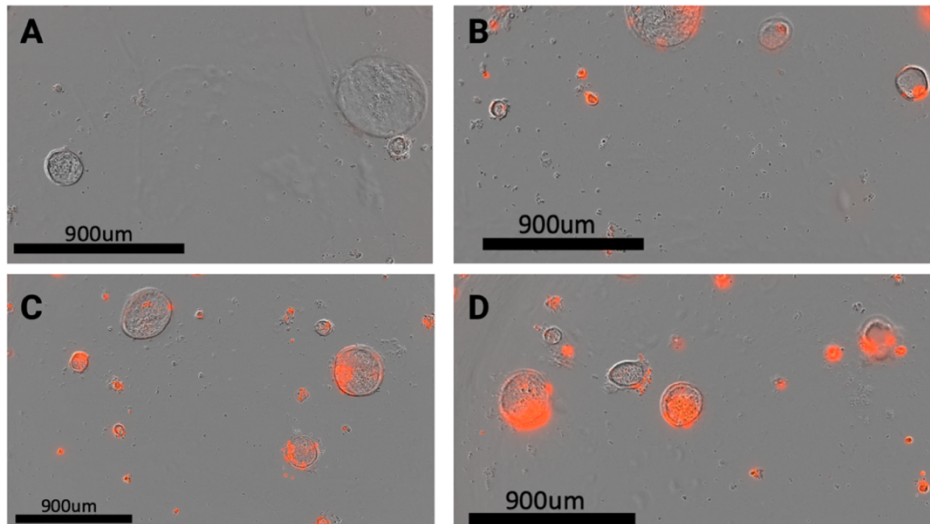
Figure 4-8 Optimisation of viral titer to achieve efficient recombination in PDAC tumour-derived organoids.

Representative fields of view containing KPF-FLIP$^{fl/fl}$ organoids following **A** 0μl/ml, **B** 0.2μl/ml, **C** 1μl/ml or **D** 1.5μl/ml titers of commercially purchased Ad-mCherry recombinant adenovirus. **E** Change in percentage of mCherry positive organoids at different viral titers over time. **F** Change in percentage of mCherry positive organoids following different treatment approaches in combination with 1μl/ml Ad-mCherry or 1μl/ml AdCre over time. Images taken using the Incucyte S3 Live Cell Analysis Platform and analysed manually. *AdCre = Cre recombinase adenovirus.*

4.3.6 Deletion of cFLIP *ex vivo* causes a significant reduction in the number but not the size of PDAC organoids

As detailed in Section 2.5.2.2, a manual count of organoids in each well correlated with organoid viability, as determined using the cell titre blue viability assay. Therefore, the manual count method was utilised to represent organoid viability at a range of time points.

The number of organoids in each well was counted at each timepoint and normalised to the number of organoids present before the addition of AdCre (FLIPi) or the Ad-mCherry empty vector (EV) control. A representative image was taken at a set focal plane from each well at each time point and used to measure the diameter of organoids.

cFLIP inhibition alone was sufficient to significantly reduce the number of PDAC organoids 48 hours post-infection (-4.7AU +/- 2.5 SEM) when compared to the EV and EV + TRAIL controls, which lead to an increase in the number of organoids at the same time point (+6.2AU +/- 3.1 SEM and +7.85 +/-2.8 SEM respectively) *(Figure 4.9 A)*. However, 72 hours post-infection, the ability of the remaining organoids to form new spheres following FLIPi appeared to be recovering (-4AU +/- 3.8 SEM). Indeed, by 96 hours, the number of organoids had increased compared to the pre-treatment baseline (+11.9AU +/- 8 SEM). Due to overlapping error bars, this increase was not significantly different to the increase in the number of organoids that was observed 96 hours following EV and EV + TRAIL controls (+20.3AU +/- 6.9 SEM and +7.4AU +/- 7.5 SEM).

Conversely, the addition of exogenous TRAIL *ex vivo* appeared to potentiate the effect of FLIPi, leading to a significant reduction in the total number of organoids 48 hours post-infection (-3.1AU +/- 2.6 SEM) when compared to the EV + TRAIL control (+ 7.8 +/- 2.8 SEM). Despite no significant difference being observed at the 72- and 96-hour time points, it does appear that the addition of TRAIL may have prevented the increase in the number of organoids that was observed 96 hours following FLIPi alone (-2.14 +/- 5.2 SEM compared to 11.9AU +/- 8 SEM respectively).

In a similar manner, TRAIL supplementation in the absence of FLIPi also appeared to impact the total number of organoids in each well. Despite an initial increase compared to the pre-infection baseline at 48 hours post-infection (+7.8AU +/- 2.8 SEM), the total number of organoids comparatively plateaus and potentially decreases in certain wells at 72- and 96-hours post-infection (-0.4AU +/- 5.3 SEM and +7.4AU +/- 7.5 SEM respectively). This contrasts with the general increase in total organoid numbers observed in the EV control at the same time points (+3.9AU +/- 2.9 SEM and +20.3AU +/- 6.9 SEM respectively).

Overall, these data suggest that FLIPi may be sufficient to initially reduce PDAC organoid viability, however, the remaining, unaffected organoids are able to ultimately overcome this sensitivity, thereby leading to an increase in the total number of organoids by 96 hours post AdCre infection. Conversely, FLIPi in combination with exogenous TRAIL appears to prevent a similar increase in the number of organoids 96 hours post AdCre infection.

Of note, both FLIPi alone and FLIPi + TRAIL did not induce a significant change in organoid diameter when compared to the pre-treatment baseline *(Figure 4.9 B)*. Both FLIPi alone and FLIPi in combination with TRAIL lead to the same exponential increase in organoid size as observed in the EV and EV +TRAIL controls. This suggests that the surviving fraction of organoids following both FLIPi and FLIPi + TRAIL are viable and able to grow as normal. This may indicate that FLIPi exclusively impacts the ability of viable organoids to sub-divide and/or form new organoids or, conversely, that successful adenoviral-mediated recombination did not occur in every organoid, thereby enabling unaffected organoids to continue growing as normal.
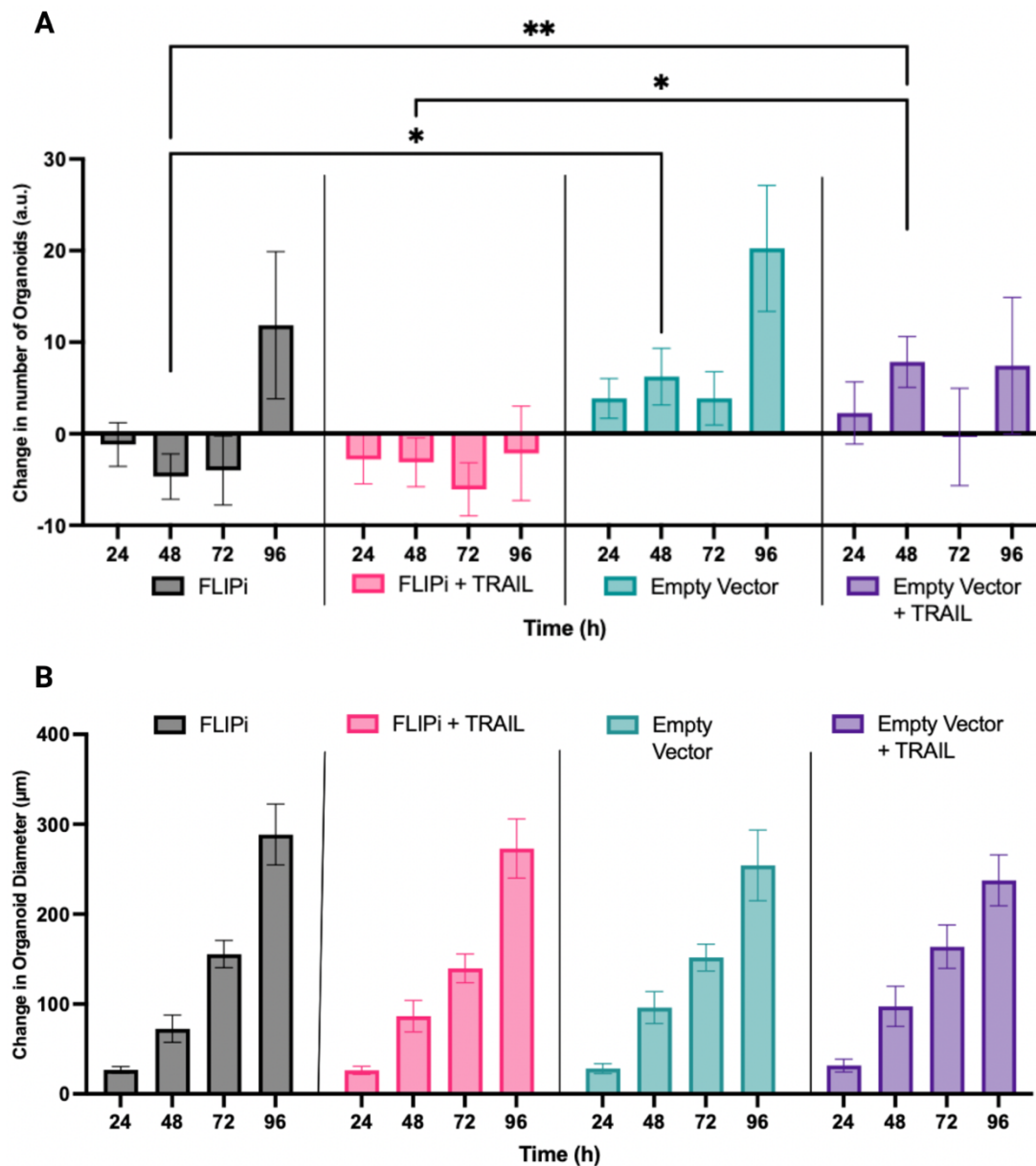
Figure 4-9 Response of PDAC tumour-derived organoids to cFLIP deletion *ex vivo*.
A Cre Recombinase adenovirus was used to delete loxP-flanked cFLIP expression in KPF-FLIP^{fl/fl} tumour-derived organoids. Total organoids per well were counted before the addition of viral vectors and during treatment, with the total number of organoids present after infection normalised to the pre-treatment count. Exogenous TRAIL was added to relevant wells at the 24h time point (24h post adenovirus). **A** Change in number of organoids per well. **B** Change in diameter of individual organoids. Data represents mean ± SEM (minimum n=3 independent repeats per time point). Statistical significance calculated using two-way ANOVA with Tukey correction for multiple comparisons. *FLIPi = Cre Recombinase Adeonvirus (Ad-CMV-iCre; Vector Biolabs)-mediated cFLIP deletion; Empty Vector = Ad-mCherry Adenovirus control (Ad-mCherry; Vector Biolabs).*

4.4 Discussion

Following promising *in vitro* results, the experiments detailed in this chapter sought to determine the efficacy of FLIPi *in vivo* and *ex vivo* through the establishment of a novel, dual-recombinase GEMM of PDAC. The KPF-FLIP^fl/fl model facilitates the conditional deletion of cFLIP within intact, KRAS- and p53-mutant PDAC tumours. Histological characterisation demonstrated that KPF-FLIP PDAC tumours closely resembled the classical PDAC KPF and KPC GEMMs, characterised by dense stromal infiltration and well-differentiated, glandular structures *(Figure 4.2)* (Hingorani et al. 2005; Schönhuber et al. 2014; Gopinathan et al. 2015). However, due to difficulties detecting the murine form of cFLIP, work to confirm cFLIP deletion within induced tumours is ongoing, as detailed in Section 2.4.8. Therefore, it is currently not possible to correlate the loss of cell viability within the tissues with a reduction in cFLIP. Unfortunately, unexpectedly low tumour incidence impaired the ability to generate sufficient experimental KPF-FLIP cohorts to achieve adequate statistical power within the necessary timeframe *(Figure 4.4)*. Therefore, increasing the sample size of each cohort should more reliably reflect the sample mean, thereby providing greater statistical power and improved estimate precision to determine whether the non-significant differences observed were a true response or purely down to chance (Priest 2005).

Compounding the penetrance of the tumour phenotype was the observation that animals housed in a more immunologically challenging environment experienced significantly altered tumour onset. The use of two different housing environments significantly impacted the model tumour latency, with its re-derivation into SOPF conditions causing a significant reduction in latency when compared to the KPF-FLIP cohort housed in the comparatively dirtier unit. Whilst all tumours appeared by 30 weeks of age under SOPF conditions, tumours arose at any point between 8-90 weeks of age in the dirtier unit. An underlying reason for such a difference has yet to be confirmed, however, many factors may have played a role. Importantly, the tumour latency observed in the SOPF unit correlated with the findings of Schönhuber et al., who reported a median survival of 61 days in the KPF model, with all animals dying from tumour burden by around 150 days (roughly 40 weeks of age; n=12) (Schönhuber et al.

2014). However, the proportion of KPF mice that ultimately developed tumours in that study was not published.

Throughout the experiments reported in this chapter, whilst the cleaner unit retained SOPF status throughout the project, the dirtier unit was unfortunately subjected to pinworm and repeated infections of *Pasteurella pneumotropica Heyl*. Whilst both infections are generally clinically silent in immune-competent animals and mandatory treatment regimens successfully cleared the infection from the colony, the infection-related immune response or the treatments themselves may have influenced tumour development (Hickman et al. 2008). For example, as parasitic helminths, pinworm infection can alter the host's antibody-mediated immunity, particularly causing a switch in T-helper (TH) cell prevalence and through the release of immune-modulatory products to facilitate a symbiotic relationship (Harris and Loke 2017). Conversely, this may ultimately lead to older animals acquiring antibody-mediated immunity to pinworm parasites. However, due to the cross-reactivity between certain pathogen antigens and tumour cell antigens, this may also result in the development of anti-tumour immunity within infected animals, potentially underlying the prolonged latency observed in KPF animals from the 'dirty' unit (Oikonomopoulou et al. 2013). Additonally, Fenbendazole (FBZ) was used in the animal diet to treat pinworm, but, high enough concentrations (>1μM) of FBZ have previously been shown to significantly reduce the viability of the ASPC-1 and Capan-2 established human PDAC cell lines (Florio et al. 2019). However, Duan et al. found no impact on tumour growth when investigating the impact of FBZ *in vivo*, using a mammary xenograft model and treating with the same diet-based delivery as was provided to the KPF-FLIP colony (approx.. 0.1μM FBZ delivered to tissues) (Duan et al. 2012). This suggests that the concentration supplied to the colony may not have been sufficient to impair tumour development, however, further investigation is required. Additionally, a combination of the fluoroquinolone (FQ) enrofloxacin (Baytril, Bayer, Germany) and a broad spectrum anti-biotic containing Sulfadiazine and Trimethoprim (Diatrim, Dechra, UK) was used to treat the multiple *Pasteurella* infections at the dirtier unit. Less information is available involving the impact of this treatment regimen on tumour cells. However, certain fluoroquinolones, such as enrofloxacin, have been shown to induce a range of potentially cancer-preventative side effects, including

inhibiting TGF-β-induced expression of Matrix Metalloproteinase-9 (MMP-9) in lung tumour cell lines *in vitro* (Huang et al. 2021a). Previous studies have highlighted the role of elevated levels of MMPs in worsening patient prognosis and increasing the invasive and metastatic capacity of many cancer types (Gialeli et al. 2011). Unfortunately, to reinstate the unit biosecurity and conform to Home Office guidelines, all treatment regimens were mandatory, but each may have contributed to the significant impact on tumour latency and incidence that was observed in the KPF-FLIP$^{fl/fl}$ model when housed in the 'dirty' environment. Equally, the underlying immune system and microbiome of each cohort were likely different due to the difference in pathogen exposure at each unit. Mice from the dirtier unit were likely to possess a more robust, often active immune compartment following repeated exposure to various pathogenic stimuli (Oikonomopoulou et al. 2013; Bach 2018). Whereas mice from the SOPF unit would have experienced minimal immune system stimulation, potentially facilitating the immune evasion of tumours. Anecdotal observation of immunological infiltrates by histology indicated no clear correlation between the clean and dirty mouse tumour tissues (data not shown). However, further investigation beyond the scope of this project, including a quantifiable comparison of tumour histological features in each unit, would be required to delineate the underlying mechanisms resulting in such a clear impact on tumour development.

Despite the difference in development, the KPF-FLIP PDAC tumours which did successfully establish in both units were morphologically comparable *(Figure 4.4 A-C)*. Given the small supply of tumours from this model, it was therefore decided to pool tumours from both units to investigate the immediate response to cFLIP deletion. Although no significant difference emerged, deletion of both cFLIP alleles (cFLIP$^{fl/fl}$) did appear associated with the greatest level of tumour apoptosis and necrosis when compared to heterozygous cFLIP deletion (cFLIP$^{fl/+}$) and the cFLIP$^{+/+}$ and cFLIP^{LD} controls *(Figure 4.6 A-B)*. However, increasing the number of mice per condition would be necessary to truly determine the impact of this intervention within the model. Equally, it is also worth exploring additional time points following tamoxifen-induced Cre induction to confirm the suitability of the 72-hour timepoint for observing an immediate apoptotic response to cFLIP deletion.

Notably, despite a trend emerging in the KPF-FLIP$^{-/-}$ tumours, no similar increase in apoptosis was observed in any of the normal, healthy pancreatic compartments in response to cFLIP deletion *(Figure 4.5)*. This suggests that any effect of cFLIP inhibition may be tumour-specific, as originally hypothesised. However, once again, additional time points, including a long-term arm would be beneficial to ensure that normal pancreatic cells remain unsusceptible to this approach.

Whilst colleagues in the Morton lab (CRUK Beatson, Glasgow, UK) kindly investigated long-term response to cFLIP deletion in the KPF-FLIP model, this study was also impacted by a small cohort of cFLIP$^{-/-}$ tumours. However, cFLIP deletion in KRAS- and p53-mutant PDAC tumours did not appear to significantly affect mouse survival or tumour growth *(Figure 4.7)*. Several factors could contribute to this lack of overall beneficial effect on tumour outcome; including inefficient recombination of the target cFLIP allele and/or compensation by clonal expansion of unaffected tumour cells. It was not possible to histologically analyse the tissues from this long-term study within the scope of this project, but tissues were collected, and their respective levels of apoptosis and necrosis will ultimately be assessed. However, it is possible that combining FLIPi with an additional therapeutic intervention may be required to influence tumour volume and overall survival. Interventions could include exogenous TRAIL delivery or potentially targeting the non-canonical pathway.

Having demonstrated a potential, albeit non-significant, FLIPi-induced increase in apoptosis *in vivo*, uninduced KPF-FLIP$^{fl/fl}$ tumours were then harvested to investigate the approach *ex vivo*, through the establishment of tumour-derived organoids. As a more time- and cost-effective model of PDAC, organoids facilitated a more robust investigation into the role of FLIPi in a 3D setting and provided a better reflection of PDAC tumour morphology and cell-cell interactions than spheroids due to the ability to culture heterogeneous populations of tumour cells (Gunti et al. 2021). However, despite retaining tumour cell polarity and contact with a supportive basement matrix (Matrigel), organoids in this study were unable to interact with other components of the *in vivo* tumour microenvironment (TME), such as immune or stromal cells. Equally, although

the KRAS- and p53-mutant organoids retained the expression of a tamoxifen-inducible Cre recombinase, the toxicity of the required dose of tamoxifen to activate Cre rendered it unsuitable for the deletion of cFLIP in this setting (Salvador Barbero & Hill, unpublished). Therefore, a codon-optimised Cre recombinase adenovirus (Ad-CMV-iCre; AdCre) was purchased to catalyse the excision of the loxP-flanked exon 2 from the gene encoding cFLIP, thereby deleting cFLIP expression in the organoids. Due to shared morphological characteristics between normal pancreatic organoids and PDAC organoids, the organoids used in this chapter were subjected to tumour-selective media conditions, whereby the absence of epidermal growth factor (EGF) enriched the KRAS-mutant PDAC population, ensuring the exclusive growth and survival of tumour cells capable of driving ligand-independent activation of RAS signalling, as demonstrated by Seino et al. (Seino et al. 2018).

An mCherry-tagged adenovirus (Ad-mCherry) was used to optimise the necessary viral titer and monitor the representative AdCre recombination level in each experimental repeat *(Figure 4.8)*. Varying Ad-mCherry titers demonstrated that even the lowest viral titer (0.2µl/ml) resulted in successful recombination in 53.67% (+/- 1.2% SEM) of all organoids per field of view by 96 hours post-infection. However, no significant difference was observed between the percentage of mCherry-expressing organoids following the mid-range (1µl/ml) and the highest viral titer (1.5µl/ml) by 96 hours post-infection. Therefore, the mid-range titer was selected as the optimal dosage and used for all subsequent studies. No mCherry expression was observed in untreated controls or in AdCre-treated organoids, demonstrating the specificity of red fluorescence for labelling successfully recombined, Ad-mCherry-treated organoids. No cytotoxicity was observed at each viral titer tested, however, it is possible that further increases to the viral titer may have ultimately induced cytopathic effects, as observed by Wang and colleagues when infecting intestinal stem cell-derived organoids with adenoviral vectors (Wang et al. 2014). Whilst all experiments were conducted within a 96-hour timeframe due to time and cost constraints, it is also worth noting that, despite the transient nature of adenoviral transfection, the same study by Wang et al recorded transgene expression in organoids for up to 10 days following infection, thereby providing the option for

future work to consider extending the timeframe to determine whether the response to FLIPi and TRAIL can be sustained.

In an endeavour to determine the most efficient method of monitoring organoid viability *ex vivo*, a range of potential methodologies were trialled, as detailed in Section 2.5.2. After extensive consideration, it was decided to manually count organoids at each time point following AdCre or Ad-mCherry infection and normalise each count to the initial number of organoids per well before the addition of adenovirus (0h time point). AdCre-mediated FLIPi alone significantly reduced the number of organoids by 48 hours post-infection *(Figure 4.9)*. However, organoids appeared to recover over time, with their number ultimately increasing compared to the pre-treatment baseline 96 hours after infection. Many reasons could underlie this recovery and further investigation is required to truly delineate the underlying mechanisms. However, it suggests that the level of endogenous TRAIL-R signalling *ex vivo*, although greater than the *in vitro* setting, was not sufficient to maintain an apoptotic response, even in the absence of cFLIP.

Indeed, a similar significant reduction in organoid number was observed following the combination of AdCre and exogenous TRAIL at 48 hours post-infection and 24 hours post-TRAIL supplementation. Although no significant difference emerged when compared to controls at later time points, AdCre combined with TRAIL did appear to minimise the recovery in organoid number that occurred following AdCre alone. Interestingly, organoids appeared to be partially sensitive to TRAIL *ex vivo*, as exogenous TRAIL alone resulted in a reduction in organoid number, although this effect was non-significant due to high levels of variation between experimental repeats. The wide variation between repeats affected all treatment arms in this study, suggesting that a more robust method of monitoring viability, such as the cell titer-glo measure of metabolically-active cells, may be beneficial to truly delineate the role of FLIPi in PDAC *ex vivo*. Furthermore, neither FLIPi nor FLIPi in combination with TRAIL significantly affected organoid size, which increased exponentially throughout the experiment.

The changes that were observed in organoid viability correspond with the findings of Montinaro et al, whereby a combination of indirect cFLIP suppression (via CDK9

inhibition) and TRAIL lead to the drastic reduction in viability of PDAC organoids derived from the KPC GEMM (Montinaro et al. 2022). Of note, combining FLIPi with TRAIL in this setting successfully induced cell death even in organoid populations that were highly resistant to conventional, standard-of-care chemotherapy, underlining the clinical potential of this approach to target the notoriously aggressive, often chemotherapy-resistant PDAC tumour cells.

The findings presented in this chapter also imply that FLIPi as a treatment approach may be specifically impacting cancer stem-like cells within an organoid, thereby preventing its ability to form new spheres but not impacting the bulk cellular population which can continue to divide and increase the size of the organoid. Pancreatic cancer stem cells were first described in 2007, with 0.2-0.8% of cells within a PDAC tumour shown to express CD44, CD24 and epithelial-specific antigen (ESA) and possess an enhanced capacity for self-renewal and to instigate tumours (Li et al. 2007). However, it may also reflect the adenoviral recombination efficiency of roughly 70-80%, meaning that around 20-30% of all organoids are not infected in any given well. These uninfected organoids may be responsible for the recovery in organoid numbers observed after 72 hours. To overcome this limitation, it would be necessary to repeat the experiment with a fluorescently labelled AdCre, which is commercially available, to identify and specifically monitor recombined cells in which cFLIP has been deleted. Alternatively, the histological analysis of formalin-fixed organoids may reveal unique characteristics of organoids in which cFLIP has been deleted. However, this was not possible within this study due to difficulties in optimising antibodies targeting the murine form of cFLIP, as detailed in Section 2.4.8. Future work could therefore involve alternative means of measuring TRAIL-R signalling activity within this model, including histological or western blot analysis of the non-canonical pathway effector, phosphorylated Akt, or of cleaved downstream canonical pathway effectors, such as cleaved caspase-3.

Finally, to interrogate the potential impact of FLIPi on the stem-like ability of organoids to form new spheres, it would also be pertinent to consider expression levels of cancer stem-like markers (CD44^{+}, CD24^{+}, epithelial-specific antigen (ESA)[+]) or through the optimisation of a bona-fide sphere-forming assay (Heinrich et al. 2021). Further studies are also required to specifically investigate apoptosis in response to FLIPi *ex vivo*. Whilst

the number of organoids roughly correlated with viability, as demonstrated in Section 2.5.2.2, understanding the mechanism by which viability is decreasing in response to FLIPi would assist in determining its potential as a therapeutic approach to treat KRAS-mutant PDAC.

4.5 Conclusions and Future Work

To conclude, the results outlined in this chapter demonstrate the establishment and characterisation of the novel, dual recombinase KPF-FLIP GEMM of PDAC. Initial data suggest that, as hypothesised, cFLIP inhibition alone in KPF-FLIP tumours may lead to increased levels of apoptosis and necrosis *in vivo*. However, this did not result in any significant impact on long-term tumour growth or overall survival. Additional subjects and time points will need to be added to the treatment arms to truly delineate the potential of FLIPi for treating PDAC in this model and to truly test the original hypothesis, that cFLIP inhibition should be sufficient to re-activate TRAIL-induced, caspase-depedent apoptosis in KRAS-mutant PDAC tumours.

Furthermore, FLIPi alone significantly reduced the number of KPF-FLIP$^{fl/fl}$ tumour-derived organoids *ex vivo*. However, exogenous TRAIL supplementation in combination with FLIPi was required to maintain this reduction. These results support the experiments reported in Chapter 3 of this thesis, namely that 2D KRAS-mutant, PDAC cell lines require TRAIL supplementation to respond to FLIPi in the absence of an intact 3D microenvironment. It appears that the 3D, heterogeneous nature of the organoids may maintain some level of endogenous TRAIL-R signalling to initially respond well to FLIPi alone, however, rapid resistance is acquired in the absence of exogenous TRAIL. This suggests that non-canonical TRAIL signalling may be driven at low levels in the *ex vivo* setting when compared to the *in vitro* setting. However, most of the signalling may be driven by a component of the *in vivo* microenvironment (such as the immune compartment) which is not present in *ex vivo* culture. Therefore, in support of the original hypothesis and of previous work conducted by Haag and colleagues, PDAC cells are primed to undergo apoptosis in response to FLIPi *in vitro* and *ex vivo* but require TRAIL delivery to activate the pathway (Haag et al. 2011). Indeed, a study by Boj et al. found no evidence of Akt phosphorylation in PDAC tumour-derived organoids,

potentially confirming that constitutive, non-canonical TRAIL signalling, and, therefore downstream Akt signalling, may be uniquely driven *in vivo* in PDAC (Boj et al. 2015). Further studies are therefore needed to evaluate the activity of the non-canonical pathway both *in vitro* and *ex vivo*.

Additionally, exploring the exact mechanism underlying the impact of FLIPi on the total number of tumour-derived organoids would be beneficial. Although more time- and cost-demanding, it may also be pertinent to explore the response to FLIPi in a panel of patient-derived human PDAC organoids, to better compare results with those obtained from human 2D cell lines, as outlined in Chapter 3 of this thesis, and to provide a more clinically-relevant reflection of inter- and intra-tumour heterogeneity. Whilst not fully recapitulating the full tumour microenvironment, such work may provide a more personalised approach to the selection of which patient tumours are most likely to respond to FLIPi.

Finally, given the findings of Montinaro et al, whereby indirect FLIPi in combination with TRAIL sensitised chemotherapy-resistant PDAC organoids to cell death, it would be interesting to investigate the potential of direct cFLIP targeting on tumour types resistant to standard-of-care approaches, both *in vivo* and *ex vivo* (Montinaro et al. 2022). Given the notoriously difficult-to-treat nature of PDAC, identifying a therapeutic approach which is reasonably well tolerated and also effective in treating chemotherapy-resistant disease is vital in the drive to improve survival rates.

5 Adapting 18^F-FDG PET/CT imaging to establish the therapeutic potential of targeting cFLIP with a novel small molecule inhibitor in Pancreatic Ductal Adenocarcinoma in vivo

5.1 Introduction

The complete and sustained genetic knockdown of a target protein can result in unexpected phenotypes due to cross-talk with alternative or non-canonical signalling pathways, as discussed in Section 3.1. Therefore, selectively targeting a protein's role in a specific signalling pathway of interest is likely to be more therapeutically relevant, with fewer off-target side effects.

In the case of cFLIP in PDAC, we aimed to target its role as an inhibitor of canonical, TRAIL-induced apoptosis through the direct inhibition of its recruitment to the DISC. Our lab's novel small molecule cFLIP inhibitor, OH14, showed limited efficacy during preliminary *in vitro* tests in PDAC cell lines, as detailed in Section 3 *(Figure 3.6).* However, OH14 did successfully sensitise the Panc10.05 EPCCL to TRAIL. In addition, OH14 in combination with various chemotherapeutics has previously induced tumour regression in a range of *in vivo* cancer models and demonstrates protein-protein inhibitory (PPI) specificity through the use of inducible cFLIP-shRNA expressing breast cancer cell lines (manuscript submitted, Clarkson Lab).

Given the limitations of 2D cell culture outlined in Chapter 3, we hypothesised that assessing the efficacy of OH14 *in vivo* would provide a better reflection of its clinical potential. The KPC (*Pdx1-Cre^{ERT2}; LSL-Kras$^{G12D/+}$; LSL-Trp53$^{R172H/+}$)* GEMM of PDAC was selected for the OH14 arm of this study due to the comparative ease in generating experimental KPC mice (three alleles of interest) compared with the complex breeding involved to produce experimental KPFs (five alleles of interest). As detailed in Chapter 4 of this thesis, the KPC GEMM was also associated with a far higher tumour incidence than the KPF model in our hands.

Due to the variable tumour latency of both the KPF and KPC models, regular manual palpation and non-invasive imaging modalities are required to detect tumours prior to the manifestation of adverse symptoms (Gopinathan et al. 2015). High-resolution ultrasound is the favoured and most commonly used method to non-invasively monitor PDAC progression in GEMMs. However, this technology was not available in the host institution, as discussed in Section 2.4.5. A previous study by Knight et al. demonstrated the ability of the clinical positron emission tomography (PET) imaging agent 18F-fluorodeoxyglucose (^{18}F-FDG) to detect KPC-derived tumours in a subcutaneously-implanted allograft model of PDAC *(Figure 5.1)* (Knight et al. 2017). When combined with spatially informative computerised tomography (CT), ^{18}F-FDG PET-CT is favoured in the clinic and recommended by the National Institute for Health and Care Excellence (NICE) for the staging of patient pancreatic tumours prior to treatment ((NICE) 2018).
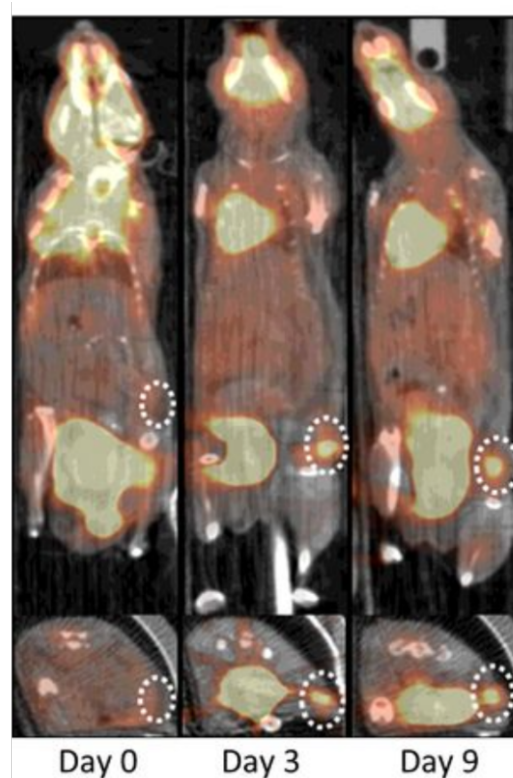
Figure 5-1 ^{18}F-FDG PET/CT to detect subcutaneous allograft model of PDAC.
Coronal (top pane) and transaxial (bottom pane) sections intersecting the centre of the allograft tumour (white dotted circle). Tumour was established subcutaneously in the right hind flank of female C57BL/6 mice, using KPC cells (B8484) that were derived from Kras[LSL-G12D/+]; Trp53[LSL-R172H/+]; Pdx1-Cre (KPC) tumours. Image adapted from Knight et al. (2017).

18F-FDG PET-CT is a highly sensitive and specific molecular imaging modality and is frequently used in the clinic to diagnose, stage and manage a range of cancers, including PDAC (Gallamini et al. 2014). As a radiolabelled glucose analogue, ^{18}F-FDG is used to image regions of high metabolism within the body. Glucose transporters (particularly GLUT-1 and GLUT-3) facilitate the cellular internalisation of ^{18}F-FDG, which is then phosphorylated by hexokinase in a similar manner to the processing of unlabelled glucose molecules (Knight et al. 2017).

Tumours are known to maintain vast increases in cell proliferation and malignant progression, regardless of blood supply, through the reprogramming of energy metabolism (Vaupel et al. 2019). First observed by Warburg in the early 20th Century, cancer cells selectively drive glycolysis, as opposed to the more efficient mitochondrial oxidative phosphorylation, under both normoxic and hypoxic conditions (Warburg 1931; Hanahan and Weinberg 2011). Tumour cells appear to compensate for the vastly reduced ATP-producing efficiency of aerobic glycolysis through the upregulation of 'high-affinity' GLUT-1 glucose transporters, thereby increasing cytoplasmic glucose uptake.

Due to increased glucose uptake, positron-emitting 18F-FDG glucose analogues rapidly accumulate and are phosphorylated within tumour cells (Laking and Price 2001; Knight et al. 2017). However, unlike glucose-6-phosphate, 18F-FDG-6-phosphate is retained within the cytoplasm due to its resistance to the downstream enzymatic processing of unlabelled glucose. Therefore, its retention in the cell directly corresponds to its isotopic decay rate and can be used as an accurate modality to non-invasively image tumours.

Despite its frequent use in the clinical management of PDAC, a thorough search of the literature indicated that cutting-edge PET/CT imaging is not regularly used to monitor PDAC GEMMs. Indeed, the only reference to the use of PET/CT to detect PDAC within a GEMM model is a study by Fendrich et al. who produced fairly diffuse, non-specific scans showing increased uptake of ^{18}F-FDG within the abdominal region of KPC mice which harboured pre-lesion PanINs and PDAC tumours *(Figure 5.2)* (Fendrich et al. 2011). Therefore, we initially focused on optimising high-resolution ^{18}F-FDG PET/CT imaging to accurately diagnose and longitudinally monitor PDAC tumour burden in the KPC model,

in collaboration with colleagues at the Wales Research & Diagnostic PET Imaging Centre (PETIC, Cardiff University). We then used this technology to monitor PDAC tumour response to both short- and long-term treatment with our novel small molecule cFLIP inhibitor, OH14.
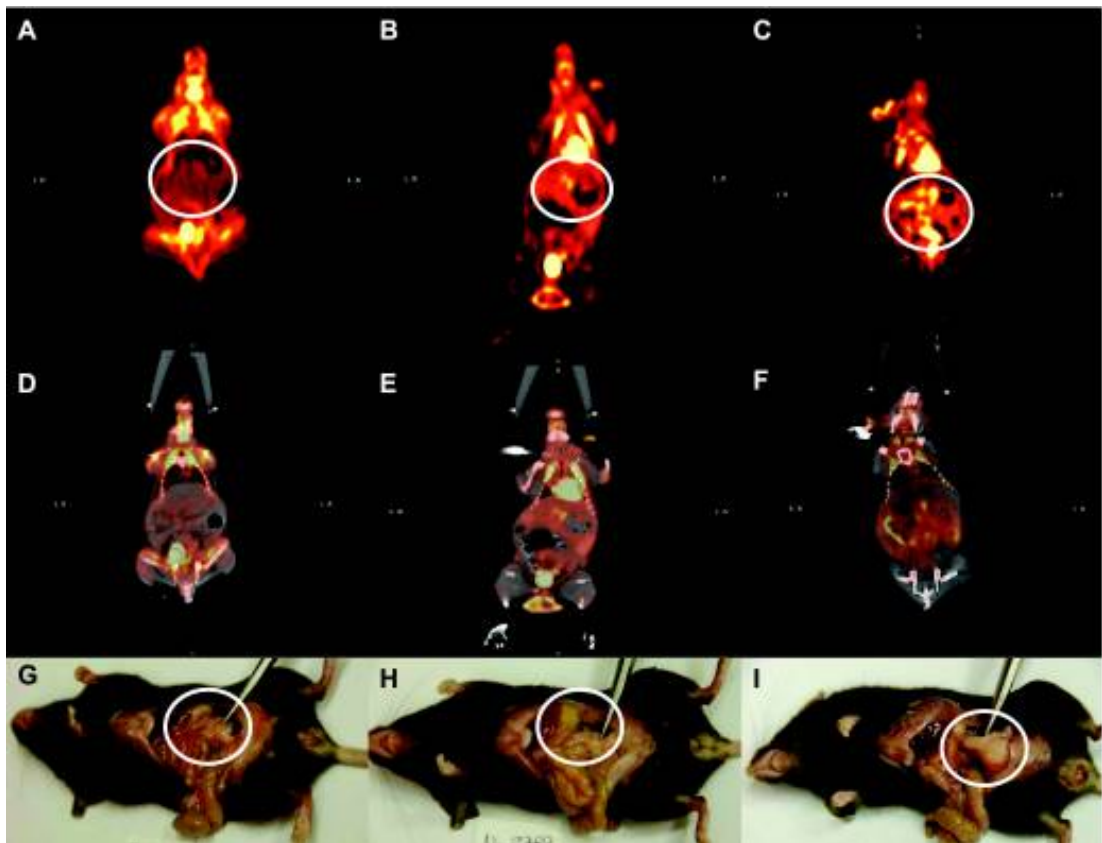
Figure 5-2 18F-FDG PET/CT to detect PDAC tumour in GEMMs of PDAC.
A-C PET scans. **D-F** Overlay of PET scan and CT acquired simultaneously. **G-I** Macroscopic evaluation of the pancreas and abdominal region (white circle). Pictures in one column were generated from an individual mouse. **A, D, G** Control wild-type mouse displaying normal abdominal FDG uptake without enrichment in pancreatic area. **B, E, H** LsL-Kras$^{G12D/+}$; Pdx1-Cre (KC) mice demonstrated a weak but visible signal in the pancreatic area (circle in B). After laparotomy, no tumour was palpable or visible macroscopically (circle in H). **C, F, I** All LsL-Kras$^{G12D/+}$; LsL-Trp$^{53R172H/+}$; Pdx1-Cre littermates showed a strong FDG uptake in the pancreatic area (circle in C), which correlates to large tumour burden following laparotomy. Image and data taken from Fendrich et al. (2011).

5.2 Chapter Aims

1. Determine the ability of ^{18}F-FDG PET/CT to accurately detect and monitor pancreatic tumour development within the KPC GEMM of PDAC.

2. Evaluate immediate response to small molecule cFLIP inhibition (OH14) within intact pancreatic tumours *in vivo*, using the classical KPC GEMM of PDAC.

3. Investigate the long-term effect of small molecule cFLIP inhibition (OH14) on intact pancreatic tumours *in vivo*, using the classical KPC GEMM of PDAC.

5.3   Results

5.3.1   18^F-FDG PET/CT enables the diagnosis of murine pancreatic tumours

As demonstrated in Section 4.2.1, the KPC (*Pdx1-Cre^{ERT2}; LSL-Kras$^{G12D/+}$; LSL-Trp53$^{R172H/+}$*) GEMM of PDAC was associated with a more reliable tumour incidence and latency than our novel KPF-FLIP model *(Figure 4.4)*. Indeed, 81% of all KPC mice developed tumours between 6 – 38 weeks post-induction of KRAS and p53 mutations. Conversely, only 11-20% of all KPF-FLIP mice developed tumours between 10 – 88 weeks of age, dependent upon the housing environment. As such, the KPC model proved to be more cost-effective and reliable for investigating the long-term response to cFLIP inhibition.

To longitudinally monitor PDAC development and response to treatment in the KPC model, a non-invasive imaging modality was required to detect abdominal tumours prior to the onset of symptoms. Although ultrasound imaging is frequently utilised, the technology was not available at the host university. Despite its minimal use in the literature for the detection of murine PDAC, high-resolution ^{18}F-FDG PET-CT imaging was readily available and, given its use in the clinical staging of human PDAC, presented a promising alternative to ultrasound.

Indeed, when combined with manual abdominal palpation, ^{18}F-FDG PET-CT was able to detect intact PDAC tumours in the KPC GEMM model, reporting tumour volumes as small as 20mm^3 (optimised using a cohort of n=9 KPC mice) *(Figure 5.3)*. Detection accuracy improved as tumours grew, as the increased signal compensated for the variable background ^{18}F-FDG (hereafter referred to as FDG for simplicity) uptake by the intestines. The generation of spatially informative, three-dimensional (3D) full-body scans facilitated the assessment of FDG distribution across all three anatomical planes (Sagittal, Coronal and Transverse; *Figure 5.3 B-D* respectively), whilst the reconstruction of two-dimensional (2D) pixels to create a computer-generated 3D maximum intensity projection (MIP) also enabled the visualisation of FDG uptake in a whole-body context *(Figure 5.3A).* MIPs of reconstructed PET/CT files are akin to those created when stitching together multiple z-stacks of conventional microscopy images. When mice reached an ethically determined endpoint, whereby tumour symptoms necessitated termination of the mouse for welfare reasons, a post-mortem laparotomy was conducted immediately following the final scan to confirm tumour burden *(Figure 5.3 E-F).*
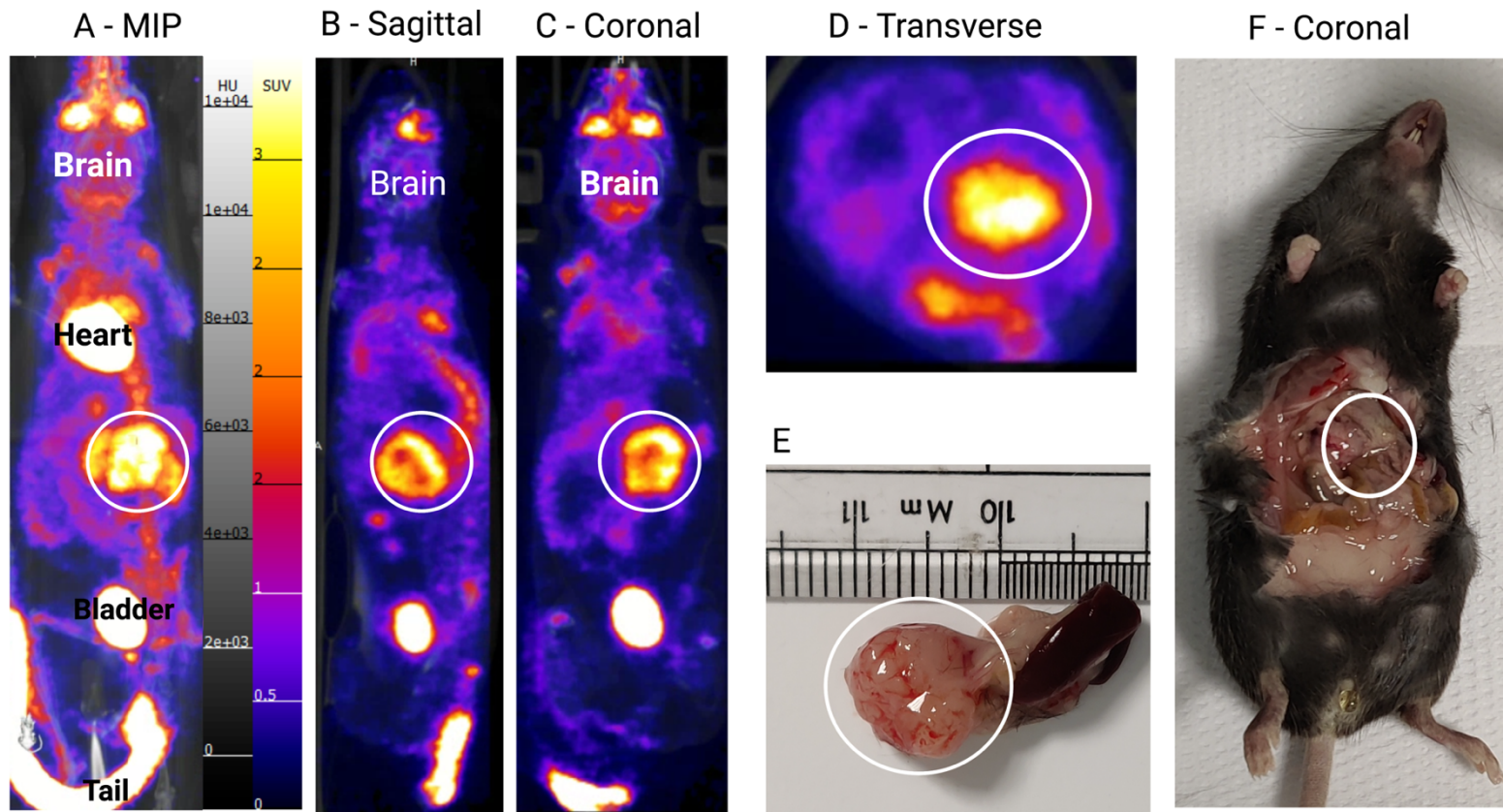
Figure 5-3 High resolution 18^F-FDG PET for the detection of PDAC tumours in the classical KPC (Pdx1-Cre; LSL-Kras$^{G12D/+}$; LSL-Trp53$^{R172H/+}$) GEMM of PDAC.

A Representative image of a computer-generated 3D Maximum intensity projection (MIP) created through the reconstruction of 2D pixels. **B-D** Sagittal, Coronal and Transverse sections intersecting the centre of the tumour (white circle). **F-E** Macroscopic evaluation of tumour burden following post-mortem laparotomy. All images from the same mouse, laparotomy (**F-E)** immediately followed PET/CT scan (**A-D**). Scale bar in **A** is applicable to each PET/CT image. Method was optimised using a total of 9 KPC mice. Figure created with Biorender.com. *PET/CT = positron emission tomography (PET)/computerised tomography (CT); PDAC = pancreatic ductal adenocarcinoma; GEMM = Genetically engineered mouse model; SUV = Specific Uptake Value; HU = Hounsfield Unit.*

5.3.2 18^F-FDG PET/CT enables longitudinal monitoring of PDAC growth

Following confirmation of tumour burden, ^{18}F-FDG PET/CT also facilitated the longitudinal monitoring of tumour growth. Sequential PET-CT scans to monitor tumour development occurred either until the ethically determined endpoint or until the maximum permissible number of scans (as determined by the Home Office Licence covering the study) were reached, as discussed in Section 2.4.5.5 *(Figure 5.4 A, C & E)*. Thresholding the PET image according to a pre-determined specific uptake value (SUV) of 3.48 and utilising the CT image to spatially contextualise FDG hotspots resulted in the creation of regions of interest (ROIs) and enabled the identification of tumours across sequential scans *(Figure 5.4 B, D & F)*. ROIs could then be used to generate data associated with FDG uptake within that region, including overall ROI volume, which was used as a surrogate, non-invasive readout of tumour volume *(Figure 5.4 G)*.

Due to variations in background FDG uptake by the intestines, sequential scanning and regular manual abdominal palpation were required to confirm the presence of a tumour, particularly at the early stages of disease progression when tumours were small (under 50mm^3). A total of 9 KPC mice underwent routine PET/CT tumour monitoring, with 6 PDAC tumours detected at an early enough stage to facilitate the longitudinal monitoring of tumour growth.

Sequential scanning of an individual mouse was sometimes needed to confirm tumour burden. Indeed, potentially ambiguous FDG hotspots that appeared in a similar abdominal region and increased in volume from one scan to the next, combined with a solid, rough-edged abdominal mass detected by manual palpation, would be used to confirm the diagnosis of PDAC and the mouse could therefore begin treatment. FDG hotspots which appeared more elongated than spherical were often not present on sequential scans and were not consistent with the detection of a palpable abdominal mass *(Figure 5.4 H-I).* Hotspots that failed to replicate on duplicate scans were therefore not designated as tumours.

PDAC

A   B   C   D   E   F

Day 0   Day 14   Day 28

No PDAC

G   H   I

+Tamoxifen (KRasG12D$^+$; p53$^-$)

Day 0   Day 14

Figure 5-4 High resolution ^{18}F-FDG PET for the longitudinal monitoring of PDAC tumours in the classical KPC (Pdx1-Cre; LSL-KrasG12D/+; LSL-Trp53R172H/+) GEMM of PDAC.
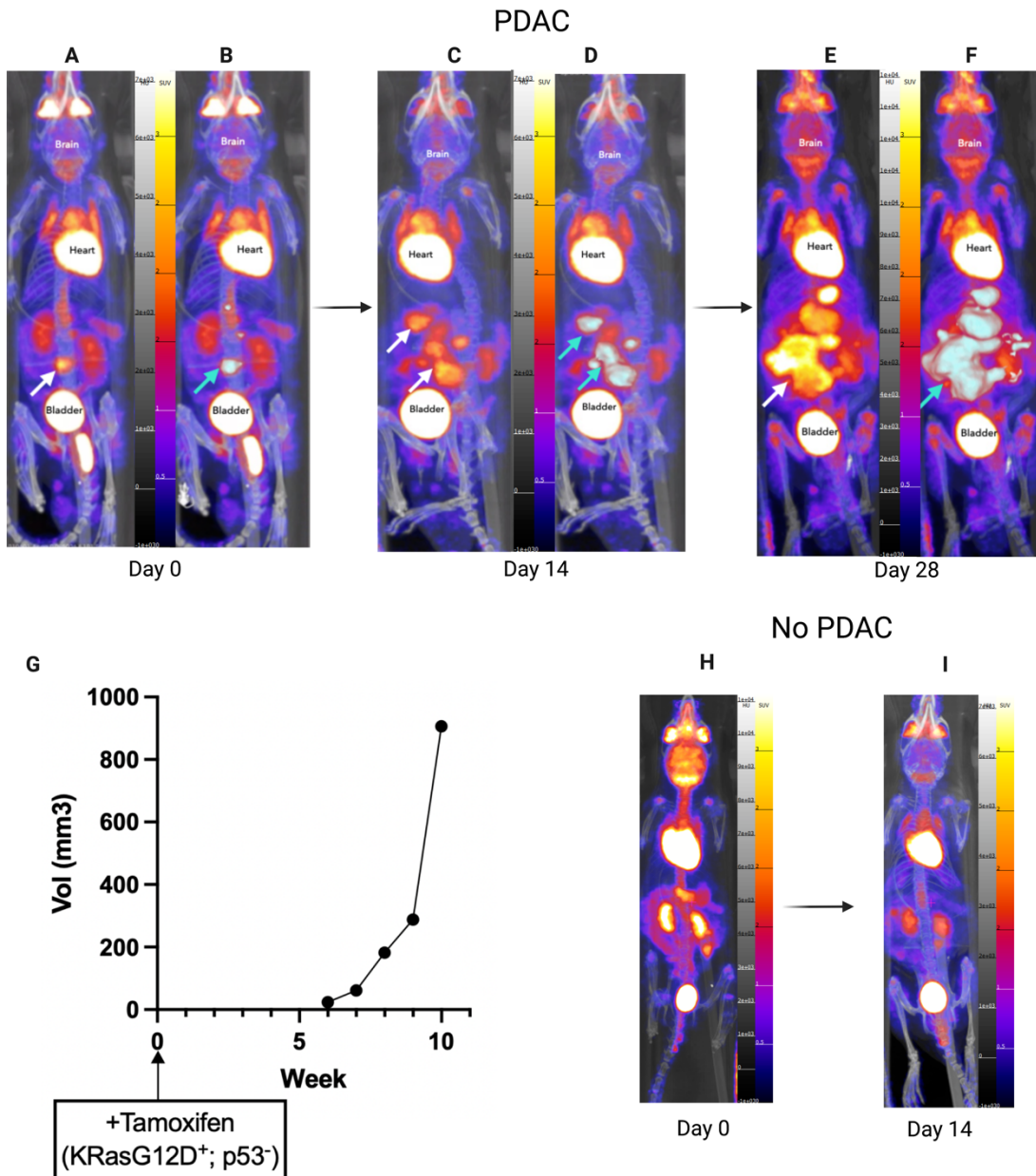
A-F & H-I Representative images of computer-generated 3D Maximum intensity projections (MIP) created through the reconstruction of 2D pixels. **A, C & E** PET/CT MIPs showing the change in abdominal FDG uptake throughout the longitudinal development of PDAC over time. Tumour burden indicated by white arrows. Day 0 = Day tumour first detected. **B, D & F** PET/CT MIPs with PDAC tumour ROIs highlighted (cyan computer-generated mask indicated by blue arrows). **G** Change in tumour ROI volume over time used as surrogate, non-invasive measurement of change in tumour volume over time. All images in **A-F** and volume data in **G** taken from the same mouse. **H-I** PET/CT MIPs showing variable background FDG uptake within the abdomen in the absence of tumour burden. Day 0 = First PET/CT scan. Figure created with Biorender.com. PET/CT imaging data processed using VivoQuant software (Invicro, USA). *ROI = Region of Interest; SUV = Specific Uptake Value; HU = Hounsfield Unit.*

151

5.3.3 Selecting ROI volume as the most appropriate quantification of PDAC growth

Several methods are available to quantify FDG accumulation in tumours, as represented by the SUV. Following the creation of tumour ROIs, as detailed in Section 2.4.5.6, it was possible to quantify the volume, mean SUV uptake, total SUV uptake (SUV Sum) and the SUV concentration of the 3x3x3 cube of voxels surrounding the voxel with the maximum SUV value in each ROI (SUV Max). Voxels refer to the 3D equivalent of a 2D pixel.

When considering PDAC tumour ROIs, change in volume and change in SUV sum were roughly identical, representing the tumour growth which was visible by eye over sequential scans *(Figure 5.5 G & I and A-F* respectively). Tumour SUV mean also increased compared to the baseline (no tumour), however, due to overlapping error bars, the average SUV of each tumour remained consistent across each sequential scan *(Figure 5.5 H)*. This suggests that glucose uptake by individual cells within the tumour was maintained at a relatively similar rate despite rapid tumour growth. An increase in tumour volume was associated with a corresponding increase in total FDG uptake (SUV sum), which was likely due to an increase in the number of viable tumour cells as opposed to an upregulation of glucose uptake at the cellular level.

Interestingly, the tumour SUV max increased along with tumour volume and SUV sum *(Figure 5.5 J)*. However, SUV max appeared to peak in the penultimate scan before decreasing by the final scan. This may reflect the slight reduction in exponential growth observed in the volumetric and SUV sum measurements, suggesting that individual tumour regions that were initially responsible for the highest level of glucose metabolism may be affected by limited blood and, therefore, glucose supply. This may reflect a common phenomenon associated with rapidly growing tumours, namely the formation of necrotic cores within the tumour due to insufficient blood vessel access.

Given the correlation between volume and overall FDG uptake within the ROI (SUV sum), it was decided to use ROI volume as a surrogate, non-invasive marker of PDAC tumour growth.

PDAC

Week 13
(tumour first detected)

Week 15

Week 18

G - Volume

H - SUV Mean

I - SUV Sum

J - SUV Max
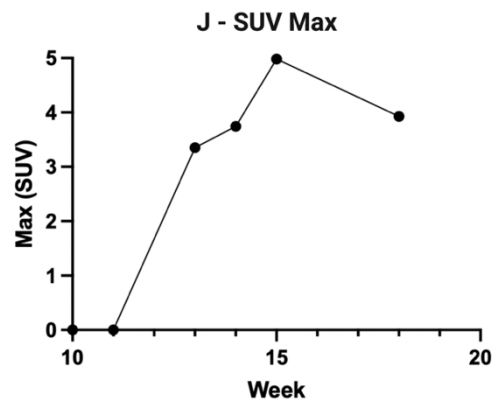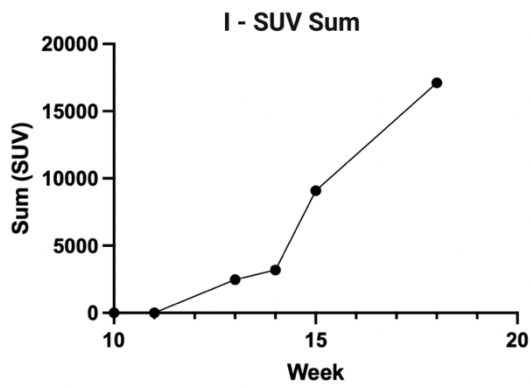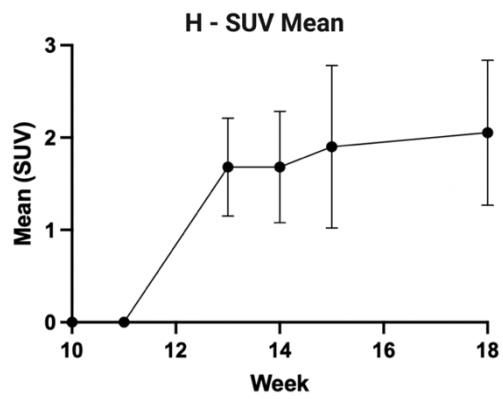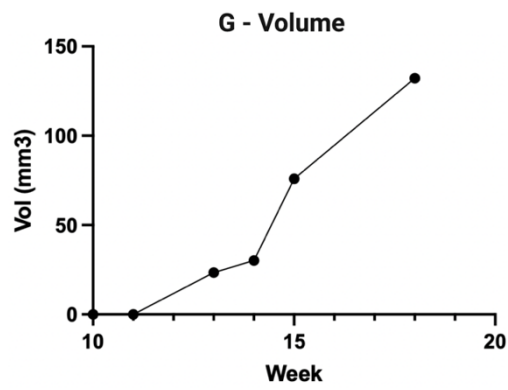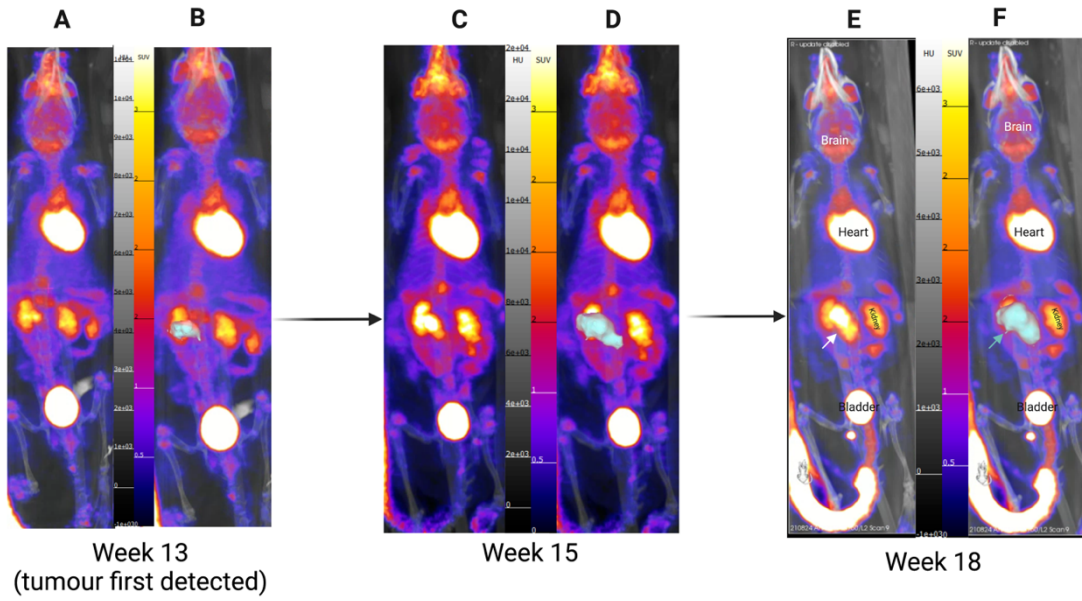
Figure 5-5 Representative data derived from high resolution 18F-FDG PET for the longitudinal monitoring of PDAC tumours in the classical KPC (Pdx1-Cre; LSL-KrasG12D/+; LSL-Trp53R172H/+) GEMM of PDAC.

A-F Representative images of computer-generated 3D Maximum intensity projections (MIP) created through the reconstruction of 2D pixels. **A, C & E** PET/CT MIPs showing the change in abdominal FDG uptake throughout the longitudinal development of PDAC (white arrow) over time. **B, D & F** PET/CT MIPs with PDAC tumour ROIs highlighted (cyan computer-generated mask indicated by blue arrows). All images in **A-F** and data in **G-J** taken from the same mouse. **G** Change in tumour ROI volume over time. **H** Change in average SUV (SUV mean +/- SD) of the tumour ROI over time. **I** Change in total SUV (SUV sum) of the tumour ROI over time. **J** Change in the SUV concentration of the 3x3x3 cube of voxels surrounding the voxel with the maximum SUV value of each tumour ROI (SUV Max) over time. Figure created with Biorender.com. PET/CT imaging data processed using VivoQuant software (Invicro, USA). *SUV = Standard Uptake Value (the tissue concentration of the 18F-FDG tracer as measured by the PET scanner when normalised to the total radioactivity injected and mouse body weight). Voxel = 3D equivalent of a 2D pixel. SD = Standard deviation of the mean.*

5.3.4 Adapting PET/CT image analysis to accurately monitor longitudinal tumour development

As demonstrated, sequential ^{18}F-FDG PET/CT imaging represents a sensitive, non-invasive tool to monitor PDAC development in the KPC GEMM model. However, due to the propensity for tumours to grow into the mobile abdominal cavity, it was discovered that certain tumours appeared to 'drift' within the abdomen over the course of several scans *(Figure 5.6 A-F)*. Although the movement was often minimal, it could impact accurate longitudinal monitoring of tumour development. To account for tumour movement and differences in the positioning of each mouse over sequential scans, it was necessary to develop a novel approach to monitor and analyse these tumours. Each consecutive 3D PET/CT scan of a single mouse was aligned according to the 3D positioning of the kidneys, as discussed in Section 2.4.5.7. This facilitated consistent positioning of the abdomen across sequential scans, as the retroperitoneal kidneys are known to be far less mobile than organs contained within the intraperitoneal cavity. This novel scan alignment approach enabled clear visualisation of tumour growth over a series of consecutive scans *(Figure 5.6 G)*.
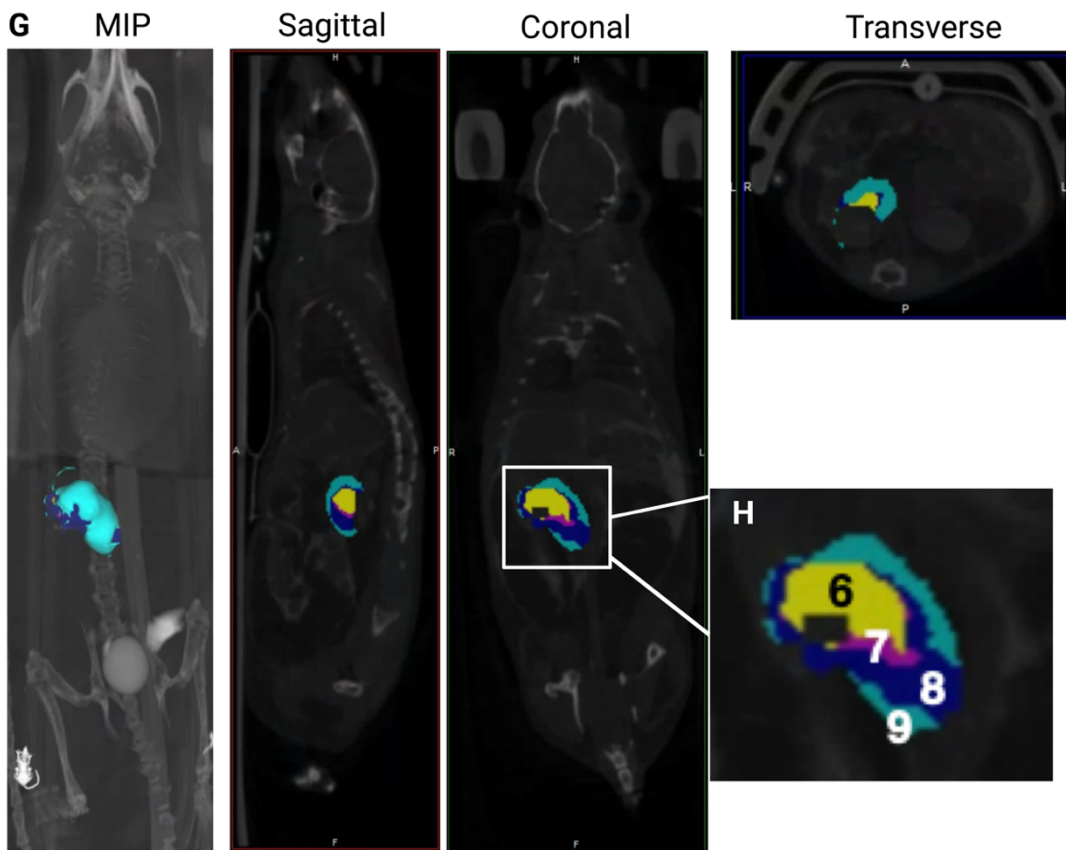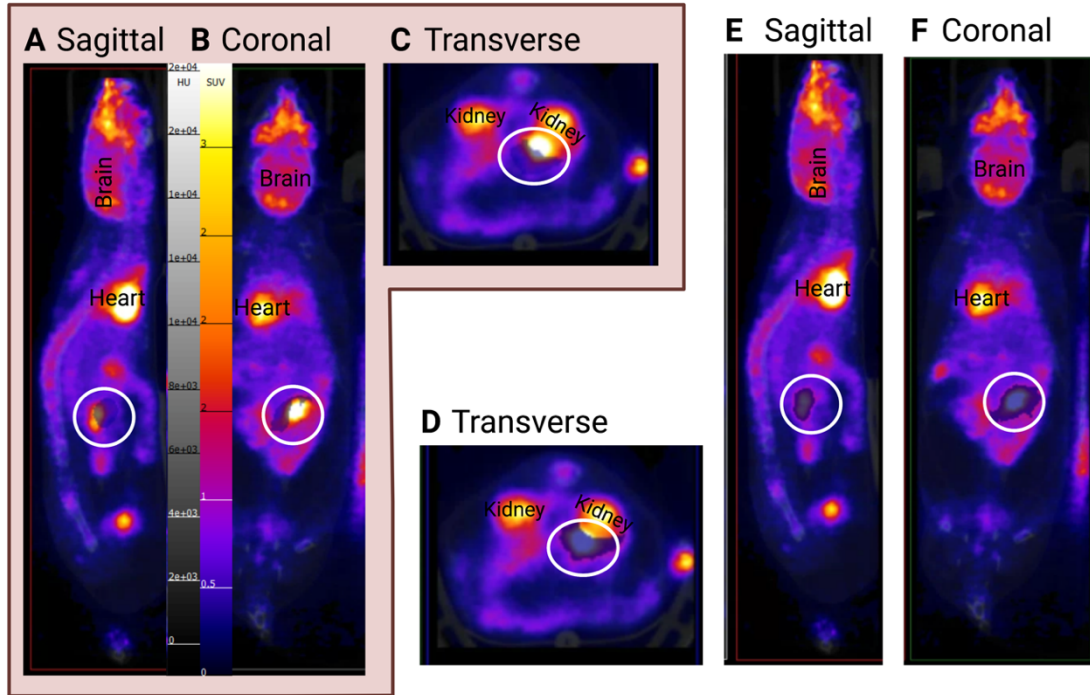
Figure 5-6 Representative high resolution ^{18}F-FDG PET/CT images demonstrating visualisation of longitudinal tumour growth over sequential scans following the application of a novel scan alignment method.
A-F Representative Sagittal, Coronal and Transverse sections intersecting the centre of the tumour (white circle). A 3D PET/CT scan was aligned to a baseline scan according to the positioning of the non-mobile, retroperitoneal kidneys. **A-C** ROI overlay (dark blue) depicts tumour localisation prior to scan alignment protocol. **D-F** ROI overlay highlights tumour localisation after scan alignment protocol. Scale bar in **A** is applicable to each PET/CT image in **A-F**. **G** Representative CT scan presented in MIP format and across all 3 anatomical planes, with sections intersecting the centre of the tumour ROIs. Tumour ROIs were taken from sequential scans (scan 6-9; **H**) of the same mouse, providing a visual method of monitoring tumour growth once each PET/CT scan was aligned to the same baseline scan, according to the positioning of the kidneys. ROI colours: Yellow = Scan 6; Magenta = Scan 7; Dark Blue = Scan 8; Cyan = Scan 9. Figure created with Biorender.com. PET/CT imaging data processed using VivoQuant software (Invicro, USA). *ROI = Region of Interest; MIP = 3D Maximum intensity projections*

5.3.5 Long-term small molecule cFLIP inhibition (OH14) does not significantly impact tumour volume but does cause a significant increase in apoptosis and necrosis in the classical KPC GEMM of PDAC

Following PDAC tumour diagnosis (minimum tumour volume = 20mm^3), daily intraperitoneal injection of the novel small molecule cFLIP inhibitor (OH14) was performed until the ethically determined endpoint for PDAC tumour burden was achieved, as described in Section 2.4.3.1. The timing of OH14 administration was standardised to be as close as possible to every 24-hours in each mouse. Previous analysis of OH14-treated animals without tumour burden had determined that the compound was well tolerated with no adverse effects observed over several weeks of administration (Clarkson, unpublished). No additional adverse effects were observed from OH14 administration of tumour-bearing mice. No significant difference was observed in KPC mouse weight when comparing OH14- and DMSO-treated mice over the course of treatment (***Figure 5.7 A).*** Tumour-bearing mice treated with long-term OH14 lost roughly 20% of body weight over the final few days of treatment. However, a similar trend was also observed in the DMSO-treated cohort, likely reflecting the drastic weight loss associated with PDAC tumour side effects as opposed to adverse reactions to long-term OH14 treatment.

Tumour response to long-term OH14 treatment was non-invasively monitored in the KPC GEMM, using the ^{18}F-FDG PET/CT imaging approach detailed in the preceding sections of this chapter. In a similar manner to long-term cFLIP deletion in the KPF-FLIP model, no significant difference in growth was observed in tumours that received long-term, daily OH14 treatment until endpoint, when compared with those treated with the DMSO vehicle ***(Figure 5.7 B)***.
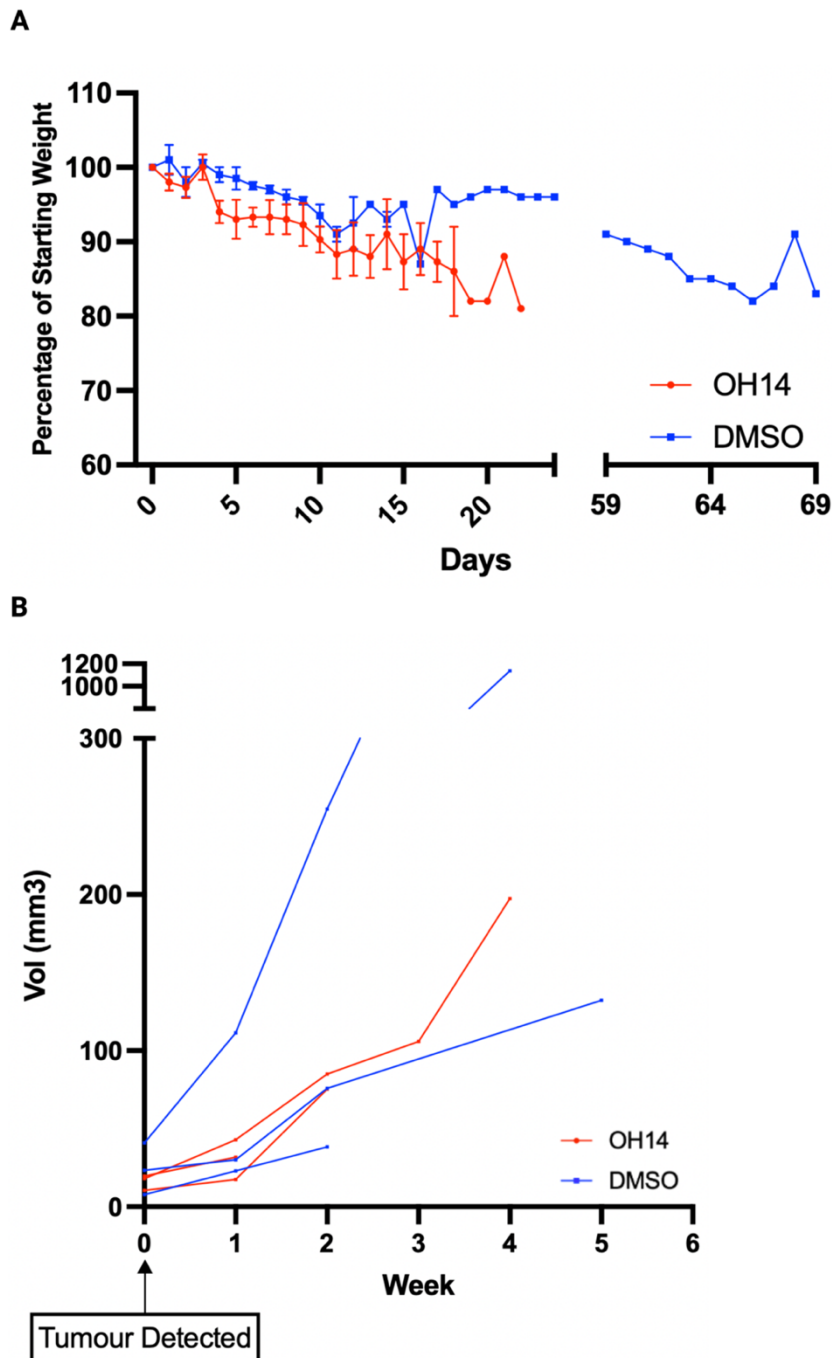
Figure 5-7 Long term treatment effects of novel cFLIP small molecule inhibitor (OH14) when used to treat PDAC tumours in the classical KPC (Pdx1-Cre; LSL-Kras$^{G12D/+}$; LSL-Trp53$^{R172H/+}$) GEMM of PDAC.
A Weight change of mice when given daily doses of either OH14 or DMSO control until the ethically determined endpoint. Each datapoint represents the mean weight change (+/- SEM) of 3 different tumour-bearing mice per treatment condition when normalised to weight at the beginning of treatment. **B** Change in PDAC tumour volume as measured by sequential 18F-FDG PET/CT scans, which were thresholded to identify and monitor the tumour region of interest. Each datapoint represents tumour volume of one independent mouse that was receiving daily doses of either OH14 (n=3) or DMSO control (n=3) until endpoint. PET/CT imaging data processed using VivoQuant software (Invicro, USA).

To investigate the impact of long-term OH14 treatment on levels of tumour apoptosis, KPC PDAC tumours were harvested for histological analysis following long-term OH14 administration. The apoptotic response was quantified according to the proportion of cleaved executioner caspase-3 (CC3) positive cells in FFPE tissue sections, as detailed in Section 2.4.7. Despite having no observable impact on tumour volume over time, long-term OH14 treatment did significantly increase the percentage of CC3-positive cells within treated tumours *(Figure 5.8 A)*. As in Section 4.2.3, the percentage of morphologically distinct necrotic tumour cells was also quantified to determine the impact of long-term OH14 on necrosis in PDAC. Daily OH14 treatment was also found to result in a significantly elevated percentage of morphologically-distinct necrotic tumour cells when compared to DMSO vehicle controls *(Figure 5.8 B).*
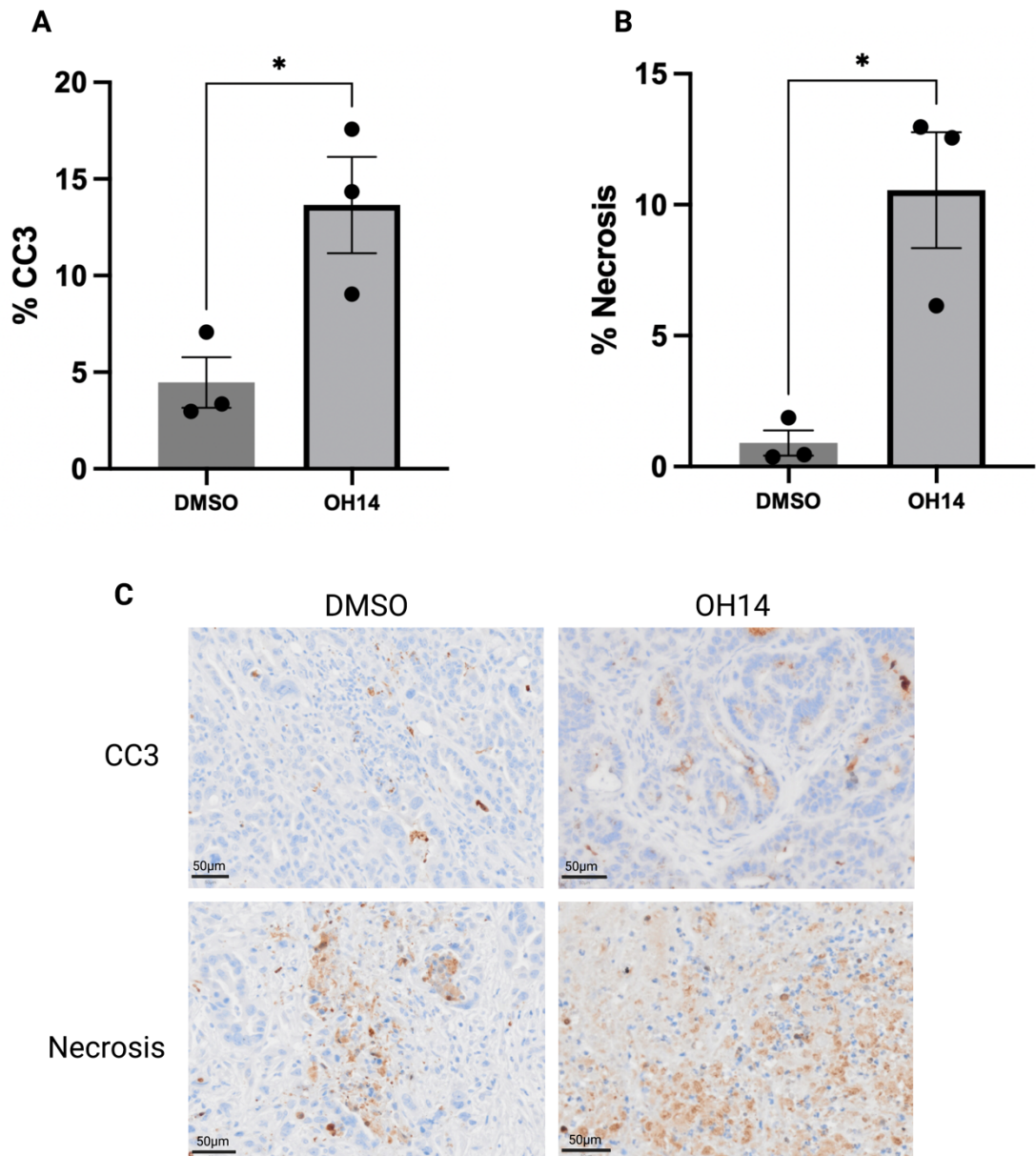
Figure 5-7 Histological quantification of apoptotic (A) and necrotic (B) levels following long term treatment of tumours with the novel small molecule cFLIP inhibitor, OH14, or DMSO control in the KPC (Pdx1-Cre; LSL-Kras$^{G12D/+}$; LSL-Trp53$^{R172H/+}$) GEMM of PDAC.
A Proportion of CC3 positive tumour cells normalised to total number of tumour cells used as a measure of tumour apoptosis. **B** Proportion of morphologically distinct necrotic tumour cells normalised to total number of tumour cells used as measure of necrosis. **C** Representative high power IHC images of PDAC tumuors stained for CC3 (brown cells) depicting regions of apoptosis and necrosis. Long term treatment schedule involved daily intraperitoneal injections of 80mg/kg OH14 or DMSO control until the ethically determined endpoint. Tumours were then harvested, and histological scoring and analysis was performed on FFPE tissue sections using QuPath software (Bankhead et al. 2017). Data was analysed using GraphPad Prism 9 for Mac (California, USA). Error bars represent the mean (+/- SEM) from 3 mice per treatment arm. Statistical difference between treatment arms calculated using an unpaired t-test with Welch's correction (* = $p<0.05$). *CC3 = Cleaved Caspase-3.*

5.3.6 Short-term small molecule cFLIP inhibition (OH14) does not significantly impact apoptosis and necrosis in classical KPC GEMM of PDAC

As discussed in Section 4.2.3, the initiation of TRAIL-induced apoptosis results in rapid cleavage of downstream caspase molecules, including CC3. Therefore, we sought to investigate the immediate apoptotic and necrotic response to OH14 using the KPC GEMM of PDAC. Once tumour burden was confirmed, mice received three doses of OH14 or DMSO vehicle control over a 48-hour period, before tumours were harvested for histological analysis. Unlike long-term treatment, this short-term OH14 treatment schedule caused no significant difference in levels of tumour apoptosis or necrosis.
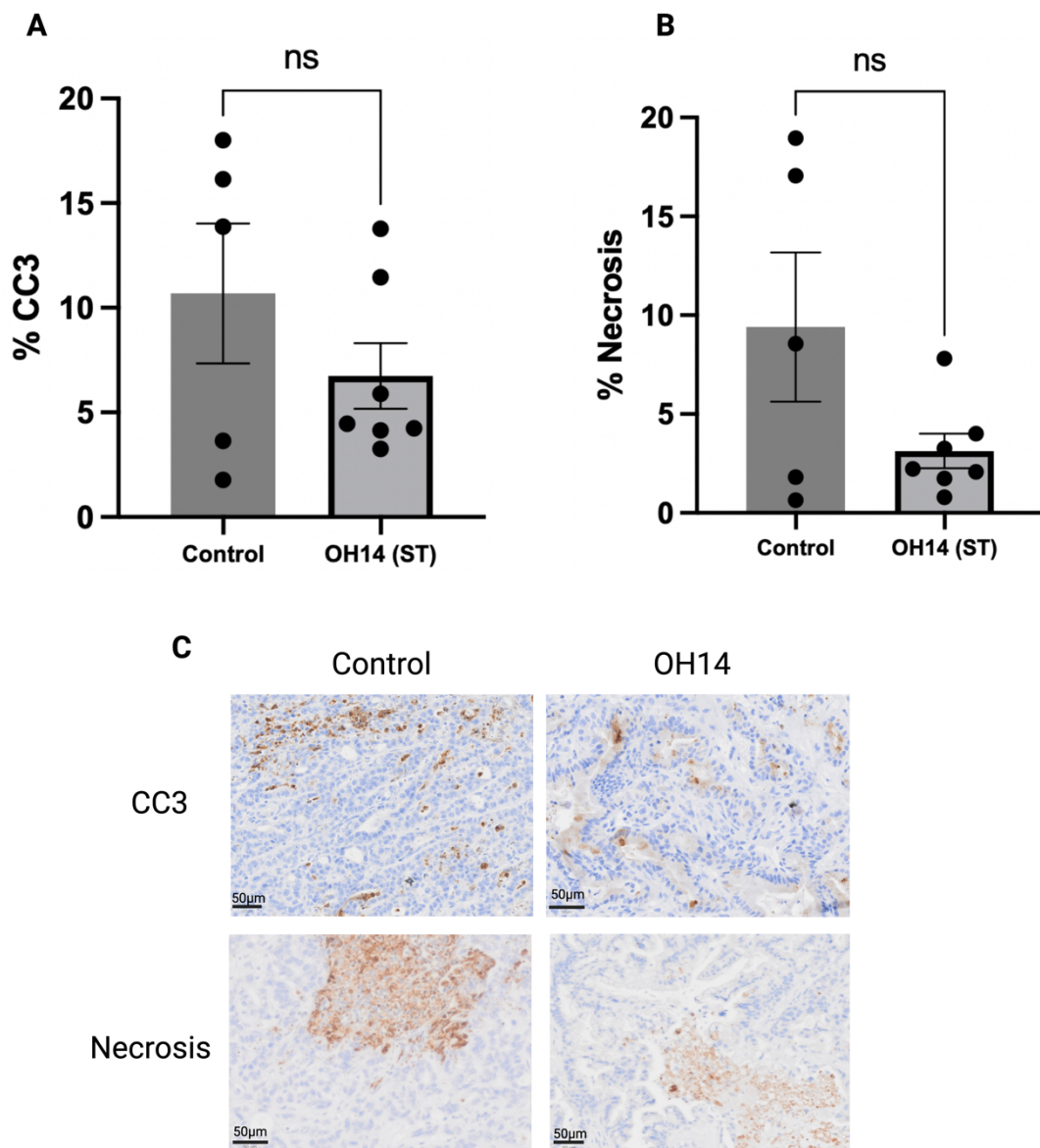
Figure 5-8 Histological quantification of apoptotic (A) and necrotic (B) levels following short term treatment of tumours with the novel small molecule cFLIP inhibitor, OH14, or DMSO control in the KPC (Pdx1-Cre; LSL-Kras$^{G12D/+}$; LSL-Trp53$^{R172H/+}$) GEMM of PDAC.

A Proportion of CC3 positive tumour cells normalised to total number of tumour cells used as a measure of tumour apoptosis. **B** Proportion of morphologically distinct necrotic tumour cells normalised to total number of tumour cells used as measure of necrosis. **C** Representative high power IHC images of PDAC tumuors stained for CC3 (brown cells) depicting regions of apoptosis and necrosis. Short term treatment schedule involved 3x daily intraperitoneal injections of 80mg/kg OH14 or DMSO control for a total of 48 hours. Tumours were then harvested, and histological scoring and analysis was performed on FFPE tissue sections using QuPath software (Bankhead et al. 2017) and data was analysed using GraphPad Prism 9 for Mac (California, USA). Error bars represent the mean (+/- SEM) from a minimum of 5 mice per treatment arm. Statistical difference between treatment arms calculated using an unpaired t-test with Welch's correction (* = p<0.05). *CC3 = Cleaved Caspase-3. FFPE = formalin-fixed paraffin embedded*

5.4   Discussion

This chapter sought to establish the potential of a novel small molecule cFLIP inhibitor (OH14) to re-activate apoptosis in the classical KPC GEMM of PDAC. Response of tumours to long-term treatment schedules in PDAC GEMMs is conventionally monitored with non-invasive ultrasound imaging modalities (Gopinathan et al. 2015). However, due to the absence of this technology at the host university, it was first necessary to optimise an alternative non-invasive tumour monitoring methodology to detect tumours prior to symptom manifestation. This optimisation facilitated long-term treatment schedules by enabling early diagnosis of tumours, prior to symptom manifestation.

Despite its extremely limited use in the literature, high-resolution ^{18}F-FDG PET/CT imaging proved capable of detecting and longitudinally monitoring PDAC tumours in our GEMM *(Figure 5.3)*. This data supports the findings of Knight et al., who demonstrated the ability of ^{18}F-FDG to detect sub-cutaneous pancreatic tumour allografts (Knight et al. 2017). PDAC tumours were identified according to the uptake of ^{18}F-FDG tracer, using spatially informative 3D images to delineate the general intestinal background from solid, spherical tumours *(Figure 5.4)*. This was assisted by a novel image analysis approach, developed in collaboration with colleagues at PETIC, whereby each consecutive 3D image was aligned according to the positioning of the immobile, retroperitoneal kidneys *(Figure 5.6).* Once each image was aligned, ^{18}F-FDG PET/CT imaging generated a range of informative data, facilitating the monitoring of tumour burden and growth dynamics over a longitudinal sequence of scans *(Figure 5.5 G-J).* Tumour region of interest (ROI) volume was selected as a surrogate marker of tumour volume, as this measure best reflected the visible change in tumour burden which could be seen across consecutive scans *(Figure 5.5 A-F)*.

However, the use of ^{18}F-FDG PET/CT imaging to detect and monitor PDAC tumours in GEMMs was associated with important limitations that do not impact the classical ultrasound imaging modality. Home Office-mandated regulations exerted a major influence on the length of treatment schedules as a single mouse could only receive a maximum of nine PET/CT scans within its lifetime, as detailed in Section 2.4.5.5. The

guidelines are in place due to the imaging protocol, which involves anaesthetising each mouse for at least two hours. However, these regulations impaired the ability to schedule routine diagnostic scans and placed greater importance on less accurate manual abdominal palpation to detect potential tumours. Manual abdominal palpation occurred at least twice a week, with potential tumours (palpable during at least two sessions) investigated with a follow-up PET/CT scan. Therefore, an unavoidable delay often occurred between the initial detection of tumour burden and the start of treatment.

An additional complication arose due to variable intestinal uptake of the ^{18}F-FDG tracer. As demonstrated in Section 5.3.2, certain intestinal uptake could resemble the appearance of small PDAC tumours. This resulted in the need for an additional PET/CT scan, often within 5-7 days of the first scan, to determine whether the region was still present and growing before mice could begin treatment. Although this did not impact every mouse, it presented a further limitation given the need for a long-term treatment window against the background of often rapidly developing PDAC-associated symptoms. To circumvent these PET/CT-associated limitations, classical ultrasound imaging provides a more robust method for the diagnosis of tumours in pre-clinical studies involving GEMMs of PDAC. However, we were able to demonstrate the ability of ^{18}F-FDG PET/CT to detect and accurately monitor the volume and metabolic activity of tumours should ultrasound technology be unavailable, or, as an informative, high-resolution imaging tool for use alongside diagnostic ultrasound methods. Minimal variability was observed between the volume reported via ^{18}F-FDG PET/CT and the actual tumour volume which was measured post mortem immediately following the final scan.

Following imaging optimisation, tumour-bearing KPC mice were separated into two cohorts. One cohort received long-term OH14 (or DMSO vehicle) treatment, whereby the drug was administered daily until symptom manifestation necessitated termination. The other received short-term OH14 (or vehicle) treatment, whereby three doses of the drug were administered over the course of 48 hours. ^{18}F-FDG PET/CT imaging facilitated each cohort's diagnosis and the longitudinal monitoring of tumours.

Whilst long-term OH14 treatment was reasonably well-tolerated, weight loss was observed as mice approached their respective ethically determined endpoints *(Figure 5.7 A)*. However, a similar level of weight loss was also recorded in the DMSO-treated cohort. This likely reflects a characteristic symptom of PDAC that is seen in roughly 70% of all patients upon cancer diagnosis and whose incidence increases with disease progression, namely cancer-induced cachexia (Dewys et al. 1980; Fearon et al. 2011; Talbert et al. 2019). As a wasting syndrome, cancer cachexia results in unintentional and irreversible weight loss due to skeletal muscle depletion. Equally, repeated exposure to anaesthesia during the course of longitudinal PET/CT imaging may also underlie the general loss in weight observed over time. To truly delineate the impact of cachexia on mouse weight loss following long-term OH14, it would be pertinent to investigate the weight of key tissues (including the heart, skeletal muscle, and adipose tissue) in treated compared to control mice, however, previous studies of OH14-treated animals determined little or no adverse effects associated with long-term treatment (Clarkson, unpublished). An additional, control arm involving KPC mice which receive no anaesthesia may also be pertinent to investigate any potential impact of repeated anaesthetic exposure on weight loss. However, such work would be complicated due to the difficulty in identifying the time at which tumours arise in the absence of diagnostic, non-invasive imaging.

Interestingly, cancer cachexia can negatively influence patient tolerance to anti-cancer therapies and severely impact survival outcomes (Fearon et al. 2011). Therefore, it is possible that cachexia may have contributed to the non-significant impact of long-term OH14 treatment on tumour volume over time *(Figure 5.7 B)*. This would suggest that combining cFLIP inhibition with strategies to minimise or relieve cachexia may facilitate longer treatment terms, giving the therapeutic approach more time to exert a visible impact on the tumour burden.

Homozygous deletion of cFLIP in our novel KPF-FLIP GEMM exerted an equally non-significant impact on PDAC tumour volume in the long term, as detailed in Section 4.3.4. Unfortunately, it was not possible to histologically assess the tumour tissue from the long-term KPF-FLIP study within the scope of this project. However, it was possible to

histologically assess the tumours harvested from the OH14 study conducted in the KPC GEMM within the time constraints of this project. Interestingly, despite the minimal impact on tumour volume, long-term OH14 treatment did appear to significantly increase levels of both apoptosis and necrosis in PDAC tumours *(Figure 5.8 A-B)*. Conversely, tumours that received short-term OH14 treatment showed no significant difference in levels of apoptosis and necrosis when compared to DMSO-treated controls *(Figure 5.9 A-B)*. This would suggest that, as hypothesised, cFLIP inhibition (via OH14 treatment) may be sufficient to increase levels of apoptosis within PDAC tumour cells due to the targeted inhibition of cFLIP's crucial anti-apoptotic function. In turn, it is possible that such a rapid increase in cell death also lead to increased levels of necrosis, as the quantity of dying cells exceeded phagocytic capacity, thereby resulting in necrotic cell rupture. However, FLIPi alone in this setting did not appear sufficient to completely eliminate tumour burden and prevent tumour growth, thereby suggesting that it may be necessary to explore OH14 in combination with alternative tumour-targeting methods, for example standard-of-care chemotherapy.

Alternatively, it is possible that the rapid development of cachexia, amongst other PDAC tumour symptoms, may underlie the minimal impact of long-term OH14 on tumour volume, despite its association with a significant increase in histological levels of cell death. This supports the implementation of a strategy to prolong mouse survival by minimising tumour symptoms, such as cachexia.

Mice were randomly allocated to either the short- or long-term treatment cohorts whenever possible. However, certain subjects had to be assigned to the short-term cohort, if tumour symptom manifestation at diagnosis suggested that they were unlikely to survive longer-term treatment. Overall, this 'enforced' selection bias resulted in the majority of 'short-term treatment' tumours beginning treatment at a far more advanced, aggressive stage than most tumours included in the long-term treatment cohort. Such a difference in initial severity complicates efforts to compare responses to short-term OH14 treatment with responses to long-term OH14 treatment. It may even underlie the poor response of PDAC tumours to short-term OH14 treatment, as more advanced, desmoplastic tumours are notoriously more difficult to treat (Erkan et al.

2012). An equally valid limitation to the 'short-term' cohort is the 48-hour treatment window, which may have been inadequate for determining the immediate response to OH14 treatment. Indeed, any OH14-induced increases in apoptotic tumour cells may have been cleared within the 48-hour window, due to the rapid cleavage of caspases and the phagocytic clearance of apoptotic cells, as detailed in Section 1.4.1. Conversely, given the significantly higher levels of apoptotic and necrotic cells following long-term OH14 treatment, three OH14 doses in a short timeframe may not have been sufficient and it may have been necessary to extend the dosing window to potentially detect a cumulative effect.

5.5   Conclusions and Future Work

To conclude, the results detailed in this chapter demonstrate the ability of ^{18}F-FDG PET/CT imaging to detect and monitor PDAC tumours in the KPC GEMM. Due to the uptake of ^{18}F-FDG by tumour cells in a similar manner to unlabelled glucose, this modality also provides insight into the underlying metabolic levels of the tumour. However, experiments discussed in this chapter also highlighted key limitations associated with this methodology compared to conventional ultrasound imaging, particularly the inability to scan an individual mouse more than nine times during its lifetime. Overall, PET/CT imaging provides a valid alternative to monitor and conduct preclinical studies involving GEMMs of PDAC, however, ultrasound offers more flexibility and a more tolerable approach for the animals. Indeed, ultrasound imaging involves 15-20 minutes of anaesthesia instead of the 2 hours associated with the ^{18}F-FDG PET/CT modality. Although PET/CT presents a viable option, future preclinical studies involving PDAC GEMMs would benefit from the inclusion of ultrasound imaging to accelerate diagnosis and facilitate longer-term monitoring.

However, the optimisation of ^{18}F-PET/CT imaging did enable the long-term monitoring of PDAC response to FLIPi using the KPC GEMM. cFLIP was targeted using a novel small molecule inhibitor (OH14) which has previously been shown to directly inhibit the anti-apoptotic role of cFLIP in the canonical TRAIL-induced signalling pathway (Clarkson lab, unpublished). Of note, long-term OH14 treatment did not significantly impact tumour volume over time in the KPC GEMM of PDAC. However, significantly elevated levels of

apoptosis and necrosis were detected at the histological level in long-term OH14-treated tumours at the ethically determined endpoint. Mice in both the OH14- and DMSO-treated cohorts underwent gradual, severe weight loss towards the end of the treatment course, potentially reflecting the development of cancer cachexia. Therefore, future studies would benefit from additional approaches to combat cachexia in long-term cohorts, limiting its potential influence over response to therapy. Finally, no significant difference in tumour apoptosis or necrosis was observed following short-term OH14 treatment.

As with the experiments detailed in Chapter 4 of this thesis, additional subjects and time points are required to elucidate the therapeutic potential of FLIPi in PDAC. However, despite their respective limitations, the findings of this Chapter suggest a potential benefit in the use of FLIPi to induce apoptosis in KRAS-mutant PDAC cells. A combination approach with additional therapeutic arms and/or better management of cachexia symptoms may be required to exert an impact on tumour volume and overall survival.

6   Final Discussion

PDAC is a deadly malignancy of the exocrine pancreas. Accounting for over 90% of all pancreatic cancer cases, it is unfortunately associated with a dismal 5-year survival rate of less than 10% (Ferlay et al. 2018; Siegel et al. 2020). Despite ongoing advances in our understanding of underlying PDAC biology, the current standard-of-care chemotherapy regime (FOLFIRONOX; combining 5-fluorouracil (5-FU), leucovorin, irinotecan, and oxaliplatin) only results in median survival of 10-12 months if patients aren't eligible for potentially curative surgical resection (Cloyd et al. 2017).

However, improvements in the molecular characterisation and stratification of PDAC tumours have revealed promising targets in the drive to develop more personalised, specific therapeutic approaches. The KRAS GTPase protein represents a particularly promising therapeutic target, due to its oncogenic mutation in over 90% of all human PDAC tumours (Grimont et al. 2022). Whilst the direct targeting of mutant KRAS isoforms continues to progress towards the clinic, only inhibitors targeting the KRAS G12C isoform, which is rarely associated with PDAC, have been granted clinical FDA approval to date (Skoulidis et al. 2021). Due to the inherent heterogeneity and plasticity of PDAC, alternative methods to exploit the prevalence of mutant KRAS will likely also be necessary for effective treatment.

Previous research has demonstrated the role of mutant KRAS in driving non-canonical, malignant TRAIL-mediated signalling in PDAC (von Karstedt et al. 2015). Whilst canonical TRAIL signalling leads to apoptosis, non-canonical signalling appears to enhance the aggression and metastatic capacity of tumour cells that are resistant to TRAIL-induced apoptosis. Indeed, a study by Johnston et al demonstrated that PDAC tumours expressing high levels of TRAIL receptor DR5 were associated with reduced disease-free survival (Johnston et al. 2020). The same study also highlighted a positive correlation between DR5 expression level and the expression of the anti-apoptotic protein cFLIP. Functioning at the beginning of the TRAIL-induced apoptotic cascade, cFLIP represents a key inhibitor of canonical TRAIL signalling. In fact, PDAC tumours expressing high levels of cFLIP have also been associated with significantly reduced disease-free survival

(Johnston et al. 2020). Underlining its importance as a potential therapeutic target in PDAC, a study by Haag et al. successfully used cFLIP inhibition (FLIPi) to sensitise a small panel of established PDAC cell lines to TRAIL-induced apoptosis *in vitro* (Haag et al. 2011).

On the basis that KRAS-mutant PDAC tumours may rely on cFLIP to facilitate the malignant driving of non-canonical TRAIL signalling (Haag et al. 2011; von Karstedt et al. 2015; Johnston et al. 2020), the experiments in Chapter 3 of this thesis firstly sought to establish the clinical relevance of this hypothesis and, subsequently, interrogate its potential *in vitro*.

Highlighting its potential as a therapeutic target, significantly increased cFLIP expression was detected in patient tumours at almost every pathological stage of PDAC, when compared to normal pancreatic samples. Tumours with high levels of cFLIP expression were also associated with significantly reduced disease-free but not overall survival. Together, these findings supported those reported by Johnston et al. and suggested that cFLIP may be more involved in therapeutic resistance and disease relapse as opposed to overall tumour malignancy (Johnston et al. 2020). Equally, expression levels of both TRAIL death receptors (DR4 and DR5) were also elevated in the tumour vs normal setting, with tumours that expressed high levels of TRAIL and both death receptors associated with significantly reduced disease-free and overall survival.

Having established the prognostic relevance of our approach, its potential was then assessed in a range of *in vitro* settings. Although each KRAS-mutant PDAC cell line possessed minimal intrinsic sensitivity to exogenous TRAIL supplementation, the combination of FLIPi with exogenous TRAIL resulted in a significant increase in apoptosis in all bar one of the established cell lines. Whilst von Karstedt et al. had reported constitutive TRAIL signalling in one PDAC cell line (Panc Tu I, not included in our study) and in KRAS-mutant PDAC tumours *in vivo*, our findings and those of Haag et al. suggest that this pathway may not be constitutively driven *in vitro*, due to the requirement for exogenous TRAIL supplementation (Haag et al. 2011; von Karstedt et al. 2015). Alternatively, a low level of endogenous TRAIL-R signalling *in vitro* may be sufficient to

drive the non-canonical signalling pathway but not canonical apoptosis *in vitro*. Further investigation into the activity of non-canonical TRAIL-R signalling in our cell line panel is therefore required.

However, once KRAS-mutant PDAC cells were stimulated with exogenous TRAIL, FLIPi was required to sensitise the inherently TRAIL-resistant panel to TRAIL-induced apoptosis, thereby supporting the use of FLIPi as a therapeutic approach to target KRAS mutant PDAC cells. Demonstrating the importance of mutant KRAS in non-canonical TRAIL-R signalling, the only KRAS-WT cell line included in the panel, BxPC3, showed intrinsic sensitivity to TRAIL-induced apoptosis. This is consistent with the hypothesis that cFLIP-mediated suppression of the canonical TRAIL-R pathway is only utilised by KRAS-mutant tumour cells. However, even in the BxPC3 line, sensitivity to TRAIL-induced apoptosis was enhanced following FLIPi, suggesting that FLIPi may prove promising for the treatment of the rarer KRAS-WT PDAC subtypes, providing sufficient TRAIL is available.

Despite an investigation into potential biomarkers of response to FLIPi, this project did not identify a strong candidate gene that would enable the stratification of cell lines. However, it should be noted that only biomarker RNA expression levels were considered. Given that RNA expression does not necessarily correlate with protein expression or activity, an in-depth exploration into biomarker expression and localisation at the protein level, using both histological and western blot techniques to determine biomarker expression levels before and after FLIPi+TRAIL, might aid in the identification of tumour sub-populations that are most likely to respond to this therapeutic approach. High-throughput sequencing of each cell line's transcriptome via RNA sequencing may also prove valuable in comparing cell lines before and following treatment to rapidly assess the expression of a huge range of potential biomarkers, selecting the most promising candidates for further interrogation at the protein-level (Yang et al. 2020). Overall, further work is needed to truly delineate the biological mechanisms underlying pancreatic tumour cell response to FLIPi.

To investigate the response of PDAC tumours to FLIPi *in vivo*, a novel *Pdx1-Flp; FSF-Kras$^{G12D/+}$; Trp53$^{frt/+}$; R26$^{CAG-FSF-CreERT2}$; CFLAR$^{fl/fl}$* (KPF-FLIP) GEMM was established following collaboration with the Morton lab (CRUK Beatson Institute, Glasgow, UK), as described in Chapter 4. Driving the sporadic development of immune-competent, KRAS- and p53-mutant PDAC, the KPF-FLIP GEMM facilitated FLIPi specifically within successfully recombined cells once a tumour had established. However, establishing the model at Cardiff University was associated with unexpected environmental influences that negatively impacted tumour incidence and latency. Therefore, only a small cohort of tumours was ultimately eligible for use to investigate the impact of FLIPi *in vivo*. Despite the small cohort, short-term tamoxifen-induced FLIPi was associated with a small, albeit non-significant, increase in apoptosis and necrosis at the histological level. However, in an equally small, long-term treatment cohort, that was housed and monitored by our collaborators in the Morton lab, FLIPi did not lead to any significant impact on tumour volume or overall survival. Such a minimal response suggests that, in this model, FLIPi alone may not be sufficient to re-activate canonical, TRAIL-induced apoptosis in KRAS-mutant PDAC tumours *in vivo*. However, given the small cohorts involved in both studies, a further investigation involving additional experimental subjects and a wider range of pre-established short-term endpoints would be required to truly identify the potential of FLIPi in this GEMM of PDAC. Equally, further optimisation is needed to confirm the successful deletion of cFLIP expression, to ensure an accurate interpretation of the results presented in Chapter 4 of this thesis.

Due to the poor tumour incidence associated with the KPF-FLIP model, certain uninduced tumours were harvested to investigate the response to FLIPi *ex vivo*. PDAC-derived organoids provided a time- and cost-effective platform to observe the impact of AdCre-mediated FLIPi in a 3D setting. Although a range of methods to quantify apoptosis was explored using the KPF-FLIP PDAC organoids, it was not possible to optimise an efficient, cost-effective method within the scope of this project, as detailed in Chapter 2 of this thesis. Therefore, the response to FLIPi *ex vivo* was monitored in terms of impact on organoid viability, as described in Chapter 4.

Although FLIPi alone resulted in an initial significant reduction in the number of organoids, this effect was not maintained, and organoid number had recovered by the end of the assay. However, whilst FLIPi in combination with exogenous TRAIL led to a similar significant decrease in organoid number, the apparent inability to form new organoids appeared to be sustained until the end of the assay. The transient response of organoids to FLIPi in the absence of TRAIL potentially suggests that the 3D, *ex vivo* environment may support higher levels of endogenous TRAIL-R signalling than that seen *in vitro*. Endogenous TRAIL-R signalling in combination with FLIPi may be sufficient to initially impact the viability of certain target cells within organoids, resulting in the transient suppression of their ability to form new spheres. However, endogenous activity may not be sufficient to maintain this effect, suggesting that exogenous TRAIL supplementation is required to prevent a recovery in organoid number and target a larger population of cells within an organoid.

Neither FLIPi nor FLIPi in combination with TRAIL significantly impacted the average size of KPF-FLIP$^{fl/fl}$ organoids. Therefore, the impact on organoid number may reflect a direct influence of FLIPi on cancer stem-like cells within organoids, namely those responsible for the formation of new spheres, as opposed to sustained growth of the bulk cell population. Further investigation into the activity of TRAIL signalling in this system and any change in cancer stem-like cell markers in response to FLIPi would be necessary to truly delineate the underlying biological mechanisms involved. Equally, additional scope to optimise a reliable method of quantifying apoptotic cell death *ex vivo* is warranted, to determine whether TRAIL-induced apoptosis underlies the decrease in organoid numbers.

Finally, the experiments in Chapter 5 of this thesis first focused on the use of the classical KPC GEMM of PDAC to establish the ability of ^{18}F-FDG PET/CT imaging to detect and monitor *in situ* PDAC tumours, thereby complementing the findings of Knight et al. who demonstrated its ability to detect subcutaneous PDAC allografts (Knight et al. 2017). A novel ^{18}F-FDG PET/CT analytical approach, developed in collaboration with colleagues at PETIC (Cardiff University), facilitated an investigation into the effect of our lab's novel small molecule cFLIP inhibitor, OH14, in KRAS- and p53-mutant PDAC. Although long-

term OH14 treatment did not significantly impact tumour growth, a significant increase in apoptosis and necrosis was detected at the histological level. Drastic weight loss was observed in both the OH14- and DMSO control-treated long-term cohorts. This suggests that cancer-induced cachexia may negatively impact response to therapy and cause mice to reach their ethically-determined endpoint before OH14-induced increases in apoptosis could impact overall tumour volume. However, as with experiments detailed in Chapter 4 of this thesis, additional experimental subjects and a wider selection of short-term time points would be necessary to truly determine the therapeutic potential of OH14-mediated FLIPi in PDAC.

In conclusion, the experiments presented in this thesis suggest that FLIPi may represent a promising therapeutic approach to induce apoptosis specifically within KRAS-mutant PDAC tumour cells. However, the greatest potential was observed *in vitro* and *ex vivo*, when FLIPi was combined with the delivery of exogenous TRAIL. It was hypothesised that the level of constitutive, non-canonical TRAIL signalling detected by von Karstedt et al. (von Karstedt et al. 2015), and the presence of TRAIL-presenting immune cells within the microenvironment, should remove the requirement for exogenous TRAIL *in vivo*. However, the inability to detect any significant impact on tumour growth following long-term cFLIP deletion in this setting, suggests that combining FLIPi with exogenous TRAIL supplementation may improve the response. It would also be pertinent to quantify immune infiltration within the tumours, to correlate the number of TRAIL-presenting immune cells with response to FLIPi.

Conversely, an important factor underlying each *in vitro* and *in vivo* experiment is the stage of the tumour at the time of cFLIP inhibition. Indeed, each *in vitro* cell line was derived from either PDAC tumours or metastasised tumours and cFLIP was only targeted *in vivo*, using both the KPF-FLIP and KPC GEMMs, once the presence of a tumour was confirmed (treatment only began once solid tumours reached >20mm^3). Due to the rapid development of invasive PDAC, as discussed in **Section 1.1.2**, tumours analysed in each study would likely have represented advanced, invasive disease. Additionally, both GEMMs relied upon the dual mutation of KRAS and p53 to drive PDAC, resulting in the formation of KRAS and p53 mutant tumours. However, as detailed in **Section 1.4.1.1**,

p53 plays an important role in apoptotic regulation, with loss of function (LOF) mutations in p53 likely to tip the cellular balance towards anti-apoptotic members of the BCL-2 family, a sub-group of regulatory proteins that function downstream to cFLIP in the TRAIL-induced apoptotic pathway. Therefore, it is possible that the presence of mutant p53 may minimise the influence of cFLIP inhibition upon the initiation of apoptosis by introducing an additional, downstream brake on the pathway. This might underlie the lack of significant response observed in terms of tumour volume following cFLIP inhibition in each study.

This also suggests that, in the absence of a p53 mutation, PDAC cells may be more primed towards an apoptotic response following cFLIP inhibition as the balance of downstream regulatory proteins will likely favour apoptotic progression. Although roughly 60% of all advanced PDAC tumours harbour some form of p53 mutation, these mutations generally arise after an initial driver mutation in KRAS leads to the development of pre-malignant PanINs, as detailed in *Section 1.1.2*. Due to the immense difficulty in effectively treating advanced, desmoplastic PDAC tumours, a key current aim in the PDAC field is to progress towards earlier detection of tumours to enable treatment at a less invasive stage. Improvement in the ability to detect potential tumours before they acquire mutations in p53 may be a requirement for the success of cFLIP inhibition as a therapeutic approach, enabling it to be introduced at a much earlier disease stage, potentially offering a non-toxic, tolerable alternative to prevent disease progression and improve PDAC survival rates.

Furthermore, given that over 90% of a PDAC tumour can consist of desmoplastic stroma, as discussed in Section 1.1.2, the therapeutic efficacy of FLIPi may be enhanced if combined with approaches targeting the tumour microenvironment. For example, the use of an enzymatic approach to degrade a key component of the PDAC TME, hyaluron, is currently being combined with standard-of-chemotherapy in clinical trials. Future work establishing the potential of FLIPi as a therapeutic approach in PDAC should consider similar approaches. Particularly, given that the targeting of PDAC stroma may decrease its immunosuppressive capacity and remove the physical barrier to immune

infiltration, thereby enabling the recruitment of more TRAIL-presenting immune cells to enhance the impact of FLIPi *in vivo.*

It is hoped that continuing the investigation into the potential of FLIPi in PDAC may lead to the development of safe and effective therapeutic approaches to induce apoptosis specifically within PDAC tumours. And, therefore, improve the poor survival outcomes of those diagnosed with this deadly disease.

References:

(NICE), N. I. f. H. a. C. E. 2018. *Pancreatic cancer in adults: diagnosis and management*. Available at: https://www.nice.org.uk/guidance/ng85/chapter/Recommendations#staging [Accessed: 10th November].

Aggarwal, B. B. 2003. Signalling pathways of the TNF superfamily: a double-edged sword. *Nature reviews. Immunology* 3(9), pp. 745-756. doi: 10.1038/nri1184

Almoguera, C., Shibata, D., Forrester, K., Martin, J., Arnheim, N. and Perucho, M. 1988. Most human carcinomas of the exocrine pancreas contain mutant c-K-ras genes. *Cell* 53(4), pp. 549-554.

Andersson, K. B., Winer, L. H., Mørk, H. K., Molkentin, J. D. and Jaisser, F. 2010. Tamoxifen administration routes and dosage for inducible Cre-mediated gene disruption in mouse hearts. *Transgenic Research* 19(4), pp. 715-725. doi: 10.1007/s11248-009-9342-4

Ashkenazi, A. et al. 1999. Safety and antitumor activity of recombinant soluble Apo2 ligand. *J Clin Invest* 104(2), pp. 155-162. doi: 10.1172/jci6926

Azijli, K., Weyhenmeyer, B., Peters, G. J., de Jong, S. and Kruyt, F. A. E. 2013. Non-canonical kinase signaling by the death ligand TRAIL in cancer cells: discord in the death receptor family. *Cell death and differentiation* 20(7), pp. 858-868. doi: 10.1038/cdd.2013.28

Bach, J.-F. 2018. The hygiene hypothesis in autoimmunity: the role of pathogens and commensals. *Nature Reviews Immunology* 18(2), pp. 105-120. doi: 10.1038/nri.2017.111

Bailey, P. et al. 2016. Genomic analyses identify molecular subtypes of pancreatic cancer. *Nature* 531(7592), pp. 47-52. doi: 10.1038/nature16965

Bankhead, P. et al. 2017. QuPath: Open source software for digital pathology image analysis. *Scientific Reports* 7(1), doi: 10.1038/s41598-017-17204-5

Bannoura, S. F., Khan, H. Y. and Azmi, A. S. 2022. KRAS G12D targeted therapies for pancreatic cancer: Has the fortress been conquered? *Front Oncol* 12, p. 1013902. doi: 10.3389/fonc.2022.1013902

Bannoura, S. F. et al. 2021. Targeting KRAS in pancreatic cancer: new drugs on the horizon. *Cancer and Metastasis Reviews* 40(3), pp. 819-835. doi: 10.1007/s10555-021-09990-2

Barnhart, B. C., Alappat, E. C. and Peter, M. E. 2003. The CD95 Type I/Type II model. *Seminars in immunology* 15(3), pp. 185-193. doi: 10.1016/S1044-5323(03)00031-9

Barretina, J. et al. 2012. The Cancer Cell Line Encyclopedia enables predictive modelling of anticancer drug sensitivity. *Nature* 483(7391), pp. 603-607. doi: 10.1038/nature11003

Biernacka, A. et al. 2016. The potential utility of re-mining results of somatic mutation testing: KRAS status in lung adenocarcinoma. *Cancer Genetics* 209(5), pp. 195-198. doi: 10.1016/j.cancergen.2016.03.001

Boj, F., Sylvia et al. 2015. Organoid Models of Human and Mouse Ductal Pancreatic Cancer. *Cell* 160(1-2), pp. 324-338. doi: 10.1016/j.cell.2014.12.021

Bouralexis, S., Findlay, D. M., Atkins, G. J., Labrinidis, A., Hay, S. and Evdokiou, A. 2003. Progressive resistance of BTK-143 osteosarcoma cells to Apo2L/TRAIL-induced apoptosis is mediated by acquisition of DcR2/TRAIL-R4 expression: resensitisation with chemotherapy. *British Journal of Cancer* 89(1), pp. 206-214. doi: 10.1038/sj.bjc.6601021

Bratton, S. B., Lewis, J., Butterworth, M., Duckett, C. S. and Cohen, G. M. 2002. XIAP inhibition of caspase-3 preserves its association with the Apaf-1 apoptosome and prevents CD95- and Bax-induced apoptosis. *Cell Death & Differentiation* 9(9), pp. 881-892. doi: 10.1038/sj.cdd.4401069

Brown, D. A., Yang, N. and Ray, S. D. 2014. Apoptosis. In: Wexler, P. ed. *Encyclopedia of Toxicology (Third Edition)*. Oxford: Academic Press, pp. 287-294.

Brumatti, G., Salmanidis, M. and Ekert, P. G. 2010. Crossing paths: interactions between the cell death machinery and growth factor survival signals. *Cellular and Molecular Life Sciences* 67(10), pp. 1619-1630. doi: 10.1007/s00018-010-0288-8

Carithers, L. J. et al. 2015. A Novel Approach to High-Quality Postmortem Tissue Procurement: The GTEx Project. *Biopreservation and Biobanking* 13(5), pp. 311-319. doi: 10.1089/bio.2015.0032

Chang, D. W. 2002. c-FLIPL is a dual function regulator for caspase-8 activation and CD95-mediated apoptosis. *The EMBO Journal* 21(14), pp. 3704-3714. doi: 10.1093/emboj/cdf356

Chauvier, D., Ankri, S., Charriaut-Marlangue, C., Casimir, R. and Jacotot, E. 2007. Broad-spectrum caspase inhibitors: from myth to reality? *Cell Death & Differentiation* 14(2), pp. 387-391. doi: 10.1038/sj.cdd.4402044

Cheng, X. and Ferrell, J. E. 2018. Apoptosis propagates through the cytoplasm as trigger waves. *Science* 361(6402), pp. 607-612. doi: 10.1126/science.aah4065

Choi, M., Bien, H., Mofunanya, A. and Powers, S. 2019. Challenges in Ras therapeutics in pancreatic cancer. *Semin Cancer Biol* 54, pp. 101-108. doi: 10.1016/j.semcancer.2017.11.015

Cloyd, J. M. et al. 2017. Preoperative Therapy and Pancreatoduodenectomy for Pancreatic Ductal Adenocarcinoma: a 25-Year Single-Institution Experience. *Journal of Gastrointestinal Surgery* 21(1), pp. 164-174. doi: 10.1007/s11605-016-3265-1

Collins, M. A. et al. 2012. Oncogenic Kras is required for both the initiation and maintenance of pancreatic cancer in mice. *Journal of Clinical Investigation* 122(2), pp. 639-653. doi: 10.1172/jci59227

Daniels, R. A. et al. 2005. Expression of TRAIL and TRAIL receptors in normal and malignant tissues. *Cell Research* 15(6), pp. 430-438. doi: 10.1038/sj.cr.7290311

Dastjerd, N. T. et al. 2022. Gene therapy: A promising approach for breast cancer treatment. *Cell biochemistry and function* 40(1), pp. 28-48. doi: 10.1002/cbf.3676

de Miguel, D., Lemke, J., Anel, A., Walczak, H. and Martinez-Lostao, L. 2016. Onto better TRAILs for cancer treatment. *Cell Death Differ* 23(5), pp. 733-747. doi: 10.1038/cdd.2015.174

Debruyne, A. C., Okkelman, I. A. and Dmitriev, R. I. 2022. Balance between the cell viability and death in 3D. *Seminars in cell & developmental biology*, doi: 10.1016/j.semcdb.2022.09.005

DeCant, B., Principe, D. R., Guerra, C., di Magliano, M. P. and Grippo, P. J. 2014. Utilizing past and present mouse systems to engineer more relevant pancreatic cancer models. *Frontiers in physiology* 5, pp. 464-464. doi: 10.3389/fphys.2014.00464

Deer, E. L. et al. 2010. Phenotype and Genotype of Pancreatic Cancer Cell Lines. *Pancreas* 39(4), pp. 425-435. doi: 10.1097/mpa.0b013e3181c15963

Degli-Esposti, M. A., Dougall, W. C., Smolak, P. J., Waugh, J. Y., Smith, C. A. and Goodwin, R. G. 1997. The Novel Receptor TRAIL-R4 Induces NF-κB and Protects against TRAIL-Mediated Apoptosis, yet Retains an Incomplete Death Domain. *Immunity* 7(6), pp. 813-820. doi: 10.1016/s1074-7613(00)80399-4

Dewys, W. D. et al. 1980. Prognostic effect of weight loss prior tochemotherapy in cancer patients. *The American journal of medicine* 69(4), pp. 491-497. doi: 10.1016/S0149-2918(05)80001-3

Discovery, H. 2023. *siRNA: To pool, or not to pool?* Available at: https://horizondiscovery.com/en/resources/featured-articles/sirna-to-pool-or-not-to-pool [Accessed: 19/08/23].

Donocoff, R. S., Teteloshvili, N., Chung, H., Shoulson, R. and Creusot, R. J. 2020. Optimization of tamoxifen-induced Cre activity and its effect on immune cell populations. *Scientific Reports* 10(1), doi: 10.1038/s41598-020-72179-0

Doran, A. C., Yurdagul, A. and Tabas, I. 2020. Efferocytosis in health and disease. *Nature Reviews Immunology* 20(4), pp. 254-267. doi: 10.1038/s41577-019-0240-6

Dreyer, S. B. et al. 2021. Targeting DNA Damage Response and Replication Stress in Pancreatic Cancer. *Gastroenterology* 160(1), pp. 362-377.e313. doi: 10.1053/j.gastro.2020.09.043

Duan, Q., Liu, Y., Booth, C. J. and Rockwell, S. 2012. Use of Fenbendazole-Containing Therapeutic Diets for Mice in Experimental Cancer Therapy Studies. *Journal of the American Association for Laboratory Animal Science* 51(2), pp. 224-230.

Dymecki, S. M. 1996. Flp recombinase promotes site-specific DNA recombination in embryonic stem cells and transgenic mice. *Proceedings of the National Academy of Sciences* 93(12), pp. 6191-6196. doi: 10.1073/pnas.93.12.6191

Emami Nejad, A. et al. 2021. The role of hypoxia in the tumor microenvironment and development of cancer stem cell: a novel approach to developing treatment. *Cancer Cell International* 21(1), doi: 10.1186/s12935-020-01719-5

Erkan, M., Hausmann, S., Michalski, C. W., Fingerle, A. A., Dobritz, M., Kleeff, J. and Friess, H. 2012. The role of stroma in pancreatic cancer: diagnostic and therapeutic implications. *Nature Reviews Gastroenterology & Hepatology* 9(8), pp. 454-467. doi: 10.1038/nrgastro.2012.115

Eser, S., Schnieke, A., Schneider, G. and Saur, D. 2014. Oncogenic KRAS signalling in pancreatic cancer. *British Journal of Cancer* 111(5), pp. 817-822. doi: 10.1038/bjc.2014.215

Farley, F. W., Soriano, P., Steffen, L. S. and Dymecki, S. M. 2000. Widespread recombinase expression using FLPeR (flipper) mice. *Genesis* 28(3-4), pp. 106-110.

Fearon, K. P. et al. 2011. Definition and classification of cancer cachexia: an international consensus. *The lancet oncology* 12(5), pp. 489-495. doi: 10.1016/S1470-2045(10)70218-7

Feil, R., Wagner, J., Metzger, D. and Chambon, P. 1997. Regulation of Cre Recombinase Activity by Mutated Estrogen Receptor Ligand-Binding Domains. *Biochemical and biophysical research communications* 237(3), pp. 752-757. doi: 10.1006/bbrc.1997.7124

Fendrich, V., Schneider, R., Maitra, A., Jacobsen, I. D., Opfermann, T. and Bartsch, D. K. 2011. Detection of Precursor Lesions of Pancreatic Adenocarcinoma in PET-CT in a Genetically Engineered Mouse Model of Pancreatic Cancer. *Neoplasia (New York, N.Y.)* 13(2), pp. 180-186. doi: 10.1593/neo.10956

Ferlay, J. et al. 2018. Cancer incidence and mortality patterns in Europe: Estimates for 40 countries and 25 major cancers in 2018. *Eur J Cancer* 103, pp. 356-387. doi: 10.1016/j.ejca.2018.07.005

Florio, R. et al. 2019. The Benzimidazole-Based Anthelmintic Parbendazole: A Repurposed Drug Candidate That Synergizes with Gemcitabine in Pancreatic Cancer. *Cancers* 11(12), p. 2042. doi: 10.3390/cancers11122042

French, R., Hayward, O., Jones, S., Yang, W. and Clarkson, R. 2015. Cytoplasmic levels of cFLIP determine a broad susceptibility of breast cancer stem/progenitor-like cells to TRAIL. doi: French, Rhiannon <http://orca.cf.ac.uk/view/cardiffauthors/A2120681.html>, Hayward, Olivia, Jones, Samuel <http://orca.cf.ac.uk/view/cardiffauthors/A1986394Z.html>, Yang, William <http://orca.cf.ac.uk/view/cardiffauthors/A434829P.html> and Clarkson, Richard <http://orca.cf.ac.uk/view/cardiffauthors/A0683012.html> 2015. Cytoplasmic levels of cFLIP determine a broad susceptibility of breast cancer stem/progenitor-like cells to TRAIL. Molecular Cancer 14 (1) , 209. 10.1186/s12943-015-0478-y <http://dx.doi.org/10.1186/s12943-015-0478-y> file <http://orca.cf.ac.uk/84192/1/art%3A10.1186%2Fs12943-015-0478-y.pdf>

Fuchs, Y. and Steller, H. 2015. Live to die another way: modes of programmed cell death and the signals emanating from dying cells. *Nature Reviews Molecular Cell Biology* 16(6), pp. 329-344. doi: 10.1038/nrm3999

Gallamini, A., Zwarthoed, C. and Borra, A. 2014. Positron Emission Tomography (PET) in Oncology. *Cancers* 6(4), pp. 1821-1889. doi: 10.3390/cancers6041821

Galluzzi, L. et al. 2018. Molecular mechanisms of cell death: recommendations of the Nomenclature Committee on Cell Death 2018. *Cell Death & Differentiation* 25(3), pp. 486-541. doi: 10.1038/s41418-017-0012-4

Gialeli, C., Theocharis, A. D. and Karamanos, N. K. 2011. Roles of matrix metalloproteinases in cancer progression and their pharmacological targeting. *FEBS Journal* 278(1), pp. 16-27. doi: 10.1111/j.1742-4658.2010.07919.x

Gil-Parrado, S. et al. 2002. Ionomycin-activated Calpain Triggers Apoptosis. *Journal of Biological Chemistry* 277(30), pp. 27217-27226. doi: 10.1074/jbc.m202945200

Gopinathan, A., Morton, J. P., Jodrell, D. I. and Sansom, O. J. 2015. GEMMs as preclinical models for testing pancreatic cancer therapies. *Disease Models & Mechanisms* 8(10), pp. 1185-1200. doi: 10.1242/dmm.021055

Green, D. R., Oguin, T. H. and Martinez, J. 2016. The clearance of dying cells: table for two. *Cell Death & Differentiation* 23(6), pp. 915-926. doi: 10.1038/cdd.2015.172

Grimont, A., Leach, S. D. and Chandwani, R. 2022. Uncertain Beginnings: Acinar and Ductal Cell Plasticity in the Development of Pancreatic Cancer. *Cellular and Molecular Gastroenterology and Hepatology* 13(2), pp. 369-382. doi: 10.1016/j.jcmgh.2021.07.014

Grover, S. and Syngal, S. 2010. Hereditary Pancreatic Cancer. *Gastroenterology* 139(4), pp. 1076-1080.e1072. doi: 10.1053/j.gastro.2010.08.012

Gu, G., Dubauskaite, J. and Melton, D. A. 2002. Direct evidence for the pancreatic lineage: NGN3+ cells are islet progenitors and are distinct from duct progenitors. *Development* 129(10), pp. 2447-2457. doi: 10.1242/dev.129.10.2447

Gunti, S., Hoke, A. T. K., Vu, K. P. and London, N. R. 2021. Organoid and Spheroid Tumor Models: Techniques and Applications. *Cancers* 13(4), p. 874. doi: 10.3390/cancers13040874

Gurumurthy, C. B. and Lloyd, K. C. K. 2019. Generating mouse models for biomedical research: technological advances. *Disease Models & Mechanisms* 12(1), p. dmm029462. doi: 10.1242/dmm.029462

Haag, C., Stadel, D., Zhou, S., Bachem, M. G., Möller, P., Debatin, K.-M. and Fulda, S. 2011. Identification of c-FLIPL and c-FLIPS as critical regulators of death receptor-induced apoptosis in pancreatic cancer cells. *Gut* 60(2), pp. 225-237. doi: 10.1136/gut.2009.202325

Hallin, J. et al. 2022. Anti-tumor efficacy of a potent and selective non-covalent KRASG12D inhibitor. *Nature Medicine* 28(10), pp. 2171-2182. doi: 10.1038/s41591-022-02007-7

Hanahan, D. 2022. Hallmarks of Cancer: New Dimensions. *Cancer Discovery* 12(1), pp. 31-46. doi: 10.1158/2159-8290.cd-21-1059

Hanahan, D. and Weinberg, R. A. 2011. Hallmarks of Cancer: The Next Generation. *Cell* 144(5), pp. 646-674. doi: https://doi.org/10.1016/j.cell.2011.02.013

Harris, N. L. and Loke, P. N. 2017. Recent Advances in Type-2-Cell-Mediated Immunity: Insights from Helminth Infection. *Immunity* 47(6), pp. 1024-1036. doi: 10.1016/j.immuni.2017.11.015

Heinrich, M. A., Mostafa, A. M. R. H., Morton, J. P., Hawinkels, L. J. A. C. and Prakash, J. 2021. Translating complexity and heterogeneity of pancreatic tumor: 3D in vitro to in vivo models. *Advanced drug delivery reviews* 174, pp. 265-293. doi: 10.1016/j.addr.2021.04.018

Hickman, D., Swan, M. and Hartman, G. P. 2008. A cost-effective and efficacious method of pinworm treatment for large colonies of mice. *Lab Animal* 37(7), pp. 308-312. doi: 10.1038/laban0708-308

Hingorani, S. R. et al. 2003. Preinvasive and invasive ductal pancreatic cancer and its early detection in the mouse. *Cancer Cell* 4(6), pp. 437-450. doi: 10.1016/s1535-6108(03)00309-x

Hingorani, S. R. et al. 2005. Trp53R172H and KrasG12D cooperate to promote chromosomal instability and widely metastatic pancreatic ductal adenocarcinoma in mice. *Cancer Cell* 7(5), pp. 469-483. doi: 10.1016/j.ccr.2005.04.023

Hobbs, G. A., Der, C. J. and Rossman, K. L. 2016. RAS isoforms and mutations in cancer at a glance. *Journal of Cell Science* 129(7), pp. 1287-1292. doi: 10.1242/jcs.182873

Hruban, R. H. et al. 2006. Pathology of genetically engineered mouse models of pancreatic exocrine cancer: consensus report and recommendations. *Cancer research (Chicago, Ill.)* 66(1), pp. 95-106. doi: 10.1158/0008-5472.CAN-05-2168

Hu, B., Zhong, L., Weng, Y., Peng, L., Huang, Y., Zhao, Y. and Liang, X.-J. 2020. Therapeutic siRNA: state of the art. *Signal Transduction and Targeted Therapy* 5(1), doi: 10.1038/s41392-020-0207-x

Hu, J. et al. 2021. Targeting mutant p53 for cancer therapy: direct and indirect strategies. *Journal of Hematology & Oncology* 14(1), doi: 10.1186/s13045-021-01169-0

Huang, C.-Y. et al. 2021a. Fluoroquinolones Suppress TGF-β and PMA-Induced MMP-9 Production in Cancer Cells: Implications in Repurposing Quinolone Antibiotics for Cancer Treatment. *International Journal of Molecular Sciences* 22(21), p. 11602. doi: 10.3390/ijms222111602

Huang, L., Guo, Z., Wang, F. and Fu, L. 2021b. KRAS mutation: from undruggable to druggable in cancer. *Signal Transduction and Targeted Therapy* 6(1), doi: 10.1038/s41392-021-00780-4

Huang, Y. et al. 2016. Overcoming resistance to TRAIL-induced apoptosis in solid tumor cells by simultaneously targeting death receptors, c-FLIP and IAPs. *International Journal of Oncology* 49(1), pp. 153-163. doi: 10.3892/ijo.2016.3525

Hughes, A., Michelle et al. 2016. Co-operative and Hierarchical Binding of c-FLIP and Caspase-8: A Unified Model Defines How c-FLIP Isoforms Differentially Control Cell Fate. *Molecular Cell* 61(6), pp. 834-849. doi: 10.1016/j.molcel.2016.02.023

Humphrey, E. S. et al. 2016. Resolution of Novel Pancreatic Ductal Adenocarcinoma Subtypes by Global Phosphotyrosine Profiling. *Molecular & cellular proteomics* 15(8), pp. 2671-2685. doi: 10.1074/mcp.M116.058313

Humphreys, L., Espona-Fiedler, M. and Longley, D. B. 2018. <scp>FLIP</scp>
        as a therapeutic target in cancer. *The FEBS Journal* 285(22), pp. 4104-4123. doi: 10.1111/febs.14523

Ihle, N. T. et al. 2012. Effect of KRAS Oncogene Substitutions on Protein Behavior: Implications for Signaling and Clinical Outcome. *JNCI: Journal of the National Cancer Institute* 104(3), pp. 228-239. doi: 10.1093/jnci/djr523

Irmler, M. et al. 1997. Inhibition of death receptor signals by cellular FLIP. *Nature* 388(6638), pp. 190-195. doi: 10.1038/40657

Ishimura, N., Isomoto, H., Bronk, S. F. and Gores, G. J. 2006. Trail induces cell migration and invasion in apoptosis-resistant cholangiocarcinoma cells. *American Journal of Physiology - Gastrointestinal and Liver Physiology* 290(1), pp. 129-136. doi: 10.1152/ajpgi.00242.2005

Jackson, E. L. et al. 2001. Analysis of lung tumor initiation and progression using conditional expression of oncogenic *K-ras*. *Genes & Development* 15(24), pp. 3243-3248. doi: 10.1101/gad.943001

Jacobson, M. D., Weil, M. and Raff, M. C. 1997. Programmed Cell Death in Animal Development. *Cell* 88(3), pp. 347-354. doi: 10.1016/s0092-8674(00)81873-5

Johnston, M. C. et al. 2020. DR5-targeted, chemotherapeutic drug-loaded nanoparticles induce apoptosis and tumor regression in pancreatic cancer in vivo models. *Journal of controlled release* 324, pp. 610-619. doi: 10.1016/j.jconrel.2020.05.046

Jost, P. J. et al. 2009. XIAP discriminates between type I and type II FAS-induced apoptosis. *Nature* 460(7258), pp. 1035-1039. doi: 10.1038/nature08229

Kale, J., Osterlund, E. J. and Andrews, D. W. 2018. BCL-2 family proteins: changing partners in the dance towards death. *Cell Death & Differentiation* 25(1), pp. 65-80. doi: 10.1038/cdd.2017.186

Kalra, A., Wehrle , C. J. and Tuma, F. 2022. *Anatomy, Abdomen and Pelvis, Peritoneum.* Treasure Island (FL): StatPearls Publishing.

Kamisawa, T., Wood, L. D., Itoi, T. and Takaori, K. 2016. Pancreatic cancer. *Lancet* 388(10039), pp. 73-85. doi: 10.1016/s0140-6736(16)00141-0

Kataoka, T. et al. 2000. The caspase-8 inhibitor FLIP promotes activation of NF-κB and Erk signaling pathways. *Current Biology* 10(11), pp. 640-648. doi: 10.1016/s0960-9822(00)00512-1

Kataoka, T. and Tschopp, J. 2004. N-Terminal Fragment of c-FLIP(L) Processed by Caspase 8 Specifically Interacts with TRAF2 and Induces Activation of the NF-κB Signaling Pathway. *Molecular and Cellular Biology* 24(7), pp. 2627-2636. doi: 10.1128/mcb.24.7.2627-2636.2004

Kaur, G. and Dufour, J. M. 2012. Cell lines. *Spermatogenesis* 2(1), pp. 1-5. doi: 10.4161/spmg.19885

Kavuri, S. M. et al. 2011. Cellular FLICE-inhibitory Protein (cFLIP) Isoforms Block CD95- and TRAIL Death Receptor-induced Gene Induction Irrespective of Processing of

Caspase-8 or cFLIP in the Death-inducing Signaling Complex. *Journal of Biological Chemistry* 286(19), pp. 16631-16646. doi: 10.1074/jbc.m110.148585

Keane, M. M., Ettenberg, S. A., Nau, M. M., Russell, E. K. and Lipkowitz, S. 1999. Chemotherapy augments TRAIL-induced apoptosis in breast cell lines. *Cancer Res* 59(3), pp. 734-741.

Kim, H., Kim, M., Im, S.-K. and Fang, S. 2018. Mouse Cre-LoxP system: general principles to determine tissue-specific roles of target genes. *Laboratory Animal Research* 34(4), p. 147. doi: 10.5625/lar.2018.34.4.147

Knight, J. C. et al. 2017. 89Zr-anti-γH2AX-TAT but not 18F-FDG Allows Early Monitoring of Response to Chemotherapy in a Mouse Model of Pancreatic Ductal Adenocarcinoma. *Clinical Cancer Research* 23(21), pp. 6498-6504. doi: 10.1158/1078-0432.ccr-17-0664

Korkolopoulou, P. et al. 2007. c-FLIP expression in colorectal carcinomas: association with Fas/FasL expression and prognostic implications. *Histopathology* 51(2), pp. 150-156. doi: 10.1111/j.1365-2559.2007.02723.x

Krueger, A., Schmitz, I., Baumann, S., Krammer, P. H. and Kirchhoff, S. 2001. Cellular FLICE-inhibitory Protein Splice Variants Inhibit Different Steps of Caspase-8 Activation at the CD95 Death-inducing Signaling Complex. *Journal of Biological Chemistry* 276(23), pp. 20633-20640. doi: 10.1074/jbc.m101780200

Laking, G. and Price, P. 2001. 18-Fluorodeoxyglucose positron emission tomography (FDG-PET) and the staging of early lung cancer. *Thorax* 56(suppl 2), pp. ii38-ii44.

Lavin, M. F. and Gueven, N. 2006. The complexity of p53 stabilization and activation. *Cell Death & Differentiation* 13(6), pp. 941-950. doi: 10.1038/sj.cdd.4401925

Lee, C. S. et al. 2017. Adenovirus-Mediated Gene Delivery: Potential Applications for Gene and Cell-Based Therapies in the New Era of Personalized Medicine. *Genes Dis* 4(2), pp. 43-63. doi: 10.1016/j.gendis.2017.04.001

Lemke, J., von Karstedt, S., Zinngrebe, J. and Walczak, H. 2014. Getting TRAIL back on track for cancer therapy. *Cell Death & Differentiation* 21(9), pp. 1350-1364. doi: 10.1038/cdd.2014.81

Li, C. et al. 2007. Identification of pancreatic cancer stem cells. *Cancer research (Chicago, Ill.)* 67(3), pp. 1030-1037. doi: 10.1158/0008-5472.CAN-06-2030

Li, L., Tong, A., Zhang, Q., Wei, Y. and Wei, X. 2021. The molecular mechanisms of MLKL-dependent and MLKL-independent necrosis. *J Mol Cell Biol* 13(1), pp. 3-14. doi: 10.1093/jmcb/mjaa055

Lin, M., Gao, M., Pandalai, P. K., Cavnar, M. J. and Kim, J. 2020. An Organotypic Microcosm for the Pancreatic Tumor Microenvironment. *Cancers* 12(4), p. 811. doi: 10.3390/cancers12040811

Ling, Y.-H. et al. 2020. Tumor necrosis as a poor prognostic predictor on postoperative survival of patients with solitary small hepatocellular carcinoma. *BMC Cancer* 20(1), doi: 10.1186/s12885-020-07097-5

Locksley, R. M., Killeen, N. and Lenardo, M. J. 2001. The TNF and TNF Receptor Superfamilies. *Cell* 104(4), pp. 487-501. doi: 10.1016/s0092-8674(01)00237-9

Low, R. R. J. et al. 2021. The Diverse Applications of Pancreatic Ductal Adenocarcinoma Organoids. *Cancers* 13(19), p. 4979. doi: 10.3390/cancers13194979

Luche, H., Weber, O., Nageswara Rao, T., Blum, C. and Fehling, H. J. 2007. Faithful activation of an extra-bright red fluorescent protein in "knock-in" Cre-reporter mice ideally suited for lineage tracing studies. *European Journal of Immunology* 37(1), pp. 43-53. doi: 10.1002/eji.200636745

Lynch, D. H. et al. 1999. Tumoricidal activity of tumor necrosis factor-related apoptosis-inducing ligand in vivo. *Nature medicine* 5(2), pp. 157-163. doi: 10.1038/5517

Maedler, K. et al. 2002. FLIP switches Fas-mediated glucose signaling in human pancreatic β cells from apoptosis to cell replication. *Proceedings of the National Academy of Sciences* 99(12), pp. 8236-8241. doi: 10.1073/pnas.122686299

Mahmood, T. and Yang, P.-C. 2012. Western blot: Technique, theory, and trouble shooting. *North American journal of medical sciences* 4(9), pp. 429-434. doi: 10.4103/1947-2714.100998

Mccourt, C. et al. 2012. Elevation of c-FLIP in Castrate-Resistant Prostate Cancer Antagonizes Therapeutic Response to Androgen Receptor–Targeted Therapy. *Clinical Cancer Research* 18(14), pp. 3822-3833. doi: 10.1158/1078-0432.ccr-11-3277

Mccubrey, J. A. et al. 2022. Effects of TP53 Mutations and miRs on Immune Responses in the Tumor Microenvironment Important in Pancreatic Cancer Progression. *Cells* 11(14), p. 2155. doi: 10.3390/cells11142155

Mcilwain, D. R., Berger, T. and Mak, T. W. 2013. Caspase Functions in Cell Death and Disease. *Cold Spring Harbor Perspectives in Biology* 5(4), pp. a008656-a008656. doi: 10.1101/cshperspect.a008656

Medema, J. P., De Jong, J., Van Hall, T., Melief, C. J. M. and Offringa, R. 1999. Immune Escape of Tumors in Vivo by Expression of Cellular Flice-Inhibitory Protein. *Journal of Experimental Medicine* 190(7), pp. 1033-1038. doi: 10.1084/jem.190.7.1033

Modiano, J. F. and Bellgrau, D. 2016. Fas ligand based immunotherapy: A potent and effective neoadjuvant with checkpoint inhibitor properties, or a systemically toxic promoter of tumor growth? *Discov Med* 21(114), pp. 109-116.

Montinaro, A. et al. 2022. Potent pro-apoptotic combination therapy is highly effective in a broad range of cancers. *Cell Death & Differentiation* 29(3), pp. 492-503. doi: 10.1038/s41418-021-00869-x

Mérino, D., Lalaoui, N., Morizot, A., Schneider, P., Solary, E. and Micheau, O. 2006. Differential inhibition of TRAIL-mediated DR5-DISC formation by decoy receptors 1 and 2. *Mol Cell Biol* 26(19), pp. 7046-7055. doi: 10.1128/mcb.00520-06

Nagy, A. 2000. Cre recombinase: the universal reagent for genome tailoring. *Genesis* 26(2), pp. 99-109.

Oberst, A. et al. 2011. Catalytic activity of the caspase-8–FLIPL complex inhibits RIPK3-dependent necrosis. *Nature* 471(7338), pp. 363-367. doi: 10.1038/nature09852

Ogasawara, J. et al. 1993. Lethal effect of the anti-Fas antibody in mice. *Nature* 364(6440), pp. 806-809. doi: 10.1038/364806a0

Oikonomopoulou, K., Brinc, D., Kyriacou, K. and Diamandis, E. P. 2013. Infection and cancer: revaluation of the hygiene hypothesis. *Clin Cancer Res* 19(11), pp. 2834-2841. doi: 10.1158/1078-0432.ccr-12-3661

Olson, S. H. et al. 2010. Allergies, obesity, other risk factors and survival from pancreatic cancer. *International Journal of Cancer* 127(10), pp. 2412-2419. doi: 10.1002/ijc.25240

Orth, M. et al. 2019. Pancreatic ductal adenocarcinoma: biological hallmarks, current status, and future perspectives of combined modality treatment approaches. *Radiation Oncology* 14(1), doi: 10.1186/s13014-019-1345-6

Park, H. J., Makepeace, C. M., Lyons, J. C. and Song, C. W. 1996. Effect of intracellular acidity and ionomycin on apoptosis in HL-60 cells. *Eur J Cancer* 32a(3), pp. 540-546. doi: 10.1016/0959-8049(95)00606-0

Parkin, A. et al. 2018. The Evolving Understanding of the Molecular and Therapeutic Landscape of Pancreatic Ductal Adenocarcinoma. *Diseases* 6(4), doi: 10.3390/diseases6040103

Parsons, B. D., Schindler, A., Evans, D. H. and Foley, E. 2009. A Direct Phenotypic Comparison of siRNA Pools and Multiple Individual Duplexes in a Functional Assay. *PLoS ONE* 4(12), p. e8471. doi: 10.1371/journal.pone.0008471

Partyka, O. et al. 2023. Overview of Pancreatic Cancer Epidemiology in Europe and Recommendations for Screening in High-Risk Populations. *Cancers* 15(14), p. 3634. doi: 10.3390/cancers15143634

Parveen, R., Harihar, D. and Chatterji, B. P. 2023. Recent histone deacetylase inhibitors in cancer therapy. *Cancer*, doi: 10.1002/cncr.34974

Peixoto, R. D. A., Speers, C., Mcgahan, C. E., Renouf, D. J., Schaeffer, D. F. and Kennecke, H. F. 2015. Prognostic factors and sites of metastasis in unresectable locally advanced pancreatic cancer. *Cancer Medicine* 4(8), pp. 1171-1177. doi: 10.1002/cam4.459

Piggott, L., Omidvar, N., Marti-Perez, S., Eberl, M. and Clarkson, R. W. E. 2011. Suppression of apoptosis inhibitor c-FLIP selectively eliminates breast cancer stem cell activity in response to the anti-cancer agent, TRAIL. doi: Piggott, Luke <http://orca.cf.ac.uk/view/cardiffauthors/A058504C.html>, Omidvar, Nader <http://orca.cf.ac.uk/view/cardiffauthors/A039332V.html>, Marti-Perez, Salvador, Eberl, Matthias <http://orca.cf.ac.uk/view/cardiffauthors/A106334V.html> and Clarkson, Richard W. E. <http://orca.cf.ac.uk/view/cardiffauthors/A0683012.html> 2011. Suppression of apoptosis inhibitor c-FLIP selectively eliminates breast cancer stem cell activity in response to the anti-cancer agent, TRAIL. Breast Cancer Research 13 (5) , R88. 10.1186/bcr2945 <http://dx.doi.org/10.1186/bcr2945> file <http://orca.cf.ac.uk/9875/1/Suppression_of_apoptosis.pdf>

Pinton, P., Giorgi, C., Siviero, R., Zecchini, E. and Rizzuto, R. 2008. Calcium and apoptosis: ER-mitochondria Ca2+ transfer in the control of apoptosis. *Oncogene* 27(50), pp. 6407-6418. doi: 10.1038/onc.2008.308

Priest, R. 2005. Statistical/Substantive, Interpretations and Data Limitations. In: Kempf-Leonard, K. ed. *Encyclopedia of Social Measurement*. New York: Elsevier, pp. 671-674.

Prior, I. A., Lewis, P. D. and Mattos, C. 2012. A comprehensive survey of Ras mutations in cancer. *Cancer Res* 72(10), pp. 2457-2467. doi: 10.1158/0008-5472.can-11-2612

Pérez–Mancera, P. A., Guerra, C., Barbacid, M. and Tuveson, D. A. 2012. What We Have Learned About Pancreatic Cancer From Mouse Models. *Gastroenterology* 142(5), pp. 1079-1092. doi: 10.1053/j.gastro.2012.03.002

Rao-Bindal, K., Koshkina, N. V., Stewart, J. and Kleinerman, E. S. 2013. The Histone Deacetylase Inhibitor, MS-275 (Entinostat), Downregulates c-FLIP, Sensitizes Osteosarcoma Cells to FasL, and Induces the Regression of Osteosarcoma Lung Metastases. *Current Cancer Drug Targets* 13(4), pp. 411-422. doi: 10.2174/1568009611313040005

Reiche, M. A. et al. 2022. When light meets biology – how the specimen affects quantitative microscopy. *Journal of Cell Science* 135(6), doi: 10.1242/jcs.259656

Ribeiro, F. M., Correia, P. M. M., Santos, A. C. and Veloso, J. F. C. A. 2022. A guideline proposal for mice preparation and care in 18F-FDG PET imaging. *EJNMMI Research* 12(1), doi: 10.1186/s13550-022-00921-y

Riley, J. S. et al. 2013. Prognostic and therapeutic relevance of FLIP and procaspase-8 overexpression in non-small cell lung cancer. *Cell Death & Disease* 4(12), pp. e951-e951. doi: 10.1038/cddis.2013.481

Roberts, N. J., Zhou, S., Diaz, L. A. and Holdhoff, M. 2011. Systemic use of tumor necrosis factor alpha as an anticancer agent. *Oncotarget* 2(10), pp. 739-751. doi: 10.18632/oncotarget.344

Roos, W. P., Thomas, A. D. and Kaina, B. 2016. DNA damage and the balance between survival and death in cancer biology. *Nature Reviews Cancer* 16(1), pp. 20-33. doi: 10.1038/nrc.2015.2

Rosenthal, N. and Brown, S. 2007. The mouse ascending: perspectives for human-disease models. *Nature Cell Biology* 9(9), pp. 993-999. doi: 10.1038/ncb437

Rubio-Viqueira, B. et al. 2006. An In vivo Platform for Translational Drug Development in Pancreatic Cancer. *Clinical cancer research* 12(15), pp. 4652-4661. doi: 10.1158/1078-0432.CCR-06-0113

Russell, W. M. S. and Burch, R. L. 1959. *The principles of humane experimental technique*. London, UK: Methuen.

Ryu, B. K., Lee, M. G., Chi, S. G., Kim, Y. W. and Park, J. H. 2001. Increased expression of cFLIP(L) in colonic adenocarcinoma. *The Journal of pathology* 194(1), pp. 15-19.

Sadowski, P. D. 1995. The Flp recombinase of the 2-microns plasmid of Saccharomyces cerevisiae. *Prog Nucleic Acid Res Mol Biol* 51, pp. 53-91.

Safa, A. 2012. c-FLIP, A MASTER ANTI-APOPTOTIC REGULATOR. *Exp Oncol* 34(3), pp. 176-184.

Safa, A. R. 2016. Resistance to Cell Death and Its Modulation in Cancer Stem Cells. *Critical Reviews™ in Oncogenesis* 21(3-4), pp. 203-219. doi: 10.1615/critrevoncog.2016016976

Safa, A. R., Kamocki, K., Saadatzadeh, M. R. and Bijangi-Vishehsaraei, K. 2019. c-FLIP, a Novel Biomarker for Cancer Prognosis, Immunosuppression, Alzheimer's Disease, Chronic Obstructive Pulmonary Disease (COPD), and a Rationale Therapeutic Target. *Biomarkers Journal* 05(01), doi: 10.36648/2472-1646.5.1.59

Safa, A. R. and Pollok, K. E. 2011. Targeting the Anti-Apoptotic Protein c-FLIP for Cancer Therapy. *Cancers (Basel)* 3(2), pp. 1639-1671. doi: 10.3390/cancers3021639

Sastra, S. A. and Olive, K. P. 2013. Quantification of Murine Pancreatic Tumors by High-Resolution Ultrasound.*Methods in Molecular Biology*. Humana Press, pp. 249-266.

Sauer, B. and Henderson, N. 1988. Site-specific DNA recombination in mammalian cells by the Cre recombinase of bacteriophage P1. *Proceedings of the National Academy of Sciences* 85(14), pp. 5166-5170. doi: 10.1073/pnas.85.14.5166

Schindelin, J. et al. 2012. Fiji: an open-source platform for biological-image analysis. *Nature Methods* 9(7), pp. 676-682. doi: 10.1038/nmeth.2019

Schmid, S. J. et al. 2013. Absence of FLICE-inhibitory protein is a novel independent prognostic marker for very short survival in pancreatic ductal adenocarcinoma. *Pancreas* 42(7), pp. 1114-1119. doi: 10.1097/MPA.0b013e31829655ed

Schneider, C. A., Rasband, W. S. and Eliceiri, K. W. 2012. NIH Image to ImageJ: 25 years of image analysis. *Nature Methods* 9(7), pp. 671-675. doi: 10.1038/nmeth.2089

Schönhuber, N. et al. 2014. A next-generation dual-recombinase system for time and host specific targeting of pancreatic cancer. *Nat Med* 20(11), pp. 1340-1347. doi: 10.1038/nm.3646

Seino, T. et al. 2018. Human Pancreatic Tumor Organoids Reveal Loss of Stem Cell Niche Factor Dependence during Disease Progression. *Cell Stem Cell* 22(3), pp. 454-467.e456. doi: 10.1016/j.stem.2017.12.009

Shabason, J., Tofilon, P. J. and Camphausen, K. 2010. HDAC inhibitors in cancer care. *Oncology (Williston Park)* 24(2), pp. 180-185.

Shin, D. W. and Kim, J. 2020. The American Joint Committee on Cancer 8th edition staging system for the pancreatic ductal adenocarcinoma: is it better than the 7th edition? *Hepatobiliary Surgery and Nutrition* 9(1), pp. 98-100. doi: 10.21037/hbsn.2019.08.06

Siegel, R. L., Miller, K. D., Fuchs, H. E. and Jemal, A. 2022. Cancer statistics, 2022. *CA: A Cancer Journal for Clinicians* 72(1), pp. 7-33. doi: 10.3322/caac.21708

Siegel, R. L., Miller, K. D. and Jemal, A. 2020. Cancer statistics, 2020. *CA: A Cancer Journal for Clinicians* 70(1), pp. 7-30. doi: 10.3322/caac.21590

Skoulidis, F. et al. 2021. Sotorasib for Lung Cancers with <i>KRAS</i> p.G12C Mutation. *New England Journal of Medicine* 384(25), pp. 2371-2381. doi: 10.1056/nejmoa2103695

Spaeth, J. M. et al. 2017. Defining a Novel Role for the Pdx1 Transcription Factor in Islet β-Cell Maturation and Proliferation During Weaning. *Diabetes* 66(11), pp. 2830-2839. doi: 10.2337/db16-1516

Takei, N. and Endo, Y. 1994. Ca2+ ionophore-induced apoptosis on cultured embryonic rat cortical neurons. *Brain Research* 652(1), pp. 65-70. doi: https://doi.org/10.1016/0006-8993(94)90317-4

Talbert, E. E. et al. 2019. Modeling Human Cancer-induced Cachexia. *Cell Reports* 28(6), pp. 1612-1622.e1614. doi: 10.1016/j.celrep.2019.07.016

Tang, Z., Kang, B., Li, C., Chen, T. and Zhang, Z. 2019. GEPIA2: an enhanced web server for large-scale expression profiling and interactive analysis. *Nucleic acids research* 47(1), pp. W556-W560. doi: 10.1093/nar/gkz430

Trauzold, A. et al. 2006. TRAIL promotes metastasis of human pancreatic ductal adenocarcinoma. *Oncogene* 25(56), pp. 7434-7439. doi: 10.1038/sj.onc.1209719

Tronche, F., Casanova, E., Turiault, M., Sahly, I. and Kellendonk, C. 2002. When reverse genetics meets physiology: the use of site-specific recombinases in mice. *FEBS Lett* 529(1), pp. 116-121. doi: 10.1016/s0014-5793(02)03266-0

Tuveson, D. and Clevers, H. 2019. Cancer modeling meets human organoid technology. *Science (American Association for the Advancement of Science)* 364(6444), pp. 952-955. doi: 10.1126/science.aaw6985

Ueffing, N., Keil, E., Freund, C., Kühne, R., Schulze-Osthoff, K. and Schmitz, I. 2008. Mutational analyses of c-FLIPR, the only murine short FLIP isoform, reveal requirements for DISC recruitment. *Cell Death & Differentiation* 15(4), pp. 773-782. doi: 10.1038/sj.cdd.4402314

Ushio, J. et al. 2021. Pancreatic Ductal Adenocarcinoma: Epidemiology and Risk Factors. *Diagnostics* 11(3), p. 562. doi: 10.3390/diagnostics11030562

Van Dijk, M., Halpin-Mccormick, A., Sessler, T., Samali, A. and Szegezdi, E. 2013. Resistance to TRAIL in non-transformed cells is due to multiple redundant pathways. *Cell Death & Disease* 4(7), pp. e702-e702. doi: 10.1038/cddis.2013.214

Vatansever, S., Erman, B. and Gümüş, Z. H. 2019. Oncogenic G12D mutation alters local conformations and dynamics of K-Ras. *Scientific Reports* 9(1), doi: 10.1038/s41598-019-48029-z

Vaupel, P., Schmidberger, H. and Mayer, A. 2019. The Warburg effect: essential part of metabolic reprogramming and central contributor to cancer progression. *International Journal of Radiation Biology* 95(7), pp. 912-919. doi: 10.1080/09553002.2019.1589653

Venza, I., Visalli, M., Oteri, R., Teti, D. and Venza, M. 2014. Class I-specific histone deacetylase inhibitor MS-275 overrides TRAIL-resistance in melanoma cells by downregulating c-FLIP. *International immunopharmacology* 21(2), pp. 439-446. doi: 10.1016/j.intimp.2014.05.024

von Karstedt, S. et al. 2015. Cancer cell-autonomous TRAIL-R signaling promotes KRAS-driven cancer progression, invasion, and metastasis. *Cancer Cell* 27(4), pp. 561-573. doi: 10.1016/j.ccell.2015.02.014

Von Karstedt, S., Montinaro, A. and Walczak, H. 2017. Exploring the TRAILs less travelled: TRAIL in cancer biology and therapy. *Nature reviews. Cancer* 17(6), pp. 352-366. doi: 10.1038/nrc.2017.28

Von Karstedt, S. and Walczak, H. 2020. An unexpected turn of fortune: targeting TRAIL-Rs in KRAS-driven cancer. *Cell Death Discovery* 6(1), doi: 10.1038/s41420-020-0249-4

Waddell, N. et al. 2015. Whole genomes redefine the mutational landscape of pancreatic cancer. *Nature* 518(7540), pp. 495-501. doi: 10.1038/nature14169

Wang, N. et al. 2014. Adenovirus-Mediated Efficient Gene Transfer into Cultured Three-Dimensional Organoids. *PLoS ONE* 9(4), p. e93608. doi: 10.1371/journal.pone.0093608

Wang, X. et al. 2022. Identification of MRTX1133, a Noncovalent, Potent, and Selective KRAS^{G12D} Inhibitor. *Journal of Medicinal Chemistry* 65(4), pp. 3123-3133. doi: 10.1021/acs.jmedchem.1c01688

Warburg, O. 1931. The Metabolism of Tumours: Investigations from the Kaiser Wilhelm Institute for Biology, Berlin-Dahlem. *JAMA: The Journal of the American Medical Association* 96(23), p. 1982. doi: 10.1001/jama.1931.02720490062043

Wei, M. C. et al. 2000. tBID, a membrane-targeted death ligand, oligomerizes BAK to release cytochrome c. *Genes & development* 14(16), pp. 2060-2071. doi: 10.1101/gad.14.16.2060

Weinlich, R. et al. 2013. Protective Roles for Caspase-8 and cFLIP in Adult Homeostasis. *Cell Reports* 5(2), pp. 340-348. doi: 10.1016/j.celrep.2013.08.045

Weinstein, J. N. et al. 2013. The Cancer Genome Atlas Pan-Cancer analysis project. *Nature Genetics* 45(10), pp. 1113-1120. doi: 10.1038/ng.2764

Werner, J., Combs, S. E., Springfeld, C., Hartwig, W., Hackert, T. and Büchler, M. W. 2013. Advanced-stage pancreatic cancer: therapy options. *Nature Reviews Clinical Oncology* 10(6), pp. 323-333. doi: 10.1038/nrclinonc.2013.66

Wu, G. S., Burns, T. F., Zhan, Y., Alnemri, E. S. and El-Deiry, W. S. 1999. Molecular cloning and functional analysis of the mouse homologue of the KILLER/DR5 tumor necrosis factor-related apoptosis-inducing ligand (TRAIL) death receptor. *Cancer research (Chicago, Ill.)* 59(12), pp. 2770-2775.

Xu, C., Li, X., Liu, P., Li, M. and Luo, F. 2018. Patient-derived xenograft mouse models: A high fidelity tool for individualized medicine (Review). *Oncology Letters*, doi: 10.3892/ol.2018.9583

Yang, X. et al. 2020. High-Throughput Transcriptome Profiling in Drug and Biomarker Discovery. *Front Genet* 11, p. 19. doi: 10.3389/fgene.2020.00019

Yao, Q. et al. 2016. Prognostic significance of TRAIL signalling molecules in cervical squamous cell carcinoma. *Journal of clinical pathology* 69(2), pp. 122-127. doi: 10.1136/jclinpath-2014-202811

Yu, J. W., Jeffrey, P. D. and Shi, Y. 2009. Mechanism of procaspase-8 activation by c-FLIP $_L$. *Proceedings of the National Academy of Sciences* 106(20), pp. 8169-8174. doi: 10.1073/pnas.0812453106

Yu, K. et al. 2019. Comprehensive transcriptomic analysis of cell lines as models of primary tumors across 22 tumor types. *Nature Communications* 10(1), doi: 10.1038/s41467-019-11415-2

Zhang, N. and He, Y. W. 2005. An essential role for c-FLIP in the efficient development of mature T lymphocytes. *J Exp Med* 202(3), pp. 395-404. doi: 10.1084/jem.20050117

Zhitao, J., Long, L., Jia, L., Yunchao, B. and Anhua, W. 2015. Temozolomide sensitizes stem-like cells of glioma spheres to TRAIL-induced apoptosis via upregulation of casitas B-lineage lymphoma (c-Cbl) protein. *Tumor Biology* 36(12), pp. 9621-9630. doi: 10.1007/s13277-015-3720-8

Zhou, Q. and Melton, D. A. 2018. Pancreas regeneration. *Nature* 557(7705), pp. 351-358. doi: 10.1038/s41586-018-0088-0
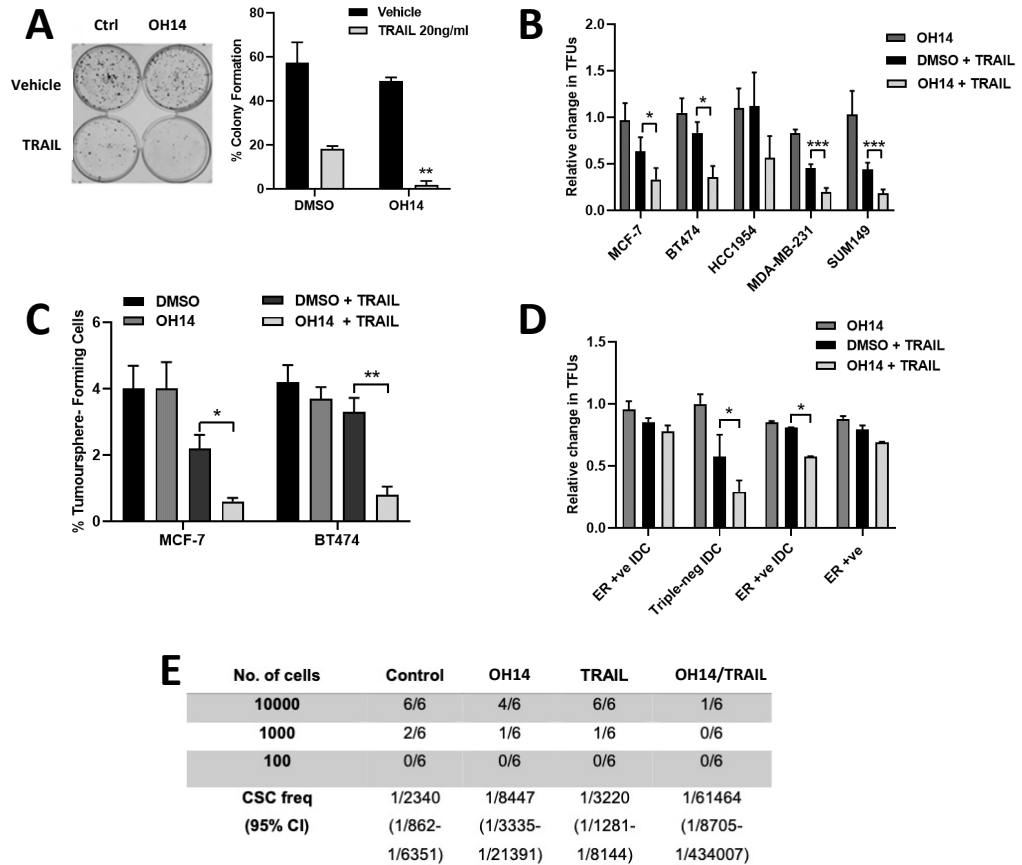
7 Appendix

For clarity, all data presented in Appendix A1 and A2 was collected and analysed by members of the Clarkson and Westwell labs *(manuscript in preparation; Rhiannon French*, Olivia Hayward*, Kok Yung Lee, Timothy Robinson, Andreia M. Ribeiro da Silva, Gilda Giancotti, Athina Varnava, Marion MacFarlane, Andrew D. Westwell, Andrea Brancale, Richard W.E. Clarkson).*
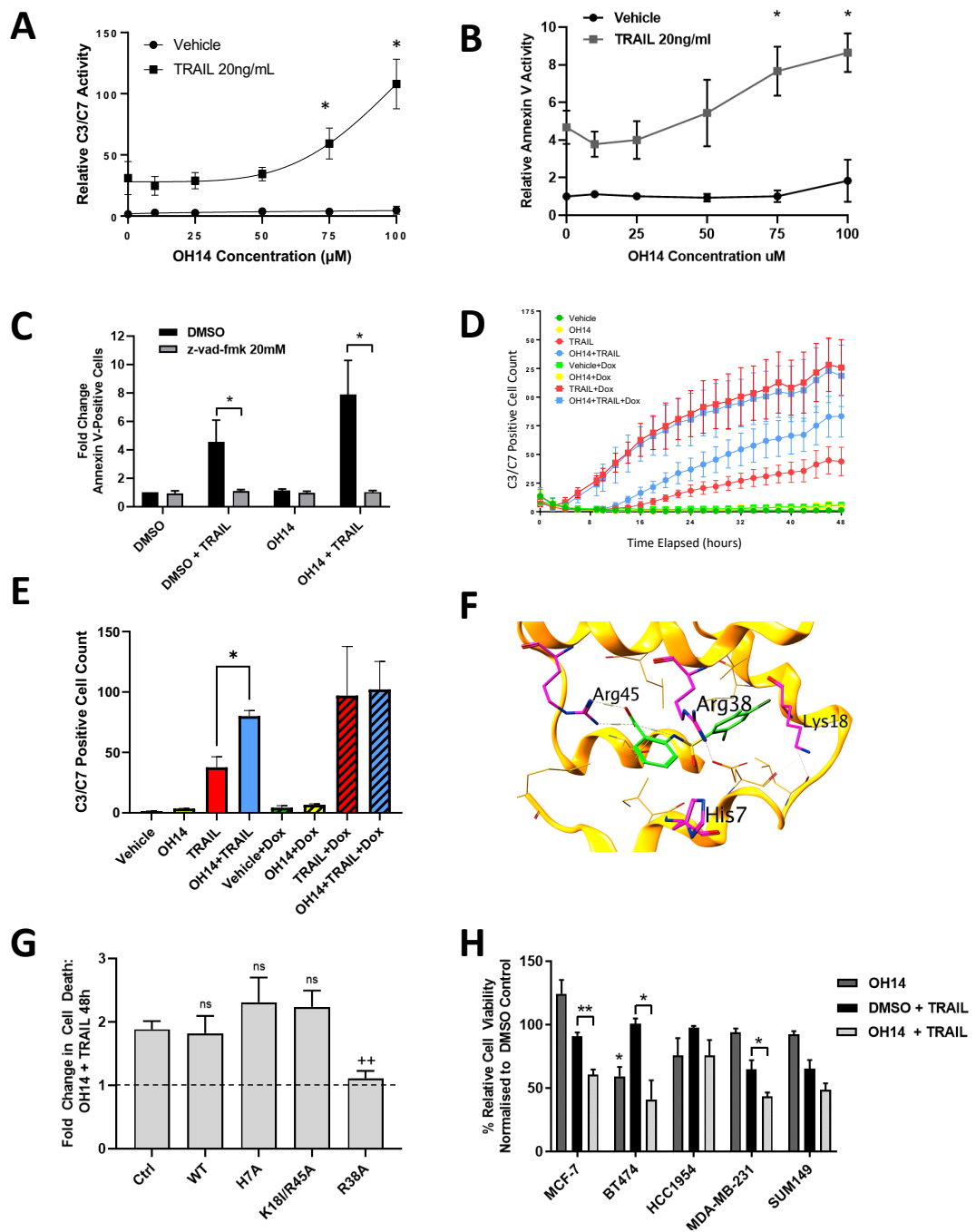
Appendix A-1 OH14 sensitises cancer cells to TRAIL via cFLIP.

A - B MCF7 cells (**A**) and HeLa cells (**B**) were treated with a range of concentrations of OH14 followed by 20ng/ml TRAIL for 48 hours and viability assessed by cleaved caspase 3/7 (**A**) and Annexin V (**B**) staining using Incucyte real-time analysis. * = $p < 0.05$ vs untreated control. **C** HeLa cells were treated with 100μM OH14 in the presence of 20mM Z-Vad-fmk pan-caspase inhibitor followed by 20ng/ml TRAIL for 18 hours and viability assessed by Annexin V staining using Incucyte real-time analysis. * = $p < 0.05$ vs untreated control. **D - E.** MCF7 cells stably overexpressing a doxycycline inducible shRNA targeting cFLIP were treated with doxycycline and/or 20ng/ml TRAIL and/or 75μM OH14 for up to 48 hours and monitored for cleaved caspase 3/7 by Incucyte real-time analysis. Graph (**D**) represents one of three independent repeats and bar chart (**E**) represents mean of 3 independent experiments at 48 hour. * = $p < 0.05$ vs TRAIL alone. **F.** Model of OH14 binding to DED1 pocket of cFLIP highlights the proximity of the interaction between OH14 (green) with Arg38. **G**. HeLa cells stably transfected with WT or mutant cFLIPL constructs were treated with 100μM OH14 followed by 20ng/ml TRAIL for 18 hours and viability assessed by Annexin V staining using Incucyte real-time analysis. Control is empty vector transfected cells. Data presented as fold change in cell death compared to TRAIL-treated cells for each construct. * = $p < 0.05$ compared to control (for absolute values of % annexin V positive cells, see Supplementary Figure 8). **H.** A panel of breast cancer cell lines were treated with 100μM OH14 followed by 20ng/ml TRAIL for 18 hours and viability assessed by cell-titre-blue assay. * = $p < 0.05$, ** = $p < 0.01$ compared to TRAIL alone. All experiments represent minimum of 3 independent replicates. Figure taken from French et al. (unpublished, manuscript in preparation).
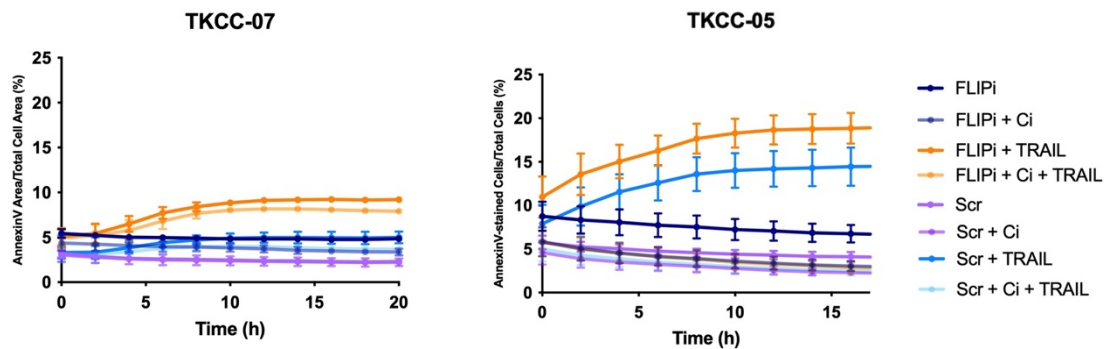
Appendix A-2 OH14 Sensitises breast cancer stem-like cells to TRAIL.
A MCF-7 cells were treated with 100microM OH14 followed by 20ng/ml TRAIL for 18 hours then assayed for colony formation. Error bars = standard error mean. **p<0.01 vs TRAIL alone. **B** A panel of breast cancer cell lines were treated with 100µM OH14 followed by 20ng/ml TRAIL for 18 hours then assayed for tumoursphere formation. Tumourspheres were counted 7 days later (TFU = tumoursphere-forming unit). Error bars = standard error mean. *p<0.05 vs control, ***p<0.001 vs control; **C** MCF-7s and BT474s from **B** were passaged in the absence of OH14 and TRAIL and secondary tumourspheres quantified after a further 7 days. *p<0.05 vs TRAIL alone, **p<0.01 vs TRAIL alone. **D** A panel of primary-derived breast cancer cell lines were treated with 100µM OH14 followed by 20ng/ml TRAIL for 18 hours then assayed for tumoursphere formation. Tumourspheres were counted 7 days later. *p<0.05 vs TRAIL alone. **E** MDA-MB-231 were pre-treated with 100µM OH14 followed by 20 ng/ml TRAIL for 18 hours then harvested and implanted into the mammary fat pad of athymic nude mice at serial dilutions. The number of tumours formed relative to transplants was determined by palpation and confirmed by histological analysis at the end of the experiment. Estimate of cancer stem cell numbers was calculated including 95% confidence limits. Figure taken from French et al. (unpublished, manuscript in preparation).
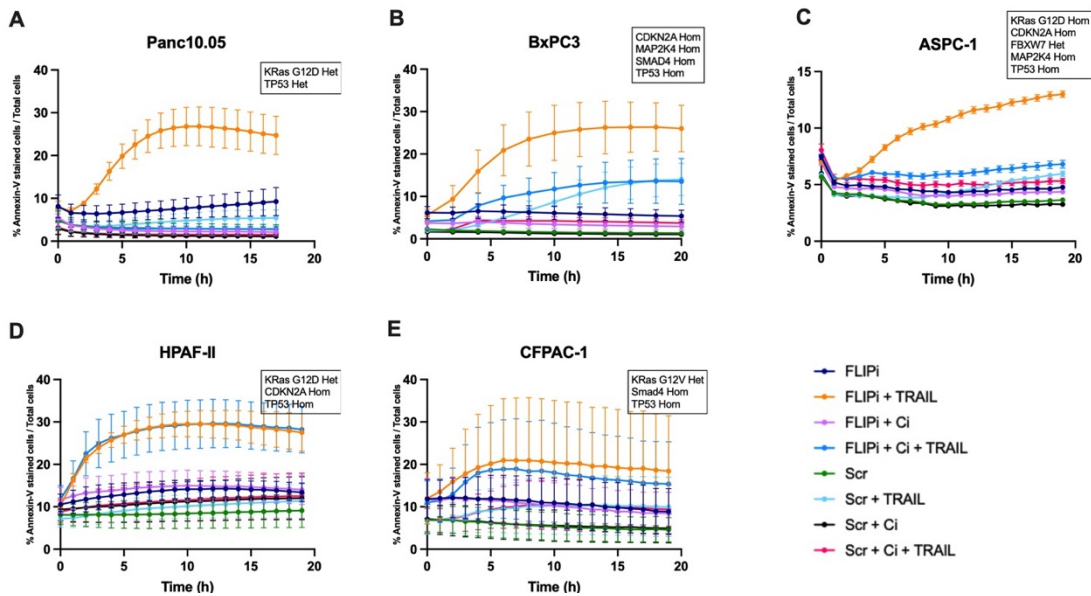
Appendix A-3 Longitudinal apoptotic response of Established Pancreatic Cancer Cell Line (EPCCL) panel to siRNA cFLIP inhibition (FLIPi) with and without exogenous TRAIL and Caspase inhibitors (Ci). Annexin-V-stained cells represent those undergoing apoptosis, which was normalised to total number of cells in each well. Cells were pre-incubated with siRNA for 48 hours prior to the addition of Annexin V (and TRAIL where relevant). 50uM caspase inhibitors were added 24 and 48 hours post-siRNA incubation where relevant. Timepoint 0h on each graph indicates the point at which Annexin V and TRAIL was added. Data represents mean ± SEM for a total of at least 3 independent repeats per cell line. Data was collected using the Incucyte S3 Live Cell Analysis platform (Essen Bioscience). FLIPi = siRNA targeting cFLIP. Scr = scrambled RNA; TRAIL = recombinant human TRAIL. Ci = 50 µM Pan Caspase Inhibitor Z Vad-FMK (R&D Systems, MN, USA).

Appendix A-4 Longitudinal apoptotic response of KRAS-mutant primary patient-derived pancreatic cancer cell lines (PDCLs) to FLIPi with and without exogenous TRAIL and Caspase inhibitors (Ci). Annexin-V-stained cells represent those undergoing apoptosis, which was normalised to total number of cells in each well. Cells were pre-incubated with siRNA for 48 hours prior to the addition of Annexin V (and TRAIL where relevant). 50uM caspase inhibitors were added 24 and 48 hours post-siRNA incubation where relevant. Timepoint 0h on each graph indicates the point at which Annexin V and TRAIL was added. Data represents mean ± SEM for a total of at least 3 independent repeats per cell line. Data was collected using the Incucyte S3 Live Cell Analysis platform (Essen Bioscience). FLIPi = siRNA targeting cFLIP. Scr = scrambled RNA; TRAIL = recombinant human TRAIL. Ci = 50 µM Pan Caspase Inhibitor Z Vad-FMK (R&D Systems, MN, USA).